The muon $g-2$: the hadronic vacuum polarisation contributions

Thesis submitted in accordance with the requirements of
the University of Liverpool for the degree of Doctor of Philosophy

by

Alexander Iraj Keshavarzi.

June 2018

Declaration

I hereby declare that the work presented in this thesis is the result of my own research activities unless reference is given to others. None of this material has been previously submitted to this or any other university. All work presented here was carried out in the Department of Mathematical Sciences at the University of Liverpool, Liverpool, U.K. and at the Fermi National Accelerator Laboratory (Fermilab), Batavia, IL, U.S.A. during the period from October 2014 to June 2018.

Contributions to this work have previously been published or are awaiting publication elsewhere in:

- D. Boito, M. Golterman, **A. Keshavarzi**, K. Maltman, D. Nomura, S. Peris and T. Teubner, '*The strong coupling from* $e^+e^- \to$ *hadrons below charm*', arXiv:1805.08176 [hep-ph], submitted to Phys. Rev. D (2018).

- A. P. Schreckenberger, A. Chapelain, A. A. Mikhailichenko, D. Rubin, D. Barak, C. Jensen, G. Krafczyk, R. Madrak, H. Nguyen, H. Pfeffer, M. Popovic, J. Stapleton, C. Stoughton, **A. Keshavarzi**, J. L. Holzbauer, N. Froemming, '*New Fast Kicker Results From The Muon* $g-2$ *E-989 Experiment at Fermilab*', IPAC THPML093, Proceedings of IPAC2018.

- **A. Keshavarzi**, D. Nomura and T. Teubner, '$\alpha(q^2)$ *in the space- and time-like region and its role in* $g-2$ *and* $\alpha(M_Z^2)$', in preparation (2018).

- **A. Keshavarzi**, D. Nomura and T. Teubner, '*The muon* $g-2$ *and* $\alpha(M_Z^2)$*: a new data-based analysis*', Phys. Rev. D **97** (2018) 114025.

- **A. Keshavarzi**, D. Nomura and T. Teubner, '*The hadronic vacuum polarisation contributions to the muon* $g-2$', arXiv:1802.06229 [hep-ph], submitted to Frascati Physics Series (2018).

- **A. Keshavarzi**, '*Measurement of the kicker pulse of the Muon* $g-2$ *experiment (E989) using a Faraday magnetometer*', E989 (Muon $g-2$ experiment) Note 129 (2017).

- A. Anastasi *et al.* [KLOE-2 Collaboration], **A. Keshavarzi**, S. E. Müller and T. Teubner, '*Combination of KLOE* $\sigma\big(e^+e^- \to \pi^+\pi^-\gamma(\gamma)\big)$ *ISR measurements and* $a_\mu^{\pi^+\pi^-}$ *between* $0.1 \leq s \leq 0.95$ GeV^2', JHEP **1803** (2018) 173.

- K. Hagiwara, **A. Keshavarzi**, A. D. Martin, D. Nomura and T. Teubner, '*g-2 of the muon: status report*,' Nucl. Part. Phys. Proc. **287-288** (2017) 33.

- **A. Keshavarzi**, '$(g-2)_\mu$*: recent improvements and outlook*', 18th meeting of the Working Group on Radiative Corrections and MC Generators for Low Energies (RadioMonteCarLOW) workshop proceedings, arXiv:1609.05651 [hep-ph].

Abstract

The anomalous magnetic moment of the muon, $a_\mu = (g-2)_\mu/2$, stands as an enduring test of the Standard Model (SM), where the $\sim 3.5\sigma$ (or higher) discrepancy between the experimental measurement $a_\mu^{\rm exp}$ and the SM prediction $a_\mu^{\rm SM}$ could be an indication of the existence of new physics beyond the SM. This work presents a complete re-evaluation of the hadronic vacuum polarisation contributions to the anomalous magnetic moment of the muon, $a_\mu^{\rm had,\,VP}$, from a combination of available $e^+e^- \to$ hadrons cross section data as input in a predominantly data driven analysis. Focus has been placed on the development of a new data combination method, that has been advocated to be free of bias and allows for the full use of any available correlated statistical and systematic uncertainties into the determination of both the resulting mean value and corresponding error.

In a related work, the three precision measurements of the cross section $\sigma\big(e^+e^- \to \pi^+\pi^-\gamma(\gamma)\big)$ using initial state radiation by the KLOE collaboration provide an important input for the prediction of the hadronic contribution to the anomalous magnetic moment of the muon. These measurements are correlated for both statistical and systematic uncertainties and, therefore, the simultaneous use of these measurements requires covariance matrices that fully describe the correlations. The construction of these matrices has allowed for the determination of a combined KLOE measurement for $\sigma\big(e^+e^- \to \pi^+\pi^-\gamma(\gamma)\big)$ and yields a two-pion contribution to the muon magnetic anomaly in the energy range $0.3162 < \sqrt{s} < 0.9747$ GeV of $a_\mu^{\pi^+\pi^-} = (489.8 \pm 1.7_{\rm stat} \pm 4.8_{\rm sys}) \times 10^{-10}$.

For the full calculation of $a_\mu^{\rm had,\,LO\,VP}$ and $a_\mu^{\rm had,\,NLO\,VP}$, all available $e^+e^- \to$ hadrons cross section data have been analysed and included, where the new data compilation has yielded the full hadronic R-ratio and its covariance matrix in the energy range $m_\pi \leq \sqrt{s} \leq 11.2$ GeV. Using these combined data and pQCD above that range results in estimates of the hadronic vacuum polarisation contributions to $g-2$ of the muon of $a_\mu^{\rm had,\,LO\,VP} = (693.26 \pm 2.46) \times 10^{-10}$ and $a_\mu^{\rm had,\,NLO\,VP} = (-9.82 \pm 0.04) \times 10^{-10}$. The new estimate for the Standard Model prediction is found to be $a_\mu^{\rm SM} = (11\,659\,182.04 \pm 3.56) \times 10^{-10}$, which is 3.7σ below the current experimental measurement. Detailed comparisons with results from similar related works are given, as well as discussions of the prospects for improving the calculation of these contributions in the future.

Contents

List of Figures

Acknowledgements

First, to my supervisor, Thomas Teubner. I want to start by saying that the guidance, support and teaching that you have given to me over the last four years has been the basis for all my achievements during this time. My development into a dedicated and passionate researcher is down to you and I can't thank you enough. Although you have been my supervisor, you have also become a colleague and a friend, and I hope this relationship will continue as I move forward. In addition, I would like to thank our collaborator, Daisuke Nomura, for the time we have spent working together and for answering every question I have ever had without any objections.

There are many at the University of Liverpool who I owe a great debt. Amongst the staff in the Theoretical Physics division of the Mathematical Sciences Department, a special mention should be given to Ian Jack and Martin Gorbahn who, along with Thomas, made the decision to provide me with studentship funding in the later years of my studies. Without this funding, it would not have been possible for me to complete my PhD and, therefore, I also wish to thank the Science and Technology Facilities Council (STFC) for awarding me the studentship under the consolidated grant ST/N504130/1. I must also show appreciation to John Gracey for not only his support during my time at Liverpool, but also for having an open door for whenever there was a conversation to be had. In the Physics department, I would like to express real gratitude to Will Turner for first involving me in the experimental muon $g-2$ efforts at Liverpool and for doing more than his fair share in helping me to become part of the experiment ever since. This gratitude must also be extended to Barry King and Themis Bowcock, who first agreed that I should be able to visit Fermilab, supported my travels to the U.S. and pushed for me to be made a member of the Muon $g-2$ collaboration.

There are also many outside of the University of Liverpool who have been an integral part of my time there. For the seemingly small task to construct the KLOE combination covariance matrices that evolved into a many-year-long project, I want to express appreciation to Graziano Venanzoni and Stefan Müller. It was a pleasure to have worked with you on such an interesting piece of work and both of you taught me more than you realise. At the Muon $g-2$ experiment, I am hugely indebted to Chris Polly, whose belief in my ability and his efforts in making it possible for me to

work on the experiment at Fermilab are something that I will always be deeply grateful for. I want to thank Chris Stoughton for taking me on as an experimental novice and teaching me over my time working at the experiment. I must particularly thank Mark Lancaster for his confidence in me, for providing me with opportunities and, along with Chris Polly, Graziano and Thomas, for supporting my postdoc applications during my final year.

I am truly grateful to Matthew Leak and Lewis Ramsden for being such good friends to me. Not only have they both helped me with my work on countless occasions, but they also made Liverpool a fun place to live, made me effortlessly laugh at any moment and made the unbearable times bearable. To my flatmate, Nuno Padrão, thank you for agreeing to move up to Liverpool with me four years ago and being the best mate a guy could ask for since. Of all the things I'm going to miss from my life in Liverpool, I'm mostly going to miss living with you. I want to thank my close friends Aidan Ward, Matt Toll, Rory More, Alex Clark and Katy Recina. They have always stayed close even though I moved 200 miles away from home and have made the effort to visit me in Liverpool on more than one occasion.

To Rachel, no single person has supported me more during this time than you. This would not have been possible without you and I want you to know that it has been through our happiness that I have managed to achieve so much. You have truly been my best friend throughout the course of this work. Thank you for everything.

To my family, this piece of work is as much a credit to you all as it is to me. To my siblings, Benjamin and Jasmin, thank you for being the best brother and sister I could ask for. To my parents, thank you for giving and sacrificing so much for me to be able to spend most of the last decade at university to get to where I am now. Not only have you helped me financially, your emotional and moral support has been unwavering. To Mum, thank you for always being there for me and being the reason why I love coming home. No one makes home like you do. To Baba, thank you for always pushing me to be the best I can be. I know you always wished that you had attempted a PhD and I hope that, maybe now, you feel more like you've achieved one. For both of you, this is for you.

'*If I have seen further, it is by standing upon the shoulders of giants.*'
Sir Isaac Newton, 1675.

Chapter 1

Introduction

The anomalous magnetic moment of the muon, $a_\mu = (g-2)_\mu/2$, stands as an enduring test of relativistic quantum field theories. In particular, it provides the ability to rigorously scrutinise the theories of quantum electrodynamics (QED) and, indeed, the Standard Model (SM). There exists an $\sim 3.5\sigma$ (or higher) discrepancy between the experimental measurement a_μ^{exp} and the SM prediction a_μ^{SM}. The experimental measurement of a_μ, as an observable, manifestly includes the effects from all contributing physical processes, whether they originate from the SM or new physics. Consequently, the current deviation between experiment and theory could be an indication of the existence of new physics beyond the SM. With extensive efforts currently being made to improve the experimental estimate, it is imperative that the SM prediction is also improved to determine whether the $g-2$ discrepancy is well established.

The magnetic moment $\vec{\mu}$ of an elementary charged particle depends on the spin $\vec{S} = \frac{1}{2}\vec{\sigma}$ (where $\vec{\sigma}$ are the Pauli matrices) of the particle, defined by the relation[1]

$$\vec{\mu} = -\frac{e}{2m} g \vec{S}\,. \tag{1.1}$$

Here, e is the electric charge, m is the mass of the particle and g is the gyromagnetic factor which describes the strength of the coupling of the spin to the magnetic moment. The Dirac equation, following from Dirac's theory describing the interaction of the electron with the photon [1,2], implies that $g = 2$ for fermions ($|\vec{S}| = \frac{1}{2}$). At tree-level, this implication holds. However, relativistic quantum field theories such as QED and the SM require the inclusion of the effects from higher order processes, commonly known as radiative corrections. These corrections provide contributions to g, therefore causing a deviation from $g = 2$. This deviation, denoted as a, is the anomalous magnetic moment and describes the contributions from all higher order SM processes that contribute to the gyromagnetic factor and, therefore, to the magnetic moment $\vec{\mu}$.

[1] The use of natural units, $\hbar = c = 1$, will be assumed throughout this work, unless specifically stated.

1.1 The anomalous magnetic moment

At tree-level, the general form of the vertex function Γ describing the electromagnetic interaction of a lepton and a photon is given by

$$\Gamma^{\mu}_{\text{tree-level}}(k_1, k_2) = \quad = -ie\gamma^{\mu}\,. \tag{1.2}$$

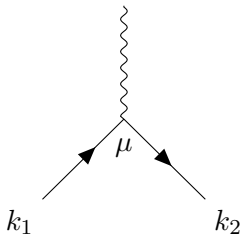

Here, μ is a Lorentz index, k represent the fermion momenta, γ^{μ} are the Dirac gamma matrices and e is the QED charge. The contribution to the gyromagnetic ratio from this diagram is precisely the Dirac prediction, $g = 2$. In QED, the physical vertex function Γ^{μ} encapsulates all higher order effects. It is given by

$$\Gamma^{\mu}(k_1, k_2) = \quad = \quad + \quad + \ldots \tag{1.3}$$

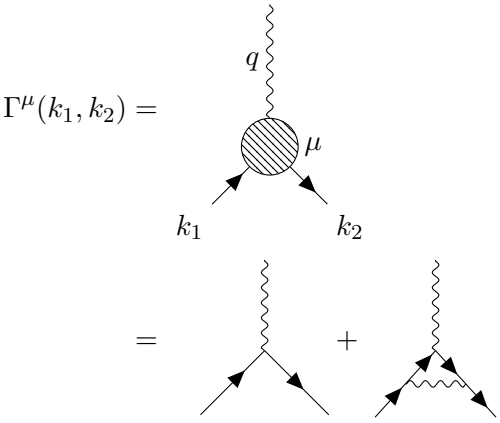

which is the sum of all one-particle-irreducible (1PI) diagrams to all orders. The anomalous magnetic moment describes the total contribution to g from all the corresponding 1PI diagrams of one-loop order and higher, as will be shown in the following.

The matrix element for the QED interaction in equation (1.3) is

$$i\mathcal{M}^{\mu} = -ie\bar{u}(k_2)\Gamma^{\mu}(k_1, k_2)u(k_1)\,. \tag{1.4}$$

In general, $q^2 = (k_2 - k_1)^2 \neq 0$ and $k_1^2 = k_2^2 = m^2$, where q is the momenta of the external photon and m denotes the fermion mass. In order for the vertex function to transform as a Lorentz four-vector, the vertex function Γ^{μ} can be constructed from any linear combination of the four-vectors γ^{μ}, k_1^{μ} and k_2^{μ}. Making the choice to use the combinations $k_2^{\mu} + k_1^{\mu}$ and $k_2^{\mu} - k_1^{\mu}$, the vertex function can be written as

$$\Gamma^{\mu}(k_1, k_2) = \gamma^{\mu}A + (k_2^{\mu} + k_1^{\mu})B + (k_2^{\mu} - k_1^{\mu})C\,, \tag{1.5}$$

where, in general, A, B and C can be considered as matrices involving k_1^{μ} and k_2^{μ}. However, as the vertex function always appears in between the on-shell spinors $\bar{u}(k_2)$

and $u(k_1)$ (as in equation (1.4)), the on-shell spinor identities, $\not{k}u(k) = mu(k)$ and $\bar{u}\not{k} = \bar{u}(k)m$, imply that A, B and C are scalar functions of q^2 (or m). Imposing the Ward identity $q_\mu \Gamma^\mu = 0$, only the first two terms in equation (1.5) vanish, implying that $C = 0$ for the Ward identity to hold. Finally, using the Gordon decomposition

$$\bar{u}(k_2)\gamma^\mu u(k_1) = \frac{1}{2m}\bar{u}(k_2)\Big[k_1^\mu + k_2^\mu + iq_\nu \sigma^{\mu\nu}\Big]u(k_1)\,, \tag{1.6}$$

the general form of the QED vertex function can be expressed as

$$\Gamma^\mu(k_1, k_2) = -ie\left[\gamma^\mu F_1(q^2) + \frac{i\sigma^{\mu\nu}q_\nu}{2m}F_2(q^2)\right], \tag{1.7}$$

where $\sigma^{\mu\nu} = \frac{i}{2}[\gamma^\mu, \gamma^\nu]$. The quantities $F_1(q^2)$ and $F_2(q^2)$ correspond to the surviving scalar functions A and B and are known as *form factors*. $F_1(q^2)$ is the electric charge form factor, which describes the radiative corrections to the electric charge of the fermion. Therefore, in the limit that $k_2 - k_1 = q \to 0$, it follows that $F_1(0) = 1$ exactly.

Assuming this and taking the non-relativistic limit of an interaction with a classical electromagnetic field A^μ, the vertex is described by the Dirac equation in the form

$$\left(\gamma^\mu(\partial_\mu - ieA_\mu) - m + \frac{eF_2(0)}{4m}F_{\mu\nu}\sigma^{\mu\nu}\right)\psi = 0\,. \tag{1.8}$$

In this limit, the effective Hamiltonian is

$$H = \left[\frac{1}{2m}(\vec{p} - e\vec{A})^2 + eA^0 + \frac{e}{2m}\big(1 + F_2(0)\big)\vec{\sigma}.\vec{B}\right], \tag{1.9}$$

where $\vec{p}$ is the momentum of the fermion and $\vec{B}$ is an external magnetic field. The last term in equation (1.9) corresponds to the magnetic interaction potential, $U = -\vec{\mu}\cdot\vec{B}$. Comparing this with the definition of the magnetic moment in equation (1.1),

$$-\vec{\mu}\cdot\vec{B} = \frac{e}{2m}\big(1 + F_2(0)\big)\vec{\sigma}.\vec{B} = \frac{e}{2m}g\vec{S}.\vec{B} = \frac{e}{4m}g\vec{\sigma}.\vec{B}\,, \tag{1.10}$$

implies

$$g = 2 + 2F_2(0)\,. \tag{1.11}$$

The form factor $F_2(0)$ is precisely the anomalous magnetic moment induced by higher order 1PI diagrams that cause the gyromagnetic factor to deviate from the Dirac (tree-level) prediction of $g = 2$. Rearranging equation (1.11) reveals the standard form of the anomalous magnetic moment,

$$a = F_2(0) = \frac{g-2}{2}\,. \tag{1.12}$$

The lowest order contribution to a comes from the one-loop diagram of a virtual

photon exchange between the two fermion lines. The Feynman rules give

$$\Gamma^{\mu}_{\text{1-loop}}(k_1,k_2) = \quad \text{ 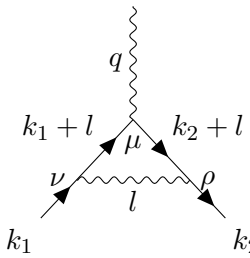 }$$

$$= e^3 \int \frac{\mathrm{d}^4 l}{(2\pi)^4} \frac{\gamma^{\rho}\big(i(\not{k}_2 + \not{l}) + m\big)\gamma^{\mu}\big(i(\not{k}_1 + \not{l}) + m\big)\gamma^{\nu}}{\big((k_2+l)^2 - m^2 - i\varepsilon\big)\big((k_1+l)^2 - m^2 - i\varepsilon\big)} \frac{g_{\nu\rho}}{\big(l^2 - i\varepsilon\big)} \,. \tag{1.13}$$

For all leptons ($l = e, \mu, \tau$), the evaluation of this integral results in a one-loop $\big(\mathcal{O}(\alpha)\big)$ contribution to the anomalous magnetic moment of

$$a_l^{1-\text{loop}} = F_2^{1-\text{loop}}(0) = \frac{e^2}{8\pi^2} = \frac{\alpha}{2\pi} \,, \tag{1.14}$$

where $\alpha = \alpha(0) \equiv e^2/4\pi$ is the fine structure constant and, therefore,

$$g_{1-\text{loop}} = 2 + \frac{\alpha}{\pi} \,. \tag{1.15}$$

This result was first determined as the one loop contribution to the anomalous magnetic moment of the electron in 1948 by Schwinger [3], where he found $a_e = 0.001162$. This was a fundamental success of relativistic quantum field theories, being the first prediction of the higher order effects that arise from the renormalisation of QED [4–6]. This, coupled with the first experimental measurements of $g_e = 2.00238 \pm 0.00010$ by Kusch and Foley [7, 8] in the same year, demonstrated the validity of QED and its prediction of the effects from radiative corrections.

1.2 The anomalous magnetic moment of the muon, a_μ

Although the current predictions [9] and measurements [10,11] of the electron anomaly a_e are the most precisely known physical quantities to date, the muon, due to its larger mass, is more sensitive to the possibility of new physics at higher energy scales [12]. For a particle with mass $M >> m_l$ (where m_l is the lepton mass), the contribution from this particle to a_l is proportional to $(m_l/M)^2$, such that the ratio of the contribution to the muon anomaly and the electron anomaly is

$$\frac{a_\mu^M}{a_e^M} \sim \frac{(m_\mu/M)^2}{(m_e/M)^2} = \left(\frac{m_\mu}{m_e}\right)^2 , \tag{1.16}$$

making the muon $\sim 4 \times 10^4$ times more sensitive to the effects from heavy particles than the electron. This being the case, the motivation to both theoretically predict and experimentally measure a_μ to a high precision is highly compelling. The anomalous

magnetic moment of the muon (muon $g-2$) receives contributions from all sectors of the SM

$$a_\mu = a_\mu^{\mathrm{QED}} + a_\mu^{\mathrm{EW}} + a_\mu^{\mathrm{had}}\,, \tag{1.17}$$

where the superscripts 'EW' and 'had' indicate the contributions from the electroweak and hadronic sectors respectively. Consequently, should the comparison of both theory and experiment yield results in clear agreement, the success of the SM would be further consolidated. However, should there exist a discrepancy between the SM prediction a_μ^{SM} and the experimental measurement a_μ^{exp}, this could be an indication of the contribution of the existence of physics beyond the SM (BSM). In this case,

$$a_\mu = a_\mu^{\mathrm{QED}} + a_\mu^{\mathrm{EW}} + a_\mu^{\mathrm{had}} + a_\mu^{\mathrm{BSM}}\,. \tag{1.18}$$

In the following, the current status of a_μ^{exp} and a_μ^{SM} are presented, with details given on the efforts to reduce the uncertainty on both estimates in order to provide a meaningful comparison.

1.2.1 The experimental measurement of a_μ: current status

The experimental measurements of the anomalous magnetic moment of the muon are dominated by the measurements made at the Brookhaven National Laboratory (BNL) [13–15], resulting in a world average of [16]

$$a_\mu^{\mathrm{exp}} = 11\ 659\ 209.1\ (5.4)_{\mathrm{stat}}\ (3.3)_{\mathrm{sys}} \times 10^{-10}\,, \tag{1.19}$$

where the uncertainties given are the statistical and systematic uncertainties respectively. With the uncertainties of the BNL measurements being statistically dominated, efforts to improve the experimental estimate at Fermilab (FNAL) [17] aim to increase the statistics of the new measurement by a factor of ~ 20 compared to those from BNL and reduce the overall experimental uncertainty by a factor of four compared to equation (1.19). Following the same methodology as the Brookhaven measurements, the Muon $g-2$ experiment at FNAL will produce and store muons in order to measure two frequencies: the frequency ω_a at which the muon spin (polarisation) turns relative to its momentum and the value of the magnetic field normalised to the Larmor frequency of a free proton, ω_p.

Assuming a perfect vertical magnetic field, with a muon on the ideal orbit, the anomalous frequency $\vec{\omega}_a$ is defined in terms of the spin frequency $\vec{\omega}_S$ and the cyclotron frequency $\vec{\omega}_C$ as

$$\vec{\omega}_a = \vec{\omega}_S - \vec{\omega}_C\,. \tag{1.20}$$

In the absence of any other external fields,

$$\vec{\omega}_S = -g\frac{Qe}{2m}\vec{B} - (1-\gamma)\frac{Qe}{\gamma m}\vec{B} \tag{1.21}$$

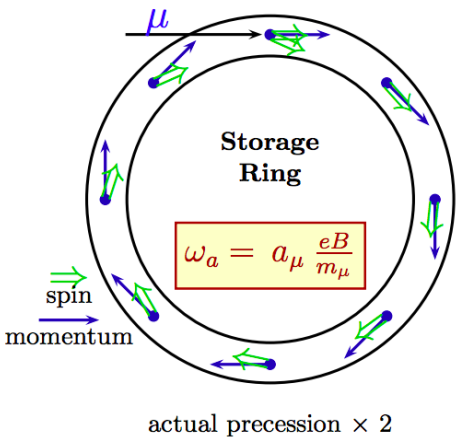

Fig. 1.1: The spin precession of muons as utilised by the Muon $g-2$ experiment in order to measure a_μ. This graphic has been taken from [18].

and

$$\vec{\omega}_C = -\frac{Qe}{m\gamma}\vec{B}\,, \tag{1.22}$$

where $Q = \pm 1$ is the electric charge, $\vec{B}$ is the external magnetic field and γ is the relativistic Lorentz factor. Therefore,[2]

$$\vec{\omega}_a = \vec{\omega}_S - \vec{\omega}_C = -\left(\frac{g-2}{2}\right)\frac{Qe}{m}\vec{B} = -a\frac{Qe}{m}\vec{B}\,. \tag{1.23}$$

Here, it is observed that should $g = 2$ exactly, then it would follow that $\vec{\omega}_S = \vec{\omega}_C$ such that the muon spin would precess with the same frequency as the orbital frequency. Consequently, it can be seen that $\vec{\omega}_a$ has two important features: it depends only on the anomaly rather than the full magnetic moment and that it depends linearly on the applied magnetic field. This is depicted in Figure 1.1. Therefore, to determine a_μ requires the experiment to measure $\vec{\omega}_a$ and the magnetic field averaged over the muon beam distribution, $\langle\vec{B}\rangle$.

The direct measurement of these properties requires the production and storage of muons. A diagram of the experimental setup is shown in Figure 1.2, where (from [17]) the experiment itself consists of the following steps:

1. Production of an appropriate pulsed proton beam by an accelerator complex.

2. Production of pions using this proton beam.

3. Polarised muons are then produced from the decay $\pi^+ \to \mu^+\nu_\mu$.

[2] As these equations assume a perfect vertical magnetic field, they are only approximations of the real behaviour of the muons inside the field. In reality, the field has longitudinal components which have an effect on the spin precession. This is accounted for in the experiment by assigning a systematic error due to the longitudinal field components.

4. To ensure a cleaner delivery of muons to the experiment than at BNL, the beam is then transported to a delivery ring. The beam circulates the delivery ring four times. During the first three rotations, essentially all remaining pions will decay to muons and any remaining heavier (slower) protons will naturally separate from the muons. This allows them to be safely removed from the beam by a kicker.

5. Transport of the muon beam into a storage ring.

6. Injection of the muon beam into the storage ring.

7. Kicking of the muon beam onto stored orbits.

8. Measuring the arrival time and energy of positrons from the muon decay $\mu^+ \rightarrow e^+ \bar{\nu}_\mu \nu_e$.

9. Precise mapping and monitoring of the precision magnetic field.

In order for the muon beam to be confined to the storage ring requires the use of an electric quadrupole field to provide vertical focusing. This introduces a new term to equation (1.23), where relativistic particles feel a motional magnetic field proportional to $\vec{\beta} \times \vec{E}$. Here, $\vec{\beta}$ denotes the muon velocity and $\vec{E}$ is the electric field. Therefore, assuming that the velocity is transverse to the magnetic field ($\vec{\beta} \cdot \vec{B} = 0$), the equation for $\vec{\omega}_a$ including the electric field reads

$$\vec{\omega}_a = -\frac{Qe}{m}\left[a_\mu \vec{B} - \left(a_\mu - \frac{1}{\gamma^2 - 1}\right)\frac{\vec{\beta} \times \vec{E}}{c}\right]. \tag{1.24}$$

The dependence on $\vec{E}$ requires a detailed knowledge of the electric field. Therefore, the experiment employs the fact that the electric field term vanishes when the experiment operates at the "magic" momentum $p_{\text{magic}} \simeq 3.09$ GeV/c ($\gamma_{\text{magic}} \simeq 29.3$), such that $a_\mu - \frac{1}{\gamma^2-1} = 0$ to leading order and the electric field does not contribute to the measurement of a_μ.

The measurement of the averaged magnetic field allows the determination of ω_p from

$$\omega_p = 2\mu_p |\vec{B}|\,, \tag{1.25}$$

where μ_p is the magnetic moment of the proton. From this, the anomalous magnetic moment of the muon can be determined from

$$a_\mu = \frac{\omega_a/\omega_p}{\mu_{\mu^+}/\mu_p - \omega_a/\omega_p} \tag{1.26}$$

where μ_{μ^+}/μ_p is the measured ratio of the muon and proton magnetic moments [19].

Achieving the required 20 times improvement in the overall statistics than those from BNL places harsh targets on the overall beam dynamics and magnetic field data. All contributing systems must function with the desired effectiveness both individually

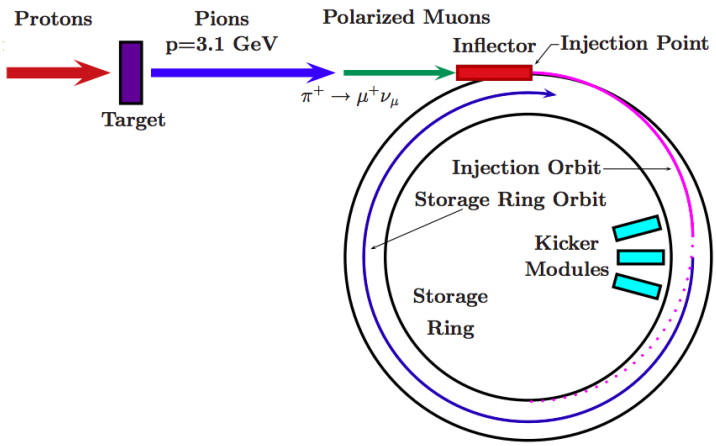

Fig. 1.2: The production, injection and storage of muons for the Muon $g-2$ experiment. This graphic has been taken from [18].

and together for the experiment to achieve this high statistics goal. The kicker system, for example, should deliver a flat magnetic pulse of 200-280 Gauss over 120ns to the muon beam in order to steer the muons onto the trajectory of the ideal orbit. To determine the effectiveness of the kicker field, a Faraday magnetometer was used to measure the kicker field and pulse shape. This has allowed detailed studies to be done into the performance of the kickers in order to maximise the muon capture efficiency and, therefore, obtain the desired statistics. Details of this work can be found in Appendix A.

In addition, a new experiment at J-PARC [20] is set to provide an independent measurement of a_μ^{exp} using an alternative approach to that of BNL/FNAL. To avoid the need for the electrostatic quadrupoles to focus the muon beam as with the Fermilab experiment, the J-PARC experiment will produce and store ultra-cold, slow muons in a homogeneous magnetic field. The slow muons will have extremely low emittance (i.e. low average spread of particles in the beam) due to their low momenta and, therefore, only very weak focusing by a magnetic field is required to confine the particle beam without significant muon losses. Consequently, the beam does not require vertical focusing from an electric field and the term proportional to $\vec{\beta} \times \vec{E}$ in equation (1.24) is omitted. In this way, $\vec{E} = 0$ for any γ, removing the requirement on the energy of the stored muons entirely. This experiment will provide an alternative experiment measurement of a_μ by still employing equation (1.26), but with a largely different set of experimental uncertainties compared to the FNAL experiment.

1.2.2 The SM prediction of a_μ: current status

From the analysis preceding this work [21] (denoted as HLMNT11), the determination of the hadronic vacuum polarisation contributions (see below) summed with the esti-

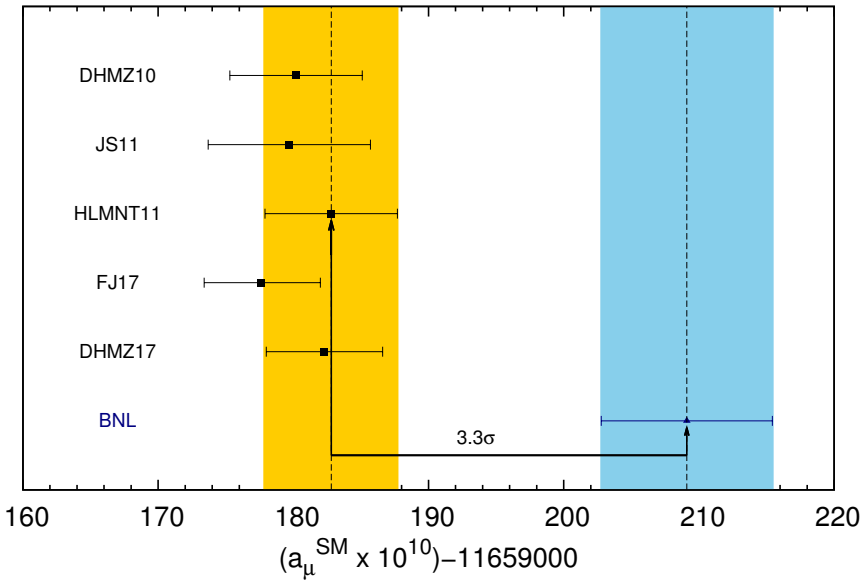

Fig. 1.3: Comparison of recent and previous evaluations of a_μ^{SM} preceding this work. The analyses listed in chronological order are: DHMZ10 [51], JS11 [52], HLMNT11 [21], FJ17 [36] and DHMZ17 [45], The central value of the estimate from the HLMNT11 collaboration is indicated by the dashed line centred in the yellow band, which defines the total uncertainty on this estimate. The current uncertainty on the experimental measurement [13–16] is given by light blue band.

mates of the other SM contributions at that time, resulted in a total SM prediction of

$$a_\mu^{\mathrm{SM}}\big(\mathrm{HLMNT11}\big) = (11\ 659\ 182.8 \pm 4.9) \times 10^{-10}\,. \tag{1.27}$$

This, compared with the experimental measurement in equation (1.19), resulted in a deviation between theory and experiment of $(26.1 \pm 8.0) \times 10^{-10}$, corresponding to a $(g-2)_\mu$ discrepancy of 3.3σ as depicted in Figure 1.3. Considering the efforts to achieve a four-fold improvement in the uncertainty of the experimental estimate at FNAL [17], it is therefore imperative that the SM prediction is also improved. Since [21], the estimates of the contributions from all sectors of the SM have been re-evaluated. These updated results, which will later be summed with the estimates of the hadronic vacuum polarisation contributions determined in this work, are summarised briefly below.

The QED contributions (where $a_\mu^{\mathrm{QED,\,1-loop}} = \alpha/2\pi$ from equation (1.14) is the one-loop QED contribution) are known up to and including five-loop accuracy. The five-loop calculation has recently been completed numerically by Kinoshita *et al.* [9,22] to evaluate all 12,762 five-loop diagrams. This calculation includes all contributions that are due to photons and leptons alone. They are found to be

$$\begin{aligned} a_\mu^{\mathrm{QED}} &= 11\ 658\ 471.8971\ (0.0007)\ (0.0017)\ (0.0006)\ (0.0072) \times 10^{-10} \\ &= (11\ 658\ 471.8971 \pm 0.007) \times 10^{-10}\,, \end{aligned} \tag{1.28}$$

where the uncertainties are owing to the uncertainty on the lepton masses, the four-loop contributions, the five-loop contributions and the determination of α using measurements of ^{87}Rb, respectively. With such a precise determination of $a_\mu^{\rm QED}$ resulting from a perturbative series that converges extremely well, the QED result seems stable. It should be noted, however, that the four-loop and five-loop contributions rely heavily on numerical integrations and independent checks of these results are crucial. This has been recently accomplished through several different analyses [23–28], which corroborate the results from Kinoshita and collaborators. Therefore, it is safe to assume that the estimate for the QED contribution is well under control.

The contribution from the EW sector is well known to two-loop accuracy [29–33]. With the mass of the Higgs now known, the updated estimate [34] gives

$$a_\mu^{\rm EW} = (15.36 \pm 0.10) \times 10^{-10}\,. \tag{1.29}$$

Although a relatively small contribution when compared to $a_\mu^{\rm QED}$, the uncertainty is not negligible considering the projected experimental accuracy but is small when compared to the hadronic uncertainties. However, with this contribution known safely to two-loop accuracy, the electroweak estimate is also very well under control.

The uncertainty of $a_\mu^{\rm SM}$ is completely dominated by the hadronic (had) contributions, $a_\mu^{\rm had}$, attributed to the contributions from the non-perturbative, low energy region of hadronic resonances. The hadronic contributions are divided into the hadronic vacuum polarisation (VP) and hadronic light-by-light (LbL) contributions, which are summed to give

$$a_\mu^{\rm had} = a_\mu^{\rm had,\,VP} + a_\mu^{\rm had,\,LbL}\,. \tag{1.30}$$

The hadronic vacuum polarisation contributions can be separated into the leading-order (LO) and higher-order contributions, where the LO and next-to-leading order (NLO) contributions are calculated in this work (see Section 1.3 and Section 4). In [21], the LO hadronic vacuum polarisation contributions were found to give

$$a_\mu^{\rm had,\,LO\,VP}\big({\rm HLMNT11}\big) = (694.91 \pm 4.27) \times 10^{-10} \tag{1.31}$$

and the NLO contributions to be

$$a_\mu^{\rm had,\,NLO\,VP}\big({\rm HLMNT11}\big) = (-9.84 \pm 0.07) \times 10^{-10}\,. \tag{1.32}$$

The calculation of the NNLO hadronic vacuum polarisation contribution been achieved for the first time in [35] (see also the evaluation in [36]) and is estimated to be

$$a_\mu^{\rm had,\,NNLO\,VP} = (1.24 \pm 0.01) \times 10^{-10}\,. \tag{1.33}$$

The hadronic LbL contributions (which enter at $\mathcal{O}(\alpha^3)$), although small compared to the hadronic vacuum polarisation sector, have only been fully determined through several different model-dependent approaches.

A commonly quoted determination of the LbL contribution is the 'Glasgow consensus' estimate of $a_\mu^{\text{had, LbL}}$('Glasgow consensus') $= (10.5 \pm 2.6) \times 10^{-10}$ [37] (alternatively, see [18, 38–40]). However, recent works [41–43] have re-evaluated the contribution to $a_\mu^{\text{had,LbL}}$ due to axial exchanges, where it has been found that this contribution has, in the past, been overestimated due to an incorrect assumption that the form factors for the axial meson contribution are symmetric under the exchange of two photon momenta [41]. Under this assumption, the determination in [38] previously found the axial vector contribution to be $a_\mu^{\text{had, LbL; axial}} = (2.2 \pm 0.5) \times 10^{-10}$. Correcting this reduces this contribution to $a_\mu^{\text{had, LbL; axial}} = (0.8 \pm 0.3) \times 10^{-10}$ [41, 42]. Applying this adjustment to the 'Glasgow consensus' result (which used a value of the axial vector contribution in [37] of $a_\mu^{\text{had, LbL; axial}} = (1.5 \pm 1.0) \times 10^{-10}$), the estimate in [43] finds

$$a_\mu^{\text{had, LbL}} = (9.8 \pm 2.6) \times 10^{-10} \ , \tag{1.34}$$

which is the chosen estimate for $a_\mu^{\text{had, LbL}}$ in this work. This result is notably lower than the previously accepted LbL estimates and will incur an overall downward shift on a_μ^{SM}. It is, however, still within the original uncertainties when comparing with the original 'Glasgow consensus' estimate. In addition, the recent work [40] has provided an estimate for the next-to-leading order hadronic LbL contribution. It has found $a_\mu^{\text{had, NLO LbL}} = (0.3 \pm 0.2) \times 10^{-10}$.

A comparison of recent and previous evaluations of a_μ^{SM} preceding this work with equation (1.19) is given in Figure 1.3. It can be seen that since [21], two newer works (FJ17 [36] and DHMZ17 [45]) have re-evaluated a_μ^{SM} to a higher precision. This analysis is a complete re-evaluation (in line with previous works [21, 46, 47]) of the hadronic vacuum polarisation contributions and, summing these with the estimates of the contributions from all other sectors of the SM listed above, will present a corresponding update of a_μ^{SM} and the resulting $(g-2)_\mu$ discrepancy. The results from this work will be compared with the FJ17 and DHMZ17 analyses in Section 4.5.

1.3 The hadronic vacuum polarisation contributions, $a_\mu^{\text{had, VP}}$

Although the contributions from QED and the electroweak sectors may be calculated reliably using perturbation theory, the running of the strong coupling constant, $\alpha_s(q^2)$, results in $\alpha_s(q^2)$ being large at low energies. Therefore, the perturbative expansion of $\alpha_s(q^2)$ is not valid for these energy domains, meaning that perturbative QCD (pQCD) is only reliable for sufficiently large q^2.[3] However, the hadronic vacuum polarisation (VP) contributions are dominated by the exchange of virtual photons with low q^2, requiring an alternative method to determine the loop integrals. In this case, the failure of pQCD

[3] Above ~ 2 GeV, the predictions of the running of $\alpha_s(q^2)$ from pQCD agree well with experimental data [16] and, therefore, perturbation theory can be safely used (away from quark threshold regions).

is overcome by utilising the tools of analyticity, unitarity and experimental hadronic cross section data, as will be discussed in the following.

The Feynman diagram of the LO hadronic VP contribution is shown in Figure 1.4, where the exchange of the photon between the muon lines (as in the standard one-loop QED case in equation (1.13)) is altered by the insertion of an internal hadronic bubble, which represents all possible hadronic states. This contribution to the photon propagator is exactly the hadronic contribution to the photon vacuum polarisation tensor, $\Pi_{\mu\nu}(q^2)$. The LO hadronic VP contribution enters at $\mathcal{O}(\alpha^2)$ and is formally, therefore, a second order contribution to a_μ^{SM}. However, of all the possible corrections to a_μ^{SM}, it is the largest single hadronic contribution. This, coupled with the invalidity of pQCD to evaluate this correction, has resulted in it being the largest contribution to the uncertainty of a_μ^{SM} for some time.

In this work, the calculation of the leading order hadronic vacuum polarisation contribution to the anomalous magnetic moment of the muon, $a_\mu^{\mathrm{had,\,LO\,VP}}$, utilises the method of dispersion relations and, as input for the low energy hadronic final states, the experimentally measured cross section $\sigma(e^+e^- \to \text{hadrons})$. Estimates of this quantity from recent works that have also used this method are given in Figure 1.5, where this work is a complete re-evaluation of the estimate by the HLMNT11 collaboration [21], also given in equation (1.31). Comparing this estimate for $a_\mu^{\mathrm{had,\,LO\,VP}}$ with the corresponding estimate for a_μ^{SM} in equation (1.27), the motivation for a re-evaluation of $a_\mu^{\mathrm{had,\,LO\,VP}}$ with an aim to improve its precision is apparent when considering that although the LO hadronic VP contribution only constitutes less than a percent of a_μ^{SM}, it is responsible for greater than 70% of the total SM uncertainty. With the estimate in equation (1.31) having already achieved a precision of $\sim 0.6\%$, a precision of better than this is one of the major aims of this work. In order to achieve this, the following section will introduce the method and tools used to evaluate the contribution to a_μ^{SM} from the Feynman diagram in Figure 1.4, first deriving the dispersion relation approach to evaluating $a_\mu^{\mathrm{had,\,LO\,VP}}$, followed by details on the use of the optical theorem to allow the use of the experimentally measured hadronic cross section data.

1.3.1 Calculating the leading order hadronic vacuum polarisation contribution, $a_\mu^{\mathrm{had,\,LO\,VP}}$

The evaluation of the contribution to a_μ from the diagram in Figure 1.4 is entirely dependent on the ability to determine the vacuum polarisation tensor $\Pi_{\mu\nu}(q^2)$. For the

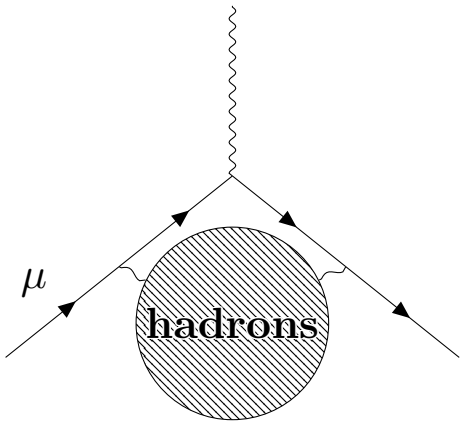

Fig. 1.4: The Feynman diagram of the leading order hadronic vacuum polarisation contribution to a_μ.

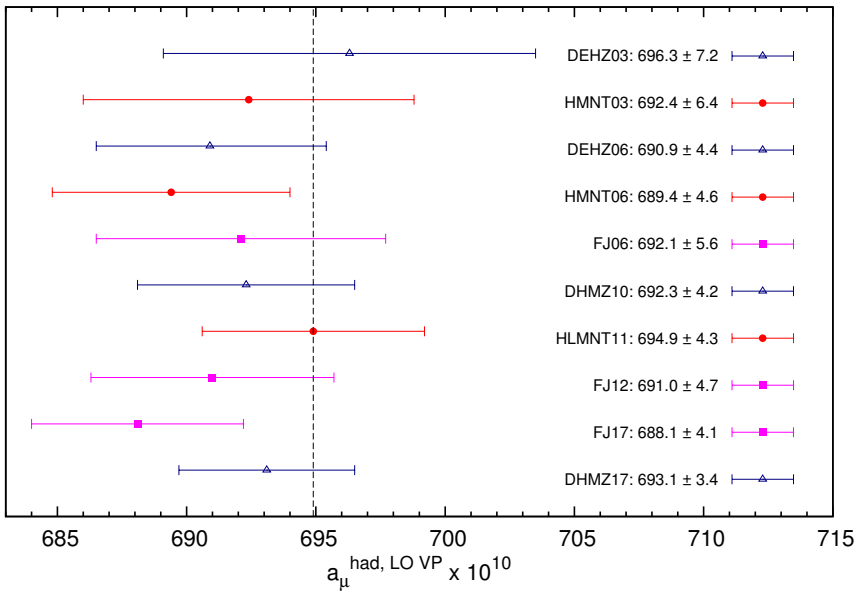

Fig. 1.5: Comparison of recent and previous evaluations of $a_\mu^{\text{had, LO VP}}$ determined from the method of dispersion relations and $e^+e^- \to$ hadrons cross section data. The analyses listed in chronological order are: DEHZ03 [48], HMNT03 [46], DEHZ06 [49], HMNT06 [47], FJ06 [50], DHMZ10 [51], HLMNT11 [21], FJ12 [52], FJ17 [36] and DHMZ17 [45], The dashed line indicates the central value of the estimate from the HLMNT11 collaboration.

VP insertion to the photon propagator, the Feynman rules give

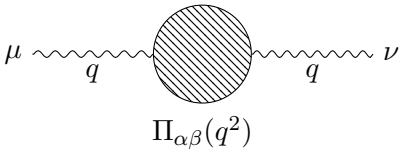

$$= \frac{-ig^{\mu\alpha}}{(q^2 - i\varepsilon)}(-ie)i\Pi_{\alpha\beta}(q^2)(-ie)\frac{-ig^{\beta\nu}}{(q^2 - i\varepsilon)}$$

$$= ie^2 \frac{\Pi^{\mu\nu}(q^2)}{(q^2 - i\varepsilon)^2}\,. \tag{1.35}$$

The general form of the VP tensor, which is purely transverse due to electromagnetic gauge invariance, is defined in this work to be

$$\Pi_{\mu\nu}(q^2) = \big(q_\mu q_\nu - q^2 g_{\mu\nu}\big)\Pi(q^2)\,, \tag{1.36}$$

where $\Pi(q^2)$ is the VP function. From analyticity, the VP function (taken here in the on-shell renormalisation scheme which imposes that $\Pi(q^2 = 0) = 0$) satisfies the subtracted dispersion relation [53]

$$\Pi(q^2) = \frac{q^2}{\pi}\int_{s_{th}}^{\infty} \mathrm{d}s \frac{\mathrm{Im}\,\Pi(s)}{s(s - q^2 - i\varepsilon)}\,, \tag{1.37}$$

where s_{th} is the lowest invariant mass squared threshold for particle production contributing to the VP. Inserting these expressions back into equation (1.35) gives

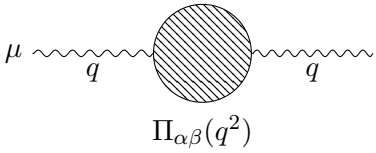

$$= \frac{ie^2 g_{\mu\nu}}{(q^2 - i\varepsilon)^2}\frac{q^4}{\pi}\int_{s_{th}}^{\infty} \mathrm{d}s \frac{\mathrm{Im}\,\Pi(s)}{s(s - q^2 - i\varepsilon)}\,, \tag{1.38}$$

where the term proportional to $q_\mu q_\nu$ can be discarded as it does not contribute to any gauge invariant quantity.

To evaluate $a_\mu^{\mathrm{had,\,LO\,VP}}$, the full VP function in (1.38) is replaced by the hadronic contribution to the VP function $\Pi_{\mathrm{had}}(s)$ and this resulting term exactly replaces the virtual photon propagator term in equation (1.13). Doing so and evaluating the corresponding expression for the contribution to $F_2(0)$ results in

$$\begin{aligned} a_\mu^{\mathrm{had,\,LO\,VP}} &= \frac{\alpha}{\pi}\int_0^1 \mathrm{d}x(1-x)\int_{s_{th}}^{\infty}\frac{\mathrm{d}s}{s}\frac{1}{\pi}\mathrm{Im}\,\Pi_{\mathrm{had}}(s)\frac{x^2}{x^2 + (s/m_\mu^2)(1-x)} \\ &= \frac{\alpha}{\pi^2}\int_{s_{th}}^{\infty}\frac{\mathrm{d}s}{s}\mathrm{Im}\,\Pi_{\mathrm{had}}(s)K(s)\,. \end{aligned} \tag{1.39}$$

The term

$$K(s) = \int_0^1 \mathrm{d}x \frac{(1-x)x^2}{x^2 + (s/m_\mu^2)(1-x)} \tag{1.40}$$

is a well-known kernel function [12,54,55] (see also [46]) that describes the contribution to a_μ from a virtual photon with invariant mass squared s and which can be solved analytically.[4] For $s \geq 4m_\mu^2$,

$$K(s > 4m_\mu^2) = x^2\left(1 - \frac{x^2}{2}\right) + (1+x)^2\left(1 + \frac{1}{x^2}\right)\left(\ln(1+x) - x + \frac{x^2}{2}\right) + \frac{1+x}{1-x}x^2\ln(x)\,, \tag{1.41}$$

where $x \equiv (1-\beta_\mu)/(1+\beta_\mu)$ and $\beta_\mu \equiv \sqrt{1 - 4m_\mu^2/s}$. For $s < 4m_\mu^2$ [75],

$$K(s < 4m_\mu^2) = \frac{1}{4a^2}\left(16(a-2)\ln\left(\frac{a}{4}\right) - 2a(8-a) - 8(a^2 - 8a + 8)\frac{\arctan(\sqrt{a-1})}{\sqrt{a-1}}\right), \tag{1.42}$$

[4] The kernel function given here is identical to that given in equation (45) of [46] but differing by a normalisation factor of $m_\mu^2/3s$.

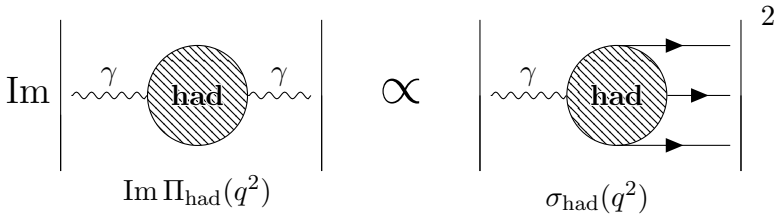

Fig. 1.6: The optical theorem relating the imaginary part of the hadronic vacuum polarisation to the total hadronic cross section.

where $a \equiv 4m_\mu^2/s$. The imaginary part of the hadronic VP function is then found via unitarity, where the optical theorem relates the imaginary part of the hadronic VP function to the total cross section of the process $e^+e^- \to$ hadrons, as depicted in Figure 1.6. This relation is given as,

$$\mathrm{Im}\,\Pi_{\mathrm{had}}(s) = \left(\frac{s}{4\pi\alpha}\right)\sigma_{\mathrm{had}}(s)\,, \tag{1.43}$$

where

$$\sigma_{\mathrm{had}}(s) \equiv \sigma(e^+e^- \to \gamma^* \to \mathrm{hadrons}) \tag{1.44}$$

and γ^* denotes the virtual photon. For the determination of the LO hadronic VP contributions, the hadronic cross section must be undressed of all leptonic and hadronic VP effects in order to avoid some double counting of these contributions with the higher order hadronic VP contributions (see Section 1.3.2). In addition, the cross section must include the effects of final state photon radiation, which should be counted as part of the total cross section. Therefore, it follows that the leading order hadronic vacuum polarisation contribution to a_μ can be determined via

$$a_\mu^{\mathrm{had,\,LO\,VP}} = \frac{1}{4\pi^3}\int_{s_{th}}^{\infty} \mathrm{d}s\,\sigma^0_{\mathrm{had},\gamma}(s)K(s)\,, \tag{1.45}$$

where $s_{th} = m_\pi^2$ is the hadronic production threshold (determined by the $\pi^0\gamma$ final state), the superscript 0 denotes the bare cross section (undressed of all vacuum polarisation effects) and the subscript γ indicates the inclusion of effects from final state photon radiation. Equation (1.45) can also be expressed as

$$a_\mu^{\mathrm{had,\,LO\,VP}} = \frac{\alpha^2}{3\pi^2}\int_{s_{th}}^{\infty} \frac{\mathrm{d}s}{s}\,R(s)K(s) \tag{1.46}$$

where the hadronic cross section has been normalised by the point (pt) cross section of the process $e^+e^- \to \mu^+\mu^-$ to yield the hadronic R-ratio given by

$$R(s) = \frac{\sigma^0_{\mathrm{had},\gamma}(s)}{\sigma_{\mathrm{pt}}(s)} \equiv \frac{\sigma^0_{\mathrm{had},\gamma}(s)}{4\pi\alpha^2/(3s)}\,. \tag{1.47}$$

With the kernel function $K(s)$ behaving as $K(s) \sim m_\mu^2/(3s)$ at low energies (coupled with the factor of $1/s$ in the integrand of equation (1.46)), the integrals in equation (1.45) and equation (1.46) are dominated by the low s regime. As pQCD is an

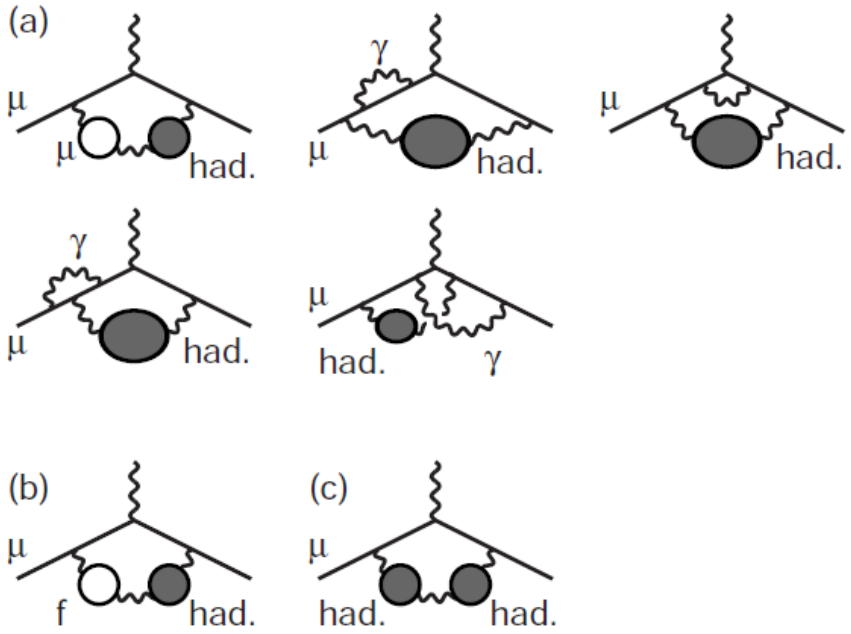

Fig. 1.7: The three classes of Feynman diagrams (a,b,c) that comprise the next-to-leading order hadronic vacuum polarisation contributions to a_μ. It should be noted that for class (a), those diagrams which involve an exchange of the massless and 'massive' (including hadronic bubble) photon propagator are assumed to be included. For class (b), f $= e, \tau$ only. This graphic has been taken from [46].

unreliable source for the cross section in this energy region, experimentally measured hadronic cross section data are used as input for $\sigma^0_{\text{had},\gamma}(s)$. This places a large dependence on these data, as the accuracy of $a_\mu^{\text{had, LO VP}}$ will largely depend on their quality and precision. Fortunately, many experiments have measured cross sections for numerous individual hadronic final states to a very high precision, which are used in this work to determine $a_\mu^{\text{had, LO VP}}$. This requires a dedicated procedure to combine all available hadronic cross section data to robustly determine the full hadronic R-ratio. This will be discussed in detail in Section 2.

1.3.2 Calculating the next-to-leading order hadronic vacuum polarisation contribution, $a_\mu^{\text{had, NLO VP}}$

The next-to-leading order hadronic vacuum polarisation contributions (that enter at $\mathcal{O}(\alpha^3)$) can be conveniently split into three classes as defined in [57]. The contributing diagrams for each class are shown in Figure 1.7. The determination of the contribution to a_μ from each class of diagram results in a corresponding dispersion integral and kernel function. These classes are:

(a) This class contains those diagrams that, in addition to the leading order hadronic bubble, contain higher order corrections from an additional virtual photon or a

muon loop. The dispersion integral in this case is

$$a_\mu^{\text{had, NLO VP, (a)}} = \frac{\alpha^3}{3\pi^3} \int_{s_{th}}^{\infty} \frac{\mathrm{d}s}{s} R(s) K^{(a)}(s) \,. \tag{1.48}$$

(b) This class contains those diagrams that, in addition to the leading order hadronic bubble, contain an additional electron or tau loop. The dispersion integral in this case is

$$a_\mu^{\text{had, NLO VP, (b)}} = \frac{\alpha^3}{3\pi^3} \int_{s_{th}}^{\infty} \frac{\mathrm{d}s}{s} R(s) K^{(b)}(s) \,. \tag{1.49}$$

(c) This class of diagram contains a second hadronic bubble in addition to the leading order hadronic bubble. Therefore, in this case, the R-ratio data must be integrated over twice. The dispersion integral is

$$a_\mu^{\text{had, NLO VP, (c)}} = \frac{\alpha^3}{9\pi^3} \int_{s_{th}}^{\infty} \mathrm{d}s \int_{s'_{th}}^{\infty} \mathrm{d}s' \, \frac{R(s)}{s} \frac{R(s')}{s'} K^{(c)}(s, s') \,. \tag{1.50}$$

In each case, the analytic expression for the kernel function as given in [57] is used. As with the LO contribution, the NLO hadronic vacuum polarisation contributions rely on the experimentally measured hadronic cross section data and their combination to determine the hadronic R-ratio.

Chapter 2

Calculating $a_\mu^{\text{had, VP}}$: data treatment and combination

The majority of hadronic data that are used to determine $a_\mu^{\text{had, VP}}$ are experimental cross section measurements of electron-positron annihilation into individual hadronic final states. In determining $R(s)$, this work aims to provide a reliable and meaningful combination of the available data which makes minimal theoretical assumptions concerning the shape and normalisation of the resulting cross section. Therefore, experimental data are used wherever possible, avoiding the use of available tools such as resonance parametrisations and pQCD where measured data are available. In this way, the estimates of $a_\mu^{\text{had, VP}}$ and the corresponding uncertainties from individual final states are as data-driven as possible. Below $\sim$ 2GeV, these individual hadronic final states are referred to as *exclusive channels*. The hadronic R-ratio in this region is predominantly constructed from the sum of the determined cross sections of all available exclusive channels. Above $\sim$ 2GeV, data for the measured total hadronic R-ratio, or *inclusive channel* (all hadronic final states), are combined. For nearly all these channels, the available data from numerous different experiments must be analysed, combined and then integrated over according to equation (1.45) to give a corresponding estimate of the contribution to $a_\mu^{\text{had, LO VP}}$. With many of these data sets having a different energy binning, different values for the given cross section and individual treatment of the corresponding uncertainties, the combination of these data is a highly non-trivial task and is the focus of this chapter. First however, any contributing data that have VP effects included, or that do not include effects from FSR, must be treated or corrected in order to combine the necessary $\sigma^0_{\text{had},\gamma}(s)$ data.

2.1 Correcting the data

As described in Section 1.3.1, the hadronic data to be input into the dispersion integrals (that determine $a_\mu^{\text{had, VP}}$) must be parametrised as the bare cross section $\sigma^0_{\text{had},\gamma}(s)$, with FSR effects included. Although more recent experimental analyses have endeavoured

to measure this exact quantity, the remaining data must have radiative corrections applied to ensure that all combined data are as consistent as possible with regards to radiative effects. Additional uncertainties are estimated and included whenever radiative corrections are applied. This is done, first and foremost, to account for any under- or over-correction that may occur due to a lack of information concerning the treatment of radiative corrections in the experimental analyses. However, these radiative correction uncertainties also account for any possible incorrect treatment in the analyses, for example missed FSR or inconsistent subtraction of VP contributions. This is especially true for older data, where there is very little or even no information at all regarding how the data have been treated. The numerical estimates of all additional radiative correction uncertainties are given in the respective sections for the individual channels in Section 4.

2.1.1 Vacuum polarisation corrections

Equation (1.45) requires the experimental cross section to be undressed of all VP (running coupling) effects, as VP corrections to the hadronic cross section are counted as part of respective higher order contributions to $a_\mu^{\mathrm{had,VP}}$. This is clear when considering both Figure 2.1 and the diagrammatic portrayal of the optical theorem in Figure 1.6. Evidently, using the dressed cross section (inclusive of vacuum polarisation effects to the photon propagator) to determine $a_\mu^{\mathrm{had,\,LO\,VP}}$ would result in contributions of the type shown in Figure 1.7. Any new and old data that have not been corrected for VP effects require undressing. However, recent data are more commonly undressed in the experimental analyses already, removing the need to apply a correction to these data sets. This benefits the data combination as new, more precise data undressed of VP effects are dominating the combination for many channels which, in turn, reduces the impact of the extra radiative correction uncertainty which is applied to each channel.

The inclusion of these VP effects to the total cross section is understood as the inclusion of the running QED coupling $\alpha(q^2)$. To determine the bare (undressed) cross section, the running $\alpha(q^2)$ must be replaced by the fine structure constant, $\alpha \equiv \alpha(0)$. The standard definition of the running of α is [58]

$$\alpha(q^2) = \frac{\alpha}{1 - \Delta\alpha(q^2)} = \frac{\alpha}{1 + 4\pi\alpha \mathrm{Re}\,\Pi(q^2)} \tag{2.1}$$

where the quantity $\Delta\alpha(q^2)$ describes the contributions to the running coupling from leptons and quarks in the convenient form

$$\Delta\alpha(q^2) = \Delta\alpha_{\mathrm{lep}}(q^2) + \Delta\alpha_{\mathrm{had}}^{(5)}(q^2) + \Delta\alpha_{\mathrm{top}}(q^2)\,. \tag{2.2}$$

Here, the subscript 'lep' denotes the contributions from leptons and the superscript (5) indicates the contributions from all quark flavours except the top quark, which is added separately. The leptonic and top quark contributions have been safely evaluated in other

works using perturbation theory [59–62]. However, as with the hadronic contributions to a_μ, the contributions from the low energy regime cannot be determined reliably using pQCD. Fortunately, following the same logic as in Section 1.3.1 to determine $a_\mu^{\text{had, LO VP}}$, analyticity and unitarity can be employed to define the dispersion relation [53]

$$\Delta\alpha^{(5)}_{\text{had}}(q^2) = -\frac{\alpha q^2}{3\pi}\text{P}\int_{s_{th}}^{\infty}\text{d}s\frac{R(s)}{s(s-q^2)}\,, \tag{2.3}$$

where P denotes the principal value integral and the data input $R(s)$ is identical to that used for $a_\mu^{\text{had, LO VP}}$ in equation (1.46). An important use of this relation, combined with the perturbative determinations of $\Delta\alpha_{\text{lep}}(q^2)$ and $\Delta\alpha_{\text{top}}(q^2)$, is the evaluation of the effective QED coupling at the Z boson mass, $\alpha(M_Z^2)$, which is the least precisely known of the three fundamental EW parameters of the SM (the Fermi constant G_F, M_Z and $\alpha(M_Z^2)$) and hinders the accuracy of EW precision fits. An updated determination of this is given in Appendix C.

To determine the contribution of vacuum polarisation effects to the hadronic cross section, the full photon propagator, $iD_{\mu\nu}(q^2)$, must be determined to all orders. This is expressed by the Dyson summation of all 1PI diagram insertions

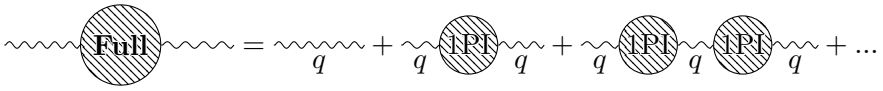

$$\begin{aligned} &= 1 + \Pi(q^2) + \Pi(q^2)\cdot\Pi(q^2) + ... \\ &= \frac{1}{1-\Pi(q^2)}\,, \end{aligned} \tag{2.4}$$

which holds as a geometric series if $|\Pi(q^2)| < 1$. Thus, to arrive at the full photon propagator, the free (undressed) propagator is modified by

$$iD^{\text{free}}_{\mu\nu}(q^2) = \frac{-ig_{\mu\nu}}{q^2 - i\varepsilon} \longrightarrow iD_{\mu\nu}(q^2) = \frac{-ig_{\mu\nu}}{q^2\big(1-\Pi(q^2)\big)}\,. \tag{2.5}$$

The dressed hadronic cross section contains the absolute square of the photon propagator

$$\sigma_{\text{had}}(s) = \sigma^0_{\text{had}}(s)\left(\frac{\alpha(s)}{\alpha}\right)^2 = \frac{\sigma^0_{\text{had}}(s)}{|1-\Pi(s)|^2}\,. \tag{2.6}$$

Therefore, it follows that to determine the bare cross section as depicted in Figure 2.1, the correction

$$\sigma^0_{\text{had}}(s) = \sigma_{\text{had}}(s)|1-\Pi(s)|^2 \tag{2.7}$$

must be applied. This requires the knowledge of both the real and imaginary parts of $\Pi(s)$, as

$$|1-\Pi(s)|^2 = 1 + [\text{Re}\,\Pi(s)]^2 + [\text{Im}\,\Pi(s)]^2 - 2\text{Re}\,\Pi(s)\,. \tag{2.8}$$

The imaginary part of the VP function is found, as in equation (1.43), via the optical theorem from the sum of the total hadronic and leptonic (lep) cross sections,

$$\text{Im}\,\Pi(s) = \frac{\alpha}{3}\Big(R_{\text{lep}}(s) + R_{\text{had}}(s)\Big)\,. \tag{2.9}$$

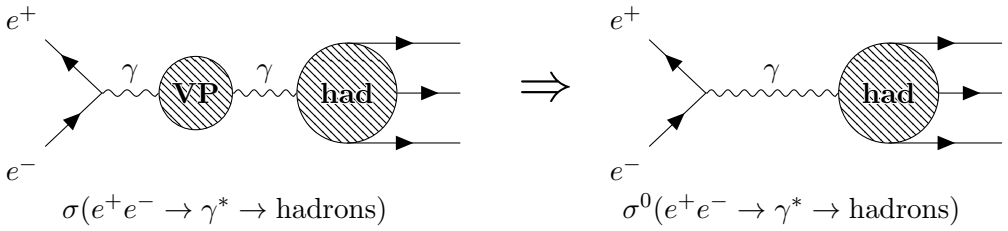

Fig. 2.1: The undressing (subtraction of vacuum polarisation effects) of the cross section $e^+e^- \to \gamma^* \to \text{hadrons}$.

Here, $R_{\text{lep}}(s)$ denotes the leptonic R-ratio and $R_{\text{had}}(s)$ is the standard hadronic R-ratio determined in this work (see Section 2.4).[1] For the purpose of equation (2.7), a self-consistent vacuum polarisation routine has been determined via an iteration of the data input into equation (2.3). This routine is used to correct any data that requires undressing in this work.

The undressing of narrow resonances in the $c\bar{c}$ and $b\bar{b}$ regions (see Section 2.4.3 and Section 4.3.2) requires special attention. These resonance contributions are determined using their respective electronic widths, Γ_{ee} [16], which contain VP (and FSR) effects and, therefore, require undressing. The extremely narrowly peaked nature of these structures causes sharply spiked contributions to $\Delta\alpha^{(5)}_{\text{had}}(q^2)$, which locally causes $|\Pi(q^2)| \geq 1$. This violates the condition for the geometric series in equation (2.4) and, hence, the Dyson summation does not converge for these regions. To overcome this, the electronic width of an individual resonance, Γ_{ee}, is undressed of vacuum polarisation effects using a parametrisation of the VP where the correction *excludes* the contribution of that resonance, such that

$$\Gamma^0_{ee} = \frac{\left(\alpha/\alpha_{\text{no res}}(M^2_{\text{res}})\right)^2}{1 + 3\alpha/(4\pi)}\Gamma_{ee} \ . \tag{2.10}$$

Here, M_{res} is the mass of the resonance and $\alpha_{\text{no res}}$ is the effective QED coupling neglecting the contribution of the resonance itself given by

$$\alpha_{\text{no res}}(s) \equiv \frac{\alpha}{1 - \Delta\alpha_{\text{no res}}(s)} \ , \tag{2.11}$$

where $\Delta\alpha_{\text{no res}}(s)$ is determined from equation (2.3) such that the input $R(s)$ does not include the resonance that is being corrected. To include the resonance would lead to an inconsistent definition of the narrow resonance.

In each channel, the difference Δa^{VP}_μ between the estimates of a_μ with and without additional VP corrections is determined. For the uncertainty due to VP, one third of the shift

$$\delta a^{\text{VP}}_\mu = \frac{1}{3}\Delta a^{\text{VP}}_\mu \tag{2.12}$$

[1] At all times in this work, unless stated otherwise, the non-specific term 'R-ratio' or '$R(s)$' refers to the hadronic R-ratio.

is taken as a conservative uncertainty. This is done in the knowledge that the VP routine, which is determined iteratively in a self-consistent way, is accurate to the level of a permille when correcting the cross section.[2] In addition, this is supported by the fact that newer data sets are also commonly undressed of VP effects in the experimental analyses with a modern routine.

2.1.2 Final state radiative corrections

For the determination of $a_\mu^{\text{had, VP}}$ (as described in Section 1.3.1), photon emission in the final state of the measured hadronic cross section formally corresponds to higher order corrections to the hadronic vacuum polarisation contributions to a_μ. These effects, as shown in Figure 2.2, cannot be determined individually and are not separately accounted for in the higher order contributions to $a_\mu^{\text{had, VP}}$ shown in Figure 1.7. Therefore, they are included as part of the LO contributions in the definition of the 1PI hadronic blobs. However, depending on the experimental analyses, some amount of real photon FSR may have been missed or removed during the event selection. Adding back these missed contributions is model dependent and not feasible for general hadronic final states. It is therefore necessary to estimate the possible effects and their impact on the accuracy of the data compilations.

It is possible to estimate the effects of single photon FSR for the $\pi^+\pi^-$ and K^+K^- channels using a scalar QED (sQED) approximation. It has been shown that sQED, which assumes point-like pions and kaons, provides a good description of photon FSR, especially in the energy range below $\sim$ 2GeV [63–65]. In this range, the low energy of the photon propagator producing these virtual mesons means that it is less likely to resolve the quark structures of the mesons. In [21, 46, 47], to estimate possible FSR effects in $\pi^+\pi^-$ and K^+K^- production in this approximation, the fully inclusive $\mathcal{O}(\alpha)$ correction to the cross section,

$$\sigma^{(0)}_{\text{had},\gamma}(s) = \sigma^{(0)}_{\text{had}}(s)\left(1 + \eta(s)\frac{\alpha}{\pi}\right), \tag{2.13}$$

has been used. Here, the term 'fully inclusive' means inclusive of effects from virtual and real (both soft and hard) one-photon emission. The function $\eta(s)$ is given in [63] and the subscript γ indicates the one photon inclusive cross section.

However, experimental cross section measurements by nature include all virtual and soft real radiation effects [66, 67].[3] Therefore, ideally only the effects from (hard) real radiation above/within resolution/cut parameters, which are specific for a given

[2] For the $\pi^+\pi^-\pi^0$ channel, for example, from equation (2.12) the additional uncertainty due to VP corrections is determined to be $\sim 0.5 \times 10^{-10}$. In comparison, the theoretical uncertainty of the VP routine for this channel is $\sim 0.05 \times 10^{-10}$.

[3] This is a consequence of the infrared (IR) finite nature of the SM, where IR divergences in QED loop corrections are cancelled by IR divergences arising from soft photon emission. Therefore, only the sum of both soft and virtual corrections is physically observable.

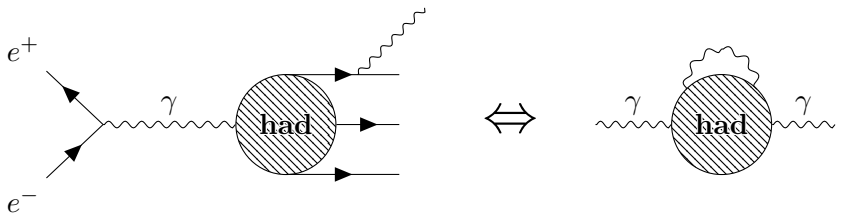

Fig. 2.2: Photon FSR in an $e^+e^- \to$ hadrons event, where although formally of higher order in α and therefore a higher order contribution to $a_\mu^{\text{had, VP}}$, it is included in the 1PI hadronic blob as part of the LO hadronic VP contributions to a_μ.

experiment or analysis, should be estimated to account for possibly missing photon FSR. Whereas in the calculation of the inclusive correction a regularisation of the virtual and real soft contributions is required to obtain the infrared finite result η, the hard-real radiation, $\eta^{\text{hard,real}}$, can be estimated numerically from [64]

$$\eta^{\text{hard,real}}(s) \;=\; \int_{4m^2}^{s-2\sqrt{s}\Lambda} ds' \rho_{\text{fin}}(s, s')\,, \tag{2.14}$$

where m is the mass of the (scalar) particle, Λ is a finite infrared cut-off parameter on the invariant mass of the emitted photon and ρ_{fin} is the radiator function (see appendix B of [64]).

In the case of the K^+K^- channel, by far the largest contribution to a_μ (and its error) comes from the energy region of the ϕ peak (see Section 4.1.7), where the phase space for real radiation is severely restricted. In [68], a study was conducted to determine an estimate of the effects from only hard photon radiation in the K^+K^- channel. Using kinematical arguments that relate the energy of an emitted final state photon to the angle at which it is emitted, it was possible to derive a relation between the cut-off parameter Λ in equation (2.14) and angular cuts in the photon acolinearity given in individual experimental analyses. This allowed studies in this work into two experimental measurements in the K^+K^- channel that had made such angular cuts [69, 169]. The results of this study are shown in Figure 2.3. Here, the fully inclusive correction $\eta(s)$ (left panel) is compared to the resulting estimates for the real hard radiation, where $\eta^{\text{hard,real}}(s)$ (right panel) now depends on the acolinearity cuts as given by the two experimental analyses. Clearly, at and around the ϕ peak, phase space restrictions strongly suppress any hard-real radiation and corresponding FSR correction. It is also evident that using the inclusive correction in equation (2.13) would lead to an overestimate of the possible FSR effects for the K^+K^- channel. In addition, although the correction due to equation (2.14) increases above the ϕ peak, the contribution of the K^+K^- channel above the ϕ to both mean value and error of a_μ is substantially smaller than the contribution from the ϕ itself. These arguments, coupled with being unable to repeat this calculation for the remaining data sets in the K^+K^- channel due to a lack of information regarding the respective experimental analysis,

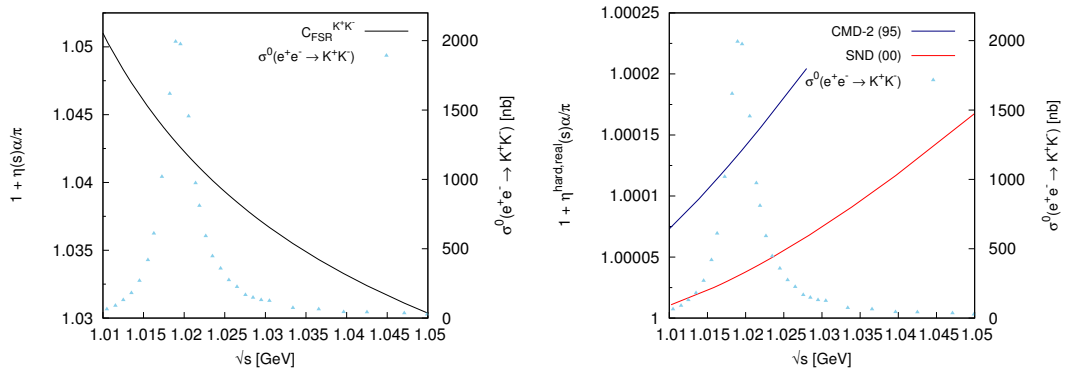

Fig. 2.3: The effect of final state radiation in the K^+K^- channel in the ϕ resonance region. Left panel: the fully inclusive FSR correction $\eta(s)$. Right panel: hard real radiation $\eta^{\text{hard,real}}(s)$, estimated with acolinearity cuts used in the two analyses [69,169]. The $e^+e^- \to K^+K^-$ cross section is also plotted for reference.

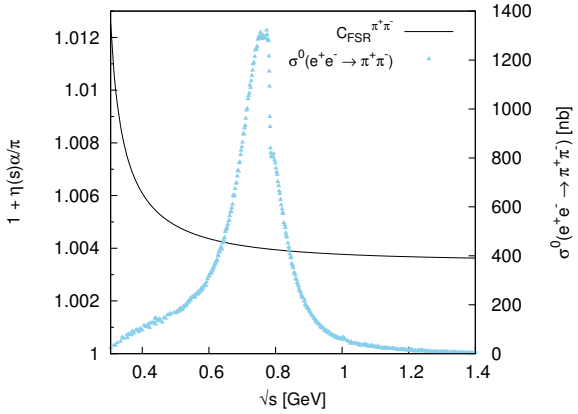

Fig. 2.4: The behaviour of the inclusive FSR correction, $\eta(s)$, for the process $e^+e^- \to \pi^+\pi^-$. The $e^+e^- \to \pi^+\pi^-$ cross section is also plotted for reference.

mean that no correction or additional error estimate due to FSR is now applied in the K^+K^- channel. For the neutral kaon channel, hard photon radiation (which would resolve the quark charges) is similarly suppressed and no FSR correction or additional error are applied in this channel either.

The situation is different in the $\pi^+\pi^-$ channel. A study similar to the two-kaon channel showed that in principle larger contributions from real radiation of the order of the inclusive correction can arise. However, these contributions are strongly dependent on the cut applied in equation (2.14) and would require a more detailed, measurement-by-measurement analysis, for which the information needed from the respective experimental analyses is not available. Therefore, as in [21, 46, 47], in data sets which are understood to not include the full FSR corrections, the fully inclusive correction (as shown in Figure 4.19) is applied to the respective $\pi^+\pi^-$ measurements. Importantly, recent sets from radiative return, where additional photons are part of the leading order cross section and are studied in detail as part of the analyses, have now

become dominant in the $\pi^+\pi^-$ channel. Consequently, the impact of the fully inclusive FSR correction to older sets is suppressed for both mean value and error in comparison to [21, 46, 47].

For the sub-leading, multi-hadron channels, there are at present no equivalent FSR calculations. Depending on the experimental analysis, they are (at least to some extent) simulated by Monte Carlo and contribute to the systematic uncertainties. However, for many data sets it is far from clear to what extent FSR effects are included in the systematic errors. Therefore, possible effects are accounted for by applying an additional uncertainty determined as a fraction of the respective contribution.

For the extra uncertainties due to FSR, there are no contributions from the K^+K^- and $K_S^0K_L^0$ channels (see the discussion above). For the $\pi^+\pi^-$ channel, the full difference between the estimates of $a_\mu^{\pi^+\pi^-}$ with and without additional FSR corrections is taken as the FSR uncertainty, resulting in an additional uncertainty on $a_\mu^{\pi^+\pi^-}$ of $\sim 0.03\%$. For all other channels, including the inclusive data combination, a fraction of 1% of the respective cross section is applied as a conservative uncertainty.

2.1.3 Converting pion form factor data

For the $\pi^+\pi^-$ channel, it is common for many experimental cross section measurements to also be given in terms of the analogous pion form factor, $|F_\pi|^2$. Some older data in this channel (see Section 4.1.2) are only available in the pion form factor representation and must be converted to the hadronic cross section in order to be combined with the other data. Contrary to the requirements concerning radiative corrections for the cross section used for the input for the determination of $a_\mu^{\mathrm{had,\,VP}}$, it is usual for the pion form factor to *include* VP effects and *exclude* FSR. In this case, the bare two-pion cross section including FSR is determined from the pion form factor by

$$\sigma^0_{\pi\pi,\gamma}(s) = \frac{\pi\alpha^2\beta_\pi^3(s)}{3s}\,|F_\pi(s)|^2\,|1-\Pi(s)|^2\Big(1+\frac{\alpha}{\pi}\eta(s)\Big)\,, \tag{2.15}$$

where $\beta_\pi(s) = \sqrt{1-4m_\pi^2/s}$.

2.2 Clustering data

Data in a given hadronic channel must be combined before integrating. The alternatives of integrating the data sets from each experiment in a given hadronic channel individually and averaging the resulting integrated values or evaluating the contributions from the data with a strict point-to-point integral, could result in inadequate representations of the contributing data. Imprecise data of poor quality could contribute with a larger weighting to $a_\mu^{\mathrm{had,\,VP}}$ than they should. In addition, unrealistic propagations of large experimental uncertainties could suppress the desired contribution of more reliable precise data. With the aim of this work to be a data-driven analysis that avoids the fitting

of data to functions or parametrisations, a re-binning of the data is applied that results in a combined cross section which appropriately incorporates the weightings from the respective experimental uncertainties.

Within each hadronic channel, data points from different experiments are assigned to *clusters*. In this work, the clustering algorithm is universal for all different channels and only differs in the assigned maximum cluster size δ (and δ_{res}, a maximum cluster size applicable at individual resonances). Data points are, by order of precision, compared to existing clusters. If data point i is being considered for assignment to the cluster m, then if the energy E_i exists between $(E_m - \delta) \leq \sqrt{s} \leq (E_m + \delta)$, then it is added to the cluster m. If not, then a new cluster is created to accommodate it. Importantly, the information regarding the data points belonging to each cluster is retained to ensure that existing points do not stray outside of the boundaries, $\pm\delta$, of their assigned cluster. If the addition of a new data point to a cluster should violate this, a new cluster is created for the data point in question.

A scan over δ (and δ_{res} if applicable) is performed to determine a suitable clustering configuration which must avoid both over- and under-clustering. Too wide or over-populated clusters would effectively lead to a re-binning of data points from individual experiments and risk loss of information, while a too narrow clustering would result, in the extreme, in an erratic point-to-point representation of the cross section and no gain in the accuracy. The preferred configuration is then chosen based on the resulting global χ^2_{min}/d.o.f. (see Section 2.3.2) and the uncertainty on $a_\mu^{\text{had,VP}}$, combined with checks by eye that the resulting spectral function does not exhibit any erratic behaviour due to the effects of over- or under-clustering.

2.3 Minimisation

Following the re-binning of the available data in a given hadronic channel into clusters, a solution for the cross section must be obtained that incorporates all the available information. In particular, the resulting cross section should include the full propagation of available uncertainty information to be used for the determination of $a_\mu^{\text{had,VP}}$ and its error. The previous analyses [21, 46, 47] employed a non-linear χ^2-minimisation utilising fitted renormalisation factors as nuisance parameters that represented the energy independent systematic uncertainties. Although this method, denoted here as the f_k method, was a powerful approach, recent literature [71] (see also [72]) have highlighted the possibility that an incorrect treatment of multiplicative normalisation uncertainties in a χ^2-minimisation can incur a systematic bias (see chapter 4 of [71]).

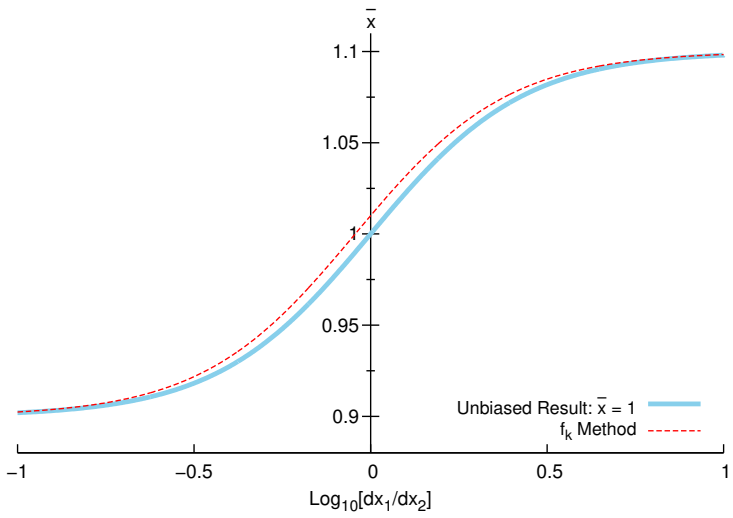

Fig. 2.5: The behaviour of the combined value $\bar{x}$ as the ratio of the multiplicative normalisation uncertainties, $\mathrm{d}x_1$ and $\mathrm{d}x_2$, of the two contributing data points, $x_1 = 0.9$ and $x_2 = 1.1$, are varied. The unbiased result, indicated by the solid light-blue line, corresponds to $\bar{x} = 1$ and should pass through this point when $\mathrm{d}x_1 = \mathrm{d}x_2$. The results from the f_k method used in [21, 46, 47] is shown by the dashed red line.

2.3.1 Systematic bias and the f_k method

With the aim to achieve a precision for $a_\mu^{\mathrm{had,\,LO\,VP}}$ that is a trusted improvement on the accuracy achieved in [21], the necessity for a reliable and robust data combination procedure is of paramount importance. In [73, 74], it has been shown that the propagation of multiplicative normalisation (systematic) uncertainties in a data combination method using the uncertainties as defined by the data alone could result in bias. This bias can be explicitly demonstrated in a mock data example of the simple combination of only two data points of arbitrary units: $x_1 = 0.9 \pm \mathrm{d}x_1 = 0.9 \pm px_1$ and $x_2 = 1.1 \pm \mathrm{d}x_2 = 1.1 \pm px_2$, where $\mathrm{d}x_1$ and $\mathrm{d}x_2$ represent the percentage uncertainty p of x_1 and x_2 respectively, and are fully correlated with each other. The corresponding covariance matrix is given as

$$C = \begin{pmatrix} p^2x_1^2 & p^2x_1x_2 \\ p^2x_2x_1 & p^2x_2^2 \end{pmatrix} . \tag{2.16}$$

As both of these data points have an uncertainty of the same percentage, each should provide an identical weighting to their combination which should result in a combined value $\bar{x}$ that is the trivial average of the two data points, $\bar{x} = 1$. However, the combination of these data points results in $\bar{x} \approx 0.98$. This bias, known as the d'Agostini bias [73], occurs as combining data with the fully correlated uncertainties defined by the data alone results in a bias towards the data point with the smaller value [73, 74], in this case x_1.

The f_k method in [21, 46, 47] employed the fitting of renormalisation factors as nui-

sance parameters through a non-linear χ^2-minimisation to avoid such a bias. However, using the f_k method to determine the combination of the same example of two points as above yields an answer of $\bar{x} = 1.0050125$, indicating that this method also exhibits the potential for bias. This effect is shown more generally in Figure 2.5 (which follows the analysis methodology in [71]), where the resulting upward shift in the combined result is clearly visible.[4] In addition, although the non-linear χ^2-minimisation used in [21] was adjusted to include covariance matrices, the method's reliance on fitting energy independent renormalisation factors prevented the use of correlated uncertainties to their full capacity. Recent precise data (specifically radiative return measurements in the $\pi^+\pi^-$ and K^+K^- channels have been released with energy dependent uncertainties and non-trivial bin-to-bin correlations for both the statistical and systematic uncertainties. Consequently, it follows that the previous combination procedure should be modified to allow the full use of all available correlations in a bias-free approach.

2.3.2 Fixing the covariance matrix: an iterated fit

In this work, as an alternative approach to the fitting of renormalisation factors (nuisance parameters) via the f_k method, an iterative fit procedure as advocated in [71] has been adopted, which re-initialises the full covariance matrices at each iteration step. The concept of this method utilises the knowledge that the use of the uncertainties/covariance matrix as defined by the data alone leads to the d'Agostini bias, which should be avoided. Notably, for large data combinations which commonly require an iteration of a fit to reach convergence, the d'Agostini bias could be further driven by the uncertainties being repeatedly defined by the data in each iteration. Therefore, the covariance matrix should be redefined in the data combination to avoid this undesirable effect. Instead of the uncertainties being defined as percentages of the data itself, they should be redefined as percentage uncertainties of some estimated theory value. In the simple two-point example, the covariance matrix is redefined to be

$$C = \begin{pmatrix} p^2\tilde{x}^2 & p^2\tilde{x}^2 \\ p^2\tilde{x}^2 & p^2\tilde{x}^2 \end{pmatrix}, \tag{2.17}$$

where $\tilde{x}$ is the estimated theory value of the combination of x_1 and x_2. In this approach, the combination of these two data points yields the unbiased result $\bar{x} = 1$. In the more complicated case of a larger data combination, the theory estimate for each contributing data point is recalculated at every step of the iteration until the fit converges.

In this work, a new method has been devised based on the concepts outlined above to replace the restricted f_k method and minimise the effect of the d'Agostini bias. Previously, in [21, 46, 47], a constant cross section had been assumed across the width of each cluster. In this work, the fitted cross section values at the cluster centres are

[4] In [71], it is explained that this bias arises due to the non-linear nature of the χ^2 function, implying that a linear function that avoids the d'Agostini bias should be explored.

obtained from an iterative χ^2-minimisation where the cross section is taken to be linear between adjacent cluster centres. This is not only a more physically realistic representation of the shape of the cross section in the data combination than the constant cross section approach, but allows for a more stable fit and is consistent with the trapezoidal rule integration utilised for the $a_\mu^{\mathrm{had,VP}}$ integrals (see Section 2.5).[5]

For each hadronic channel, if data points at energies $\sqrt{s} = E_i^{(m)}$ are combined into cluster m, then the weighted average of the cross section value R_m and energy E_m for the *cluster centre* are

$$R_m = \left[\sum_{i=1}^{N^{(m)}} \frac{R_i^{(m)}}{\left(\mathrm{d}\tilde{R}_i^{(m)}\right)^2}\right]\left[\sum_{i=1}^{N^{(m)}} \frac{1}{\left(\mathrm{d}\tilde{R}_i^{(m)}\right)^2}\right]^{-1} \tag{2.18}$$

and

$$E_m = \left[\sum_{i=1}^{N^{(m)}} \frac{E_i^{(m)}}{\left(\mathrm{d}\tilde{R}_i^{(m)}\right)^2}\right]\left[\sum_{i=1}^{N^{(m)}} \frac{1}{\left(\mathrm{d}\tilde{R}_i^{(m)}\right)^2}\right]^{-1}, \tag{2.19}$$

where $R_i^{(m)}$ is the cross section value of data point i contributing to cluster m, $N^{(m)}$ is the total number of data points contributing to cluster m and

$$\mathrm{d}\tilde{R}_i^{(m)} = \sqrt{(\mathrm{d}R_{i;\ \mathrm{stat}}^{(m)})^2 + (\mathrm{d}R_{i;\ \mathrm{sys}}^{(m)})^2}\,. \tag{2.20}$$

$\mathrm{d}R_{i;\ \mathrm{stat}}^{(m)}$ and $\mathrm{d}R_{i;\ \mathrm{sys}}^{(m)}$ denote the absolute statistical and systematic uncertainties, respectively. With a linear cross section now assumed, if data point i belongs to cluster m and $E_i^{(m)} > E_m$, then its interpolant cross section value $\mathcal{R}_m^i$ is given by

$$\mathcal{R}_m^{i+} = R_m + \frac{(E_i^{(m)} - E_m)}{(E_{m+1} - E_m)}(R_{m+1} - R_m)\,, \tag{2.21}$$

where the superscript '+' indicates that $E_i^{(m)} > E_m$. If, on the other hand, $E_i^{(m)} < E_m$ then

$$\mathcal{R}_m^{i-} = R_{m-1} + \frac{(E_i^{(m)} - E_{m-1})}{(E_m - E_{m-1})}(R_m - R_{m-1})\,, \tag{2.22}$$

where the superscript '$-$' indicates that $E_i^{(m)} < E_m$. For data points at the borders where no interpolation is possible, $\mathcal{R}_m^i$ is found by linear extrapolation.

A covariance matrix is constructed for the combination which contains all the uncertainty and correlation information of all data points. Importantly, this matrix should be constructed to satisfy the necessary mathematical properties of a covariance matrix. Any covariance matrix, C, of dimension $n \times n$ must satisfy the following requirements:

[5] In this work, the high population of data points and, therefore, resulting number of clusters for the numerous hadronic channels means the linear/trapezoidal rule representation of the cross section is much more reliable than in the previous analyses [21,46,47]. In Section 2.5, comparisons with higher order polynomial determinations of the cross section are shown which highlight that differences between these and the linear approach are small due to the densely populated data content.

- As the diagonal elements of any covariance matrix are populated by the corresponding variances, all the diagonal elements of the matrix are positive. Therefore, the trace of the covariance matrix must also be positive

$$\text{Trace}(C) = \sum_{i=1}^{n} C(i,i) = \sum_{i=1}^{n} \text{Var}_i > 0. \tag{2.23}$$

- It is a symmetric matrix, $C(i,j) = C(j,i)$, and is, therefore, equal to its transpose, $C(i,j) = C^T(i,j)$.

- It is a positive, semi-definite matrix,

$$\mathbf{a}^T C\ \mathbf{a} \geq 0\ ;\ \mathbf{a} \in R^n, \tag{2.24}$$

  where $\mathbf{a}$ is an eigenvector of the covariance matrix C.

- The eigenvalues $\lambda_{\mathbf{a}}$ of the covariance matrix must be real, non-negative and the distinct eigenvectors must be orthogonal

$$\mathbf{b}^T C\ \mathbf{a} = \lambda_{\mathbf{a}}(\mathbf{b}\cdot\mathbf{a}) = \mathbf{a}^T C\ \mathbf{b} = \lambda_{\mathbf{b}}(\mathbf{a}\cdot\mathbf{b}) \tag{2.25}$$

$$\therefore \text{if } \lambda_{\mathbf{a}} \neq \lambda_{\mathbf{b}} \Rightarrow (\mathbf{a}\cdot\mathbf{b}) = 0. \tag{2.26}$$

- Its determinant is greater than or equal to zero: $\text{Det}\big(C(i,j)\big) \geq 0$.

With many experimental analyses providing error contributions from multiple sources of uncertainty for both statistics and systematics, the contributions of these individual sources must be summed correctly in order to satisfy the necessary conditions for a covariance matrix. In general, should sources of uncertainty be correlated, the element (i,j) of a covariance matrix that describes the total covariance σ_{ij} between the two data points should be constructed as

$$C(i,j) \equiv \sigma_{ij} = \sum_{\alpha}\sum_{\beta} \sigma_i^{\alpha}\rho_{ij}^{\alpha\beta}\sigma_j^{\beta}\ .$$

Here, α and β denote individual sources of uncertainty, σ_i^{α} is the standard deviation of the data point i due to the uncertainty source α, σ_j^{β} is the standard deviation of the data point j due to the uncertainty source β and $\rho_{ij}^{\alpha\beta}$ is the correlation coefficient that describes the correlation $(-1 \leq \rho \leq 1)$ between the uncertainty source α of data point i and the uncertainty source β of data point j. In general, unless stated otherwise, different sources of uncertainty are assumed to be independent and, therefore, uncorrelated $(\rho_{ij}^{\alpha\beta}|_{\alpha\neq\beta} = 0)$. Correspondingly, the element (i,j) of the covariance matrix is determined from

$$C(i,j) = \sum_{\alpha} \rho_{ij}^{\alpha}\sigma_i^{\alpha}\sigma_j^{\alpha} = \sum_{\alpha} C^{\alpha}(i,j)\ , \tag{2.27}$$

where $C^{\alpha}(i,j)$ is the covariance matrix specifically due to the uncertainty source α. It follows that to define the total covariance of two data points, the correlation coefficient and absolute error of each data point for each source of uncertainty must be known, which are then summed in accordance with equation (2.27). In this work, if the experimental analysis does not provide covariance matrices or corresponding correlation information, then statistical uncertainties are assumed to be uncorrelated ($\rho_{ij}^{\alpha} = 0$) and systematic uncertainties are assumed to be fully correlated ($\rho_{ij}^{\alpha} = 1$) between all bins in a given experimental measurement.

For each channel, the total covariance matrix $\mathbf{C}\big(i^{(m)}, j^{(n)}\big)$ is given as the sum of the statistical covariance matrix $\mathrm{C}^{\mathrm{stat}}\big(i^{(m)}, j^{(n)}\big)$ and the systematic covariance matrix $\mathrm{C}^{\mathrm{sys}}\big(i^{(m)}, j^{(n)}\big)$. As described above, using the covariance matrix as defined by the data alone could result in bias. The covariance matrix is therefore redefined at each step of the iteration using the fitted R_m values. At each stage of the iteration, it is defined as

$$\mathbf{C}_I\big(i^{(m)}, j^{(n)}\big) = \mathrm{C}^{\mathrm{stat}}\big(i^{(m)}, j^{(n)}\big) + \frac{\mathrm{C}^{\mathrm{sys}}\big(i^{(m)}, j^{(n)}\big)}{R_i^{(m)} R_j^{(n)}} \mathcal{R}_m^{i,(I-1)} \mathcal{R}_n^{j,(I-1)} \,, \tag{2.28}$$

where the quantities $\mathcal{R}_m^{i,I}$ and $\mathcal{R}_n^{j,I}$ are the interpolant cross sections given by either equation (2.21) or (2.22) and I denotes the iteration number of the fit. This is then used as input into the now *linear* χ^2-function,

$$\chi_I^2 = \sum_{i=1}^{N_{\mathrm{tot}}} \sum_{j=1}^{N_{\mathrm{tot}}} \big(R_i^{(m)} - \mathcal{R}_m^{i,I}\big) \mathbf{C}_I^{-1}\big(i^{(m)}, j^{(n)}\big) \big(R_j^{(n)} - \mathcal{R}_n^{j,I}\big) \,, \tag{2.29}$$

where N_{tot} is the total number of contributing data points in the given channel and $\mathbf{C}_I^{-1}\big(i^{(m)}, j^{(n)}\big)$ is simply the inverse of the covariance matrix defined in equation (2.28). Performing the minimisation yields a system of linear equations

$$\sum_{j=1}^{N_{\mathrm{tot}}} \left[\big(R_j^{(n)} - \mathcal{R}_n^{j,I}\big) \frac{\partial \mathcal{R}_m^i}{\partial R_a} \right] V_I^{-1}\big(m^{(i)}, n^{(j)}\big) = 0 \,, \quad i = 1, ..., N_{\mathrm{tot}} \,, \tag{2.30}$$

where,

$$V_I^{-1}\big(m^{(i)}, n^{(j)}\big) = \sum_{i=1}^{N^{(m)}} \sum_{j=1}^{N^{(n)}} \mathbf{C}_I^{-1}\big(i^{(m)}, j^{(n)}\big) \,. \tag{2.31}$$

As in equations (2.21) and (2.22), the term $\mathcal{R}_n^j$ is to be taken as either $\mathcal{R}_n^{j+}$, if $E_j^{(n)} > E_n$, or $\mathcal{R}_n^{j-}$, if $E_j^{(n)} < E_n$. Subsequently, if $E_i^{(m)} > E_m$, then

$$\left.\frac{\partial \mathcal{R}_m^i}{\partial R_a}\right|_{E_i^{(m)} > E_m} = \frac{\partial \mathcal{R}_m^{i+}}{\partial R_a} = \left(1 - \frac{(E_i^{(m)} - E_m)}{(E_{m+1} - E_m)}\right)\delta_{ma} + \frac{(E_i^{(m)} - E_m)}{(E_{m+1} - E_m)}\delta_{m+1,a} \tag{2.32}$$

and, if $E_i^{(m)} < E_m$, then

$$\left.\frac{\partial \mathcal{R}_m^i}{\partial R_a}\right|_{E_i^{(m)} < E_m} = \frac{\partial \mathcal{R}_m^{i-}}{\partial R_a} = \left(1 - \frac{(E_i^{(m)} - E_{m-1})}{(E_m - E_{m-1})}\right)\delta_{m-1,a} + \frac{(E_i^{(m)} - E_{m-1})}{(E_m - E_{m-1})}\delta_{ma} \,, \tag{2.33}$$

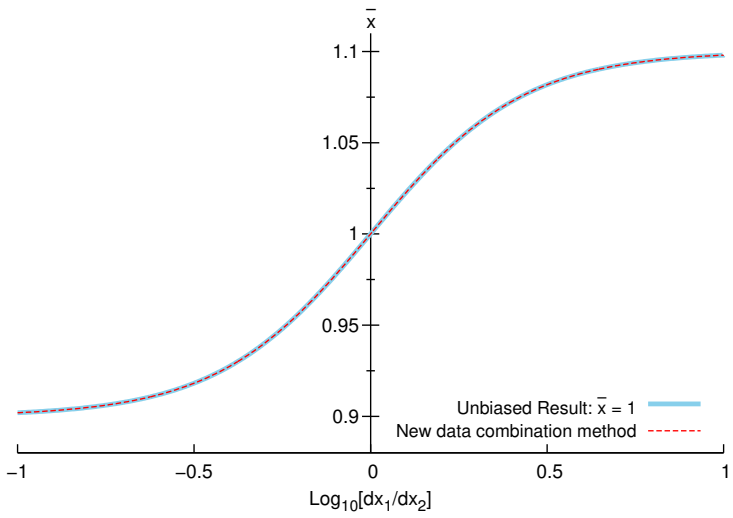

Fig. 2.6: The behaviour of the combined value $\bar{x}$ as the ratio of the multiplicative normalisation uncertainties, $\mathrm{d}x_1$ and $\mathrm{d}x_2$, of the two contributing data points, $x_1 = 0.9$ and $x_2 = 1.1$, are varied. The unbiased result, indicated by the solid light-blue line, corresponds to $\bar{x} = 1$ and should pass through this point when $\mathrm{d}x_1 = \mathrm{d}x_2$. The result from the new data combination method used in this work is shown by the dashed red line.

where δ denotes the Kronecker delta. The solution to equation (2.30) yields the cluster centres R_m. The overall quality of the data combination is described by the global $\chi^2_{\mathrm{min}}/\mathrm{d.o.f.}$. In addition, the output of the method includes the local $\chi^2_{\mathrm{min}}/\mathrm{d.o.f.}$ for each cluster and the total output covariance matrix $V_I\big(m,n\big)$, which describes the correlation between the errors $\mathrm{d}R_m$ and $\mathrm{d}R_n$. For each channel, this matrix is checked to ensure it satisfies the required properties of a covariance matrix as described above. As in [21], in order to account for any tensions between the data, the output matrix is inflated according to the local $\chi^2_{\mathrm{min}}/\mathrm{d.o.f.}$ by

$$\tilde{V}\big(m,n\big) = V_I\big(m,n\big)\sqrt{\chi^2_{\mathrm{min}}/\mathrm{d.o.f.}(m)}\sqrt{\chi^2_{\mathrm{min}}/\mathrm{d.o.f.}(n)} \tag{2.34}$$

if the local $\chi^2_{\mathrm{min}}/\mathrm{d.o.f.} > 1$ for each cluster.

In [71], it was stated that for the fit of parton distribution functions, convergence is expected to occur after very few iterations, which is also observed here. The use of the full covariance matrix allows for the inclusion of any-and-all uncertainties and correlations that may exist between the measurements. The flexibility to now make use of fully energy dependent uncertainties ensures that the appropriate influence of the correlations is incorporated into the determination of the cluster centres R_m, with the correct propagation of all experimental errors to the $g-2$ uncertainty.

Channel	This work	Potential d'Agostini biased	Difference
$\pi^+\pi^-$	502.99 ± 1.97	500.36 ± 1.95	2.63
$\pi^+\pi^-\pi^0$	47.82 ± 0.89	45.94 ± 0.73	1.88
$\pi^+\pi^-\pi^+\pi^-$	15.17 ± 0.21	14.61 ± 0.15	0.56
$\pi^+\pi^-\pi^0\pi^0$	19.80 ± 0.79	16.58 ± 0.71	3.22
K^+K^-	23.05 ± 0.22	22.40 ± 0.22	0.65
$K^0_S K^0_L$	13.05 ± 0.19	12.89 ± 0.17	0.16

Table 2.1: Comparison of the contributions to $a_\mu^{\mathrm{had,\,LO\,VP}}$ from leading and major subleading hadronic channels determined with the data combination method devised in this work and with the normalisation uncertainties defined by the data alone. All results are found in the energy range $\sqrt{s} \leq 2$ GeV and are given in units of $a_\mu^{\mathrm{had,\,LO\,VP}} \times 10^{10}$. The first column indicates the final state or individual contribution, the second column gives the estimate of $a_\mu^{\mathrm{had,\,LO\,VP}}$ from this work, the third column states the corresponding potentially d'Agostini bias affected results and the last column gives the difference between the two evaluations.

2.3.3 Data combination analysis

The results of the simple two-point example now determined with the new data combination method are shown in Figure 2.6, where both the d'Agostini bias and the bias arising from the non-linear nature of the f_k method are now eliminated. Concerning the d'Agostini bias, although it not possible to predict the unbiased result for the full data combination of an individual channel as in the simple two-point example, marked differences should be visible in the results of data combined with the covariance matrices as defined by the data alone and the fixed iterative method used in this work. A comparison of results using both approaches in shown in Table 2.1, where the differences in the results for all channels are significant and outside of the quoted errors. Interestingly however, in all cases the new method produces results that are larger than those determined with the normalisation uncertainties defined by the data alone, suggesting that there is a strong effect of the d'Agostini bias driving the results towards smaller values in the latter case.

Comparative results from the f_k method and the new data combination method with identical input for the hadronic cross section data are shown in Table 2.2.[6] Note that, for all channels, the differences between the old and the new data combination procedures lead to changes of $a_\mu^{\mathrm{had,VP}}$ within the quoted errors. Importantly, as shown in Table 2.3, examples of combining data which have only global normalisation uncertainties result in negligible differences between [21] and this work, indicating that previous results were largely unaffected by the potential bias issue.

A final interesting study is to understand the impact of defining the cross section

[6] In Section 4.5.1, a full comparison between this work and the previous analysis in [21] is given. However, as there is much new data included in this work that was not available in [21], it would not be possible in the full analysis comparison to distinguish whether any differences observed are due to the new data combination method or the new data input.

Channel	This work	f_k method [21]	Difference
$\pi^+\pi^-$	505.06 ± 2.23	505.77 ± 3.09	-0.71
$\pi^+\pi^-\pi^0$	47.38 ± 0.99	47.51 ± 0.99	-0.13
$\pi^+\pi^-\pi^+\pi^-$	14.59 ± 0.47	14.65 ± 0.47	-0.06
$\pi^+\pi^-\pi^0\pi^0$	20.57 ± 1.24	20.37 ± 1.26	0.20
K^+K^-	22.09 ± 0.42	22.15 ± 0.46	-0.06
$K^0_S K^0_L$	13.46 ± 0.17	13.33 ± 0.16	0.13

Table 2.2: Comparison of the contributions to $a_\mu^{\mathrm{had,\,LO\,VP}}$ from leading and major sub-leading hadronic channels determined with the data combination method devised in this work and using the f_k method. Here, for the purpose of this comparison, all data that have been released more recently than the HLMNT11 analysis [21] are omitted. All results are found in the energy range $\sqrt{s} \leq 2$ GeV and are given in units of $a_\mu^{\mathrm{had,\,LO\,VP}} \times 10^{10}$. The first column indicates the final state or individual contribution, the second column gives the estimate of $a_\mu^{\mathrm{had,\,LO\,VP}}$ from this work, the third column states the estimate using the f_k method and the last column gives the difference between the two evaluations.

Channel	This work	f_k method [21]	Difference
$\pi^+\pi^-$ [123–125]	481.42 ± 4.05	481.42 ± 4.26	0.00
K^+K^- [86]	16.92 ± 0.71	16.93 ± 0.81	-0.01

Table 2.3: Comparison of results from this work and using the f_k method when combining data which have only global normalisation uncertainties. All results are found in the full energy range of the combined data and are given in units of $a_\mu^{\mathrm{had,\,LO\,VP}} \times 10^{10}$. The first column indicates the final state or individual contribution, the second column gives the estimate of $a_\mu^{\mathrm{had,\,LO\,VP}}$ from this work, the third column states the estimate using the f_k method and the last column gives the difference between the two evaluations.

Channel	This work (linear)	Constant cross section	Difference
$\pi^+\pi^-$	502.99 ± 1.97	502.49 ± 1.98	0.50
$\pi^+\pi^-\pi^0$	47.82 ± 0.89	48.11 ± 0.93	-0.29
$\pi^+\pi^-\pi^+\pi^-$	15.17 ± 0.21	15.07 ± 0.16	0.10
$\pi^+\pi^-\pi^0\pi^0$	19.80 ± 0.79	19.89 ± 0.53	-0.09
K^+K^-	23.05 ± 0.22	23.34 ± 0.32	-0.29
$K^0_S K^0_L$	13.05 ± 0.19	13.13 ± 0.17	-0.08

Table 2.4: Comparison of the contributions to $a_\mu^{\mathrm{had,\,LO\,VP}}$ from leading and major sub-leading hadronic channels determined in this work (where the clusters are defined to be linear between each bin) and the constant cross section representation of the clusters. All results are found in the energy range $\sqrt{s} \leq 2$ GeV and are given in units of $a_\mu^{\mathrm{had,\,LO\,VP}} \times 10^{10}$. The first column indicates the final state or individual contribution, the second column gives the estimate of $a_\mu^{\mathrm{had,\,LO\,VP}}$ from this work, the third column states the estimate using the constant cross section representation and the last column gives the difference between the two evaluations.

of each cluster as linear instead of constant across the width of each cluster. Although the integration method is unchanged from a linear trapezoidal rule integral since the

previous analysis [21] (see Section 2.5), the representation of the cross section as linear between each bin in the χ^2-function in equation (2.29) can cause variations in the final fit solution for all clusters in a given channel. Results comparing the two methods are given in Table 2.4. Again, the differences between the two approaches are not outside the quoted errors, indicating there was not a large misrepresentation of the cross section in the constant representation.

2.4 Determining the full hadronic R-ratio

Once the combination procedure has been applied to each individual hadronic channel, the resulting determined cross section data and corresponding covariance matrices must be summed to determine the full hadronic R-ratio, $R(s)$. With the data from each channel having a different binning as a result of its individual combination, the sum of these states requires an interpolation of both the cross section and its covariance matrix. This process is described in detail in Section 2.4.5. Importantly, the covariance matrix for the full hadronic R-ratio has not been previously fully determined by any other work and is achieved here. Before this, any missing contributions that are not available from experimental measurements must be estimated through various means in order to determine the most comprehensive representation of the full hadronic spectrum that is possible. These missing contributions include threshold contributions, narrow resonances and those hadronic channels that have not been measured at all by experiment.

2.4.1 Estimating contributions: chiral perturbation theory (ChPT)

For some hadronic final states, the available experimental data do not extend to the physical lower energy limit of the respective hadronic production thresholds. The $\pi^0\gamma$ channel, for example, defines the lower energy border of the dispersion integral in equation (1.45) to be $s = m_\pi^2$. However, the available $\pi^0\gamma$ data only reach a lower energy limit of 0.6 GeV. With the dispersion integrals being weighted towards lower energies, the energy range $m_\pi \leq \sqrt{s} < 0.6$ GeV is an important contribution and should not be excluded. This is also true for the $\pi^+\pi^-$, $\pi^+\pi^-\pi^0$ and $\eta\gamma$ channels, all of which do not have data available that extend down to their respective thresholds.

Without experimental data, the contributions from low energy regions for these final states must be estimated.[7] As in [21, 46, 47], this is achieved via previously determined chiral perturbation theory (ChPT) determinations of these threshold contributions. ChPT is a low-energy effective theory describing the hadronic interactions of low-mass mesons such as pions. In this setup, as opposed to an expansion in the strong coupling constant α_s like in pQCD (which is a divergent expansion at low energies as $\alpha_s >> 1$),

[7] As the low energy cross sections are not linear in s, an extrapolation of the available data down to production threshold would result in overestimates of these low energy contributions.

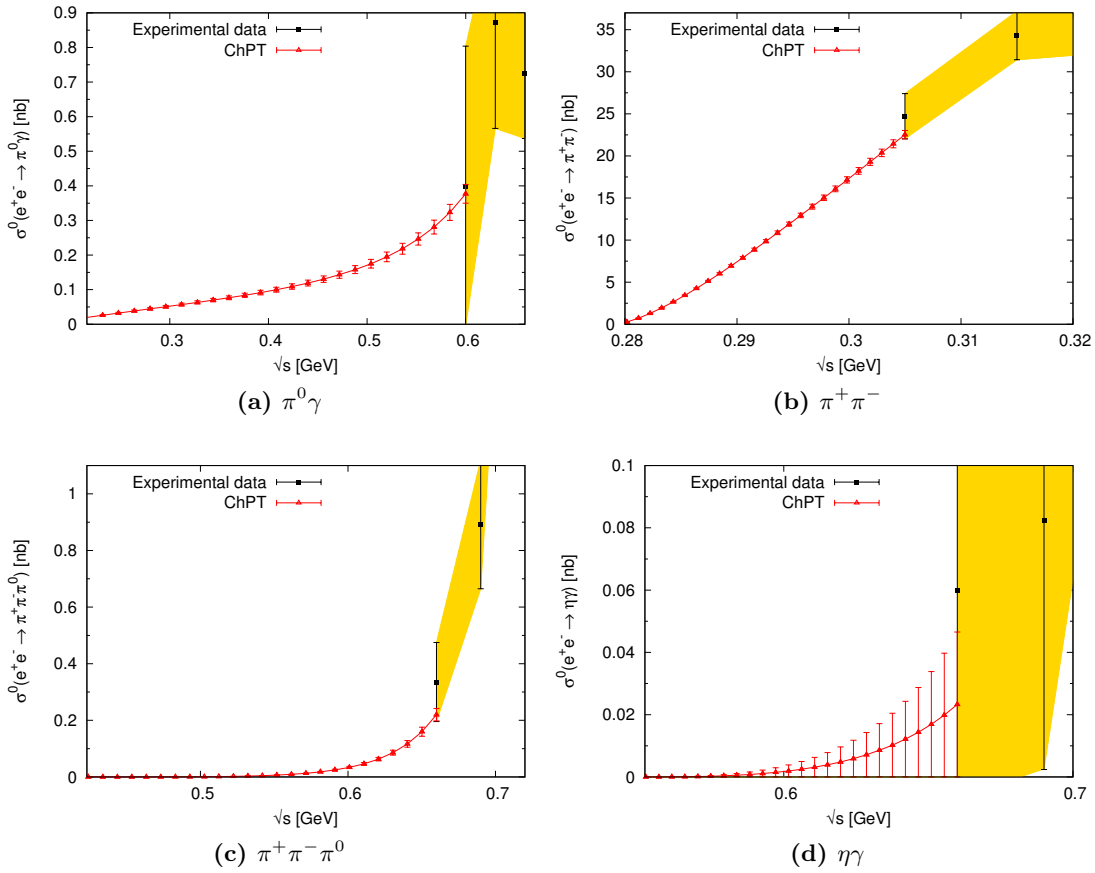

(a) $\pi^0\gamma$ **(b)** $\pi^+\pi^-$

(c) $\pi^+\pi^-\pi^0$ **(d)** $\eta\gamma$

Fig. 2.7: The threshold contributions of the $\pi^0\gamma$, $\pi^+\pi^-$, $\pi^+\pi^-\pi^0$ and $\eta\gamma$ channels as estimated using chiral perturbation theory. In each case, the ChPT estimate is given by the red line (with the theoretical uncertainties determined by the ChPT relation and input parameters, e.g. masses, of each respective final state), whilst the yellow band represents the uncertainty of the corresponding experimental data.

an expansion is performed in small momenta p or the light quark masses m_q, which are chiral symmetry breaking parameters. Massless particles have chiral symmetry and, consequently, the introduction of quark masses spontaneously breaks the chiral nature of the theory. Therefore, in ChPT, the quarks and gluons from pQCD are replaced by mesons, which are the Nambu-Goldstone bosons of spontaneous chiral symmetry breaking. The expansion is performed in the ratio of these parameters with some safe energy scale Λ $\left(\frac{p}{\Lambda}\text{ or }\frac{m_q}{\Lambda}\right)$, where $p, m_q << \Lambda$ and, therefore, the expansion is well-defined. At leading order, this expansion assumes that the mesons are point-like particles that couple to the photon.

Fortunately, in other dedicated works, the theoretical low-energy cross sections have been determined using ChPT and can be implemented here for the purpose of extending the lower boundary of the relevant experimental data to their production thresholds. For the $\pi^0\gamma$ channel, the contribution in the range $m_\pi \leq \sqrt{s} < 0.6$ GeV is determined

from the theoretical description of the low energy cross section given in [75] as

$$\sigma(e^+e^- \to \pi^0\gamma) = \frac{8\pi\alpha\Gamma(\pi^0 \to 2\gamma)}{3m_{\pi^0}^2}\left(1 - \frac{m_{\pi^0}^2}{s}\right)^3\left(\frac{m_\omega^2}{m_\omega^2 - s}\right)^2 . \tag{2.35}$$

Here, $\Gamma(\pi^0 \to 2\gamma)$ is the decay width of the process $\pi^0 \to 2\gamma$ (which dominates the decay of the π^0 meson [16]) and m_ω is the mass of the ω resonance. The last term in equation (2.35) is an improvement of the pure ChPT cross section using a vector meson dominance approach [75]. This accounts for the presence of the ω resonance in the $\pi^0\gamma$ channel by replacing the virtual photon propagator with the resonant form

$$\frac{1}{s} \to \frac{1}{s}\frac{m_\omega^2}{m_\omega^2 - s} . \tag{2.36}$$

For the $\pi^+\pi^-$ threshold contribution in the range $2m_\pi \leq \sqrt{s} < 0.305$ GeV, a compact prediction for the pion form factor given in [76] as

$$F_\pi(s) = 1 + \frac{1}{6}\langle r^2\rangle_\pi s + c_\pi s^2 + \mathcal{O}(s^3) , \tag{2.37}$$

where the coefficients $\langle r^2\rangle_\pi = 0.431 \pm 0.026$ (fm^2) and $c_\pi = 3.2 \pm 1.0$ (GeV^{-4}), are found in [76] by fitting to space-like pion scattering data [77]. The $\pi^+\pi^-\pi^0$ contribution between $3m_\pi \leq \sqrt{s} < 0.66$ GeV is estimated using the ChPT prescription in [78, 79]. The threshold $\eta\gamma$ contribution in the range $m_\eta \leq \sqrt{s} < 0.66$ GeV is estimated according to Appendix A.2 of [46], although it provides a negligible contribution to a_μ. For all four of these channels, the estimated cross sections are displayed in Figure 2.7, where each plot shows the point where the ChPT prediction is overtaken by the measured experimental data. In all cases, there is good agreement between the ChPT estimate and the data.

2.4.2 Estimating contributions: isospin

For many of the sub-leading hadronic final states, there are no experimental measurements of their cross sections. Many of these contributions, although small compared to the leading contributions, have production thresholds that are below the boundary where the sum of exclusive final states is replaced by the inclusive data. It is clear that, for a high precision analysis, these should be included in the exclusive sum to ensure that they contribute to the hadronic R-ratio and, therefore, the determination of $a_\mu^{\text{had,VP}}$.

Following [21, 46, 47], the cross sections for these final states are estimated using relations based on the Pais isospin class [80]. As a simple example of this setup, consider the process of electron-positron annihilation into a two-pion final state. The three pions (π^+, π^0, π^-) form a triplet under isospin symmetry, where the quark contents of each are described by the wave-functions

$$|\pi^+\rangle : -|u\bar{d}\rangle \ , \ |\pi^0\rangle : |\frac{1}{\sqrt{2}}(u\bar{u} - d\bar{d})\rangle \ , \ |\pi^-\rangle : -|d\bar{u}\rangle . \tag{2.38}$$

Pions are eigenstates of G-parity ($G = \pm 1$),

$$G \equiv CR_2 = Ce^{-i\pi T_2} = e^{-i\pi \frac{\sigma_2}{2}} , \tag{2.39}$$

which is a symmetry described by combination of a π rotation about the 2-axis in isospin space R_2 with charge conjugation C. Under G-parity, the pion triplet transforms as

$$G \begin{pmatrix} |\pi^+\rangle \\ |\pi^0\rangle \\ |\pi^-\rangle \end{pmatrix} = \begin{pmatrix} -|\pi^+\rangle \\ -|\pi^0\rangle \\ -|\pi^-\rangle \end{pmatrix} . \tag{2.40}$$

It follows that pions have a G-parity quantum number $G = -1$ [16]. The photon can be either be isospin $I = 0$ or $I = 1$, implying that isospin is not conserved in photon interactions and resulting in

$$G|\gamma_{I=0}\rangle = -|\gamma_{I=0}\rangle \ , \ G|\gamma_{I=1}\rangle = |\gamma_{I=1}\rangle . \tag{2.41}$$

However, from this it can be seen for the process $e^+e^- \to \gamma^* \to n\pi$, the G-parity assignment for n pions in the final state is given by $G^{n\,\text{pions}} = (-1)^n$, conserving $G = -1$ for odd n and conserving $G = 1$ for even n [81].[8] Using this setup and the knowledge that the photon is either $I = 0$ or $I = 1$, the two-pion final states consistent with the isospin of the photon can be constructed from the table of Clebsch-Gordan coefficients [16] as

$$\begin{aligned} |0,0\rangle &= \frac{1}{\sqrt{3}}|\pi^+\pi^-\rangle - \frac{1}{\sqrt{3}}|\pi^0\pi^0\rangle + \frac{1}{\sqrt{3}}|\pi^-\pi^+\rangle \\ |1,0\rangle &= \frac{1}{\sqrt{2}}|\pi^+\pi^-\rangle - \frac{1}{\sqrt{2}}|\pi^-\pi^+\rangle . \end{aligned} \tag{2.42}$$

The process $\gamma \to \pi^0\pi^0$ is forbidden due to charge conjugation symmetry (with $C^\gamma = -1$ and $C^{\pi^0} = +1$) and, therefore, only the second final state is allowed. Hence, the use of isospin has shown that the only allowed two-pion final is the process $e^+e^- \to \gamma^* \to \pi^+\pi^-$ and, in the isospin limit, can be constructed from the valid relation in equation (2.42).

This theoretical setup can be extended to derive relations for hadronic final states for which there is no experimental data available. Specifically, the missing states are approximated using theoretical forms of the cross section determined from isospin relations to measured cross section data as derived in [51]. In this work, the channels that are estimated via these relations are $\pi^+\pi^-3\pi^0$, $\pi^+\pi^-4\pi^0$, $KK3\pi$, $\omega 2\pi$, $\omega 3\pi$, ωKK and

[8] This is an important result and is responsible for the dominant decay of $\rho \to \pi^+\pi^-$ instead of $\rho \to \pi^+\pi^-\pi^0$. The ρ resonance has $G^\rho = +1$ [16] and the decay of the ρ to an odd number of pions is almost entirely suppressed by G-parity [81]. This is also true for the decay of the ω resonance, where $G^\omega = -1$ and consequently the ω dominantly decays to $\pi^+\pi^-\pi^0$ instead of to $\pi^+\pi^-$. The presence of the ω resonance in the $\pi^+\pi^-$ cross section (clearly visible in its interference with the ρ resonance) is evidence of isospin being an inexact symmetry of nature and is, therefore, an isospin breaking effect.

$\eta\pi^+\pi^-2\pi^0$.[9] In each case, the isospin relation used from [51], along with the corresponding estimated contribution to $a_\mu^{\text{had, LO VP}}$, is given in the respective discussion of each channel in Section 4.2. The use of these relations is far from preferable, as it has been shown that for some final states the isospin relations can result in poor estimates of the resulting cross section (see, for example, the discussion of the $KK2\pi$ channel in Section 4.1.8). However, with no better alternative approach available, it is important that these channels are included in some form. In addition, all of the estimated states provide small contributions to $a_\mu^{\text{had, LO VP}}$ below ~ 2 GeV and will not drastically alter the final result. It should also be noted that, in many cases, the estimates for the channels have conservative errors applied to account for any incorrect approximation.

2.4.3 Estimating contributions: narrow resonances

The narrow resonances in the $c\bar{c}$ and $b\bar{b}$ regions are not resolved by the measured data and, therefore, must be estimated and added separately to the inclusive R-ratio data. These resonances are the J/ψ, ψ' and $\Upsilon(1S-4S)$ states.[10] This is achieved using the Breit-Wigner (BW) resonance approximation given by

$$\sigma_{\text{BW}}(s) = \frac{12\pi}{M_{\text{res}}^2}\frac{\Gamma_{ee}^0}{\Gamma}\frac{s\Gamma^2}{(s-M_{\text{res}}^2)^2 + M_{\text{res}}^2\Gamma^2}\,, \tag{2.43}$$

where M_{res} is the mass of the resonance, Γ is the full width of the resonance and Γ_{ee}^0 is the undressed electronic width of the resonance as given in equation (2.10). The input values and uncertainties of these quantities are taken from [16], all of which are propagated to determine the total uncertainty of the estimated cross section σ_{BW}. Ensuring a fine enough binning, the cross sections of resonance contributions are individually estimated and added to the compilation for the total hadronic R-ratio.

2.4.4 pQCD and $R(\to\infty)$

For the determination of $a_\mu^{\text{had, VP}}$ at higher energies ($11.2 \leq \sqrt{s} \leq 1000.2$ GeV), $R(s)$ is determined via pQCD using the dedicated and publicly available code `rhad` [238]. As stated previously, at these energies and away from quark flavour thresholds, pQCD provides a good prediction of the hadronic cross section and is safe to use. The physical rapid variations that are part of the hadronic spectrum in the regions of flavour thresholds are not present in the determination of $R(s)$ as calculated by `rhad`. Fortunately, the energy region > 11.1985 GeV is above the bottom quark production threshold and,

[9] New measured data contributing to the channels $KK\pi$ and $KK2\pi$ have allowed for these states to be determined without the need for dedicated isospin relations as was previously done in [21, 46, 47]. This is explained in detail with a comparison of the estimates for these states from the experimental data and isospin relations in Section 4.1.8.

[10] From [82], the inclusion of R_b data [234] has resolved the resonances of the $\Upsilon(5S)$ and $\Upsilon(6S)$ states, removing the need to estimate these structures as was done in [21, 46, 47]. This is discussed in further detail in Section 4.3.2.

therefore, the contributions from the first five quark flavours are included as part of the data compilation described above. For the top quark, the low energy weighting of the integrand and kernel function in equation (1.46) means the variations due to top quark production provide a very small contribution to $a_\mu^{\mathrm{had,\,VP}}$ and can be safely neglected.[11] In this work, all relevant input parameters used by `rhad` have been updated to the most recent values [16] and an uncertainty on $R(s)$ is determined from the uncertainties of $\alpha_s(M_Z^2)$, the mass of the bottom quark, the mass of the top quark and a variation of the renormalisation scale.

The contribution to the dispersion integral above the pQCD cut-off and up to $s = \infty$ is negligibly small. It can be approximated using the knowledge that in this relevant, six quark flavour region, $R(\sqrt{s} \gtrsim 1\ \mathrm{TeV}) \simeq 5$. In addition, if the kernel function $K(s)$ in equation (1.46) is modified to be

$$\hat{K}(s) = \frac{3s}{m_\mu^2} K(s)\,, \tag{2.44}$$

then $\hat{K}(s)$ is a monotonically increasing kernel function with $\hat{K}(s \to \infty) \to 1$. Applying these assumptions to the corresponding dispersion integral modified from equation (1.46) results in

$$\begin{aligned} a_\mu^{\mathrm{had,\,LO\,VP}}(\sqrt{s} \gtrsim 1\,\mathrm{TeV}) &= \left(\frac{\alpha m_\mu}{3\pi}\right)^2 \int_{1\,\mathrm{TeV}}^{\infty} \frac{\mathrm{d}s}{s^2}\, R(s)\hat{K}(s) \\ &\simeq 5\left(\frac{\alpha m_\mu}{3\pi}\right)^2 \int_{1\,\mathrm{TeV}}^{\infty} \frac{\mathrm{d}s}{s^2} \\ &\simeq 0.0003 \times 10^{-10}\,, \end{aligned} \tag{2.45}$$

which is insignificant compared to HLMNT11 estimate of $a_\mu^{\mathrm{had,\,LO\,VP}}$ given in equation (1.31).

2.4.5 Combining all contributions

In this work, the full hadronic R-ratio is determined by summing all determined cross section data and corresponding covariance matrices, either taken from the data combination or from the estimated contributions listed above. In the works preceding this analysis [21, 46, 47], the contributions to $a_\mu^{\mathrm{had,\,VP}}$ were found by integrating over the data for various channels/contributions individually and then summing the separate contributions to $a_\mu^{\mathrm{had,\,VP}}$ and its error. Although this approach is equivalent to summing the data before integrating, the previous works had not achieved the sum of correlated uncertainties to produce a covariance matrix for the total R-ratio. This

[11] This is not true for the dispersion integral used to determine $\Delta\alpha_{\mathrm{had}}$ in equation (2.3), where due to a different weighting of the integrand, the top quark threshold provides larger contributions. Hence, in this case, `rhad` is used to determine $R^{(5)}(s)$ above 11.1985 GeV using only five active quark flavours and, as described in Section 2.1.1, equation (2.3) is only used to calculate the contributions from the first five quark flavours. The top quark contributions are evaluated separately [62].

is accomplished in this work for the first time and is described here. The resulting data vector and corresponding covariance matrix of the hadronic R-ratio in the range $m_\pi \leq \sqrt{s} \leq 1000.1985$ GeV is determined in this work.[12] However, the contributions to $a_\mu^{\text{had, VP}}$ from individual channels are still determined as a major part of the individual channel analysis. All results from individual channels are given in Section 4.

Before summing the data from different channels, the uncertainties from all error sources must be combined to define a total covariance matrix for each channel. The output covariance $\tilde{V}\big(m,n\big)$ of the χ^2-minimisation contains all experimental uncertainties and is inflated by local χ^2_{min}/d.o.f. according to equation (2.34). For any additional uncertainty due to VP corrections, a covariance matrix $V_{\text{VP}}(m,n)$ is constructed according to equation (2.12) as

$$V_{\text{VP}}(m,n) = \frac{1}{3}(R_m - R_m^{\text{no VP}})\frac{1}{3}(R_n - R_n^{\text{no VP}})\,, \tag{2.46}$$

where the superscript 'no VP' indicates the cross section value of the cluster without a VP correction applied. For the additional uncertainty due to FSR radiative corrections, following the discussion in Section 2.1.2, the FSR uncertainty covariance matrix $V_{\text{FSR}}(m,n)$ for the $\pi^+\pi^-$ channel is found from

$$V_{\text{FSR}}^{\pi^+\pi^-}(m,n) = (R_m^{\pi^+\pi^-} - R_m^{\pi^+\pi^-,\text{ no FSR}})(R_n^{\pi^+\pi^-} - R_n^{\pi^+\pi^-,\text{ no FSR}})\,, \tag{2.47}$$

where the superscript 'no FSR' indicates the cross section value of the cluster without a FSR correction applied. For all other channels requiring an additional FSR correction uncertainty, the corresponding covariance matrix is given by

$$V_{\text{FSR}}(m,n) = (0.01)R_m(0.01)R_n\,. \tag{2.48}$$

Therefore, for each channel, the total covariance matrix is found from the sum

$$V\big(m,n\big) = \tilde{V}\big(m,n\big) + V_{\text{VP}}(m,n) + V_{\text{FSR}}(m,n)\,. \tag{2.49}$$

Following this, the total value $R(\sqrt{s} = E_a)$ is found from the sum of the linear interpolants of all available cross section data. The energy array E_a is defined by the energies of all clusters, from all channels, contributing to the total R-ratio. For all channels X, if $E_m^X < E_a < E_{m+1}^X$, then

$$R(E_a) = \sum_X \left[R_m^X + \frac{(E_a - E_m^X)}{(E_{m+1}^X - E_m^X)}(R_{m+1}^X - R_m^X)\right]. \tag{2.50}$$

Therefore, if $E_m^X < E_a < E_{m+1}^X$ and $E_n^X < E_b < E_{n+1}^X$, then the calculation of the total covariance matrix $V\big(E_a,E_b\big)$ follows accordingly using the standard error propagation formula

$$V\big(E_a,E_b\big) = \sum_X \sum_{p=m}^{m+1}\sum_{q=n}^{n+1} \frac{\partial R(E_a)}{\partial R_p^X} V\big(E_p^X, E_q^X\big)\frac{\partial R(E_b)}{\partial R_q^X}\,, \tag{2.51}$$

[12] The data for the R-ratio in the range $m_\pi \leq \sqrt{s} \leq 11.1985$ GeV is available upon request from the authors of [87].

where $V\big(E_p^X, E_q^X\big)$ is the covariance matrix of the channel X at the cluster energies $E_p^X = E_m^X, E_{m+1}^X$ and $E_q^X = E_n^X, E_{n+1}^X$.[13]

2.5 Integration

Once the determination of the total R-ratio and its covariance matrix is complete, or for the contribution from each channel individually, the integral over the available data given in equation (1.46) is found using a trapezoidal rule integral that is consistent with the linear cross section representation of the clusters that has been adopted in the χ^2-minimisation. In the respective available energy range $E_{\min} \leq \sqrt{s} \leq E_{\max}$ GeV, the integral to be determined, I, is given as

$$I[a_\mu^{\text{had, LO VP}}] = \frac{\alpha^2}{3\pi^2} \int_{E_{\min}^2}^{E_{\max}^2} \frac{\mathrm{d}s}{s}\, R(s) K(s) = \frac{2\alpha^2}{3\pi^2} \int_{E_{\min}}^{E_{\max}} \frac{\mathrm{d}E}{E}\, R(E^2) K(E^2)\,. \tag{2.53}$$

If the lower integral boundary exists between the clusters $E_m < E_{\min} < E_{m+1}$ or the upper boundary exists between $E_{n-1} < E_{\max} < E_n$, then the cross section values $R(E_{\min}^2)$ or $R(E_{\max}^2)$ are found by linear interpolation. Alternatively, if either integral boundary required are beyond the borders of the available energy of the data, then the integral boundaries are found by linear extrapolation. The trapezoidal rule integral is therefore given by[14]

$$\begin{aligned} I = \frac{2\alpha^2}{3\pi^2} \Bigg[& \left(\frac{E_{m+1} - E_{\min}}{2E_{\min}} R\big(E_{\min}^2\big) K\big(E_{\min}^2\big) + \frac{E_{m+2} - E_{\min}}{2E_{m+1}} R_{m+1} K\big(E_{m+1}^2\big) \right) \\ & + \left(\sum_{k=m+2}^{n-2} \frac{E_{k+1} - E_{k-1}}{2E_k} R_k K\big(E_k^2\big) \right) \\ & + \left(\frac{E_{\max} - E_{n-2}}{2E_{n-1}} R_{n-1} K\big(E_{n-1}^2\big) + \frac{E_{\max} - E_{n-1}}{2E_{\max}} R\big(E_{\max}^2\big) K\big(E_{\max}^2\big) \right) \Bigg]. \end{aligned} \tag{2.54}$$

The error of the integral, ΔI, is then found from the covariance matrix using

$$\Delta I = \left(\sum_{k=\min}^{\max} \sum_{l=\min}^{\max} \frac{\partial I}{\partial R_k} V\big(k,l\big) \frac{\partial I}{\partial R_l} \right)^{\frac{1}{2}}, \tag{2.55}$$

where the sums run between the lower and upper integral boundaries,

[13] Note that, in this work, no correlation is assumed between separate hadronic channels due to the lack of experimental information. However, should this information become available, this can be easily incorporated to the error contribution of $R(s)$ by extending equation (2.51) to include a second sum over all channels X'. Therefore, if $E_m^X < E_a < E_{m+1}^X$ of the channel X and $E_n^{X'} < E_b < E_{n+1}^{X'}$ of the channel X', then

$$V\big(E_a, E_b\big) = \sum_X \sum_{X'} \sum_{p=m}^{m+1} \sum_{q=n}^{n+1} \frac{\partial R(E_a)}{\partial R_p^X} V\big(E_p^X, E_q^{X'}\big) \frac{\partial R(E_b)}{\partial R_q^{X'}}\,. \tag{2.52}$$

Here, $V\big(E_p^X, E_q^{X'}\big)$ is the covariance matrix describing the correlation between the channel X and the channel X' at the cluster energies $E_p^X = E_m^X, E_{m+1}^X$ and $E_q^{X'} = E_n^{X'}, E_{n+1}^{X'}$.

[14] Note that exceptions to this trapezoidal rule definition of the integral exist in special cases such as $E_{\max} < E_{m+1}$, $E_{\max} < E_{m+2}$, etc.

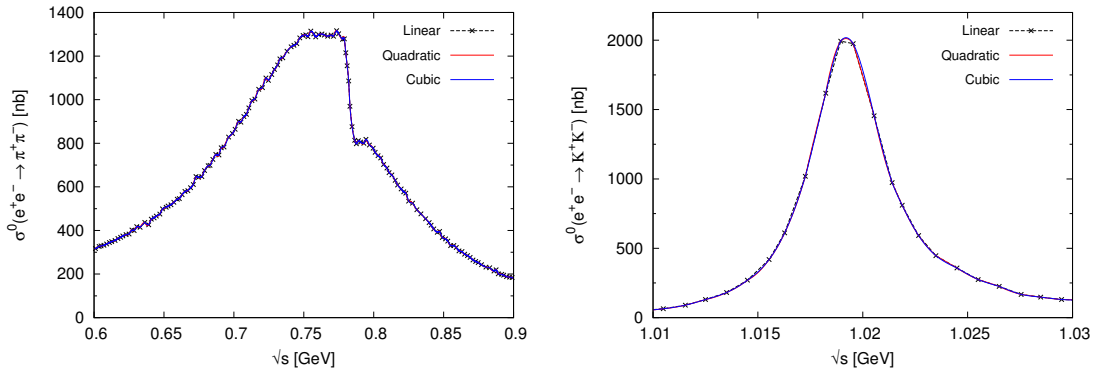

(a) The $\rho - \omega$ resonance region of the $\pi^+\pi^-$ channel.

(b) The ϕ resonance region of the K^+K^- channel.

Fig. 2.8: The differences observed using linear, quadratic and cubic integration routines in prominent resonance regions in the $\pi^+\pi^-$ and K^+K^- channels.

$$k, l = \min, m+1, m+2, ..., n-2, n-1, \max\,, \tag{2.56}$$

as given by equation (2.54). Importantly, in this work, the calculation of the uncertainty of $a_\mu^{\mathrm{had,VP}}$ has been modified to improve the determination of the error contribution at the integral boundaries. Should the integral boundaries $R\big(E^2_{\mathrm{min}}\big)$ or $R\big(E^2_{\mathrm{max}}\big)$ be found by linear interpolation (or extrapolation if it is necessary to extend the integral boundaries), then the covariance matrix $V\big(k,l\big)$ is interpolated (extrapolated) accordingly using the standard error propagation formula

$$V\big(k,l\big) = \sum_p \sum_q \frac{\partial R_k}{\partial R_p} V\big(p,q\big) \frac{\partial R_l}{\partial R_q}\,, \tag{2.57}$$

where p, q run over all clusters and $V\big(l,k\big) = V\big(k,l\big)$.

In principle, the use of the trapezoidal rule integral could lead to unreliable results due to the form of the kernel function or at narrow resonances if data are sparse. However, with the current density of cross section measurements, especially in the dominant hadronic channels, the differences between trapezoidal rule integration and any higher order polynomial approximation are consequently small (less than 10% of the error in the largest instance of the K^+K^- channel) and of no concern. This can be seen in the plots in Figure 2.8.

Chapter 3

Combination of KLOE $\sigma\left(e^+e^- \to \pi^+\pi^-\gamma(\gamma)\right)$ measurements

The three precision measurements of the cross section $\sigma\left(e^+e^- \to \pi^+\pi^-\gamma(\gamma)\right)$ using initial state radiation by the KLOE collaboration [88–90] provide an important input for the prediction of the hadronic contribution to the anomalous magnetic moment of the muon. These measurements are correlated for both statistical and systematic uncertainties and, therefore, the simultaneous use of these measurements requires covariance matrices that fully describe the correlations. The study and construction of these covariance matrices, coupled with their use to determine a combined KLOE measurement for $\sigma\left(e^+e^- \to \pi^+\pi^-\gamma(\gamma)\right)$, demonstrate the importance of the correct construction of experimental covariance matrices and provide a prominent example of the power of the data combination method described in the previous section.

3.1 The KLOE measurements of $\sigma\left(e^+e^- \to \pi^+\pi^-\gamma(\gamma)\right)$

The KLOE collaboration have made three precise measurements of the cross section $\sigma\left(e^+e^- \to \pi^+\pi^-\gamma(\gamma)\right)$ in 2008 [88,91], 2010 [89,92] and 2012 [90,93]. The contribution of the $\pi^+\pi^-$ final state to the anomalous magnetic moment of the muon, $a_\mu^{\pi^+\pi^-}$, is over 70% of the total estimate of $a_\mu^{\text{had},\text{LO VP}}$ and is also the largest contributor to its uncertainty. As such, the three measurements of the cross section $\sigma\left(e^+e^- \to \pi^+\pi^-\gamma(\gamma)\right)$ by the KLOE collaboration provide an important input to precisely determine $a_\mu^{\pi^+\pi^-}$.

The simultaneous input of the three KLOE measurements requires a detailed analysis to attain the correct combination of the three, which will have a non-trivial influence on $a_\mu^{\pi^+\pi^-}$. Although each of the KLOE measurements of $\sigma\left(e^+e^- \to \pi^+\pi^-\gamma(\gamma)\right)$ has individual covariance matrices provided for both statistical and systematic uncertainties, the measurements themselves are, in part, highly correlated, necessitating the construction of full statistical and systematic covariance matrices describing the cor-

relation between the bins of all three measurements to be used in any combination of these data. To combine the data without the correlations would result in an underestimate of the uncertainty of $a_\mu^{\text{had},\text{LO VP}}$ and, potentially, a bias of its mean value. The construction of these covariance matrices must be statistically robust in order to ensure that they correctly describe the correlated relationship of the three measurements.

From the experimental analysis, all three published cross sections are bare (undressed of all VP effects) and include FSR effects ($\sigma^0_{\pi\pi,\gamma}$). For the first two, denoted here as KLOE08 [88] and KLOE10 [89], the bare cross section is obtained according to the procedure described in Section 2.1.1, but using a different publicly available VP routine [94, 95]. For the third measurement of $\sigma^0_{\pi\pi,\gamma}$, namely KLOE12 [90], the data were normalised bin-by-bin by a reciprocal measurement of the $\mu^+\mu^-$ cross section. The ratio of the $\pi^+\pi^-\gamma$ and $\mu^+\mu^-\gamma$ cross sections benefits from the cancellation of the luminosity correction, the radiator function for initial state radiation (ISR) and the VP correction, manifestly resulting in a bare cross section.[1] For all three measurements, the FSR contribution to the $\pi^+\pi^-$ production is included according to Section 2.1.2.

The KLOE08 measurement consists of 60 data points in the range $0.5916 < \sqrt{s} < 0.9746$ GeV, covering the dominant ρ resonance structure and the $\rho - \omega$ interference region in the $\pi^+\pi^-$ final state. The uncertainties of the cross section are dominated by the systematics uncertainties, especially in the region where the cross section is large. From [88], integrating the originally published KLOE08 data (following the integral procedure in Section 2.5), results in[2]

$$a_\mu^{\pi^+\pi^-}(\text{KLOE08}, 0.5916 < \sqrt{s} < 0.9746 \text{ GeV}) = (387.2 \pm 0.5_{\text{stat}} \pm 3.3_{\text{sys}}) \times 10^{-10} \,. \quad (3.2)$$

The KLOE10 measurement totals 75 data points in the range $0.3162 < \sqrt{s} < 0.9220$ GeV. The fifty energy bins of the data in the range $0.5916 < \sqrt{s} < 0.9220$ GeV are identical to the fifty KLOE08 bins in the same interval. From [89], the original KLOE10 cross section results in

$$a_\mu^{\pi^+\pi^-}(\text{KLOE10}, 0.3162 < \sqrt{s} < 0.9220 \text{ GeV}) = (478.5 \pm 2.0_{\text{stat}} \pm 6.7_{\text{sys}}) \times 10^{-10} \,. \quad (3.3)$$

As previously described, the KLOE12 measurement was determined as a $\mu^+\mu^-\gamma$ normalised cross section. The $\mu^+\mu^-$ cross section was measured for the KLOE12 analysis,

[1] For the same invariant mass squared, the ratio of the measured $\pi^+\pi^-\gamma$ and $\mu^+\mu^-\gamma$ differential cross sections allows the relation

$$\sigma^0_{\pi\pi,\gamma}(s) = \frac{\mathrm{d}\sigma\big(\pi^+\pi^-\gamma\big)/\mathrm{d}s}{\mathrm{d}\sigma\big(\mu^+\mu^-\gamma\big)/\mathrm{d}s} \times \sigma^0_\gamma(e^+e^- \to \mu^+\mu^-, s) \,, \quad (3.1)$$

where $s = M^2_{\pi\pi} = M^2_{\mu\mu}$. As both these processes exist only through s-channel exchange, the contributions to the photon vacuum polarisation are both purely time-like and exactly cancel in the ratio.

[2] The emphasis on the originally published data is relevant here as studies into the construction of the covariance matrices resulted in the experimental analysis of each KLOE measurement of $\sigma\big(e^+e^- \to \pi^+\pi^-\gamma(\gamma)\big)$ being reviewed and, in some cases, updated in order to ensure a more precise and consistent combination of the three measurements. The changes to the results given here are presented in Section 3.2.

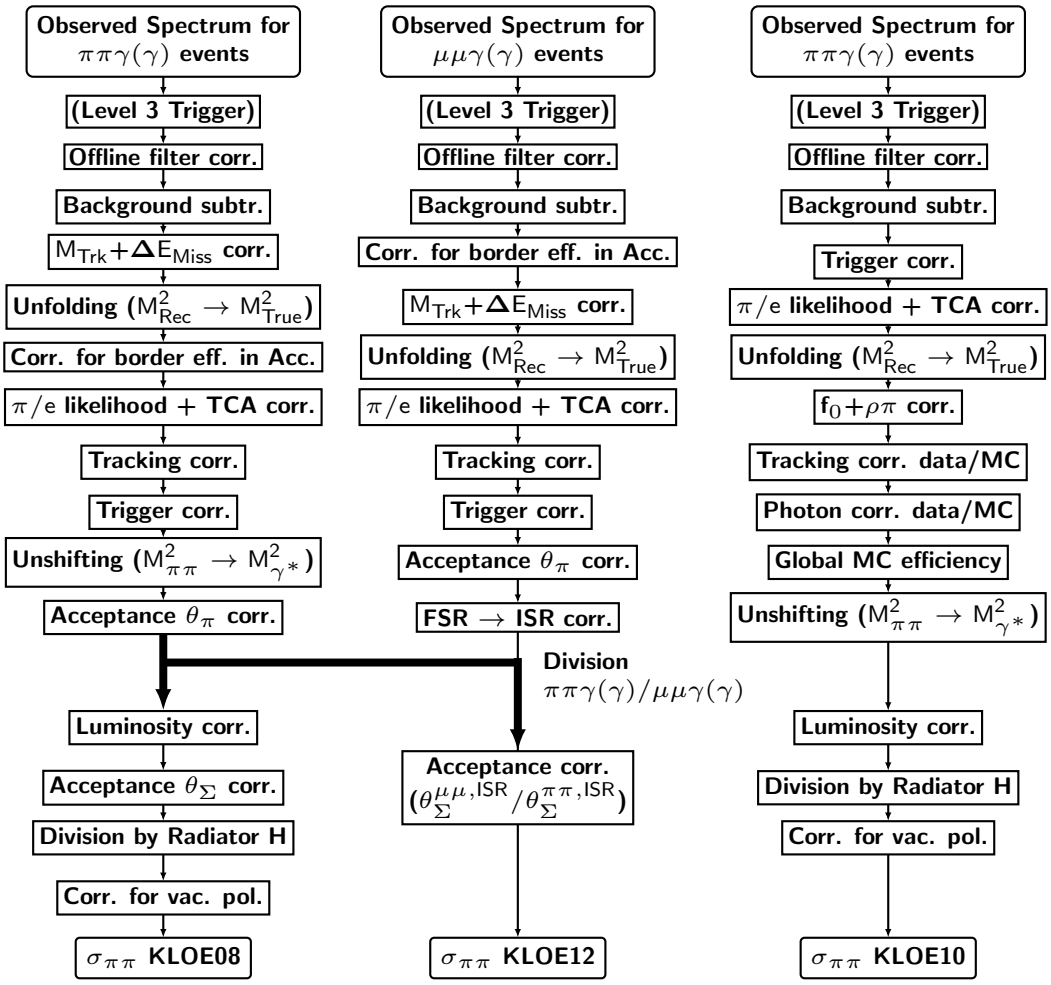

Fig. 3.1: The flow of the experimental analyses of all three $\sigma\big(e^+e^- \to \pi^+\pi^-\gamma(\gamma)\big)$ cross section measurements. The point where the KLOE08 $\pi^+\pi^-\gamma(\gamma)$ data enter the KLOE12 analysis is indicated by the bold black arrows.

whereas the KLOE08 $\pi^+\pi^-$ data were used as the input for the two-pion cross section, with the KLOE12 measurement having an identical binning and energy range to KLOE08. From [90], the original KLOE12 data give a contribution to $a_\mu^{\pi^+\pi^-}$ of

$$a_\mu^{\pi^+\pi^-}(\text{KLOE12}, 0.5916 < \sqrt{s} < 0.9746 \text{ GeV}) = (385.1 \pm 1.1_{\text{stat}} \pm 2.7_{\text{sys}}) \times 10^{-10} \,. \quad (3.4)$$

As KLOE08 and KLOE12 share the same two-pion data, these measurements are highly correlated, and it is important that they be treated as such in any combination of the two measurements.

The flow of the experimental analyses for the KLOE08, KLOE10 and KLOE12 measurements is shown in Figure 3.1. Each stage in the flow diagram corresponds to a specific part of the experimental analysis or a specific correction to the cross section measurement. In the case of the KLOE12 measurement, the beginning of the flow refers to the measurement of $\mu^+\mu^-\gamma(\gamma)$. The point where the KLOE08 $\pi^+\pi^-\gamma(\gamma)$ data enters

is clearly marked. This diagram exhibits the extent of the correlation between KLOE08 and KLOE12, with correlations existing for all elements of the KLOE08 $\sigma^0_{\pi\pi,\gamma}$ analysis from the observed spectrum of $\pi^+\pi^-\gamma(\gamma)$ events up to the acceptance correction. In addition, the degree of correlation between KLOE08 and KLOE10 or KLOE10 and KLOE12 is clearly shown, with many parts of the experimental analyses being common to a pair of measurements or having been obtained through a similar method.

3.1.1 The initial combination of the KLOE data

In [96, 97], a construction of the necessary statistical and systematic covariance matrices for the three measurements was attempted. These were released to use in a combination of the three measurements to incorporate the various correlations depicted in Figure 3.1. The preliminary combination of these data in [97,98] utilised a method that neglected the correlations of the systematic uncertainties in the combination to avoid the d'Agostini bias. The data combination method used in this work safely allows for all correlated uncertainties (statistical and systematic) to fully influence the results of the data combination.

The results of this combination, where the covariance matrices constructed in [96,97] were used as input into the routine described in Section 2.3, are shown in Figure 3.2. In plot (a), the comparison of the KLOE10 data with the combination in the non-overlapping, low energy data region shows that the influence of the correlated uncertainties at higher energies has produced erratic variations in the combined cross section. In the high energy region, where only KLOE08 and KLOE12 data are present, the combined cross section has seemingly jumped in a step-like fashion to be distinctly higher than the contributing data. In plot (b), it is clear that overall the fit is higher than all the contributing data. In addition to this, results for $a_\mu^{\pi^+\pi^-}$ in the overlapping data range of $0.6 < \sqrt{s} < 0.9$ GeV from the three KLOE measurements and the combination are compared in Table 3.1. Here, it can be seen that the combination yields a noticeably higher value than the individual measurements contributing to it. Together, all these results indicate that the covariance matrices as constructed in [97, 98] do not appropriately describe the correlations of these data, with the behaviour of both the combined cross section and the value of $a_\mu^{\pi^+\pi^-}$ being different from what would be expected from the combination of these data. A study into the structure of these covariance matrices revealed that the matrices had not been constructed to satisfy the necessary properties of a covariance matrix as described in Section 2.3.2. In particular, the eigenvalues of the systematic covariance matrix were not all ≥ 0 and, consequently, it was not a positive semi-definite matrix.[3] It followed that it was necessary for new matrices to be constructed, ensuring that they were robust with regards to the mathematical structure

[3]The eigenvalues ranged from -18.9 to 4148.9. The causes of the negative eigenvalues are discussed in Section 3.2.2.

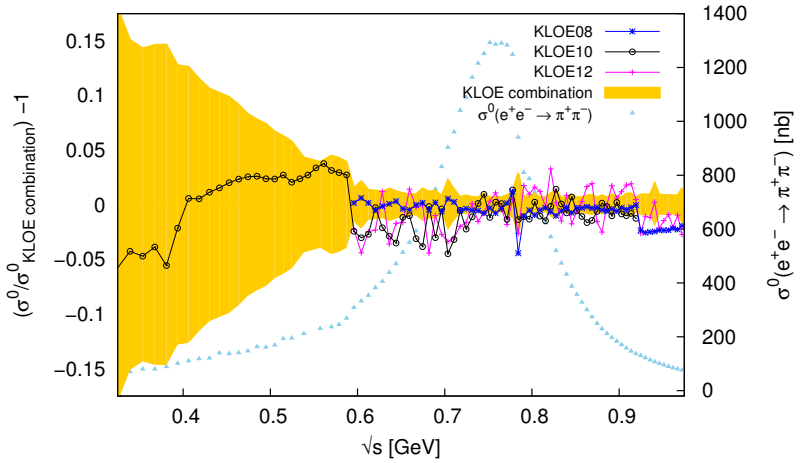

(a) Normalised difference in the full data range

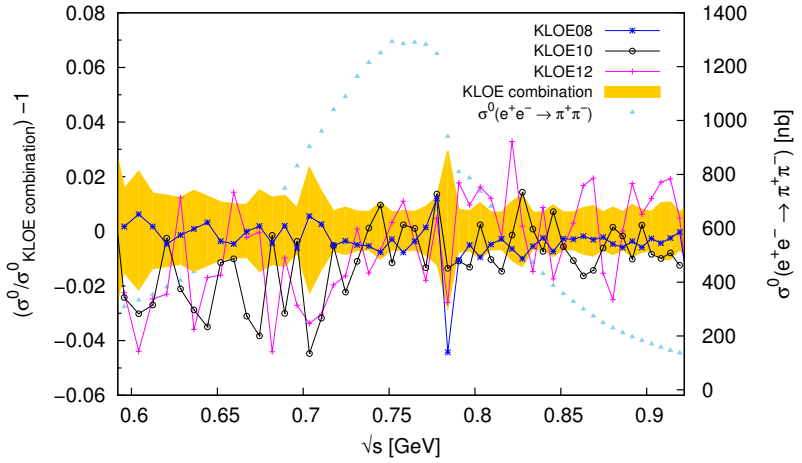

(b) Normalised difference in the overlapping data range

Fig. 3.2: The normalised difference of the KLOE combination and the individual KLOE measurements, where the KLOE combination has been determined using the previously constructed KLOE covariance matrices [96, 97]. The yellow band represents the statistical and systematic uncertainties of the KLOE combination summed in quadrature and the KLOE08, KLOE10 and KLOE12 cross section measurements are given by the blue, black and pink markers, respectively.

and fulfilled the required properties of a covariance matrix.

3.2 Constructing the KLOE combination covariance matrices

In the process of constructing the KLOE combination covariance matrices, the experimental analysis of each KLOE measurement of $\sigma\big(e^+e^- \to \pi^+\pi^-\gamma(\gamma)\big)$ has been reviewed and, in some cases, updated in order to ensure a more precise and consistent combination of the three measurements. The KLOE08, KLOE10 and KLOE12 data have been updated with respect to [88–90] to incorporate the following necessary

KLOE $\pi^+\pi^-\gamma(\gamma)$ data set	$a_\mu^{\pi^+\pi^-}(0.6 < \sqrt{s} < 0.9\ \text{GeV})$
KLOE08	$368.3 \pm 3.3_{\text{tot}}$
KLOE10	$366.0 \pm 3.2_{\text{tot}}$
KLOE12	$366.6 \pm 3.5_{\text{tot}}$
KLOE combination	$369.6 \pm 2.9_{\text{tot}}$

Table 3.1: Comparative results of the values obtained for $a_\mu^{\pi^+\pi^-}(0.6 < \sqrt{s} < 0.9\ \text{GeV})$ from the KLOE combination and the individual KLOE measurements, where the KLOE combination has been calculated using the previously constructed KLOE covariance matrices [96, 97]. All results are given in units of $a_\mu^{\pi^+\pi^-} \times 10^{10}$.

changes:

- The data have been undressed of VP effects using an updated routine [95] compared to the one used previously [94], which now corrects the data using a more appropriate energy grid parametrisation for the determination of the VP.
- The VP correction contains both real and imaginary parts, whereas previously the data were only corrected for the real part of the VP.
- The data are not rounded as they were in [88] to ensure that the statistical and systematic uncertainties correspond to the variances that enter into the diagonal elements of the corresponding covariance matrices.
- The calculation of the cross section has been updated with respect to the precision of input parameters and fundamental constants [16].

Using the updated KLOE data yields two-pion contributions to the anomalous magnetic moment of the muon from each measurement of

$$\begin{aligned}
a_\mu^{\pi^+\pi^-}(\text{KLOE08}, 0.5916 < \sqrt{s} < 0.9746\ \text{GeV}) &= (386.6 \pm 0.4_{\text{stat}} \pm 3.3_{\text{sys}}) \times 10^{-10}\,, \\
a_\mu^{\pi^+\pi^-}(\text{KLOE10}, 0.3162 < \sqrt{s} < 0.9220\ \text{GeV}) &= (477.9 \pm 2.0_{\text{stat}} \pm 6.7_{\text{sys}}) \times 10^{-10}\,, \\
a_\mu^{\pi^+\pi^-}(\text{KLOE12}, 0.5916 < \sqrt{s} < 0.9746\ \text{GeV}) &= (385.1 \pm 1.2_{\text{stat}} \pm 2.3_{\text{sys}}) \times 10^{-10}\,.
\end{aligned} \tag{3.5}$$

Here, the estimates from the KLOE08 and KLOE10 data exhibit a decrease in the mean value of $a_\mu^{\pi^+\pi^-}$ when compared to the estimates quoted in equation (3.2) and equation (3.3) respectively, which is largely due to the updated determination of the VP. This does not apply to the KLOE12 data which, as stated previously, benefits from the cancellation of the VP correction due to the normalisation by the $\mu^+\mu^-\gamma$ cross section. However, for KLOE12 the error has reduced when comparing to equation (3.4), where a flaw in the previous error calculation resulted in an overestimation of the published systematic uncertainty and, as a result, there have also been necessary changes to the KLOE12 systematic covariance matrix construction.

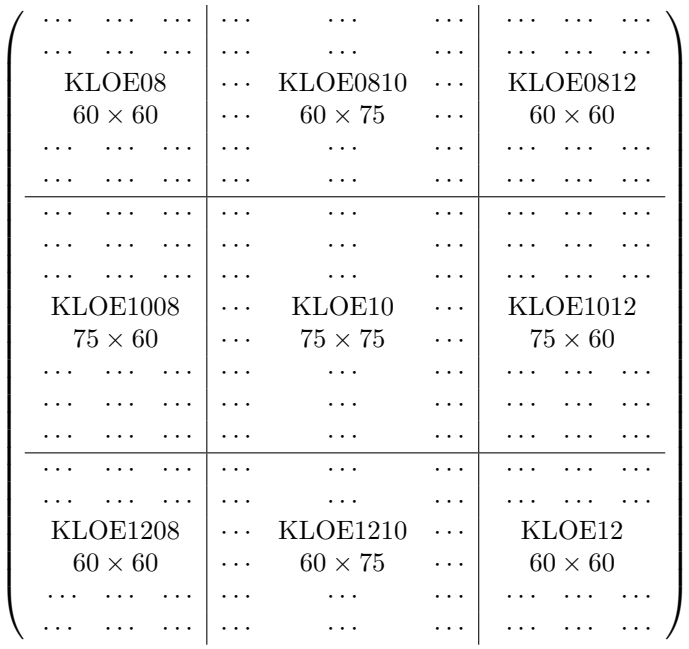

Fig. 3.3: The KLOE $\pi^+\pi^-\gamma(\gamma)$ combination matrix structure for both the statistical and systematic covariance matrices.

In this work, the KLOE statistical and systematic combination covariance matrices have been carefully constructed to satisfy all the necessary mathematical properties of a covariance matrix as described in Section 2.3.2, where the eigenvalues of the matrix now range from 0.0 to 5131.3. They are 195×195 matrices and are depicted in Figure 3.3. The KLOE08, KLOE10 and KLOE12 diagonal blocks are simply the covariance matrices of the individual measurements. The KLOE0810 block describes the correlation between KLOE08 and KLOE10, with corresponding definitions for KLOE0812 and KLOE1012. Statistical uncertainties are, in general, uncorrelated and only contribute to the diagonal elements of the corresponding correlation block of the combination covariance matrix. The exceptions to this are the unfolding [99–101] and unshifting [99] corrections, which both contribute to the non-diagonal elements of the statistical matrix (see Section 3.2.1). The unfolding correction accounts for the smearing due to the detector resolution and the unshifting is a redistribution correction of the observed value of s from $M^2_{\pi\pi} \to (M^0_{\pi\pi})^2$ where, here, $M^2_{\pi\pi}$ denotes the squared invariant mass of the pion pair. This accounts for photons emitted through final state radiation that shift s away from the squared invariant mass of the virtual photon, s^*_γ [102]. For systematic (sys) uncertainties, all data points are taken to be 100% correlated or anti-correlated. The resulting correlation structures for both the statistical and systematic matrix are shown in Figure 3.4.

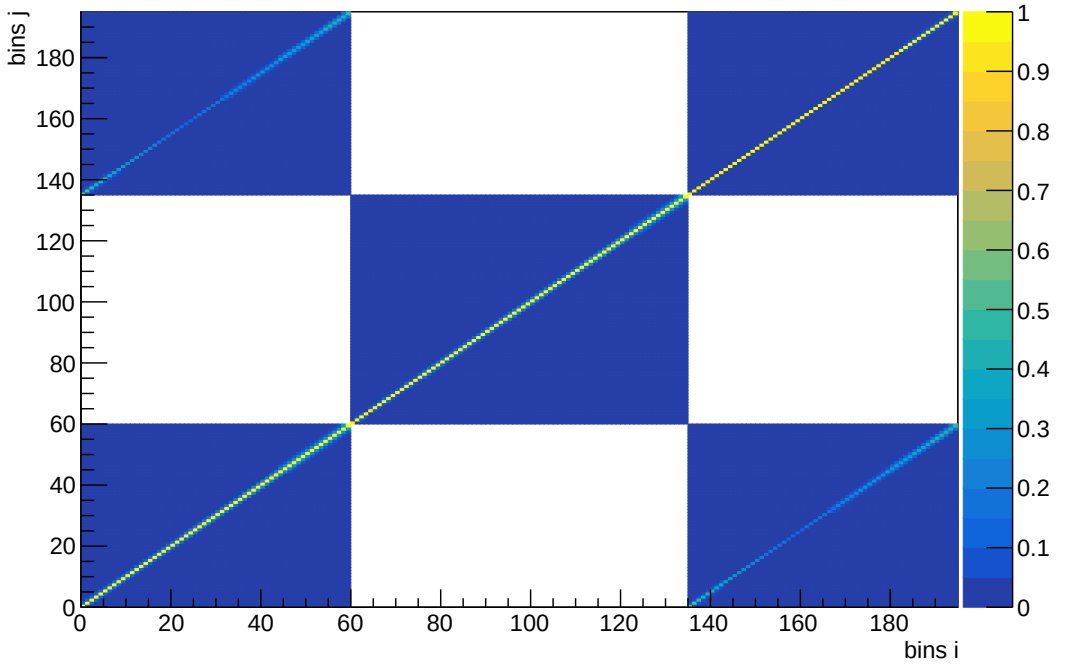

(a) Statistical correlation matrix

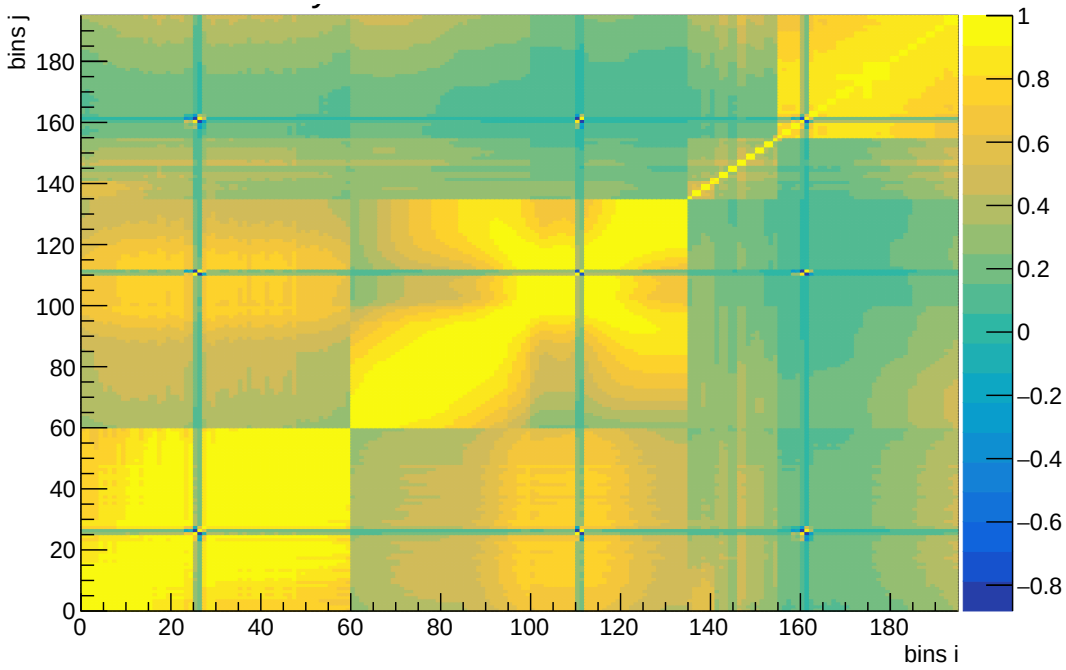

(b) Systematic correlation matrix

Fig. 3.4: The correlation structure of the 195x195 statistical and systematic combination matrices. In each case, the axis on the right represents the overall correlation coefficient ($\rho_{ij} = -1 \leq \rho \leq 1$), where the corresponding colour indicates the degree of correlation at each point in the respective matrix. For the statistical matrix, correlations are only present between the KLOE08 and KLOE12 measurements, which share the same two-pion data.

3.2.1 Statistical correlations

Other than those that exist as part of the individual analyses for the KLOE08, KLOE10 and KLOE12 diagonal sub-matrices in the statistical 195×195 combination covariance matrix depicted in Figure 3.3, the only statistical correlations that are present are those due to the two-pion data that are shared between KLOE08 and KLOE12. These occupy the KLOE0812 and KLOE1208 blocks of the statistical combination covariance matrix. As no statistical correlations exist between KLOE08 and KLOE10 or KLOE10 and KLOE12, all elements of the KLOE0810 (KLOE1008) and KLOE1012 (KLOE1210) correlation blocks of the statistical covariance matrix are zero. This can be seen diagrammatically in Figure 3.4.

The individual KLOE08, KLOE10 and KLOE12 statistical covariance matrices (corresponding to the diagonal blocks of the statistical combination matrix given by Figure 3.3) describe all statistical uncertainties inherent in the respective experimental analysis. The contributions to the statistical covariance matrices from the unfolding and unshifting procedures are partially correlated, where the correlation coefficients are defined by the unfolding [99–101] and unshifting [99] procedures themselves.

The KLOE0812 statistical correlation block receives contributions from all corrections to the KLOE08 $\pi^+\pi^-\gamma(\gamma)$ data up to the point where these data enter the KLOE12 analysis. Following the experimental analysis flow for KLOE08 in Figure 3.1, these include the detector resolution correction (unfolding), the correction for border efficiency in the acceptance, the pion identification efficiency (π/e likelihood), the tracking efficiency, the trigger corrections, the unshifting of $M^2_{\pi\pi} \to (M^0_{\pi\pi})^2$ and the acceptance for the cuts in θ_π and $\theta_{\pi\pi}$ [91]. All corrections prior to the unfolding in the analysis flow are included in the unfolded KLOE08 $\pi^+\pi^-\gamma(\gamma)$ spectrum and, therefore, manifestly enter the KLOE0812 correlations through the correlations of the unfolding. As the unfolding (unf) and unshifting (uns) corrections are identically correlated for the KLOE08 and KLOE12 statistical covariance matrices, these correlations must be reflected in the KLOE0812 correlation block exactly in the form

$$\rho_{ij}^{0812,\mathrm{unf/uns}} = \rho_{ji}^{1208,\mathrm{unf/uns}} = \rho_{ij}^{08,\mathrm{unf/uns}} = \rho_{ij}^{12,\mathrm{unf/uns}} \,. \tag{3.6}$$

Not doing so would result in the statistical covariance matrix having negative eigenvalues, therefore violating the condition that the covariance matrix is a positive semi-definite matrix.[4] All remaining correlated statistical uncertainties only enter into the diagonal elements of the KLOE0812 correlation block, as they are fully correlated only for the same energy bins between the two measurements.

[4] This is also true for the systematic covariance matrix and, in fact, was a contribution to negative eigenvalues of the systematic covariance matrix constricted in [96, 97].

3.2.2 Systematic correlations

All correlation blocks in Figure 3.3 receive contributions from systematic uncertainties, as can be seen clearly in Figure 3.4. Unless stated otherwise, for any two bins i and j, systematic uncertainties where correlations exist are fully correlated ($\rho_{ij} = +1$) or anti-correlated ($\rho_{ij} = -1$).

For the individual measurements, apart from two exceptions, all sources of systematic uncertainty are fully correlated between all energy bins. The first exception is the systematic uncertainty due to the unfolding, which only contributes at the sharp descent of the cross section in the $\rho - \omega$ interference region. Here, an identical unfolding uncertainty enters for five bins of the KLOE08 and KLOE12 analyses and is anti-correlated only for pairs of bins that are on different sides of this sharp descent of the cross section. For KLOE10, the only two affected bins are those directly before and directly after the sharp descent in the cross section, where the uncertainties are fully anti-correlated between these two bins. The second exception is the weighted background subtraction for KLOE12, where in the experimental analysis the weights of the fitted $e^+e^-\gamma$, $\pi\pi\gamma$ and $\pi\pi\pi$ backgrounds to the $\mu^+\mu^-\gamma(\gamma)$ spectrum are distributed over neighbouring two-bin intervals from 0.32 to 0.96 GeV^2 (with each bin covering an energy interval of 0.01 GeV^2). For the KLOE12 systematic covariance matrix, this results in only neighbouring bins from 0.36 to 0.94 GeV^2 being correlated with each other for this background subtraction uncertainty, where the first and last bin remain entirely uncorrelated in this case.

Importantly, for the KLOE12 systematic covariance matrix, the trigger, L3 (software trigger), trackmass, tracking efficiency, acceptance and background subtraction corrections are applied to both the $\pi^+\pi^-\gamma$ and $\mu^+\mu^-\gamma$ data that enter into the normalisation ratio and, therefore, the corresponding uncertainties from a given source between the $\pi^+\pi^-\gamma$ and $\mu^+\mu^-\gamma$ data are correlated.[5] Formally, the ratio of these correction uncertainties results in a reduction of the total uncertainty of $a_\mu^{\pi^+\pi^-}$, where the contributions of the positive correlations between the KLOE08 and KLOE12 uncertainties contribute negatively to the overall uncertainty due to the partial derivative of the $\mu^+\mu^-\gamma$ data in the denominator of the ratio. However, the uncertainties due to a given source are defined in terms of the ratio of $\pi^+\pi^-\gamma$ over $\mu^+\mu^-\gamma$, such that the contributions from both data sources are already fully incorporated.

In addition, the KLOE12 systematic uncertainty vector for the non-weighted background subtraction was constructed in [90, 93] such that it contained the ratio of the contributions from the corrections of the $ee \to ee\pi\pi$ and $ee \to ee\mu\mu$ background processes, along with a trackmass (M_{trk}) tail correction, summed in quadrature. For this

[5] This only refers to the correlation of uncertainties from a specific source between the $\pi^+\pi^-\gamma$ analysis and the $\mu^+\mu^-\gamma$ analysis that enter into the KLOE12 ratio. The correlation between the KLOE08 $\pi^+\pi^-\gamma$ data and the KLOE12 cross section ratio are described in detail in the discussion of the KLOE0812 block of the systematic covariance matrix.

analysis, in order to correctly correlate these independent sources of systematic uncertainty according to equation (2.27), these contributions are separated and correlated individually. This has contributed to the reduction of the KLOE12 error estimate in equation (3.5), where previously the correlation of the combined vector resulted in an incorrect overestimate of the systematic uncertainty.

For KLOE08 and KLOE10, the contributions to the systematic uncertainty from the trackmass, tracking efficiency, L3 (software trigger) efficiency, acceptance, luminosity, radiator function, vacuum polarisation correction and final state radiation correction are considered to be fully correlated in the KLOE0810 (KLOE1008) covariance matrix blocks. For the correlation of the systematic uncertainty due to the acceptance, only half of the KLOE10 uncertainty is correlated with the KLOE08 uncertainty in order to ensure that the photon detection acceptance that enters into the KLOE10 uncertainty (that is not present in the KLOE08 analyses) is not correlated and only the correlation of the pion tracks is duly accounted for. Importantly, although the KLOE08 and KLOE10 measurements only overlap for the 50 data points in the energy range 0.35 to 0.85 GeV^2, all energy bins in the 60×75 KLOE0810 (75×60 KLOE1008) correlation block must be fully correlated. Note that this is a change with respect to the previous construction in [96, 97], where 100% correlation was applied to only the overlapping 50×50 region which contributed to the systematic matrix having negative eigenvalues.

Again, for KLOE0812 (KLOE1208), the systematic uncertainties inherent in the $\pi^+\pi^-\gamma(\gamma)$ data shared between the two analyses are correlated between the KLOE08 and KLOE12 measurements. These include the uncertainties from the L3 efficiency, the background subtraction, the trackmass ($M_{\rm trk}$), the unfolding, the tracking efficiency, the trigger efficiency and the acceptance from the KLOE08 analysis. The determined uncertainties for the L3, $M_{\rm trk}$, tracking, trigger and acceptance corrections for KLOE12 are fully correlated for KLOE0812 such that the anti-correlation that occurs due to the ratio in KLOE12 is propagated accordingly. This is also true for the non-weighted background subtraction contribution, ensuring that only the corrections for the $ee \to ee\pi\pi$ background from the KLOE08 analysis are correlated with the ratio of the corrections of the $ee \to ee\pi\pi$ and $ee \to ee\mu\mu$ background processes as they enter in the KLOE12 analysis. The unfolding uncertainties for the KLOE0812 correlation block are, in part, anti-correlated as they are for KLOE08 and KLOE12 individually. All other systematic uncertainties are 100% correlated between KLOE08 and KLOE12.

With the same $\pi^+\pi^-\gamma(\gamma)$ data being shared between the KLOE08 and KLOE12 measurements, the KLOE1012 (KLOE1210) correlation blocks follow a similar structure to the KLOE0810 (KLOE1008) correlation blocks. The caveats to this statement are that there are no correlated uncertainties here due to the luminosity, radiator function or vacuum polarisation correction, as these effects cancel in the ratio of the $\pi^+\pi^-\gamma(\gamma)$ data over the $\mu^+\mu^-\gamma(\gamma)$ data for the KLOE12 measurement. Therefore,

the correlated systematic uncertainties for KLOE1012 are the trackmass, tracking efficiency, L3 efficiency, acceptance and final state radiation correction uncertainties, where it is again necessary to correlate only half of the KLOE10 acceptance uncertainty with KLOE12 in order to ensure that only the effect due to the acceptance of the pion tracks is incorporated.

3.3 Combination and results

The updated data vectors for the three cross section measurements and the newly constructed covariance matrices have been combined according to Section 2.3.2. The combination of the KLOE data represents a simpler case than the combination of all available data with different energy bins for an entire hadronic channel, as the identical binning of the KLOE data means that the clustering of data points is trivial, and no linear interpolation is required for the data between bins in the minimisation. The resulting combined cross section and corresponding pion form factor data are listed in Table B.1 in Appendix B.[6] Figure 3.5 shows the combined cross section and the individual measurements. Figure 3.6, in comparison with Figure 3.2, shows the normalised differences of the individual KLOE measurements and the new combination. Here, the erratic behaviour observed in Figure 3.2 is no longer present and good agreement is observed between the data and the combination. KLOE12 exhibits the largest fluctuations when comparing to the fitted combination but is well within the errors of the data. In plot (a) of Figure 3.6, it can be seen that the KLOE0810 and KLOE1012 systematic uncertainties have a non-trivial effect in the lower energy region where only the KLOE10 data exist, exhibiting the power and flexibility of the new data combination method to incorporate the influence of the correlated uncertainties to their full capacity. In this case, the correlations provide an expected upward pull (which is well within the errors of the combination) to the KLOE combination cross section away from the KLOE10 data points.

For the two-pion contribution to the anomalous magnetic moment of the muon in the full energy range, the KLOE combination results in

$$a_\mu^{\pi^+\pi^-}(0.3162 < \sqrt{s} < 0.9747 \text{ GeV}) = (489.8 \pm 1.7_{\text{stat}} \pm 4.8_{\text{sys}}) \times 10^{-10}\,. \qquad (3.7)$$

For the overlapping energy region of all three measurements, the estimates for $a_\mu^{\pi^+\pi^-}$ from the KLOE combination and the individual measurements are given in Table 3.2 and Figure 3.7. For both these comparisons, unlike previously in Table 3.1, it can be seen that the influence of the correlations from the now correctly constructed covariance matrices result in the KLOE combination agreeing well with the estimate from the three individual measurements. In all cases, the errors include all correlation contributions.

[6] The input cross section vectors and combination covariance matrices, along with the combined output cross section vector and total covariance matrix are available from [103].

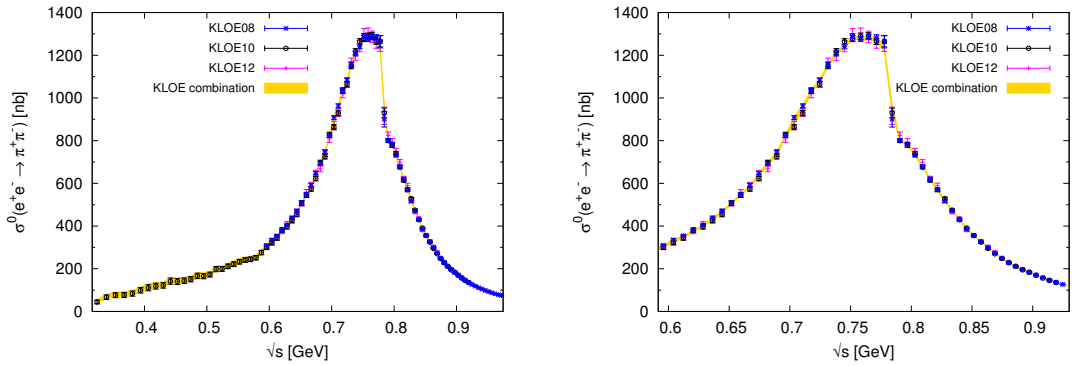

(a) Cross section in the full data range

(b) Cross section in the overlapping data range

Fig. 3.5: The KLOE combination (yellow band) plotted with the individual cross section measurements, where the KLOE08, KLOE10 and KLOE12 cross section measurements are given by the blue, black and pink markers, respectively. In all cases, the error bars shown are the statistical and systematic uncertainties summed in quadrature.

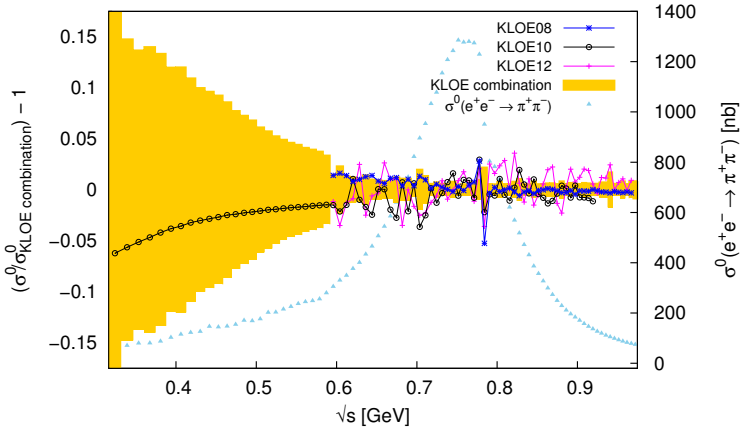

(a) Normalised difference in the full data range

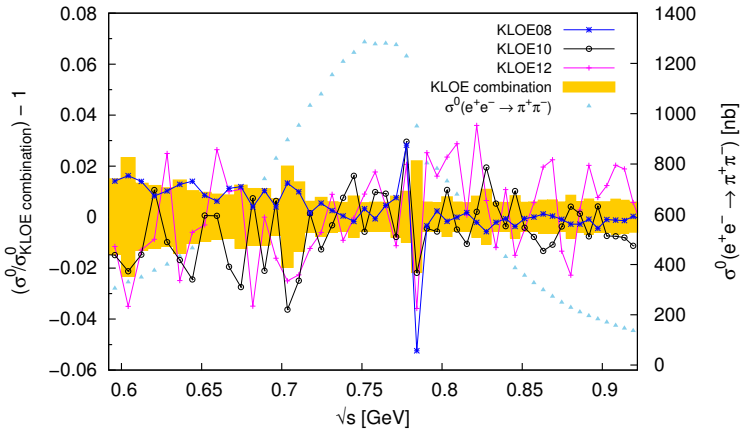

(b) Normalised difference in the overlapping data range

Fig. 3.6: The normalised difference of the KLOE combination and the individual KLOE measurements, where the yellow band represents the statistical and systematic uncertainties of the KLOE combination summed in quadrature and the KLOE08, KLOE10 and KLOE12 cross section measurements are given by the blue, black and pink markers, respectively. Here, the errors bars of the individual measurements are not shown in order to be able to distinguish the data points but are in good agreement with the KLOE combination.

KLOE $\pi^+\pi^-\gamma(\gamma)$ data set	$a_\mu^{\pi^+\pi^-}(0.6 < \sqrt{s} < 0.9$ GeV)
KLOE08	$368.2 \pm 3.1_{\text{tot}}$
KLOE10	$365.5 \pm 3.3_{\text{tot}}$
KLOE12	$366.7 \pm 2.5_{\text{tot}}$
KLOE combination	$366.9 \pm 2.1_{\text{tot}}$

Table 3.2: Comparison of the values obtained for $a_\mu^{\pi^+\pi^-}(0.6 < \sqrt{s} < 0.9$ GeV) from the individual KLOE measurements and the full combination. All results are given in units of $a_\mu^{\pi^+\pi^-} \times 10^{10}$.

For the combination, they have been inflated according to the local χ^2_{min}/d.o.f. in each energy bin according to Section 2.3.2. This local effect is shown in Figure 3.8 and has resulted in an increase to the overall uncertainty of the estimate of $a_\mu^{\pi^+\pi^-}$ of $\sim 13\%$. While the statistical uncertainty of $a_\mu^{\pi^+\pi^-}$ from the combination is dominated by KLOE08 (which has the smallest statistical uncertainty of the three individual measurements), the combination mean value of $a_\mu^{\pi^+\pi^-}$ is closest to that obtained with the KLOE12 data alone, which has the smallest systematic and, therefore, the smallest total error of the three. This in turn leads to the improved systematic error of the combined result and, consequently, its improved total error.

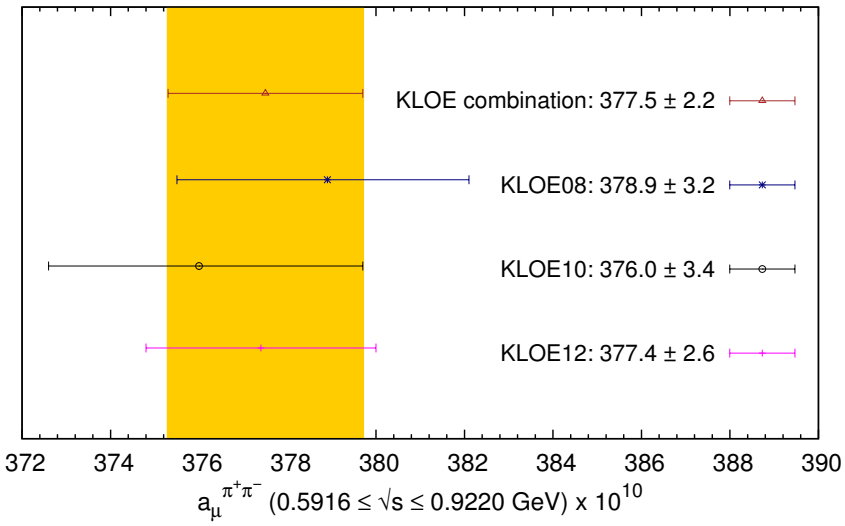

Fig. 3.7: Comparison of estimates of $a_\mu^{\pi^+\pi^-}$ from the KLOE combination and the individual KLOE measurements in the entire overlapping data range $0.5916 < \sqrt{s} < 0.9220$ GeV. The KLOE combination is represented by the yellow band. In all cases, the uncertainties shown are the statistical and systematic uncertainties summed in quadrature. All results are given in units of $a_\mu^{\pi^+\pi^-} \times 10^{10}$. Note that the results presented here differ to those given in Table 3.2 due to the slightly increased energy range.

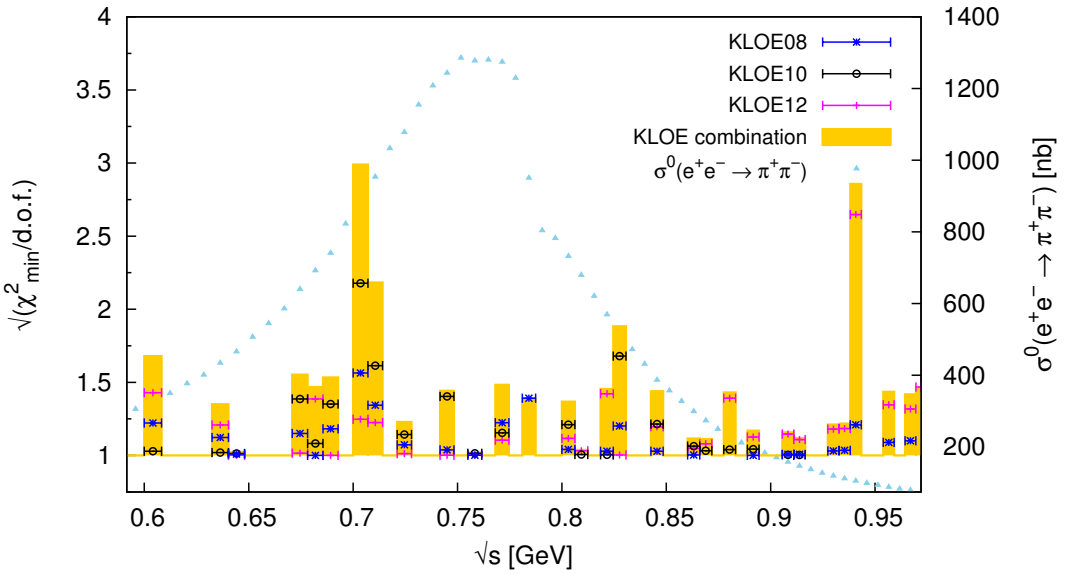

Fig. 3.8: The effect of the local $\chi^2_{\rm min}$/d.o.f. error inflation on the KLOE combination, which is applied in each energy bin if the local $\chi^2_{\rm min}$/d.o.f. > 1. The total effect on the KLOE combination is represented by the yellow blocks. The relative contributions to each local $\chi^2_{\rm min}$/d.o.f. from the KLOE08, KLOE10 and KLOE12 measurements individually are given by the blue, black and pink markers respectively.

Chapter 4

Results

The following section summarises the data combination and estimates of $a_\mu^{\mathrm{had,\,LO\,VP}}$ from all data-based and estimated hadronic final states. In total, the compilation of these various sources results in 43 hadronic channels which are combined. All contributions from the exclusive hadronic channels are evaluated up to 1.937 GeV, which is the chosen transition point between the sum of exclusive channels and the inclusive R-ratio data in this work. This is discussed in detail in Section 4.3.1. Each contribution to $a_\mu^{\mathrm{had,\,LO\,VP}}$ is quoted with its respective statistical uncertainty δ_{stat}, systematic uncertainty δ_{sys}, VP correction uncertainty δ_{vp} and FSR correction uncertainty δ_{fsr} individually. This is followed by the contribution with the total uncertainty δ_{tot}, determined from the individual sources added in quadrature,

$$\begin{aligned} a_\mu^{\mathrm{had,\,LO\,VP}} &= a_\mu^{\mathrm{had,\,LO\,VP}} \pm \delta_{\mathrm{stat}} \pm \delta_{\mathrm{sys}} \pm \delta_{\mathrm{vp}} \pm \delta_{\mathrm{fsr}} \\ &= a_\mu^{\mathrm{had,\,LO\,VP}} \pm \delta_{\mathrm{tot}}\,. \end{aligned} \tag{4.1}$$

In all cases, the uncertainties include all available correlations and local χ^2 inflation. In the following, for each channel, all contributing data sets are referenced and the corresponding combinations are discussed individually. For the exclusive channels, the purely data-based channels (including the threshold contributions estimated using ChPT) are discussed first in Section 4.1 and the channels estimated using dedicated isospin relations are discussed in Section 4.2. Results from the combination of the inclusive data, the narrow resonances and pQCD are discussed in Section 4.3. Summing all contributions, the total predictions of $a_\mu^{\mathrm{had,\,LO\,VP}}$ and $a_\mu^{\mathrm{had,\,NLO\,VP}}$ from this work are given in Section 4.4. Following this, comparisons with other similar works (including the HLMNT11 analysis) are given in Section 4.5. A discussion of future prospects to improve the determination of the contributions to $a_\mu^{\mathrm{had,\,VP}}$ is given in Section 5.2.

4.1 Data-based exclusive channels

4.1.1 $\pi^0\gamma$ channel

The $\pi^0\gamma$ final state defines the lower integral border of equation (1.45) to be $s = m_\pi^2$. As the available data starts at only 0.60 GeV, the threshold contribution is estimated using ChPT (see Section 2.4.1). The channel now combines four data sets [104–107], with the most recent being the precise, new measurement by the SND collaboration between $0.60 \leq \sqrt{s} \leq 1.35$ GeV [107]. The data set defines the maximum available energy range for the data combined in this channel, extending the higher energy border slightly since [21]. The contribution from this channel is found to be

$$\begin{aligned} a_\mu^{\pi^0\gamma}[0.60 \leq \sqrt{s} \leq 1.35 \text{ GeV}] &= (4.46 \pm 0.04 \pm 0.07 \pm 0.06 \pm 0.04) \times 10^{-10} \\ &= (4.46 \pm 0.10) \times 10^{-10} \,. \end{aligned} \tag{4.2}$$

The resulting cross section $\sigma^0(e^+e^- \to \pi^0\gamma)$ and all contributing data are shown in Figure 4.1, where the ω and ϕ resonance structures are visible. The threshold contribution is found from ChPT to give

$$a_\mu^{\pi^0\gamma}(\text{ChPT})[m_\pi \leq \sqrt{s} < 0.60 \text{ GeV}] = (0.12 \pm 0.01) \times 10^{-10} \,. \tag{4.3}$$

4.1.2 $\pi^+\pi^-$ channel

The $\pi^+\pi^-$ channel dominates the contributions to $a_\mu^{\text{had, VP}}$, accounting for over 70% of the total value of $a_\mu^{\text{had, LO VP}}$. This is due to the large ρ resonance structure in the low energy region below 1 GeV that almost exclusively decays as $\rho \to \pi^+\pi^-$ and is highly weighted by $K(s)$ in equation (1.45).[1] Consequently, it also dominates the uncertainty of the hadronic vacuum polarisation contributions resulting in many experiments having measured this final state in an attempt to more precisely determine $a_\mu^{\pi^+\pi^-}$. It is therefore the largest individual data combination for a single hadronic channel, combining twenty-six data sets [88–90, 108–128] that total almost one thousand data points. In addition to the inclusion of the KLOE combination described in Section 3, the BESIII collaboration [127] have also released a new measurement in the important ρ region, which has contributed to the improvement of the estimate of this final state since [21]. These measurements, coupled with the precise, finely binned measurement by the BaBar experiment [126] (which defines both the lower and upper boundaries of the available $\pi^+\pi^-$ data combination to be $0.305 \leq \sqrt{s} \leq 3.00$ GeV), constitute all the data in the two-pion channel measured via radiative return which now entirely dominate this data combination. For these radiative return measurements, all the respective

[1] The ω resonance is also present in this channel. However, the decay of $\omega \to \pi^+\pi^-$ in the same energy region as the ρ resonance causes a mixing of these two structures. This mixing is apparent when observing the $\pi^+\pi^-$ cross section in Figure 4.3, which exhibits the familiar $\rho - \omega$ interference structure in the peak of the resonance and distorts the otherwise Breit-Wigner resonance configuration of the ρ.

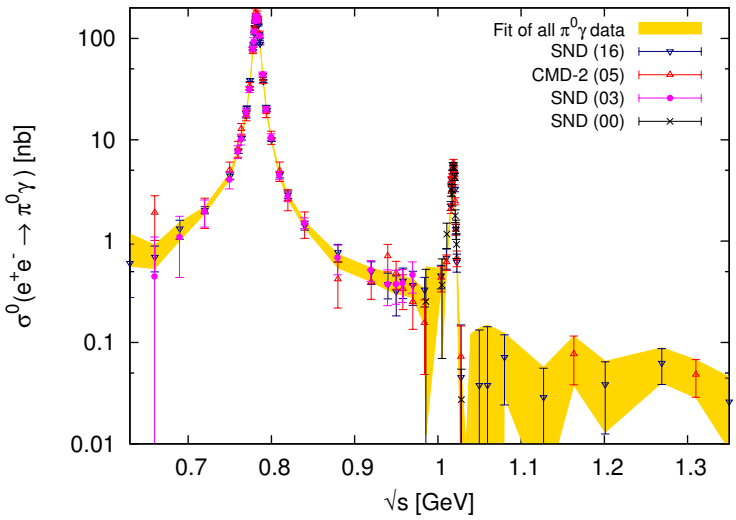

(a) Full data range.

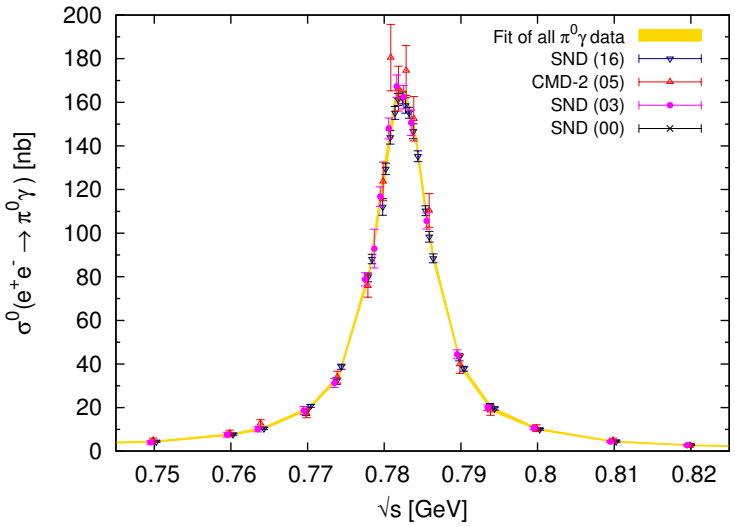

(b) The ω resonance.

Fig. 4.1: The cross section $\sigma^0(e^+e^- \to \pi^0\gamma)$ in the range $0.60 \leq \sqrt{s} \leq 1.35$ GeV, with an enlargement in the prominent ω resonance region.

experimental analyses have provided full statistical and systematic covariance matrices (with the covariance matrices for the combination of the three KLOE measurements being described in Section 3), which are fully incorporated into the determination of both $a_\mu^{\pi^+\pi^-}$ and its uncertainty using the data combination procedure detailed in this work. In addition, all these data are provided by their respective experimental analyses as the bare cross section with FSR effects included, $\sigma^0_{\pi\pi,\gamma}$, minimising the effect of radiative corrections and corresponding additional uncertainties.

Tension exists between the BaBar measurement and all other data, where the BaBar data are considerably higher over much of the available energy range. This is evident from Figure 4.2, which compares the estimates of $a_\mu^{\pi^+\pi^-}$ from the full data combina-

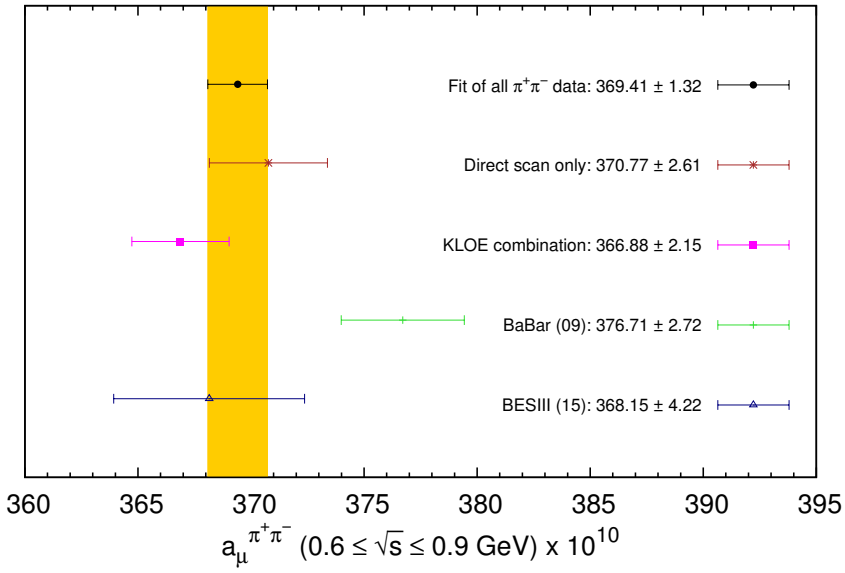

Fig. 4.2: The comparison of the integration of the individual radiative return measurements and the combination of direct scan $\pi^+\pi^-$ measurements between $0.6 \leq \sqrt{s} \leq 0.9$ GeV.

tion, the radiative return measurements and all other measurements in this channel (measured via direct energy scan) in the dominant ρ region. Noticeable disagreement is evident in all comparisons with the BaBar data, where the deviation between the estimates from KLOE combination and the BaBar data in this range is $\sim 2.8\sigma$. With the highly correlated nature of the KLOE combination now having a dominating influence overall, a large disagreement is also noted between the full $\pi^+\pi^-$ data combination and the integral of the BaBar data alone. It is clear that the full $\pi^+\pi^-$ data combination agrees well with the new BESIII data, the KLOE data and the combination of the remaining direct scan data. Consequently, although BaBar still influences $a_\mu^{\pi^+\pi^-}$ with an increase due to its fine binning and high statistics, the agreement between the other radiative return measurements and the direct scan data largely compensates for this effect. This is made more apparent when considering this along with the plots of the resulting cross section in Figure 4.3 and Figure 4.4. Interestingly however, it can be seen from these that the BESIII data is in better agreement with the BaBar data at the peak of the resonance where the cross section is largest, slightly alleviating the disagreement between the full $\pi^+\pi^-$ data combination and the BaBar data. The resulting global $\sqrt{\chi^2_{\text{min}}/\text{d.o.f.}}$ is ~ 1.3, reflecting the good agreement between most of the data in this channel. The tension between data sets is, however, reflected and accounted for in the local χ^2 error inflation, which results in an $\sim 15\%$ increase in the uncertainty of $a_\mu^{\pi^+\pi^-}$. The effect of this energy dependent error inflation is shown in Figure 4.5, where the difference in using a local scaling of the error instead of a global one is clearly

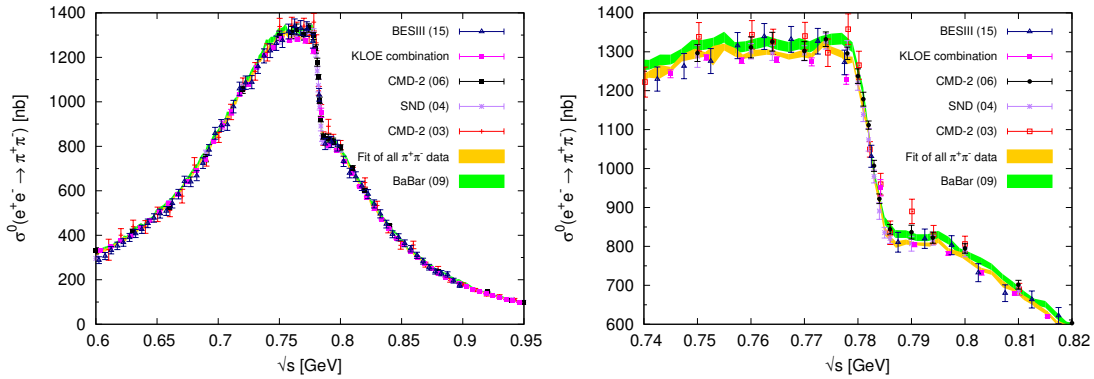

Fig. 4.3: Contributing data in the ρ resonance region of the $\pi^+\pi^-$ channel plotted against the new fit of all data (left panel), with an enlargement of the $\rho-\omega$ interference region (right panel).

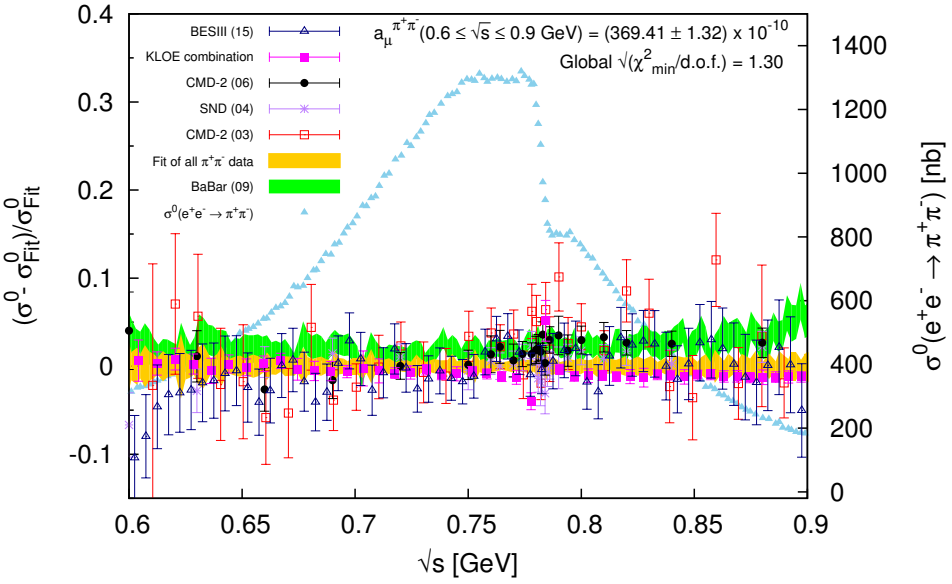

Fig. 4.4: The relative difference of the radiative return and important direct scan data sets contributing to $a_\mu^{\pi^+\pi^-}$ and the fit of all data. For comparison, the individual sets have been normalised against the fit and have been plotted in the ρ region. The light green band represents the BaBar data and their errors (statistical and systematic, added in quadrature). The yellow band represents the full data combination which incorporates all correlated statistical and systematic uncertainties. However, the width of the yellow band simply displays the square root of the diagonal elements of the total output covariance matrix of the fit.

visible. Penalties arise in particular in the ρ resonance region, where the cross section is large and there is significant tension between the KLOE and BaBar data.

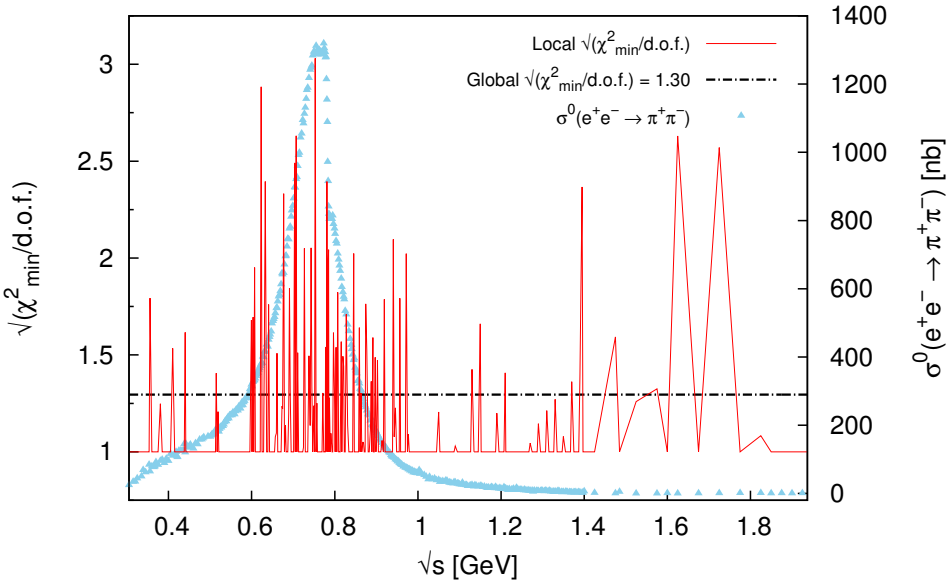

Fig. 4.5: The effect of the local $\sqrt{\chi^2_{\text{min}}/\text{d.o.f.}}$ inflation and the overall global $\sqrt{\chi^2_{\text{min}}/\text{d.o.f.}}$ in the $\pi^+\pi^-$ channel, which is plotted against the $e^+e^- \to \pi^+\pi^-$ cross section for reference.

In the desired energy range, the full combination of all $\pi^+\pi^-$ data is found to give

$$a_\mu^{\pi^+\pi^-}[0.305 \leq \sqrt{s} \leq 1.937 \text{ GeV}] = (502.97 \pm 1.14 \pm 1.59 \pm 0.06 \pm 0.14) \times 10^{-10}$$
$$= (502.97 \pm 1.97) \times 10^{-10}\,. \qquad (4.4)$$

Although this value of $a_\mu^{\pi^+\pi^-}$ stays well within the error estimate of [21], it exhibits a substantial decrease of the mean value and the uncertainty has reduced by approximately one third. These effects are due to the new, precise radiative return data which dominate the $\pi^+\pi^-$ fit and suppress the influence of BaBar in the ρ resonance region, the improvement of the overall data combination procedure to fully incorporate the energy dependent correlations into the determination of the mean value as well as the uncertainty and the suppression of additional radiative corrections uncertainties from these cross section data being experimentally provided as $\sigma^0_{\pi\pi,\gamma}$ data. A more detailed comparison of the estimates of $a_\mu^{\pi^+\pi^-}$ between [21] and this work is given in Section 4.5.1, where a full comparison with the HLMNT11 analysis is discussed.

In comparison with equation (4.4), the BaBar data alone in the same energy range give an estimate of $a_\mu^{\pi^+\pi^-}(\text{BaBar data only}) = (513.2 \pm 3.8) \times 10^{-10}$. Should all available $\pi^+\pi^-$ data be combined using a simple weighted average as in equation (2.18) (which only provides the error weighting to each cluster by its local uncertainty), the estimate for $a_\mu^{\pi^+\pi^-}$ would be $a_\mu^{\pi^+\pi^-}(\text{Naive weighted average}) = (509.1 \pm 2.9) \times 10^{-10}$. In this case, the estimate is strongly pulled up by the fine binning and high statistics of the BaBar data that dominate when no correlations are taken into account for the mean value.

This difference of nearly 2σ when comparing to equation (4.4) indicates the importance of fully incorporating all available correlated uncertainties in any combination of the data. This influence of the correlations and the stability of the data combination with respect to the contrasting BaBar data is reinforced when considering the two-pion data combination in the range $0.32 \leq \sqrt{s} \leq 1.937$ GeV, which defines the contributing energy range with the BaBar data excluded. In this range, the full $\pi^+\pi^-$ data combination results in $a_\mu^{\pi^+\pi^-}(\text{All data}) = (501.4 \pm 1.9) \times 10^{-10}$, whilst the combination without the BaBar data gives $a_\mu^{\pi^+\pi^-}(\text{No BaBar}) = (500.3 \pm 2.7) \times 10^{-10}$. Although the agreement between these results is an encouraging indication that the full data combination results in a good representation of the contributing data, the large change in the uncertainty indicates the importance of the precise BaBar data as a high statistics measurement in this channel.

As described in Section 2.4.1, the threshold contribution from $2m_\pi \leq \sqrt{s} < 0.305$ GeV is determined using ChPT. The estimation of the cross section in this region is found to give

$$a_\mu^{\pi^+\pi^-}(\text{ChPT})[2m_\pi \leq \sqrt{s} < 0.305 \text{ GeV}] = (0.87 \pm 0.02) \times 10^{-10}\,. \tag{4.5}$$

4.1.3 $\pi^+\pi^-\pi^0$ channel

The $\pi^+\pi^-\pi^0$ final state is the second largest contribution to $a_\mu^{\text{had, LO VP}}$ after the two-pion channel, with the cross section receiving prominent contributions from the ω and ϕ resonances. This channel combines 14 data sets [69,120,121,129–132,134–137] covering an energy range of $0.66 \leq \sqrt{s} \leq 2.98$ GeV. Since [21], there has only been one new addition to the $\pi^+\pi^-\pi^0$ channel [137]. This new data set improves this channel away from resonance, where previously only the BaBar data [135] had provided a contribution of notable precision. In this work, an additional change is applied to three separate data scans over the ϕ resonance in a measurement by CMD-2 [136]. Following discussions with members of the CMD-2 collaboration concerning the potential for correlation between several data scans taken for the same measurement, the systematic uncertainties between the three scans are now taken to be fully correlated [138].[2] These changes, along with the new data combination routine, have resulted in an improved estimate of

$$\begin{aligned} a_\mu^{\pi^+\pi^-\pi^0}[0.66 \leq \sqrt{s} \leq 1.937 \text{ GeV}] &= (47.79 \pm 0.22 \pm 0.71 \pm 0.13 \pm 0.48) \times 10^{-10} \\ &= (47.79 \pm 0.89) \times 10^{-10}\,. \end{aligned} \tag{4.6}$$

With a global $\sqrt{\chi^2_{\text{min}}/\text{d.o.f.}} \sim 2.1$, the quality of this data combination for this channel is far from ideal. This is largely due to older data that is still included in this channel

[2] Similar changes regarding the correlation of systematic uncertainties have also been applied to measurements in the $3\pi^+3\pi^-$, K^+K^-, $K_S^0K_L^0$, $\eta\gamma$, $n\bar{n}$ and inclusive channels, with details given in the separate discussions of each channel.

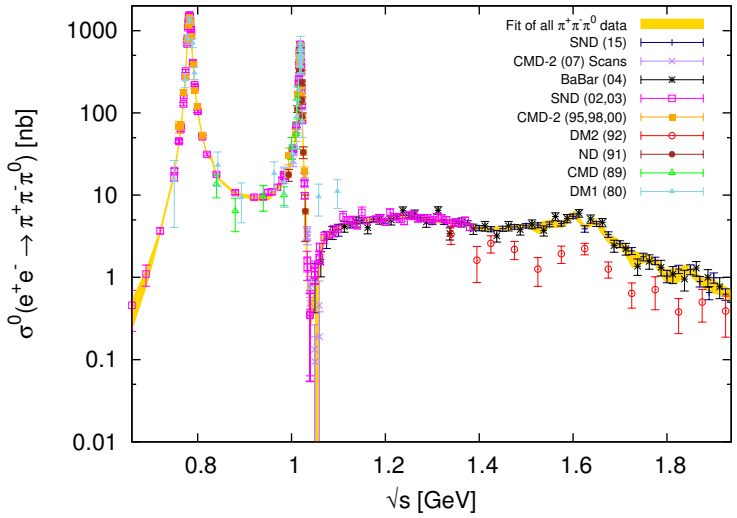

Fig. 4.6: The cross section $\sigma^0(e^+e^- \to \pi^+\pi^-\pi^0)$ in the range $0.66 \leq \sqrt{s} \leq 1.937$ GeV, where the prominent ω and ϕ resonances are clearly visible.

being at tension with newer, precise data. This is true, for example, of the CMD data measured between the two resonances [130], which contributes almost 20% of the this global $\chi^2_{\rm min}$/d.o.f.. Again, these tensions are accounted for in the local error inflation, which in this channel increases the uncertainty on $a_\mu^{\pi^+\pi^-\pi^0}$ by $\sim 32\%$. Figure 4.6 shows the full integral range of the data for the $\pi^+\pi^-\pi^0$ cross section. Figure 4.7 shows an enlargement of the ω and ϕ resonance regions in this channel.

As with the $\pi^0\gamma$ and $\pi^+\pi^-$ channels, the threshold cross section (for which there is no data for this final state) is determined using ChPT. This results in a contribution to $a_\mu^{\pi^+\pi^-\pi^0}$ of

$$a_\mu^{\pi^+\pi^-\pi^0}(\text{ChPT})[3m_\pi \leq \sqrt{s} < 0.66 \text{ GeV}] = (0.01 \pm 0.00) \times 10^{-10}\,. \tag{4.7}$$

4.1.4 4π channels

The four-pion channels are the $\pi^+\pi^-\pi^0\pi^0$ and $\pi^+\pi^-\pi^+\pi^-$ final states, with the process $e^+e^- \to \gamma^* \to \pi^0\pi^0\pi^0\pi^0$ being forbidden from charge conjugation symmetry. These channels dominate $R(s)$ above the ϕ resonance and up to 1.937 GeV. In [21], the data for both these channels was limited and of fairly poor quality, especially in the $\pi^+\pi^-\pi^0\pi^0$ channel where there had been no data measured of this final state since 2003.

The $\pi^+\pi^-\pi^+\pi^-$ channel now combines 14 data sets [120, 139–151], with two new additions since [21]. First, an improved statistics measurement by the BaBar collaboration in the range $0.6125 \leq \sqrt{s} \leq 4.4875$ GeV [150] supersedes their previous measurement in this channel [152]. More recently, a data set by the CMD-3 collaboration in the range $0.92 \leq \sqrt{s} \leq 1.06$ GeV [151] has been completed, which better resolves the interference pattern of the $\phi \to \pi^+\pi^-\pi^+\pi^-$ transition that is clearly evident in the

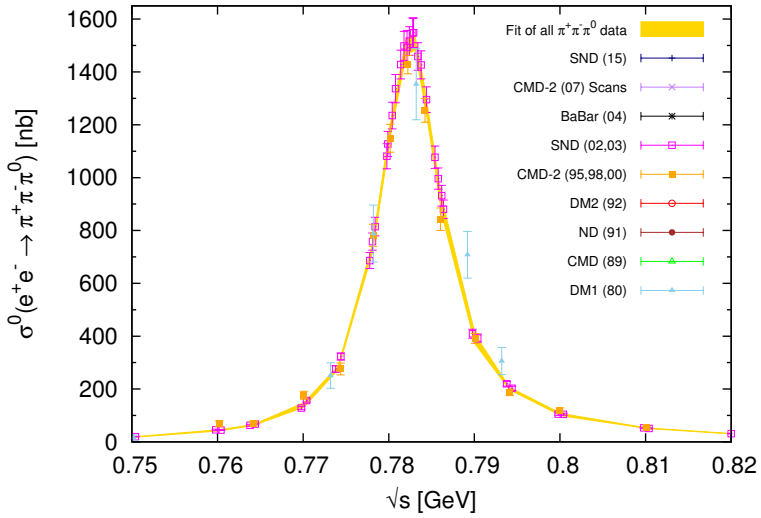

(a) The ω resonance.

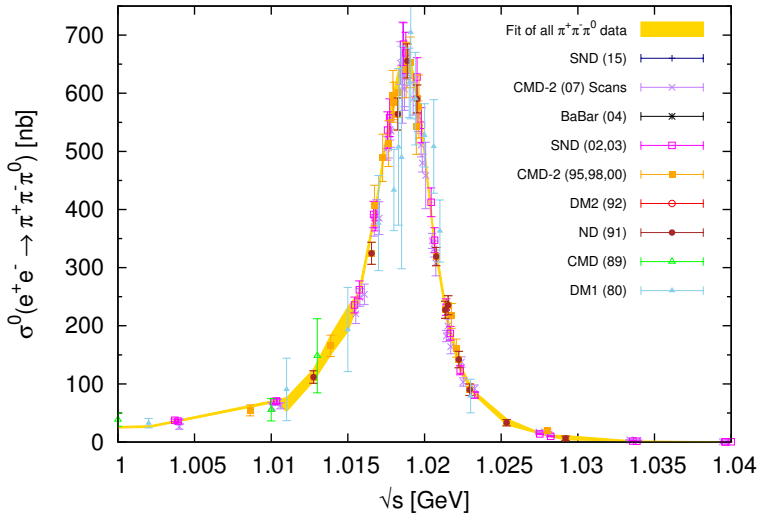

(b) The ϕ resonance.

Fig. 4.7: Enlargements of the resonance regions in the $\pi^+\pi^-\pi^0$ final state.

non-resonant cross section. In addition, the M3N thesis data [153] that were included in the analyses preceding this work [21,46,47] are now discarded on the basis that they are not published, are of poor quality and are not consistent with the more recent cross section data in this channel.[3] With these changes,

$$a_\mu^{\pi^+\pi^-\pi^+\pi^-}[0.6125 \leq \sqrt{s} \leq 1.937 \text{ GeV}] = (14.87 \pm 0.02 \pm 0.13 \pm 0.03 \pm 0.15) \times 10^{-10}$$
$$= (14.87 \pm 0.20) \times 10^{-10}\,. \qquad (4.8)$$

Here, the mean value has increased since [21] largely due to the new BaBar data. The uncertainty has decreased by more than 50% due to the inclusion of the new BaBar

[3] This is true for all channels which previously included data from the M3N thesis [153] and is stated accordingly in the discussions of the relevant channels.

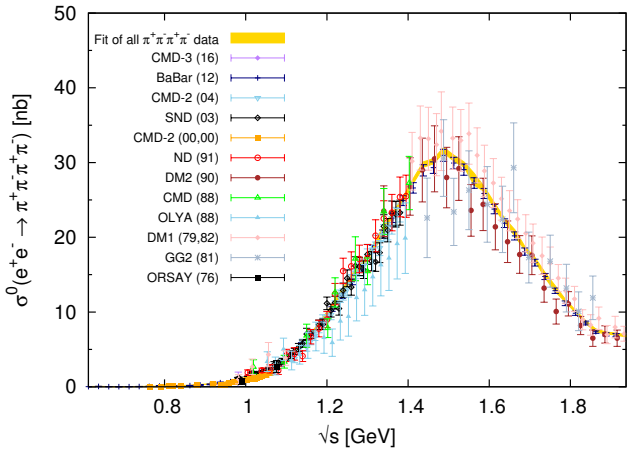

Fig. 4.8: The cross section $\sigma^0(e^+e^- \to \pi^+\pi^-\pi^+\pi^-)$ in the range $0.6125 \leq \sqrt{s} \leq 1.937$ GeV.

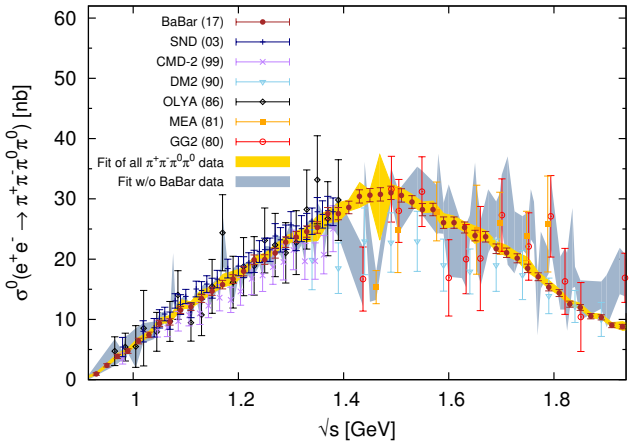

Fig. 4.9: The cross section $\sigma^0(e^+e^- \to \pi^+\pi^-\pi^0\pi^0)$ in the range $0.850 \leq \sqrt{s} \leq 1.937$ GeV.

and CMD-3 data coupled with the new data combination method. The combined cross section and data are displayed in Figure 4.8.

The picture for the $\pi^+\pi^-\pi^0\pi^0$ final state has also improved, with a new measurement of this channel by BaBar [154] being the only new data in this channel since 2003, which extends the lower border of the data from 0.915 GeV in [21] to 0.85 GeV in this work . In total, this channel now combines eight data sets [139,145,148,154–158] where, as with the $\pi^+\pi^-\pi^+\pi^-$ channel, the M3N data [153] in this channel have been omitted. The estimate for this channel is

$$a_\mu^{\pi^+\pi^-\pi^0\pi^0}[0.850 \leq \sqrt{s} \leq 1.937 \text{ GeV}] = (19.39 \pm 0.09 \pm 0.74 \pm 0.04 \pm 0.19) \times 10^{-10} = (19.39 \pm 0.78) \times 10^{-10}\,. \quad (4.9)$$

The improvement since [21] is substantial, where the combination of this channel with the BaBar data omitted results in $a_\mu^{\pi^+\pi^-\pi^0\pi^0}(\text{no BaBar}) = (20.07 \pm 1.19) \times 10^{-10}$. The

mean value has reduced by a notable amount, although this change is well with the error estimate of [21]. The reason for this can be seen in Figure 4.9, which shows the new combination of the data for the bare cross section $e^+e^- \to \pi^+\pi^-\pi^0\pi^0$ and includes the data combination without the new BaBar data for comparison. The reduction in the mean value can be seen above $\sim$ 1.6 GeV, where the now smooth cross section has replaced the higher, more erratic cross section without the BaBar data.[4] Across the entire available energy range, the large improvement provided by the new BaBar is clear. The uncertainty contribution from $\pi^+\pi^-\pi^0\pi^0$ is, however, still relatively large and requires better, new data. With a fractional contribution to $a_\mu^{\text{had, LO VP}}$ of $\sim 3\%$, it contributes $\sim 10\%$ to the total uncertainty. A large proportion of this uncertainty comes from the local χ^2_{min}/d.o.f. error inflation, which can be seen clearly, for example, at the peak of the cross section in Figure 4.9, where the new BaBar data disagree with the old MEA [155] and GG2 [156] data.

4.1.5 5π channels

The five-pion channels include the $2\pi^+2\pi^-\pi^0$ and $\pi^+\pi^-3\pi^0$ final states, with the process $e^+e^- \to \gamma^* \to 5\pi^0$ being forbidden from charge conjugation symmetry. As the only data currently available for the $\pi^+\pi^-3\pi^0$ channel are those presented in the M3N thesis [153] discussed earlier, this channel is estimated via an isospin relation and discussed in detail in Section 4.2.1.

The $\pi^+\pi^-\pi^+\pi^-\pi^0$ data combination includes data from six measurements [120, 144, 155, 156, 159, 160], where there has been no new data since [21]. To ensure no double counting of contributions from different channels with similar resonant decay modes, it is necessary in many cases for the branching fractions of the decay of these resonances to specific final states to be removed from the experimental data. For the $\pi^+\pi^-\pi^+\pi^-\pi^0$ channel, potential double counting can arise with the $\eta\pi^+\pi^-$ channel (from the decay $\eta \to \pi^+\pi^-\pi^0$) and the $\omega\pi^+\pi^-$ channel (from the decay $\omega \to \pi^+\pi^-\pi^0$). In this work, the channel $\omega(\to \text{npp})2\pi$ (detailed in Section 4.2.4) is determined such that 'npp' denotes the ω resonance decaying to only non-purely-pionic modes, hence avoiding the double counting with the $\pi^+\pi^-\pi^+\pi^-\pi^0$ channel. For the decay of the η resonance, the branching fraction $\mathcal{B}(\eta \to \pi^+\pi^-\pi^0)$ is removed from the $\pi^+\pi^-\pi^+\pi^-\pi^0$ data [16], indicated by the subscript 'no η'. This is achieved by correcting the cross section data using the relation

$$\sigma^0[(2\pi^+2\pi^-\pi^0)_{\text{no }\eta}](s) = \sigma^0[2\pi^+2\pi^-\pi^0](s) - \sigma^0[\eta\pi^+\pi^-](s) \times \mathcal{B}(\eta \to \pi^+\pi^-\pi^0)\,. \quad (4.10)$$

To accomplish this, the contributing cross sections and covariance matrices are linearly

[4] This is an important factor contributing to the decision to shift the transition region between the exclusive and inclusive data from 2.0 GeV in [21] to 1.937 GeV is this work, as discussed in Section 4.3.1.

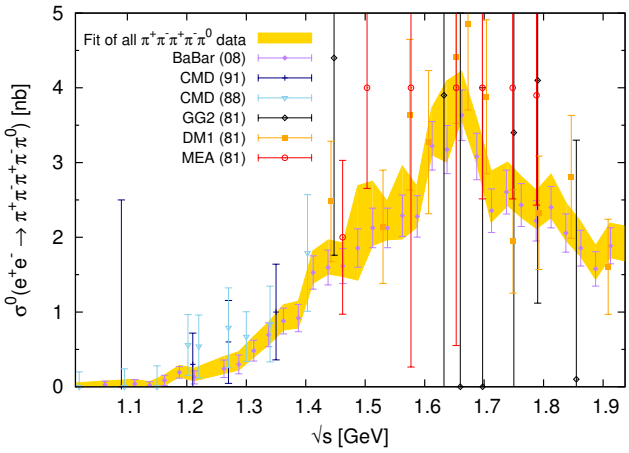

Fig. 4.10: The cross section $\sigma^0(e^+e^- \to \pi^+\pi^-\pi^+\pi^-\pi^0)$ in the range $1.0127 \leq \sqrt{s} \leq 1.937$ GeV.

interpolated following the prescription in Section 2.4.5.[5] For the $2\pi^+2\pi^-\pi^0$ channel, combining the data results and applying this correction results in

$$a_\mu^{(2\pi^+2\pi^-\pi^0)_{\text{no }\eta}}[1.0127 \leq \sqrt{s} \leq 1.937 \text{ GeV}] = (0.99 \pm 0.04 \pm 0.08 \pm 0.01 \pm 0.01) \times 10^{-10} = (0.99 \pm 0.09) \times 10^{-10}\,. \quad (4.11)$$

This combined cross section is shown in Figure 4.10, where it can be seen that other than the BaBar measurement, the data quality is poor and results in sizeable local error inflation across the majority of the available energy range of the data.

4.1.6 6π channels

The six-pion channels are composed of the $3\pi^+3\pi^-$, $2\pi^+2\pi^-2\pi^0$ and $\pi^+\pi^-4\pi^0$ final states, with the process $e^+e^- \to \gamma^* \to 6\pi^0$ being forbidden from charge conjugation symmetry. Experimental cross section data are available for the $3\pi^+3\pi^-$ and $2\pi^+2\pi^-2\pi^0$ channels, but not for the $\pi^+\pi^-4\pi^0$ channel which is estimated via an isospin relation (see Section 4.2.2).

For the $3\pi^+3\pi^-$ channel, seven data sets are combined [144,161–164]. In comparison with [21], three scans of the cross section measured by the CMD-3 collaboration [164] are included (with the systematic uncertainties of all three taken to be fully correlated between the scans [138]) and the M3N thesis data [153] previously included in this channel are omitted. The combination of these data results in

$$a_\mu^{3\pi^+3\pi^-}[1.3125 \leq \sqrt{s} \leq 1.937 \text{ GeV}] = (0.23 \pm 0.01 \pm 0.01 \pm 0.00 \pm 0.00) \times 10^{-10} = (0.23 \pm 0.01) \times 10^{-10}\,. \quad (4.12)$$

The resulting cross section is shown in Figure 4.11.

[5] In all cases in this work where a resonance contribution is removed, a corresponding relation is applied to the relevant cross section data. Should the relations involve data from different channels, the cross section data and covariance matrices are also linearly interpolated as described in Section 2.4.5.

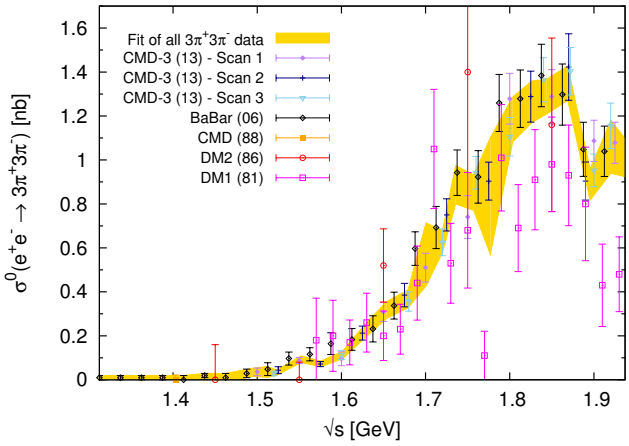

Fig. 4.11: The cross section $\sigma^0(e^+e^- \to 3\pi^+3\pi^-)$ in the range $1.3125 \leq \sqrt{s} \leq 1.937$ GeV.

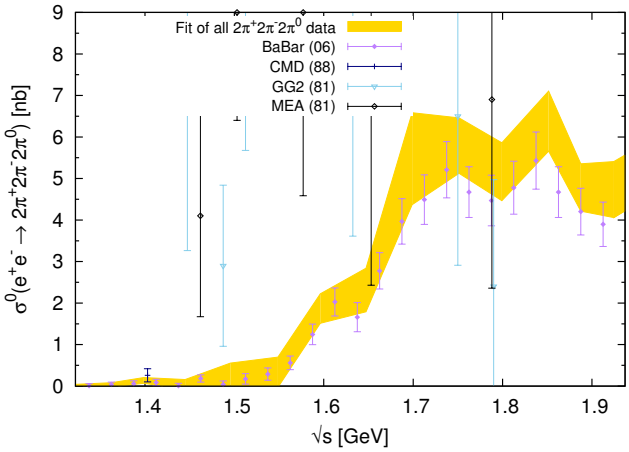

Fig. 4.12: The cross section $\sigma^0(e^+e^- \to 2\pi^+2\pi^-2\pi^0)$ in the range $1.3223 \leq \sqrt{s} \leq 1.937$ GeV.

In the $2\pi^+2\pi^-2\pi^0$ channel, four data sets are combined [144, 155, 156, 163], where no new data for this final state has been made available since [21]. To avoid a double counting of the η and ω resonance contributions with the $\eta\omega$ and $\eta\pi^+\pi^-\pi^0$ channels, the relevant branching fraction corrections are applied to the combined data resulting in

$$a_\mu^{(2\pi^+2\pi^-2\pi^0)_{\text{no }\eta\omega}}[1.3223 \leq \sqrt{s} \leq 1.937 \text{ GeV}] = (1.35 \pm 0.08 \pm 0.15 \pm 0.02 \pm 0.01) \times 10^{-10}$$
$$= (1.35 \pm 0.17) \times 10^{-10}\,. \qquad (4.13)$$

The combined cross section is shown in Figure 4.12.

4.1.7 $K\bar{K}$ channels

The $K\bar{K}$ channels are the K^+K^- and $K_S^0K_L^0$ channels, both of which are dominated by the ϕ resonance. In this work, the K^+K^- channel combines 15 data sets [69, 108,

110, 120, 165–173]. Since [21], one major change to this channel is the inclusion of the precise and finely binned measurement by the BaBar collaboration, supplemented with full statistical and systematic covariance matrices [171]. This is the first and only example to date of the release of energy dependent, correlated uncertainties outside of the $\pi^+\pi^-$ channel and they, like the correlated uncertainties in the two-pion final state, have an overwhelming influence on the data combination. There is also a new measurement in this channel of the ϕ resonance by the CMD-3 collaboration [173]. The existing CMD-2 scans in the same region [86] are omitted from this work as they suffer from an overestimation of the trigger efficiency for slow kaons [173] and are awaiting reanalysis [174]. In addition, two new scans by the SND collaboration measured at the tail of the ϕ and into the continuum are included [172]. The systematic uncertainties of these two scans, along with the existing two scans by SND [169], are considered to be fully correlated [138]. The resulting cross section is shown in Figure 4.13, where the combination of the available K^+K^- data results in

$$\begin{aligned} a_\mu^{K^+K^-}[0.9875 \leq \sqrt{s} \leq 1.937 \text{ GeV}] &= (23.03 \pm 0.08 \pm 0.20 \pm 0.03 \pm 0.00) \times 10^{-10} \\ &= (23.03 \pm 0.22) \times 10^{-10} \,. \end{aligned} \tag{4.14}$$

The resulting cross section of the process $e^+e^- \to K^+K^-$ is displayed in Figure 4.13. This estimate of $a_\mu^{K^+K^-}$ exhibits an increase of the mean value of more than 1σ from the estimate in [21] attributed to the inclusion of the new BaBar and CMD-3 data. This can be seen in Figure 4.14. In [21], the data combination in the ϕ resonance region for this channel was dominated by the SND scans [169] visible in Figure 4.14 and the now omitted CMD-2 scans [86], which were in good agreement. The BaBar data [171], which due to their precision and correlated uncertainties now dominate the K^+K^- data combination, are higher in this region than both the SND and CMD-2 data. The most recent CMD-3 data are higher still [173]. The reanalysis of the CMD-2 data will prove crucial in resolving the current differences in this channel and, should they agree further with the BaBar and CMD-3 data, would result in a further increase of the estimate from this channel.

The uncertainty has drastically improved since [21] with much of the change being due to a finer clustering over the ϕ resonance after the inclusion of the new high statistics BaBar data. However, the disagreement between the data seen in Figure 4.14 results in a poor global $\sqrt{\chi^2_{\text{min}}/\text{d.o.f.}} \sim 2.1$ and is accounted for in the local error inflation which provides an increase to the uncertainty of $a_\mu^{K^+K^-}$ of $\sim 20\%$. Following from the discussion in Section 2.1.2, there is now no FSR correction applied to this channel and, therefore, there is no extra radiative correction uncertainty due to FSR. It should also be noted that any FSR correction would result in an increase of $a_\mu^{K^+K^-}$, showing again the strong influence the new data have had in this channel to increase the mean value since [21], where previously an FSR correction was applied.

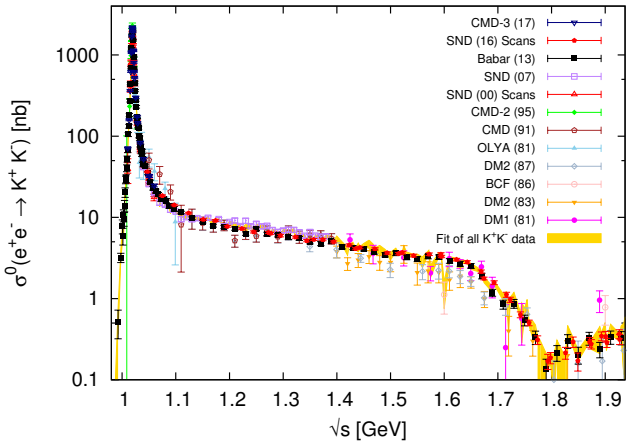

(a) Full range of the cross section $\sigma^0(e^+e^- \to K^+K^-)$.

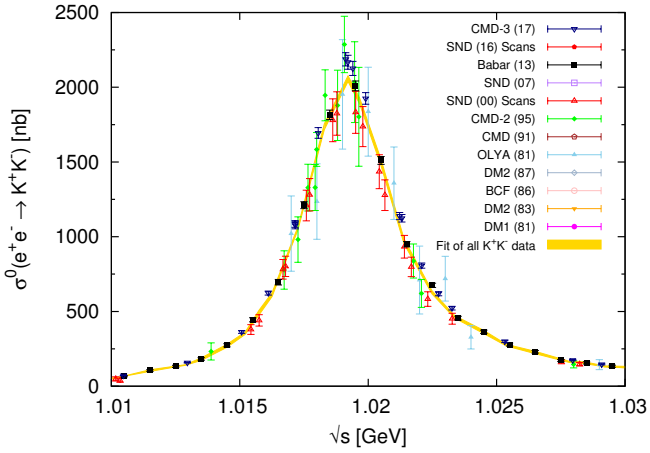

(b) The ϕ resonance.

Fig. 4.13: The cross section $\sigma^0(e^+e^- \to K^+K^-)$ in the range $0.9875 \leq \sqrt{s} \leq 1.937$ GeV and an enlargement of the ϕ resonance. The large influence of the BaBar data (black squares) overwhelms the older data.

In the $K^0_S K^0_L$ channel, 13 data sets are combined [169, 175–180]. Since [21], new data for the $K^0_S K^0_L$ final state is included from the BaBar collaboration above the ϕ resonance [179] and from the CMD-3 collaboration on the ϕ [180]. In addition, two existing measurements in this channel [169, 176] each consist of four data scans, of which the systematic uncertainties are now taken to be fully correlated [138]. This combination results in a contribution of

$$\begin{aligned} a_\mu^{K^0_S K^0_L}[1.00371 \leq \sqrt{s} \leq 1.937 \text{ GeV}] &= (13.04 \pm 0.05 \pm 0.16 \pm 0.10 \pm 0.00) \times 10^{-10} \\ &= (13.04 \pm 0.19) \times 10^{-10}\,. \end{aligned} \tag{4.15}$$

Again, there is no additional FSR correction uncertainty applied to this channel, with the reasoning in Section 2.1.2 enforced by the probability of photon emission being highly suppressed for a neutral final state and given the limited phase space. The cross

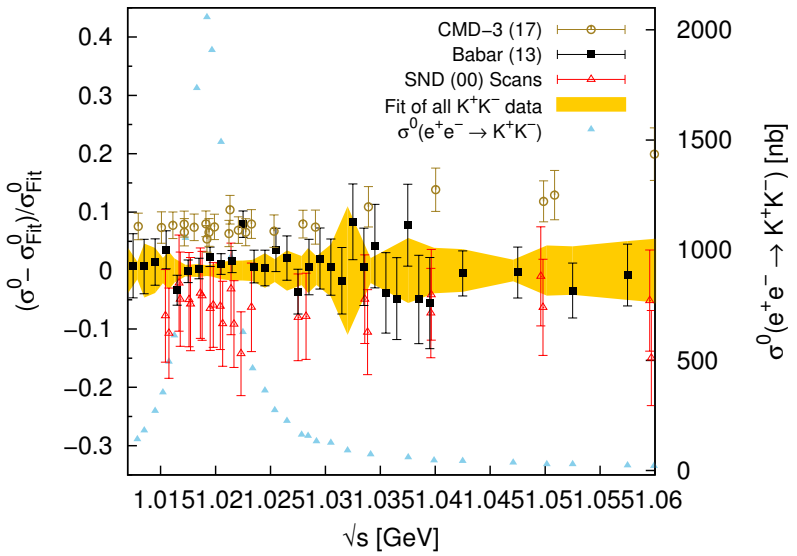

Fig. 4.14: The relative difference of the dominant data in the K^+K^- channel measured in the ϕ resonance region and the fit of all data. For comparison, the individual sets have been normalised against the fit. The yellow band represents the full data combination which incorporates all correlated statistical and systematic uncertainties. However, the width of the yellow band simply displays the square root of the diagonal elements of the total output covariance matrix of the fit.

section of the process $e^+e^- \to K^0_S K^0_L$ is displayed in Figure 4.15.

4.1.8 $K\bar{K}n\pi$ channels

The $K\bar{K}n\pi$ channels included are the $K\bar{K}\pi$, $K\bar{K}2\pi$ and $K\bar{K}3\pi$ final states. In the previous analyses [21, 46, 47], the lack of experimentally measured neutral modes that contributed to these channels resulted in all three being estimated using isospin relations. In this work, the data required to complete the $K\bar{K}\pi$ and $K\bar{K}2\pi$ channels have now been experimentally measured and have removed the reliance on dedicated isospin relations to estimate these final states. For the $KK3\pi$ channel, the data content is still incomplete and, consequently, this channel is still estimated using an isospin relation as described in Section 4.2.3.

For the $K\bar{K}\pi$ channel, the contributing modes are $K^0_S K^\pm \pi^\mp$ [181–184], $K^0_L K^\pm \pi^\mp$, $K^+K^-\pi^0$ [182–184], and $K^0_S K^0_L \pi^0$ [185, 186]. The combinations of the available data

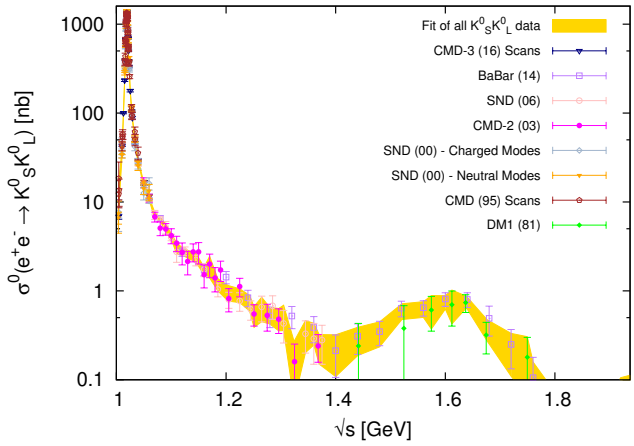

(a) Full range of the cross section $\sigma^0(e^+e^- \to K_S^0 K_L^0)$.

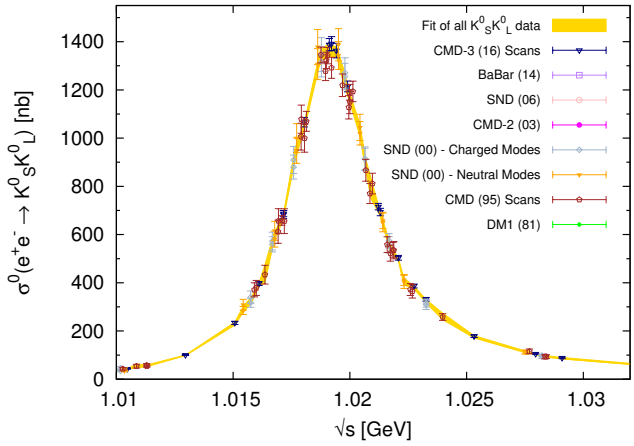

(b) The ϕ resonance.

Fig. 4.15: The cross section $\sigma^0(e^+e^- \to K_S^0 K_L^0)$ with an enlargement of the ϕ resonance.

for the respective modes result in individual contributions to a_μ of [6]

$$
\begin{aligned}
a_\mu^{K_S^0 K^\pm \pi^\mp}[1.260 \leq \sqrt{s} \leq 1.937 \text{ GeV}] &= (0.88 \pm 0.05) \times 10^{-10}\,, \\
a_\mu^{K^+ K^- \pi^0}[1.370 \leq \sqrt{s} \leq 1.937 \text{ GeV}] &= (0.17 \pm 0.01) \times 10^{-10}\,, \\
a_\mu^{K_S^0 K_L^0 \pi^0}[1.325 \leq \sqrt{s} \leq 1.937 \text{ GeV}] &= (0.79 \pm 0.07) \times 10^{-10}\,. \qquad (4.16)
\end{aligned}
$$

In this work, the neutral final state $K_S^0 K_L^0 \pi^0$ has been measured by BaBar [185] and SND [186] for the first time, removing the reliance on isospin for this channel (other

[6] Here, the errors of these estimates only display the experimental uncertainties. The additional radiative correction uncertainties are determined individually for each mode and their sum in quadrature is given in the estimate for $K\bar{K}\pi$ in equation (4.18). This is also the case for the discussions of the $K\bar{K}2\pi$ and $\eta K\bar{K}$ channels.

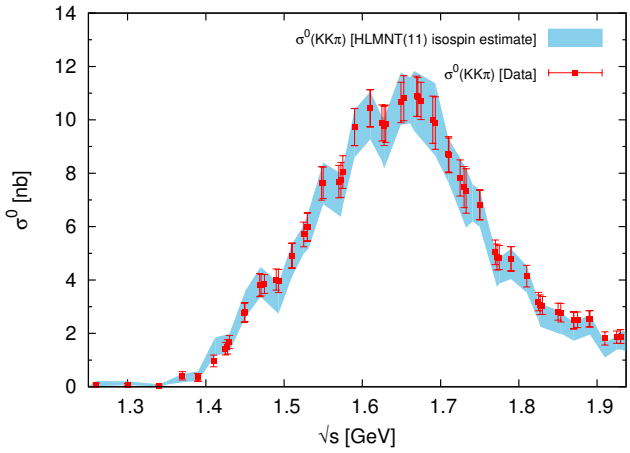

Fig. 4.16: The measured cross section $\sigma^0(KK\pi)$ compared to the estimate from the previously used isospin relation.

than $K^0_S \simeq K^0_L$). Therefore, the $K\bar{K}\pi$ cross section is now calculated using

$$\begin{aligned}\sigma(K\bar{K}\pi) &= \sigma(K^0_S K^\pm \pi^\mp) + \sigma(K^0_L K^\pm \pi^\mp) + \sigma(K^+K^-\pi^0) + \sigma(K^0_S K^0_L \pi^0) \\ &\simeq 2\sigma(K^0_S K^\pm \pi^\mp) + \sigma(K^+K^-\pi^0) + \sigma(K^0_S K^0_L \pi^0)\,, \end{aligned} \tag{4.17}$$

resulting in a contribution of

$$\begin{aligned} a_\mu^{K\bar{K}\pi}[1.260 \leq \sqrt{s} \leq 1.937 \text{ GeV}] &= (2.71 \pm 0.05 \pm 0.11 \pm 0.01 \pm 0.01) \times 10^{-10} \\ &= (2.71 \pm 0.12) \times 10^{-10}\,. \end{aligned} \tag{4.18}$$

In [21], the isospin estimate in the same energy range yielded

$$a_\mu^{K\bar{K}\pi}(\text{HLMNT11 isospin estimate}) = (2.65 \pm 0.14) \times 10^{-10}. \tag{4.19}$$

This good agreement between the HLMNT11 isospin estimate and the data-based approach in this analysis is also demonstrated in Figure 4.16.

For $K\bar{K}2\pi$, BaBar have measured the previously missing modes $K^0_S K^0_L \pi^+\pi^-$ [179], $K^0_S K^0_S \pi^+\pi^-$ [179], $K^0_S K^0_L 2\pi^0$ [185] and $K^0_S K^\pm \pi^\mp \pi^0$ [187]. These, summed with the other contributing modes $K^0_L K^0_L \pi^+\pi^-$, $K^0_L K^\pm \pi^\mp \pi^0$, $K^+K^-\pi^0\pi^0$ [188, 189] and $K^+K^-\pi^+\pi^-$ [152, 182, 188–191] (again assuming $K^0_S \simeq K^0_L$), have removed the reliance on isospin for this channel also. The combinations of the available data from each mode are found to give

$$\begin{aligned} a_\mu^{K^0_S K^0_L \pi^+\pi^-}[1.425 \leq \sqrt{s} \leq 1.937 \text{ GeV}] &= (0.17 \pm 0.03) \times 10^{-10}\,, \\ a_\mu^{K^0_S K^0_S \pi^+\pi^-}[1.630 \leq \sqrt{s} \leq 1.937 \text{ GeV}] &= (0.03 \pm 0.00) \times 10^{-10}\,, \\ a_\mu^{K^0_S K^0_L \pi^0\pi^0}[1.350 \leq \sqrt{s} \leq 1.937 \text{ GeV}] &= (0.14 \pm 0.05) \times 10^{-10}\,, \\ a_\mu^{K^0_S K^\pm \pi^\mp \pi^0}[1.510 \leq \sqrt{s} \leq 1.937 \text{ GeV}] &= (0.33 \pm 0.02) \times 10^{-10}\,, \\ a_\mu^{K^+K^-\pi^0\pi^0}[1.460 \leq \sqrt{s} \leq 1.937 \text{ GeV}] &= (0.12 \pm 0.01) \times 10^{-10}\,, \\ a_\mu^{K^+K^-\pi^+\pi^-}[1.434 \leq \sqrt{s} \leq 1.937 \text{ GeV}] &= (0.78 \pm 0.03) \times 10^{-10}\,. \end{aligned} \tag{4.20}$$

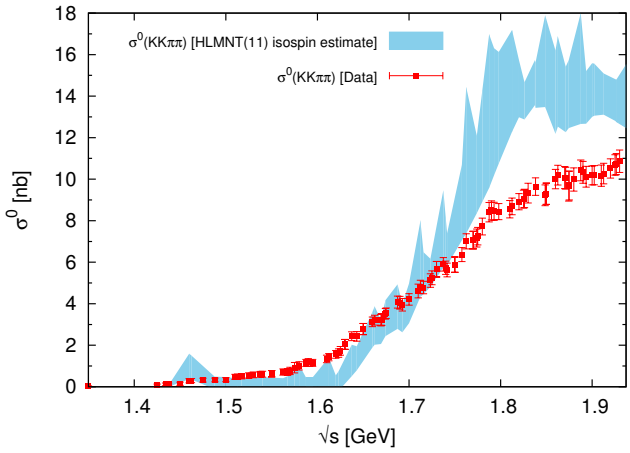

Fig. 4.17: The cross section $\sigma^0(KK\pi\pi)$ compared to the previous estimate using isospin relations.

In this work, the $K\bar{K}2\pi$ contribution is now determined using

$$\begin{aligned}\sigma(K\bar{K}2\pi) &= \sigma(K^+K^-\pi^0\pi^0) + \sigma(K^+K^-\pi^+\pi^-) + \sigma(K^0\bar{K^0}\pi^+\pi^-) + \sigma(K_S^0K_L^02\pi^0) \\ &+ \ \sigma(K_S^0K^\pm\pi^\mp\pi^0) + \sigma(K_L^0K^\pm\pi^\mp\pi^0) \\ &\simeq \sigma(K^+K^-\pi^0\pi^0) + \sigma(K^+K^-\pi^+\pi^-) + \sigma(K^0\bar{K^0}\pi^+\pi^-) + \sigma(K_S^0K_L^02\pi^0) \\ &+ \ 2\sigma(K_S^0K^\pm\pi^\mp\pi^0)\,, \end{aligned} \tag{4.21}$$

where,

$$\begin{aligned}\sigma(K^0\bar{K^0}\pi^+\pi^-) &= \sigma(K_S^0K_L^0\pi^+\pi^-) + \sigma(K_S^0K_S^0\pi^+\pi^-) + \sigma(K_L^0K_L^0\pi^+\pi^-) \\ &\simeq \sigma(K_S^0K_L^0\pi^+\pi^-) + 2\sigma(K_S^0K_S^0\pi^+\pi^-)\,. \end{aligned} \tag{4.22}$$

Therefore, the estimate in this channel is now found to be

$$\begin{aligned}a_\mu^{K\bar{K}2\pi}[1.350 \leq \sqrt{s} \leq 1.937 \text{ GeV}] &= (1.93 \pm 0.03 \pm 0.07 \pm 0.01 \pm 0.01) \times 10^{-10} \\ &= (1.93 \pm 0.08) \times 10^{-10}\,. \end{aligned} \tag{4.23}$$

Comparing equation (4.23) with the HLMNT11 isospin estimate in the same energy range of

$$a_\mu^{K\bar{K}2\pi}(\text{HLMNT11 isospin estimate}) = (2.51 \pm 0.35) \times 10^{-10} \tag{4.24}$$

and examining Figure 4.17, it is evident that the isospin relations provided a poor estimate of this final state. Using the data, $K\bar{K}2\pi$ contributes a much smaller mean value with a greatly reduced uncertainty.

4.1.9 η, ω and ϕ channels

In the $\eta\gamma$ channel, there are many measurements of the cross section for a relatively small contribution to a_μ, with 9 data sets [69, 104, 106, 192–196] now being combined.

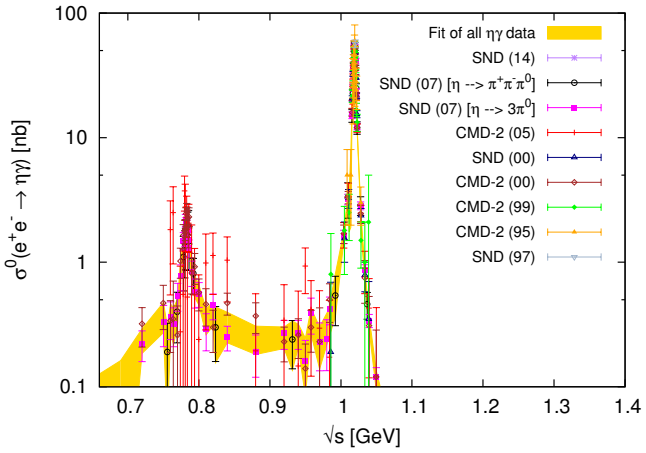

Fig. 4.18: The cross section $\sigma^0(e^+e^- \to \eta\gamma)$ in the range $0.66 \leq \sqrt{s} \leq 1.4$ GeV.

In this work, the systematic uncertainties of two scans in the same measurement by SND [195] are now taken to be correlated by 30% between the bins of the respective scans [138].[7] This results in a contribution of

$$\begin{aligned} a_\mu^{\eta\gamma}[0.66 \leq \sqrt{s} \leq 1.76 \text{ GeV}] &= (0.70 \pm 0.02 \pm 0.01 \pm 0.00 \pm 0.01) \times 10^{-10} \\ &= (0.70 \pm 0.02) \times 10^{-10} \,. \end{aligned} \tag{4.25}$$

The combined cross section of the $\eta\gamma$ final state is shown in Figure 4.18. The $\eta\gamma$ channel is the last of the four channels with a threshold contribution that has not been measured by experiment. From Section 2.4.1, the threshold contribution is found from ChPT to give a negligible value (within rounding) of

$$a_\mu^{\eta\gamma}(\text{ChPT})[m_\eta \leq \sqrt{s} < 0.66 \text{ GeV}] = (0.00 \pm 0.00) \times 10^{-10} \,. \tag{4.26}$$

Four measurements of the process $e^+e^- \to \eta\pi^+\pi^-$ have been included [197–200]. The combination of these data yields a contribution to a_μ of

$$\begin{aligned} a_\mu^{\eta\pi^+\pi^-}[1.091 \leq \sqrt{s} \leq 1.937 \text{ GeV}] &= (1.29 \pm 0.02 \pm 0.05 \pm 0.01 \pm 0.01) \times 10^{-10} \\ &= (1.29 \pm 0.06) \times 10^{-10} \,, \end{aligned} \tag{4.27}$$

with the resulting cross section displayed in Figure 4.19.

The $\eta\pi^+\pi^-\pi^0$ final state is included in this work for the first time, where it was previously not measured by experiment and its contribution was not estimated in the

[7] The two data sets of the cross section in [195] are determined from the different decay channels of $\eta \to 3\pi^0$ and $\eta \to \pi^+\pi^-\pi^0$, respectively. In this case, for the $\eta \to 3\pi^0$ mode, a normalisation to the process $e^+e^- \to \gamma\gamma$ was used and, for $\eta \to \pi^+\pi^-\pi^0$, the normalisation to Bhabha scattering was used. For the correlation of these data, 30% correlation between the total systematic uncertainties of both has been estimated. This is due to the acceptance efficiency [138] (which dominates the systematic uncertainties), where different angles were used to determine the acceptance of either the 2γ or Bhabha final state and, clearly, 100% correlation would result in an overestimate of the correlated nature of these sources of uncertainty.

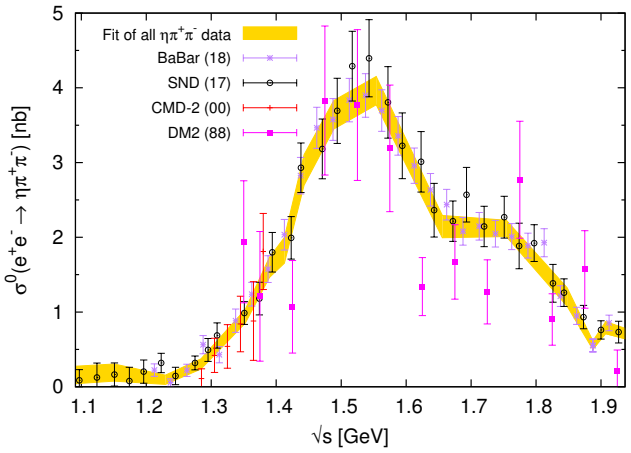

Fig. 4.19: The cross section $\sigma^0(e^+e^- \to \eta\pi^+\pi^-)$ in the range $1.091 \leq \sqrt{s} \leq 1.937$ GeV.

previous analyses [21, 46, 47]. It has since been measured by the CMD-3 collaboration [201] and is included with the decay of $\omega \to \pi^+\pi^-\pi^0$ removed to avoid double counting of this resonance contribution with the $\eta\omega$ channel. This results in

$$a_\mu^{(\eta\pi^+\pi^-\pi^0)_{\text{no }\omega}}[1.3325 \leq \sqrt{s} \leq 1.937 \text{ GeV}] = (0.60 \pm 0.03 \pm 0.14 \pm 0.01 \pm 0.01) \times 10^{-10} = (0.60 \pm 0.15) \times 10^{-10}\,. \quad (4.28)$$

The $\eta 2\pi^+ 2\pi^-$ channel currently consists of only a single experiment measurement of the cross section [160] which, when integrated over, gives

$$a_\mu^{\eta 2\pi^+ 2\pi^-}[1.3375 \leq \sqrt{s} \leq 1.937 \text{ GeV}] = (0.08 \pm 0.01 \pm 0.01 \pm 0.00 \pm 0.00) \times 10^{-10} = (0.08 \pm 0.01) \times 10^{-10}\,. \quad (4.29)$$

Another new addition to this work with respect to [21] is the $\eta K\bar{K}$ channel, which consists of the ηK^+K^- [184] and $\eta K_S^0 K_L^0$ [185] final states. The data for each channel results in

$$a_\mu^{\eta(K^+K^-)_{\text{no }\phi}}[1.690 \leq \sqrt{s} \leq 1.937 \text{ GeV}] = (0.01 \pm 0.00) \times 10^{-10}\,,$$
$$a_\mu^{\eta K_S^0 K_L^0}[1.575 \leq \sqrt{s} \leq 1.937 \text{ GeV}] = (0.17 \pm 0.03) \times 10^{-10}\,. \quad (4.30)$$

For both of these contributions, to avoid double counting with the $\eta\phi$ channel, the contributions of the decays of $\eta \to$ purely-pionic states and $\phi \to K\bar{K}$ are omitted from the respective data. Therefore, the contribution from the determined cross section of $\eta(\to \text{npp})(K\bar{K})_{\text{no }\phi}$ gives a contribution to a_μ of

$$a_\mu^{\eta(\to\text{npp})(K\bar{K})_{\text{no }\phi}}[1.5693 \leq \sqrt{s} \leq 1.937 \text{ GeV}] = (0.01 \pm 0.01 \pm 0.01 \pm 0.00 \pm 0.00) \times 10^{-10} = (0.01 \pm 0.02) \times 10^{-10}\,. \quad (4.31)$$

The $\eta\omega$ channel combines three data sets [163, 201, 202], resulting in an estimate of

$$\begin{aligned} a_\mu^{\eta\omega}[1.3325 \leq \sqrt{s} \leq 1.937 \text{ GeV}] &= (0.31 \pm 0.01 \pm 0.02 \pm 0.00 \pm 0.00) \times 10^{-10} \\ &= (0.31 \pm 0.03) \times 10^{-10} \,. \end{aligned} \tag{4.32}$$

The $\eta\omega\pi^0$ channel is now included in this data compilation for the hadronic R-ratio, having been measured for the first time by SND [203]. It provides a small contribution to a_μ of

$$\begin{aligned} a_\mu^{\eta\omega\pi^0}[1.550 \leq \sqrt{s} \leq 1.937 \text{ GeV}] &= (0.35 \pm 0.09 \pm 0.01 \pm 0.00 \pm 0.00) \times 10^{-10} \\ &= (0.35 \pm 0.09) \times 10^{-10} \,. \end{aligned} \tag{4.33}$$

The combination of two measurements of the $\eta\phi$ final state [160, 184] results in a contribution of

$$\begin{aligned} a_\mu^{\eta\phi}[1.5693 \leq \sqrt{s} \leq 1.937 \text{ GeV}] &= (0.42 \pm 0.03 \pm 0.02 \pm 0.01 \pm 0.00) \times 10^{-10} \\ &= (0.42 \pm 0.03) \times 10^{-10} \,. \end{aligned} \tag{4.34}$$

Data for the $\omega\pi^0$ final state are multiplied by the branching fraction $\mathcal{B}(\omega \to \pi^0\gamma) = (0.0828 \pm 0.0028)$ [16], so that this data is only included as the $\omega(\to \pi^0\gamma)\pi^0$ channel. This is done to ensure that there is no double counting with multi-pion channels. The data content for this channel is abundant, with a combination of 12 data sets [120, 145, 154, 158, 204–210] (multiplied by the given branching fraction) resulting in a contribution of

$$\begin{aligned} a_\mu^{\omega(\omega\to\pi^0\gamma)\pi^0}[0.9245 \leq \sqrt{s} \leq 1.937 \text{ GeV}] &= (0.88 \pm 0.01 \pm 0.02 \pm 0.00 \pm 0.01) \times 10^{-10} \\ &= (0.88 \pm 0.02) \times 10^{-10} \,. \end{aligned} \tag{4.35}$$

The last of these resonant contributions to be included in this work is the $\phi \to$ unaccounted channel, which represents the contributions from the decay of the ϕ resonance to modes that are not already included as part of the $\pi^0\gamma$, $\pi^+\pi^-$, $\pi^+\pi^-\pi^0$, $\pi^+\pi^-\pi^+\pi^-$, K^+K^-, $K_S^0K_L^0$, $\eta\gamma$ and $\omega\pi^0$ channels. The argument for doing this is based on the knowledge that the sum of the branching fractions of the ϕ resonance to all the modes listed above only accounts for 99.87% of the total contribution from the ϕ, meaning that the branching fraction $\mathcal{B}(\phi \to \text{unaccounted}) = 0.0013$ should be included. To estimate this contribution, the total cross section contribution from the ϕ is determined using the cross section of $\phi \to K^+K^-$ in the energy range between $2m_K \leq \sqrt{s} \leq 1.03$ GeV and the branching fraction $\mathcal{B}(\phi \to K^+K^-) = 0.498 \pm 0.005$,

$$\sigma^0[\phi](s) = \frac{\sigma^0[K^+K^-; 2m_K \leq \sqrt{s} \leq 1.03 \text{ GeV}](s)}{\mathcal{B}(\phi \to K^+K^-)} \,. \tag{4.36}$$

The cross section for $\phi \to$ unaccounted is then determined from

$$\sigma^0[\phi \to \text{unaccounted}](s) = \sigma^0[\phi](s) \times \mathcal{B}(\phi \to \text{unaccounted}) \,. \tag{4.37}$$

Integrating over these calculated data, and applying a 100% uncertainty, results in a contribution of

$$a_\mu^{\phi\to\text{unaccounted}}[2m_K \le \sqrt{s} \le 1.03\text{ GeV}] = (0.04 \pm 0.04) \times 10^{-10}\,. \tag{4.38}$$

4.1.10 $p\bar{p}$ and $n\bar{n}$ channels

The thresholds of the $p\bar{p}$ and $n\bar{n}$ channels begin very close to the transition point between the exclusive and inclusive data at 1.937 GeV and, therefore, their exclusive data contributions provide only very small contributions to a_μ. The $p\bar{p}$ channel combines seven measurements [211–217] which, when combined, result in a contribution of

$$\begin{aligned} a_\mu^{p\bar{p}}[1.8895 \le \sqrt{s} \le 1.937\text{ GeV}] &= (0.03 \pm 0.00 \pm 0.00 \pm 0.00 \pm 0.00) \times 10^{-10} \\ &= (0.03 \pm 0.00) \times 10^{-10}\,. \end{aligned} \tag{4.39}$$

The $n\bar{n}$ channel combines four data sets [217–219], where two recent scans in the same measurement by the SND collaboration [219] are taken to be fully correlated [138]. These data give

$$\begin{aligned} a_\mu^{n\bar{n}}[1.9115 \le \sqrt{s} \le 1.937\text{ GeV}] &= (0.03 \pm 0.00 \pm 0.00 \pm 0.00 \pm 0.00) \times 10^{-10} \\ &= (0.03 \pm 0.01) \times 10^{-10}\,. \end{aligned} \tag{4.40}$$

4.2 Isospin estimated exclusive channels

Following the discussion in Section 2.4.2 regarding those exclusive channels that must be estimated using isospin relations, this section lists those exclusive channels, their respective isospin relations and estimated contributions to a_μ. In all cases, the relations used are those derived in [51] and subsequently have been used in the previous analyses [21, 46, 47]. For the determination of the resulting data of each estimated channel, the cross section and covariance matrix data of the contributing channels are linearly interpolated according to the prescription in Section 2.4.5 and are then used as input into the relevant isospin relation.

4.2.1 5π channels

The relevant five-pion channel which is estimated here is the $\pi^+\pi^-3\pi^0$ channel, for which no experimental measurements currently exist. The isospin relation for this channel is [51]

$$\sigma^0[(\pi^+\pi^-3\pi^0)_{\text{no }\eta}](s) = \frac{1}{2}\sigma^0[(2\pi^+2\pi^-\pi^0)_{\text{no }\eta}](s)\,, \tag{4.41}$$

where the contribution from the η resonance is necessarily omitted for this relation as the final state $\eta 2\pi^0$ is forbidden due to charge conjugation symmetry. It follows that the contribution to a_μ from this channel is

$$a_\mu^{(\pi^+\pi^-3\pi^0)_{\text{no }\eta}}[1.0127 \le \sqrt{s} \le 1.937\text{ GeV}] = (0.50 \pm 0.04) \times 10^{-10}\,. \tag{4.42}$$

4.2.2 6π channels

For the unmeasured $\pi^+\pi^-4\pi^0$ final state, the relation

$$\sigma^0[(\pi^+\pi^-4\pi^0)_{\text{no }\eta}](s) = 0.0625\,\sigma^0[3\pi^+3\pi^-](s) + 0.145\,\sigma^0[(2\pi^+2\pi^-2\pi^0)_{\text{no }\eta}](s) \quad (4.43)$$

is used [51]. This, including an error of 100% to account for the uncertainty of this relation [51], results in

$$a_\mu^{(\pi^+\pi^-4\pi^0)_{\text{no }\eta}}[1.3125 \leq \sqrt{s} \leq 1.937 \text{ GeV}] = (0.21 \pm 0.21) \times 10^{-10}\,. \quad (4.44)$$

4.2.3 $K\bar{K}n\pi$ channels

The $K\bar{K}3\pi$ channel is the last of the $K\bar{K}n\pi$ channels to be included in this data compilation . To estimate this channel, it is assumed that below 1.937 GeV the $K\bar{K}3\pi$ cross section is dominated by $K\bar{K}\omega$ and, therefore, the contributions from modes involving three neutral pions are small and can be neglected. This leaves the $K^+K^-\pi^+\pi^-\pi^0$ and $K^0\bar{K}^0\pi^+\pi^-\pi^0$ modes, where data currently exists for only $K^+K^-\pi^+\pi^-\pi^0$. The $K^+K^-\pi^+\pi^-\pi^0$ data consists of only one measurement [160] which, when integrated, results in a contribution to a_μ of

$$a_\mu^{K^+K^-\pi^+\pi^-\pi^0}[1.6125 \leq \sqrt{s} \leq 1.937 \text{ GeV}] = (0.06 \pm 0.01) \times 10^{-10}\,. \quad (4.45)$$

To ensure no double counting with the $\eta\phi$ channel, the branching fractions of the decays of $\eta \to \pi^+\pi^-\pi^0$ and $\phi \to K^+K^-$ are removed from this channel. The isospin relation for this channel is then based on the assumption that $\sigma^0[(K^0\bar{K}^0\pi^+\pi^-\pi^0)_{\text{no }\eta}](s) \simeq \sigma^0[(K^+\bar{K}^-\pi^+\pi^-\pi^0)_{\text{no }\eta}](s)$ [51] and, therefore,

$$\sigma^0[K\bar{K}3\pi](s) = 2\sigma^0[(K^+\bar{K}^-\pi^+\pi^-\pi^0)_{\text{no }\eta}](s)\,. \quad (4.46)$$

Integrating these calculated data gives a small contribution of

$$a_\mu^{K\bar{K}3\pi}[1.5693 \leq \sqrt{s} \leq 1.937 \text{ GeV}] = (0.03 \pm 0.02) \times 10^{-10}\,. \quad (4.47)$$

4.2.4 $\omega(\to \text{npp})$ and η channels

The $\omega(\to \text{npp})2\pi$ channel accounts for those modes where the ω decays only to non-purely-pionic modes. This is done so that, should the ω decay to $\pi^+\pi^-\pi^0$, there is no double counting with the $2\pi^+2\pi^-\pi^0$ or $\pi^+\pi^-3\pi^0$ channels and, should the ω decay to $\pi^+\pi^-$, there is no double counting with the $2\pi^+2\pi^-$ or $\pi^+\pi^-2\pi^0$ channels. In order to remove these decays, the branching fraction $\mathcal{B}(\omega \to \text{npp})$ is defined as [16]

$$\mathcal{B}(\omega \to \text{npp}) = 1 - \mathcal{B}(\omega \to \pi^+\pi^-\pi^0) - \mathcal{B}(\omega \to \pi^+\pi^-) = 0.0927\,. \quad (4.48)$$

The experimental data contribution to the isospin relation for this channel comes from the measurements of the $\omega\pi^+\pi^-$ final state [131, 159, 198]. The combination of these data in the available energy range gives

$$a_\mu^{\omega\pi^+\pi^-}[1.285 \leq \sqrt{s} \leq 1.937 \text{ GeV}] = (0.72 \pm 0.10) \times 10^{-10}\,. \quad (4.49)$$

For the $\omega(\to \text{npp})2\pi$ channel, the isospin estimate for this cross section is [51]

$$\sigma^0[\omega(\to \text{npp})2\pi](s) = 1.5\,\sigma^0[\omega\pi^+\pi^-](s) \times \mathcal{B}(\omega \to \text{npp})\,, \tag{4.50}$$

resulting in

$$a_\mu^{\omega(\to\text{npp})2\pi}[1.285 \leq \sqrt{s} \leq 1.937\ \text{GeV}] = (0.10 \pm 0.02) \times 10^{-10}\,. \tag{4.51}$$

For the $\omega(\to \text{npp})3\pi$ channel, no measurements of the modes contributing to $\omega 3\pi$ currently exist. The $\omega 3\pi$ cross section is estimated from the measured $2\pi^+2\pi^-2\pi^0$ data using [51]

$$\sigma^0[\omega 3\pi](s) = 1.145\,\frac{\sigma^0[2\pi^+2\pi^-2\pi^0](s)}{\mathcal{B}(\omega \to \pi^+\pi^-\pi^0)}\,. \tag{4.52}$$

The decay of ω to non-purely-pionic states is then removed in a similar fashion to the $\omega(\to \text{npp})2\pi$ channel,

$$\sigma^0[\omega(\to \text{npp})3\pi](s) = \sigma^0[\omega 3\pi](s) \times \mathcal{B}(\omega \to \text{npp}) \tag{4.53}$$

and yields a contribution to a_μ of

$$a_\mu^{\omega(\to\text{npp})3\pi}[1.3223 \leq \sqrt{s} \leq 1.937\ \text{GeV}] = (0.17 \pm 0.03) \times 10^{-10}\,. \tag{4.54}$$

The $\omega(\to \text{npp})K\bar{K}$ channel is estimated in a similar way to the $\omega(\to \text{npp})3\pi$ channel, with the cross section for $\omega K\bar{K}$ being determined from the relation [51]

$$\sigma^0[\omega K\bar{K}](s) = 2\,\frac{\sigma^0[K\bar{K}3\pi](s)}{\mathcal{B}(\omega \to \pi^+\pi^-\pi^0)}\,. \tag{4.55}$$

Then, applying

$$\sigma^0[\omega(\to \text{npp})K\bar{K}](s) = \sigma^0[\omega K\bar{K}](s) \times \mathcal{B}(\omega \to \text{npp}) \tag{4.56}$$

to ensure that only the decay of the ω resonance to non-purely-pionic states is accounted for (to avoid double counting with the $K\bar{K}n\pi$ channels), results in a negligible contribution to a_μ of

$$a_\mu^{\omega(\to\text{npp})K\bar{K}}[1.5693 \leq \sqrt{s} \leq 1.937\ \text{GeV}] = (0.00 \pm 0.00) \times 10^{-10}\,. \tag{4.57}$$

The $\eta\pi^+\pi^-2\pi^0$ final state is estimated from

$$\sigma^0[\eta\pi^+\pi^-2\pi^0](s) = \sigma^0[\eta 2\pi^+2\pi^-](s)\,, \tag{4.58}$$

where 50% of the contribution is taken as a conservative error to account for the uncertainty of this relation [51]. This results in

$$a_\mu^{\eta\pi^+\pi^-2\pi^0}[1.3375 \leq \sqrt{s} \leq 1.937\ \text{GeV}] = (0.08 \pm 0.04) \times 10^{-10}\,. \tag{4.59}$$

4.3 Inclusive R-ratio data

The data for the inclusive hadronic R-ratio data are used in the energy range $1.937 \leq \sqrt{s} \leq 11.1985$ GeV, covering both the $c\bar{c}$ and $b\bar{b}$ threshold regions that cannot be predicted by pQCD. This channel combines 20 data sets [220–237], of which three are new data additions since [21]. These new data are recent precise measurements by the KEDR collaboration: one set between $1.84 \leq \sqrt{s} \leq 3.05$ GeV [237] and two scans in the energy range $3.12 \leq \sqrt{s} \leq 3.72$ GeV [236]. For the latter, the systematic uncertainties are taken to be fully correlated [138]. The fit of the inclusive data in the range $1.937 \leq \sqrt{s} \leq 3.80$ GeV is shown in Figure 4.20, which demonstrates the good agreement between KEDR and pQCD. In [21], the decision was made to use pQCD in the range $2.6 \leq \sqrt{s} \leq 3.73$ GeV, where the quality of inclusive data was poor, with an error inflated according to the percentage errors of the inclusive BES data in this region [235]. With the new KEDR data [236, 237], the inclusive data combination is much improved, as shown in Figure 4.20. In this range, the data combination results in

$$a_\mu^{\text{had, LO VP}}[\text{inc.}, 2.60 \leq \sqrt{s} \leq 3.73 \text{ GeV}] = (11.19 \pm 0.17) \times 10^{-10} \,, \tag{4.60}$$

whereas using pQCD (with an inflated uncertainty [21]), the estimate is

$$a_\mu^{\text{had, LO VP}}[\text{pQCD}, 2.60 \leq \sqrt{s} \leq 3.73 \text{ GeV}] = (10.82 \pm 0.35) \times 10^{-10} \,. \tag{4.61}$$

For the larger energy range $1.937 \leq \sqrt{s} \leq 11.1985$ GeV, the resulting data combination is displayed in Figure 4.21. As well as the differences observed between the data and pQCD below the charm threshold, the data above it (unchanged since [21]) also show a slight variation from the prediction of pQCD. Considering that with the new, precise KEDR data the differences between the inclusive data and pQCD are not as large as previously and that this work is aiming at a predominantly data-driven analysis, the contributions in the entire inclusive data region are now estimated using the inclusive data alone (other than the contributions from the narrow resonances, which are added separately). Hence, for this analysis, the contribution from the inclusive data is found to be

$$\begin{aligned} a_\mu^{\text{had, LO VP}}[\text{inc.}, 1.937 \leq \sqrt{s} \leq 11.2 \text{ GeV}] &= (43.67 \pm 0.17 \pm 0.48 \pm 0.01 \pm 0.44) \times 10^{-10} \\ &= (43.67 \pm 0.67) \times 10^{-10} \,. \end{aligned} \tag{4.62}$$

4.3.1 Transition region between exclusive and inclusive data

With the inclusion of the new KEDR data since [21], the transition region between the sum of exclusive states and the inclusive R-ratio data is of interest and deserves re-examination. For the sum of exclusive channels, whilst many measurements extend to 2

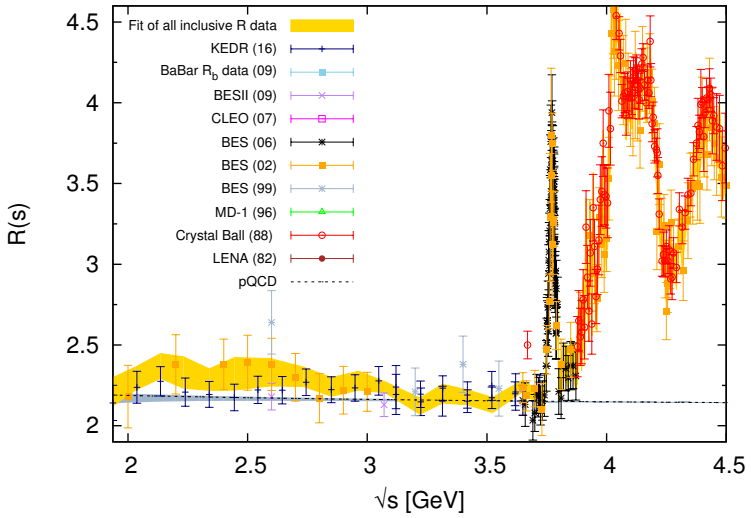

Fig. 4.20: The combination of inclusive R data in the region $1.937 \leq \sqrt{s} \leq 4.50$ GeV. For comparison, the fit and the contributing data are plotted against the estimate of pQCD, represented by the dashed line and grey band.

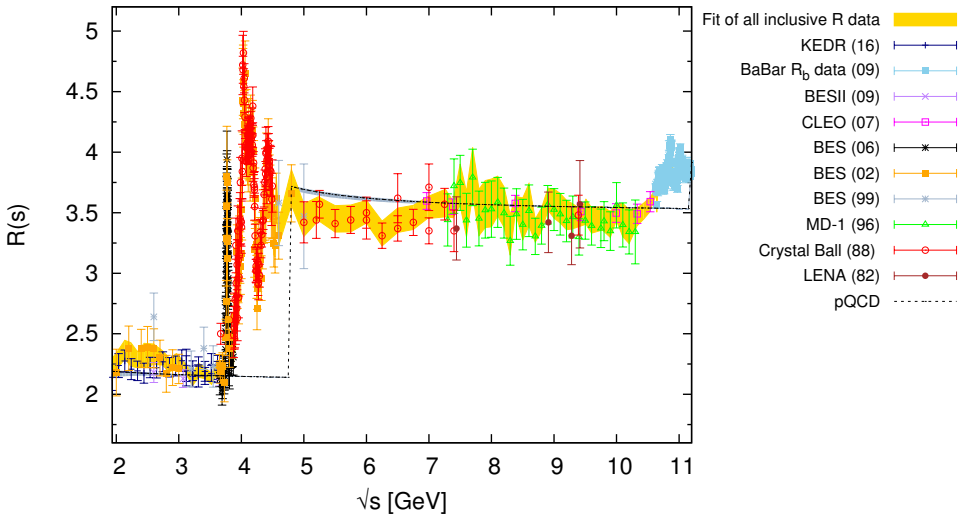

Fig. 4.21: Compilation of inclusive data in range $1.937 \leq \sqrt{s} \leq 11.2$ GeV. The dashed line and surrounding grey band shows the estimate from pQCD for comparison. The yellow band represents the total uncertainty of the inclusive data combination.

GeV or beyond, with increasing energy the inclusion of more and more multi-hadronic final states is required to achieve a reliable estimate of the total hadronic cross section. Previously, in [21], the sum of exclusive data was used up to 2 GeV, which defined the transition point between the exclusive sum and the inclusive data combination. In this analysis, the new KEDR data [237] contribute two data points below 2 GeV, extending the lower boundary of the inclusive data down to 1.841 GeV (compared to 2 GeV in [21]) and providing an opportunity to reconsider the previous choice concerning the data input in this region.

Input	$a_\mu^{\text{had, LO VP}}[1.841 \leq \sqrt{s} \leq 2.00 \text{ GeV}] \times 10^{10}$
Exclusive sum	6.06 ± 0.17
Inclusive data	6.67 ± 0.26
pQCD	6.38 ± 0.11
Exclusive (< 1.937 GeV) + inclusive (> 1.937 GeV)	6.23 ± 0.13

Table 4.1: Comparison of results for $a_\mu^{\text{had, LO VP}}[1.841 \leq \sqrt{s} \leq 2.00 \text{ GeV}]$ from the different available inputs in this region.

From the lower boundary of the KEDR measurement up to 2 GeV, the resulting contributions to $a_\mu^{\text{had, LO VP}}$ from the sum of exclusive states, the inclusive data combination and pQCD are given in Table 4.1. The integrated values of the inclusive data and pQCD agree within errors. However, the contribution from the sum of exclusive states disagrees with the estimates from both the inclusive data and pQCD, where the sum of exclusive states provides a smaller contribution. This is particularly visible in Figure 4.22, where although the sum of exclusive states agrees with the two inclusive data points below 2 GeV at their respective energies, the combined sum of exclusive states is lower in general. This is largely attributed to the new data for the $\pi^+\pi^-\pi^0\pi^0$ final state, where Figure 4.9 shows that these new data result in a clear reduction of the fitted cross section below 2 GeV.[8] Due to this effect, the previous transition point in [21] between the sum of exclusive states and the inclusive data combination at 2 GeV is no longer the preferred choice in this work, where it is clear from Figure 4.22 that these two different choices for the data input are largely incompatible at this point. A more natural choice for this transition point is 1.937 GeV, where it can be seen from Figure 4.22 that all available data choices at this energy are in agreement within errors. This is further substantiated by Table 4.1, where the value for $a_\mu^{\text{had, LO VP}}$ from the contribution from exclusive states below 1.937 GeV summed with the contribution from the inclusive data combination above 1.937 GeV is, within errors, in agreement with the integrated values of all other choices for the data input. Consequently, in this work, this is chosen to be the transition point between the sum of exclusive states and the inclusive R-ratio data.

4.3.2 Narrow resonances

Following the discussion in Section 2.4.3, the contributions from the experimentally unresolved narrow J/ψ, ψ' and $\Upsilon(1S - 4S)$ resonances in the $c\bar{c}$ and $b\bar{b}$ regions are estimated using the Breit-Wigner resonance parametrisation and added separately to the data compilation. In a separate work [82], the inclusion of R_b data measured by the

[8] Interestingly, as can be seen from Figure 4.22, the sum of exclusive states is in good agreement with the imprecise and, therefore, unused inclusive hadronic cross section data that exist between $1.43 \leq \sqrt{s} \leq 2.00$ GeV. This is in contrast with the findings in the previous analyses [21, 46, 47], which observed that the inclusive data in this range were lower than the sum of exclusive states.

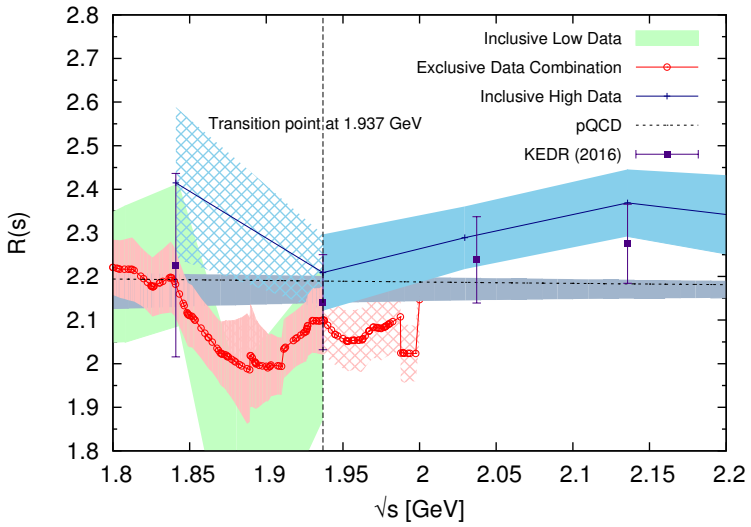

Fig. 4.22: The energy region between $1.8 \leq \sqrt{s} \leq 2.2$ GeV where the fit of inclusive R ratio measurements (light blue band) replaces the sum of exclusive hadronic final states (red band) from 1.937 GeV to 2 GeV. The patterned light blue band and patterned red band show the continuation of the inclusive data combination below 1.937 GeV and the continuation of the exclusive sum above 1.937 GeV respectively. The recent KEDR data are individually marked and included in the inclusive data fit. The light green band shows the data combination of old inclusive hadronic cross section data that exist between $1.43 \leq \sqrt{s} \leq 2.00$ GeV, which were previously discussed in [21] and are not used due to their lack of precision. The estimate from pQCD is included for comparison as a dashed line with an error band which is dominated by the variation of the renormalisation scale μ in the range $\frac{1}{2}\sqrt{s} < \mu < 2\sqrt{s}$.

BaBar collaboration between $10.54 \leq \sqrt{s} \leq 11.20$ GeV [234] has resolved the resonances of the $\Upsilon(5S)$ and $\Upsilon(6S)$ states, removing the need to estimate these structures as was done in [21, 46, 47].[9] These data are shown in Figure 4.23, together with the previously used resonance parametrisations which are clearly very different from the $b\bar{b}$ cross section as measured by BaBar. Note that apart from the CLEO(98) data point [228] at 10.52 GeV, the CLEO(07) data point [233] at 10.538 GeV and the CUSB data point at 11.09 GeV [222], there are no other data in this $b\bar{b}$ resonance region.

For each of the narrow resonances, the cross section is determined according to equation (2.43) (with the electronic width of each resonance undressed according to

[9] In [82], these data were deconvoluted of the effects from initial state radiation (ISR), had the radiative tails of the resonances from the $\Upsilon(1S - 4S)$ states removed and then added to the pQCD estimate of R_{udsc} [238] to be included as an accurate data set in the inclusive channel in this region.

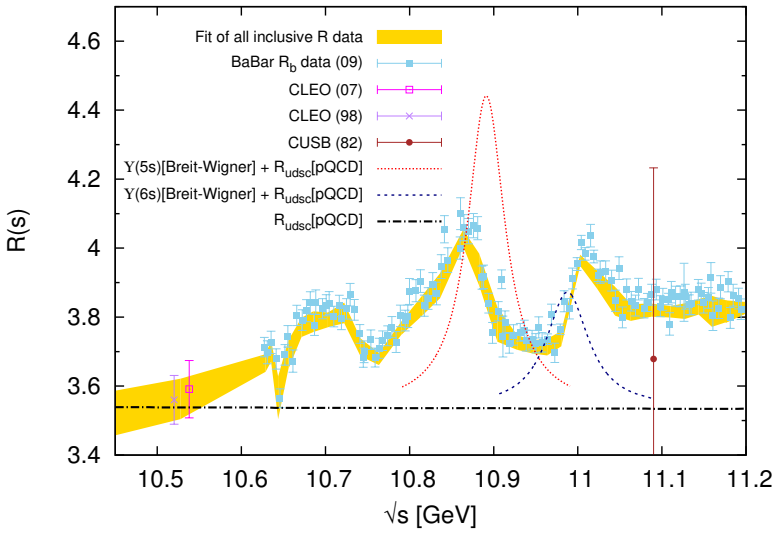

Fig. 4.23: The fit of inclusive R data in the region of the BaBar R_b data, with the BaBar R_b is shown as light blue markers. The resonance structures of the $\Upsilon(5S)$ and $\Upsilon(6S)$ states are clearly visible.

equation (2.10)) and are found to give contributions to a_μ of

$$\begin{aligned} a_\mu^{J/\psi} &= (6.26 \pm 0.19) \times 10^{-10}\,, \\ a_\mu^{\psi'} &= (1.58 \pm 0.04) \times 10^{-10}\,, \\ a_\mu^{\Upsilon(1S)} &= (0.05 \pm 0.00) \times 10^{-10}\,, \\ a_\mu^{\Upsilon(2S)} &= (0.02 \pm 0.00) \times 10^{-10}\,, \\ a_\mu^{\Upsilon(3S)} &= (0.01 \pm 0.00) \times 10^{-10}\,, \\ a_\mu^{\Upsilon(4S)} &= (0.01 \pm 0.00) \times 10^{-10}\,. \end{aligned} \tag{4.63}$$

Here, the uncertainty of each resonance includes an additional VP correction uncertainty due to the undressing of the electronic width.

4.3.3 pQCD

From the discussion in Section 2.4.4, the hadronic R-ratio in the range $11.1985 \leq \sqrt{s} \leq 1000.1985$ GeV is estimated from pQCD using the dedicated program `rhad` [238]. The contribution to a_μ from this is found to be

$$a_\mu^{\text{pQCD}}[11.1985 \leq \sqrt{s} \leq 1000.1985 \text{ GeV}] = (2.07 \pm 0.00) \times 10^{-10}\,, \tag{4.64}$$

where the error on $R(s)$ is determined from the uncertainties of $\alpha_s(M_Z^2)$, the mass of the bottom quark, the mass of the top quark and a variation of the renormalisation scale μ in the range $\frac{1}{2}\sqrt{s} < \mu < 2\sqrt{s}$.

Channel	**Energy range (GeV)**	$a_\mu^{\text{had, LO VP}} \times 10^{10}$	**New data**
Chiral perturbation theory (ChPT) threshold contributions			
$\pi^0\gamma$	$m_\pi \leq \sqrt{s} \leq 0.600$	0.12 ± 0.01	-
$\pi^+\pi^-$	$2m_\pi \leq \sqrt{s} \leq 0.305$	0.87 ± 0.02	-
$\pi^+\pi^-\pi^0$	$3m_\pi \leq \sqrt{s} \leq 0.660$	0.01 ± 0.00	-
$\eta\gamma$	$m_\eta \leq \sqrt{s} \leq 0.660$	0.00 ± 0.00	-
Data based channels ($\sqrt{s} \leq 1.937$ GeV)			
$\pi^0\gamma$	$0.600 \leq \sqrt{s} \leq 1.350$	4.46 ± 0.10	[107]
$\pi^+\pi^-$	$0.305 \leq \sqrt{s} \leq 1.937$	502.97 ± 1.97	[90, 127]
$\pi^+\pi^-\pi^0$	$0.660 \leq \sqrt{s} \leq 1.937$	47.79 ± 0.89	[137]
$\pi^+\pi^-\pi^+\pi^-$	$0.613 \leq \sqrt{s} \leq 1.937$	14.87 ± 0.20	[150, 151]
$\pi^+\pi^-\pi^0\pi^0$	$0.850 \leq \sqrt{s} \leq 1.937$	19.39 ± 0.78	[154]
$(2\pi^+2\pi^-\pi^0)_{\text{no } \eta}$	$1.013 \leq \sqrt{s} \leq 1.937$	0.99 ± 0.09	-
$3\pi^+3\pi^-$	$1.313 \leq \sqrt{s} \leq 1.937$	0.23 ± 0.01	[164]
$(2\pi^+2\pi^-2\pi^0)_{\text{no } \eta\omega}$	$1.322 \leq \sqrt{s} \leq 1.937$	1.35 ± 0.17	-
K^+K^-	$0.988 \leq \sqrt{s} \leq 1.937$	23.03 ± 0.22	[171–173]
$K_S^0K_L^0$	$1.004 \leq \sqrt{s} \leq 1.937$	13.04 ± 0.19	[179, 180]
$KK\pi$	$1.260 \leq \sqrt{s} \leq 1.937$	2.71 ± 0.12	[185, 186]
$KK2\pi$	$1.350 \leq \sqrt{s} \leq 1.937$	1.93 ± 0.08	[179, 185, 187]
$\eta\gamma$	$0.660 \leq \sqrt{s} \leq 1.760$	0.70 ± 0.02	[196]
$\eta\pi^+\pi^-$	$1.091 \leq \sqrt{s} \leq 1.937$	1.29 ± 0.06	[199, 200]
$(\eta\pi^+\pi^-\pi^0)_{\text{no } \omega}$	$1.333 \leq \sqrt{s} \leq 1.937$	0.60 ± 0.15	[201]
$\eta2\pi^+2\pi^-$	$1.338 \leq \sqrt{s} \leq 1.937$	0.08 ± 0.01	-
$\eta\omega$	$1.333 \leq \sqrt{s} \leq 1.937$	0.31 ± 0.03	[201, 202]
$\omega(\to \pi^0\gamma)\pi^0$	$0.920 \leq \sqrt{s} \leq 1.937$	0.88 ± 0.02	[209, 210]
$\eta\phi$	$1.569 \leq \sqrt{s} \leq 1.937$	0.42 ± 0.03	-
$\phi \to$ unaccounted	$0.988 \leq \sqrt{s} \leq 1.029$	0.04 ± 0.04	-
$\eta\omega\pi^0$	$1.550 \leq \sqrt{s} \leq 1.937$	0.35 ± 0.09	[203]
$\eta(\to \text{npp})K\bar{K}_{\text{no } \phi\to K\bar{K}}$	$1.569 \leq \sqrt{s} \leq 1.937$	0.01 ± 0.02	[184, 185]
$p\bar{p}$	$1.890 \leq \sqrt{s} \leq 1.937$	0.03 ± 0.00	[216]
$n\bar{n}$	$1.912 \leq \sqrt{s} \leq 1.937$	0.03 ± 0.01	[219]
Estimated contributions ($\sqrt{s} \leq 1.937$ GeV)			
$(\pi^+\pi^-3\pi^0)_{\text{no } \eta}$	$1.013 \leq \sqrt{s} \leq 1.937$	0.50 ± 0.04	-
$(\pi^+\pi^-4\pi^0)_{\text{no } \eta}$	$1.313 \leq \sqrt{s} \leq 1.937$	0.21 ± 0.21	-
$KK3\pi$	$1.569 \leq \sqrt{s} \leq 1.937$	0.03 ± 0.02	-
$\omega(\to \text{npp})2\pi$	$1.285 \leq \sqrt{s} \leq 1.937$	0.10 ± 0.02	-
$\omega(\to \text{npp})3\pi$	$1.322 \leq \sqrt{s} \leq 1.937$	0.17 ± 0.03	-
$\omega(\to \text{npp})KK$	$1.569 \leq \sqrt{s} \leq 1.937$	0.00 ± 0.00	-
$\eta\pi^+\pi^-2\pi^0$	$1.338 \leq \sqrt{s} \leq 1.937$	0.08 ± 0.04	-
Other contributions ($\sqrt{s} > 1.937$ GeV)			
Inclusive channel	$1.937 \leq \sqrt{s} \leq 11.199$	43.67 ± 0.67	[234, 236, 237]
J/ψ	-	6.26 ± 0.19	-
ψ'	-	1.58 ± 0.04	-
$\Upsilon(1S-4S)$	-	0.09 ± 0.00	-
pQCD	$11.199 \leq \sqrt{s} \leq \infty$	2.07 ± 0.00	-
Total	$m_\pi \leq \sqrt{s} \leq \infty$	693.26 ± 2.46	-

Table 4.2: Summary of the contributions to $a_\mu^{\text{had, LO VP}}$ calculated in this analysis. The first column indicates the hadronic final state or individual contribution, the second column gives the respective energy range of the contribution, the third column states the determined value of $a_\mu^{\text{had, LO VP}}$ and the last column indicates any new data that have been included since [21]. The last row describes the total contribution obtained from the sum of the individual final states, with the uncertainties added in quadrature.

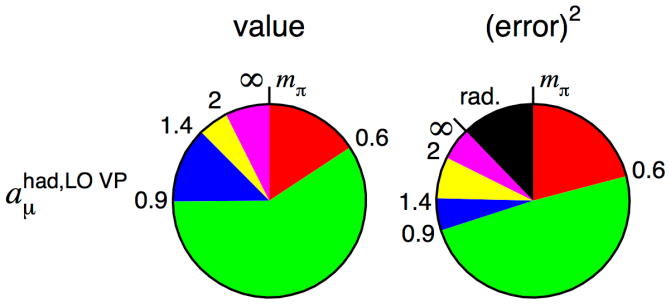

Fig. 4.24: Pie charts showing the fractional contributions to the total mean value (left pie chart) and (error)^2 (right pie chart) of $a_\mu^{\text{had, LO VP}}$ from various energy intervals. The energy intervals for $a_\mu^{\text{had, LO VP}}$ are defined by the boundaries m_π, 0.6, 0.9, 1.43, 2.0 and ∞ GeV. The (error)^2 includes all experimental uncertainties (including all available correlations) and local χ^2_{min}/d.o.f. inflation. The fractional contribution to the (error)^2 from the radiative correction uncertainties are shown in black and indicated by 'rad.'.

4.4 Total contribution of $a_\mu^{\text{had,LOVP}}$ and $a_\mu^{\text{had,NLOVP}}$

Table 4.2 lists all contributions from individual channels contributing to $a_\mu^{\text{had, LO VP}}$, with the corresponding total. From the sum of these contributions, the estimate for $a_\mu^{\text{had, LO VP}}$ from this work is

$$\begin{aligned} a_\mu^{\text{had, LO VP}} &= (693.26 \pm 1.19_{\text{stat}} \pm 2.01_{\text{sys}} \pm 0.22_{\text{vp}} \pm 0.71_{\text{fsr}}) \times 10^{-10} \\ &= (693.26 \pm 2.46_{\text{tot}}) \times 10^{-10} \ , \end{aligned} \tag{4.65}$$

where the uncertainties include all available correlations and local χ^2 inflation. The total error is clearly dominated by the systematic uncertainties, mostly due to the large amount of correlated data that is now present as part of the full data compilation. For the radiative corrections, there is a notable error contribution from the additional FSR correction uncertainty (although relatively small when added in quadrature with the experimental uncertainties). This is due to the conservative choice to take an uncertainty of 1% of the mean value for the possibility of missed FSR for all channels that require an FSR correction (other than $\pi^+\pi^-$) and for which there currently no calculations of these possible effects. The fractional contributions to the total mean value and uncertainty of $a_\mu^{\text{had, LO VP}}$ from various energy intervals is shown in Figure 4.24. Here, the dominance of the energy region below 0.9 GeV for $a_\mu^{\text{had, LO VP}}$ and its uncertainty is clearly evident, with this being predominantly due to the contributions from the $\pi^+\pi^-$ channel. Figure 4.25 shows the contributions from all hadronic final states to the hadronic R-ratio and its uncertainty below 1.937 GeV. Here, the individual final states are displayed separately as well as with the resulting total hadronic

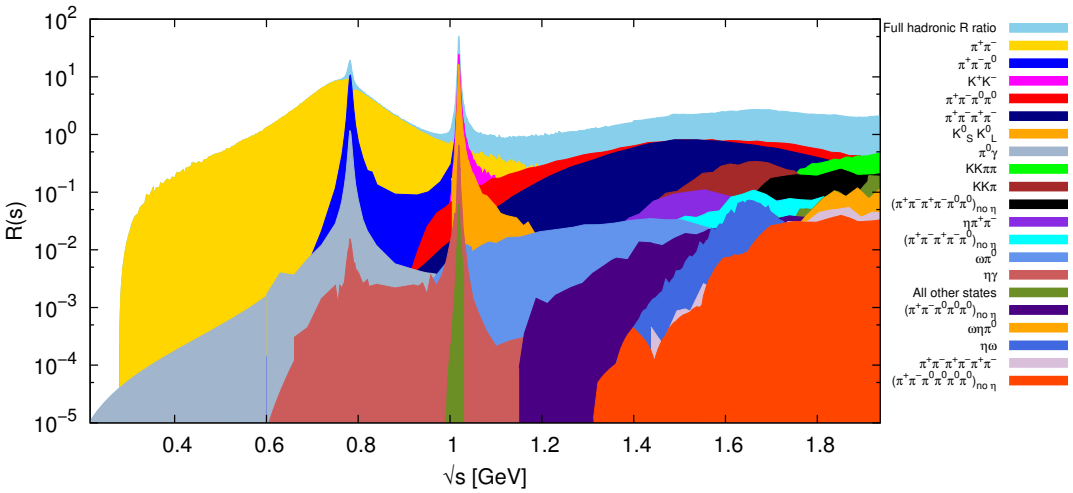

(a) The hadronic R-ratio.

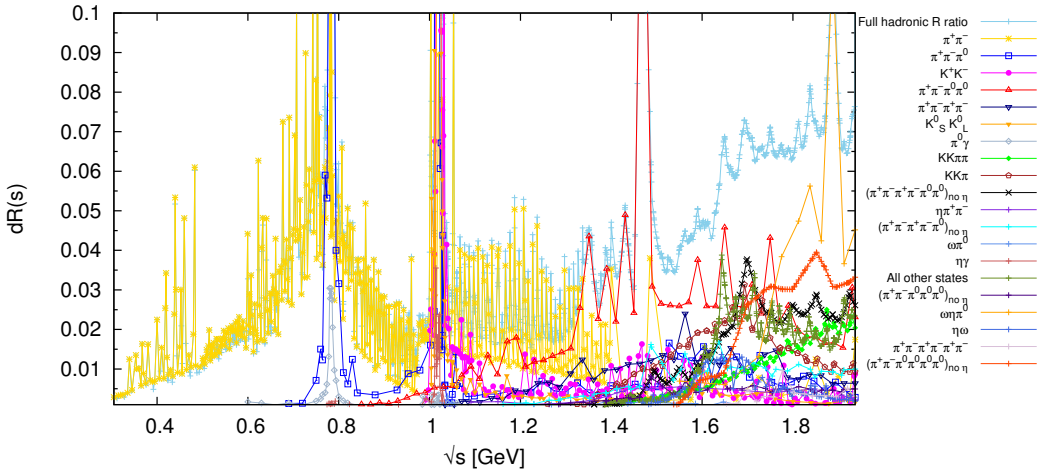

(b) The uncertainty of the hadronic R-ratio.

Fig. 4.25: Contributions to the total hadronic R-ratio from the different final states (upper panel) and their uncertainties (lower panel) below 1.937 GeV. The full R-ratio and its uncertainty is shown in light blue in each plot, respectively. Each final state is included as a new layer on top in decreasing order of the size of its contribution to $a_\mu^{\text{had, LO VP}}$.

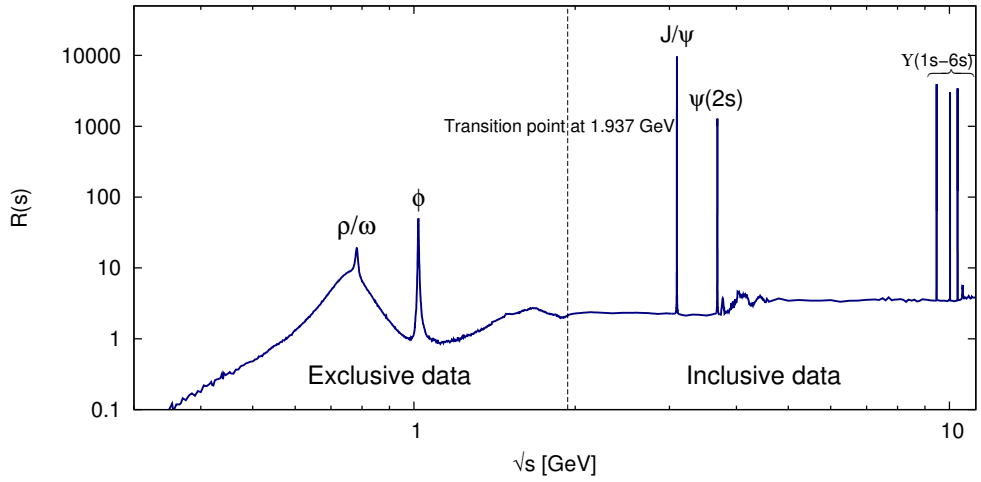

Fig. 4.26: The resulting hadronic R-ratio shown in the range $m_\pi \leq \sqrt{s} \leq 11.1985$ GeV, where the prominent resonances are labelled.

R-ratio. Following the discussion concerning the determination of the hadronic R ratio and its covariance matrix in Section 2.4.5, the full compilation for the hadronic R-ratio is shown in Figure 4.26. The integral over these calculated data are found to yield exactly the same result for $a_\mu^{\text{had, LO VP}}$ as from the sum of all channels given in Table 4.2 and equation (4.65). In addition, checks of the covariance matrix confirm that it is a positive semi-definite matrix, correctly containing the available correlation information for all hadronic channels and, therefore, all the data points in the resulting vector for $R(s)$. The data vector and corresponding covariance matrix of the hadronic R-ratio in the range $m_\pi \leq \sqrt{s} \leq 11.1985$ GeV determined in this work are publicly available upon request from the authors of [87].

Using the same data compilation as described for the calculation of $a_\mu^{\text{had, LO VP}}$, the dispersion integrals for the different classes of diagram for the NLO contributions to $a_\mu^{\text{had,VP}}$ are found according to Section 1.3.2 to give,

$$\begin{aligned}
a_\mu^{\text{had, NLO VP, (a)}} &= (-20.77 \pm 0.03_{\text{stat}} \pm 0.06_{\text{sys}} \pm 0.01_{\text{vp}} \pm 0.03_{\text{fsr}}) \times 10^{-10} \\
&= (-20.77 \pm 0.08_{\text{tot}}) \times 10^{-10}\,, \\
a_\mu^{\text{had, NLO VP, (b, e−loop)}} &= (10.61 \pm 0.02_{\text{stat}} \pm 0.03_{\text{sys}} \pm 0.00_{\text{vp}} \pm 0.01_{\text{fsr}}) \times 10^{-10} \\
&= (10.61 \pm 0.04_{\text{tot}}) \times 10^{-10}\,, \\
a_\mu^{\text{had, NLO VP, (b, }\tau\text{−loop)}} &= (0.01 \pm 0.00_{\text{stat}} \pm 0.00_{\text{sys}} \pm 0.00_{\text{vp}} \pm 0.00_{\text{fsr}}) \times 10^{-10} \\
&= (0.01 \pm 0.00_{\text{tot}}) \times 10^{-10}\,, \\
a_\mu^{\text{had, NLO VP, (c)}} &= (0.34 \pm 0.00_{\text{stat}} \pm 0.01_{\text{sys}} \pm 0.00_{\text{vp}} \pm 0.00_{\text{fsr}}) \times 10^{-10} \\
&= (0.34 \pm 0.01_{\text{tot}}) \times 10^{-10}\,. \qquad (4.66)
\end{aligned}$$

For all the results quoted above, the errors from the individual channels and sources of uncertainty are added in quadrature to determine the total error. Combining the

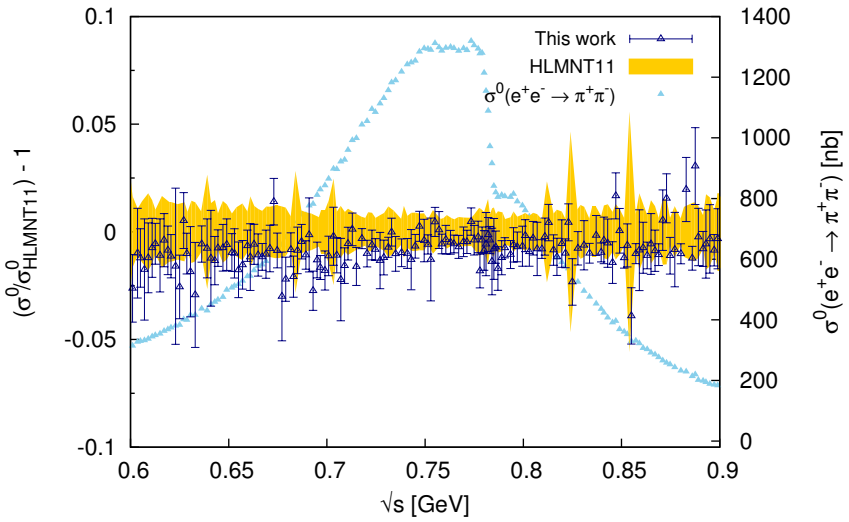

Fig. 4.27: The normalised difference of the clusters of the $\pi^+\pi^-$ data fit from this analysis with respect to those from the HLMNT11 analysis in the range $0.6 \leq \sqrt{s} \leq 0.9$ GeV. The width of the yellow band represents the total uncertainties of the clusters of the HLMNT11 analysis. The $\pi^+\pi^-$ cross section is displayed for reference.

contributions from these different classes, the correlation due to the use of the identical data input for $R(s)$ must be accounted for. With the contribution from class (a) being negative, the correlation between the uncertainty from this class and the other classes results in a reduction in the total uncertainty. Therefore, summing these separate contributions results in total NLO contribution of

$$\begin{aligned} a_\mu^{\text{had, NLO VP}} &= (-9.82 \pm 0.02_{\text{stat}} \pm 0.03_{\text{sys}} \pm 0.01_{\text{vp}} \pm 0.02_{\text{fsr}}) \times 10^{-10} \\ &= (-9.82 \pm 0.04_{\text{tot}}) \times 10^{-10} \ . \end{aligned} \tag{4.67}$$

An evaluation of $\Delta\alpha_{\text{had}}^{(5)}(M_Z^2)$ using the same data compilation as for $a_\mu^{\text{had, LO VP}}$ and $a_\mu^{\text{had, NLO VP}}$ as input into the relevant dispersion integral in equation (2.3) has also been determined as part of this work. A discussion of this and results for $\Delta\alpha_{\text{had}}^{(5)}(M_Z^2)$ and $\alpha(M_Z^2)$ are given in Appendix C.

4.5 Comparison with other works

4.5.1 Comparison with the HLMNT11 evaluation

To understand further how the changes in the data combination/input have altered the estimate of $a_\mu^{\text{had, LO VP}}$ and its uncertainty, a comparison of the results from this analysis and the previous HLMNT11 evaluation [21] is particularly interesting. Table 4.3 gives a channel-by-channel comparison of the two works, highlighting the differences in the individual contributions for each channel and the total sum over their respective energy

Channel	**This work**	**HLMNT11** [21]	**Difference**
Chiral perturbation theory (ChPT) threshold contributions			
$\pi^0\gamma$	0.12 ± 0.01	0.12 ± 0.01	0.00
$\pi^+\pi^-$	0.87 ± 0.02	0.87 ± 0.02	0.00
$\pi^+\pi^-\pi^0$	0.01 ± 0.00	0.01 ± 0.00	0.00
$\eta\gamma$	0.00 ± 0.00	0.00 ± 0.00	0.00
Data based channels ($\sqrt{s} \leq 2$ GeV)			
$\pi^0\gamma$	4.46 ± 0.10	4.54 ± 0.14	-0.08
$\pi^+\pi^-$	502.99 ± 1.97	505.77 ± 3.09	-2.78
$\pi^+\pi^-\pi^0$	47.82 ± 0.89	47.51 ± 0.99	0.31
$\pi^+\pi^-\pi^+\pi^-$	15.17 ± 0.21	14.65 ± 0.47	0.52
$\pi^+\pi^-\pi^0\pi^0$	19.80 ± 0.79	20.37 ± 1.26	-0.57
$(2\pi^+2\pi^-\pi^0)_{\text{no }\eta}$	1.08 ± 0.10	1.20 ± 0.10	-0.12
$3\pi^+3\pi^-$	0.28 ± 0.02	0.28 ± 0.02	0.00
$(2\pi^+2\pi^-2\pi^0)_{\text{no }\eta\omega}$	1.60 ± 0.20	1.80 ± 0.24	-0.20
K^+K^-	23.05 ± 0.22	22.15 ± 0.46	0.90
$K^0_S K^0_L$	13.05 ± 0.19	13.33 ± 0.16	-0.28
$KK\pi$	2.80 ± 0.12	2.77 ± 0.15	0.03
$KK2\pi$	2.42 ± 0.09	3.31 ± 0.58	-0.89
$\eta\gamma$	0.70 ± 0.02	0.69 ± 0.02	0.01
$\eta\pi^+\pi^-$	1.32 ± 0.06	0.98 ± 0.24	0.34
$(\eta\pi^+\pi^-\pi^0)_{\text{no }\omega}$	0.63 ± 0.15	-	0.63
$\eta 2\pi^+2\pi^-$	0.11 ± 0.02	0.11 ± 0.02	0.00
$\eta\omega$	0.31 ± 0.03	0.42 ± 0.07	-0.11
$\omega(\to \pi^0\gamma)\pi^0$	0.88 ± 0.02	0.77 ± 0.03	0.11
$\eta\phi$	0.45 ± 0.04	0.46 ± 0.03	-0.01
$\phi \to$ unaccounted	0.04 ± 0.04	0.04 ± 0.04	0.00
$\eta\omega\pi^0$	0.42 ± 0.10	-	0.42
$\eta(\to \text{npp})K\bar{K}_{\text{no }\phi\to K\bar{K}}$	0.01 ± 0.01	-	0.01
$p\bar{p}$	0.07 ± 0.00	0.06 ± 0.00	0.01
$n\bar{n}$	0.06 ± 0.01	0.07 ± 0.02	-0.01
Estimated contributions ($\sqrt{s} \leq 2$ GeV)			
$(\pi^+\pi^-3\pi^0)_{\text{no }\eta}$	0.53 ± 0.05	0.60 ± 0.05	-0.07
$(\pi^+\pi^-4\pi^0)_{\text{no }\eta}$	0.25 ± 0.25	0.28 ± 0.28	-0.03
$KK3\pi$	0.08 ± 0.03	0.08 ± 0.04	0.00
$\omega(\to \text{npp})2\pi$	0.10 ± 0.02	0.11 ± 0.02	-0.01
$\omega(\to \text{npp})3\pi$	0.20 ± 0.04	0.22 ± 0.04	-0.02
$\omega(\to \text{npp})KK$	0.01 ± 0.00	0.01 ± 0.00	0.00
$\eta\pi^+\pi^-2\pi^0$	0.11 ± 0.05	0.11 ± 0.06	0.00
Other contributions ($\sqrt{s} > 2$ GeV)			
Inclusive channel	41.27 ± 0.62	41.40 ± 0.87	-0.13
J/ψ	6.26 ± 0.19	6.24 ± 0.16	0.02
ψ'	1.58 ± 0.04	1.56 ± 0.05	0.02
$\Upsilon(1S-4S)$	0.09 ± 0.00	0.10 ± 0.00	-0.01
pQCD	2.07 ± 0.00	2.06 ± 0.00	0.01
Total	693.26 ± 2.46	694.91 ± 4.27	-1.64

Table 4.3: Comparison of the contributions to $a_\mu^{\text{had, LO VP}}$ calculated in the HLMNT11 analysis [21] and in this work, where all results are given in units of $a_\mu^{\text{had, LO VP}} \times 10^{10}$. The first column indicates the final state or individual contribution, the second column gives the estimate from this work, the third column states the HLMNT11 estimate and the last column gives the difference between the two evaluations.

Channel	This work	HLMNT11 [21]
$\pi^+\pi^-$	1.3	1.4
$\pi^+\pi^-\pi^0$	2.1	3.0
$\pi^+\pi^-\pi^+\pi^-$	1.8	1.7
$\pi^+\pi^-\pi^0\pi^0$	2.0	1.3
$(2\pi^+2\pi^-\pi^0)_{\text{no }\eta}$	1.0	1.2
$(2\pi^+2\pi^-2\pi^0)_{\text{no }\eta\omega}$	3.5	4.0
K^+K^-	2.1	1.9
$K^0_SK^0_L$	0.8	0.8

Table 4.4: Comparison of the global $\sqrt{\chi^2_{\text{min}}/\text{d.o.f.}}$for the leading and major sub-leading channels determined in the HLMNT11 analysis [21] and in this work. The first column indicates the final state or individual contribution, the second column gives the value from this work, the third column states the HLMNT11 value.

ranges.[10] The largest difference occurs in the $\pi^+\pi^-$ channel, where the mean value in this work is lower by almost 1σ of the HLMNT11 analysis and the uncertainty has reduced by approximately one third. Being the dominant hadronic contribution to a_μ, a similar trend is seen in the final results for $a_\mu^{\text{had, LO VP}}$ and its uncertainty. As described in the in-depth discussion of the 2π contribution in Section 4.1.2, this is largely due to the new, precise and highly correlated radiative return data from KLOE and BESIII and the capability of the new data combination method to utilise the correlations to their full capacity. The global $\sqrt{\chi^2_{\text{min}}/\text{d.o.f.}}$of the leading and major sub-leading channels in this work are compared to those from the HLMNT11 analysis [21] in Table 4.4. The reduction of the global $\sqrt{\chi^2_{\text{min}}/\text{d.o.f.}}$for the $\pi^+\pi^-$ channel further highlights that the data combination for this channel has improved. The energy dependent changes in the resonance region are shown in Figure 4.27, where it can be seen that, as expected from the comparison of the $\pi^+\pi^-$ results in Table 4.3, the data combination from this work is in good agreement with the HLMNT11 analysis but sits lower overall.

The K^+K^- channel shows tension with the HLMNT11 analysis, where the new data in this channel from BaBar [171] and CMD-3 [173] have incurred a large increase in the mean value, whilst also improving the uncertainty despite the small increase in global $\sqrt{\chi^2_{\text{min}}/\text{d.o.f.}}$. This is also the case for the $\pi^+\pi^-\pi^+\pi^-$ channel. Other tensions include the $K^0_SK^0_L$, $\eta\pi^+\pi^-$, $\eta\omega$ and $\omega(\to\pi^0\gamma)\pi^0$ channels, where again, the new, more precise data have resulted in changes outside the quoted HLMNT11 uncertainties. As discussed in Section 4.1.8, the $KK2\pi$ channel exhibits a similar change due to the previously inadequate isospin estimate used in [21]. All other channels are in good agreement

[10]Note that the results for individual contributions to $a_\mu^{\text{had, LO VP}}$ from this work that are listed in Table 4.3 differ from those given earlier in this section and in Table 4.2, as for a comparison with HLMNT11 [21], contributions to $a_\mu^{\text{had, LO VP}}$ from exclusive channels are evaluated up to 2 GeV. However, to consistently compare the final results for $a_\mu^{\text{had, LO VP}}$ between the two works, the total result from this analysis given in Table 4.3 is not determined as the sum of the individual contributions listed above it, but is the final result for $a_\mu^{\text{had, LO VP}}$ calculated in this work using the exclusive channels evaluated up to 1.937 GeV. Summing the values from this work listed in Table 4.3 (i.e. choosing to evaluate the sum of exclusive states from this work up to 2 GeV), results in $a_\mu^{\text{had, LO VP}} = (693.06 \pm 2.45) \times 10^{-10}$.

between the different analyses. Following the discussion in Section 4.1.4, a marked improvement is seen in the $\pi^+\pi^-\pi^0\pi^0$ channel, where the new BaBar data [154] has reduced both the mean value and uncertainty of this final state. It is important to note that this work includes three channels that were not included as part of the HLMNT11 analysis: $(\eta\pi^+\pi^-\pi^0)_{\text{no }\omega}$, $\eta\omega\pi^0$ and $\eta\big(\rightarrow \text{non-purely pionic (npp)}\big)K\bar{K}_{\text{no }\phi\rightarrow K\bar{K}}$, where these final states were previously unmeasured by experiment and not estimated through isospin relations.

Overall, due to the large reduction in the $\pi^+\pi^-$ channel, it is found that the estimate of $a_\mu^{\text{had, LO VP}}$ has decreased between the HLMNT11 analysis and this work, although this decrease is well within the uncertainty of the HLMNT11 estimate. In total, the uncertainty has been reduced by $\sim 42\%$ with respect to the HLMNT11 analysis. This simultaneous reduction in mean value and uncertainty has the effect of increasing the current deviation between a_μ^{SM} and a_μ^{exp}. Similar changes are also observed in the NLO contribution, where the HLMNT11 analysis found $a_\mu^{\text{had, NLO VP}}(\text{HLMNT11}) = (-9.84 \pm 0.07) \times 10^{-10}$.

4.5.2 Comparison with other similar works

The DHMZ group have recently released a new estimate of $a_\mu^{\text{had, LO VP}}$ [45] which, due to a similar data input, is directly comparable with this work and provides insight into how choices with regards to the data combination can affect results. In particular, with the uncertainties of $a_\mu^{\text{had, LO VP}}$ from both this work and the DHMZ17 analysis now being less than 0.5% of the respective mean values, it is important that these differences are understood in order to quantify the reliability of different approaches and results. In [45], the authors provide a channel-by-channel breakdown of their estimates for the different final states, which are compared to the respective estimates from this work in Table 4.5. For the exclusive data channels, the DHMZ group choose to take the contributions from these data up to 1.8 GeV, relying on estimates from pQCD above this (with inflated errors for the pQCD data below the $c\bar{c}$ threshold). As such, the estimates from this work in Table 4.5 have been recalculated to mimic the chosen energy regions of the DHMZ analysis and allow for a consistent comparison.

When comparing the total estimate of $a_\mu^{\text{had, LO VP}}$ from the two analyses, the results seem to be in very good agreement. However, as can be seen from Table 4.5, this masks much larger differences in the estimates from individual channels. The most striking of these is the estimate for the $\pi^+\pi^-$ channel, where there is a tension of slightly more than 1σ between this work and DHMZ17 result. This is unexpected when considering the data input for both analyses are likely to be similar and, therefore, points to marked differences in the way the data are combined. The higher value of the DHMZ17 estimate seems to suggest that their data combination favours the data from the BaBar measurement, with this data set being the only single set that could influence

Channel	This work	DHMZ17 [45]	Difference
Data based channels ($\sqrt{s} \leq 1.8$ GeV)			
$\pi^0\gamma$ (data + ChPT)	4.58 ± 0.10	4.29 ± 0.10	0.29
$\pi^+\pi^-$ (data + ChPT)	503.74 ± 1.96	507.14 ± 2.58	−3.40
$\pi^+\pi^-\pi^0$ (data + ChPT)	47.70 ± 0.89	46.20 ± 1.45	1.50
$\pi^+\pi^-\pi^+\pi^-$	13.99 ± 0.19	13.68 ± 0.31	0.31
$\pi^+\pi^-\pi^0\pi^0$	18.15 ± 0.74	18.03 ± 0.54	0.12
$(2\pi^+2\pi^-\pi^0)_{\text{no }\eta}$	0.79 ± 0.08	0.69 ± 0.08	0.10
$3\pi^+3\pi^-$	0.10 ± 0.01	0.11 ± 0.01	−0.01
$(2\pi^+2\pi^-2\pi^0)_{\text{no }\eta\omega}$	0.77 ± 0.11	0.72 ± 0.17	0.05
K^+K^-	23.00 ± 0.22	22.81 ± 0.41	0.19
$K_S^0K_L^0$	13.04 ± 0.19	12.82 ± 0.24	0.22
$KK\pi$	2.44 ± 0.11	2.45 ± 0.15	−0.01
$KK2\pi$	0.86 ± 0.05	0.85 ± 0.05	0.01
$\eta\gamma$ (data + ChPT)	0.70 ± 0.02	0.65 ± 0.02	0.05
$\eta\pi^+\pi^-$	1.18 ± 0.05	1.18 ± 0.07	0.00
$(\eta\pi^+\pi^-\pi^0)_{\text{no }\omega}$	0.48 ± 0.12	0.39 ± 0.12	0.09
$\eta2\pi^+2\pi^-$	0.03 ± 0.01	0.03 ± 0.01	0.00
$\eta\omega$	0.29 ± 0.02	0.32 ± 0.03	−0.03
$\omega(\to \pi^0\gamma)\pi^0$	0.87 ± 0.02	0.94 ± 0.03	−0.07
$\eta\phi$	0.33 ± 0.03	0.36 ± 0.03	−0.03
$\phi \to$ unaccounted	0.04 ± 0.04	0.05 ± 0.00	−0.01
$\eta\omega\pi^0$	0.10 ± 0.05	0.06 ± 0.04	0.04
$\eta(\to \text{npp})K\bar{K}_{\text{no }\phi\to K\bar{K}}$	0.00 ± 0.01	0.01 ± 0.01	− 0.01*
Estimated contributions ($\sqrt{s} \leq 1.8$ GeV)			
$(\pi^+\pi^-3\pi^0)_{\text{no }\eta}$	0.40 ± 0.04	0.35 ± 0.04	0.05
$(\pi^+\pi^-4\pi^0)_{\text{no }\eta}$	0.12 ± 0.12	0.11 ± 0.11	0.01
$KK3\pi$	$- 0.02 \pm 0.01$	$- 0.03 \pm 0.02$	0.01
$\omega(\to \text{npp})2\pi$	0.08 ± 0.01	0.08 ± 0.01	0.00
$\omega(\to \text{npp})3\pi$	0.10 ± 0.02	0.36 ± 0.01	−0.26
$\omega(\to \text{npp})KK$	0.00 ± 0.00	0.01 ± 0.00	−0.01
$\eta\pi^+\pi^-2\pi^0$	0.03 ± 0.01	0.03 ± 0.01	0.00
Other contributions			
J/ψ	6.26 ± 0.19	6.28 ± 0.07	−0.02
ψ'	1.58 ± 0.04	1.57 ± 0.03	0.01
$\Upsilon(1S-4S)$	0.09 ± 0.00	-	0.09**
Contributions by energy region			
$1.8 \leq \sqrt{s} \leq 3.7$ GeV	34.54 ± 0.56 (data)	33.45 ± 0.65 (pQCD)***	1.09
$3.7 \leq \sqrt{s} \leq 5.0$ GeV	7.33 ± 0.11 (data)	7.29 ± 0.03 (data)	0.04
$5.0 \leq \sqrt{s} \leq 9.3$ GeV	6.62 ± 0.10 (data)	6.86 ± 0.04 (pQCD)	−0.24
$9.3 \leq \sqrt{s} \leq 12.0$ GeV	1.12 ± 0.01 (data+pQCD)	1.21 ± 0.01 (pQCD)	−0.09
$12.0 \leq \sqrt{s} \leq 40.0$ GeV	1.64 ± 0.00 (pQCD)	1.64 ± 0.00 (pQCD)	0.00
> 40.0 GeV	0.16 ± 0.00 (pQCD)	0.16 ± 0.00 (pQCD)	0.00
Total	693.3 ± 2.5	693.1 ± 3.4	0.2

*DHMZ have not removed the decay of η to pionic states which incurs a double counting of this contribution with the $KKn\pi$ channels.
**DHMZ include the contributions from the Υ resonances in the energy region $9.3 \leq \sqrt{s} \leq 12.0$ GeV.
***DHMZ have inflated errors to account for differences between data and pQCD.

Table 4.5: Comparison of the contributions to $a_\mu^{\text{had, LO VP}}$ calculated by DHMZ17 and in this work, where all results are given in units $a_\mu^{\text{had, LO VP}} \times 10^{10}$. The first column indicates the final state or individual contribution, the second column gives the estimate from this work, the third column states the DHMZ17 estimate and the last column gives the difference between the two evaluations. For the final states in this work that have low energy contributions estimated from chiral perturbation theory (see [46]), the contributions from these regions have been added to the contributions from the respective data.

the mean value of the $\pi^+\pi^-$ channel to be as high. This behaviour is similar to the result obtained from combining the $\pi^+\pi^-$ data using only a simple weighted average as discussed in Section 4.1.2. In turn, this effect is compensated by other major sub-leading final states having larger estimates in this work compared to the DHMZ17 analysis. Specifically, the $\pi^+\pi^-\pi^0$, $\pi^+\pi^-\pi^+\pi^-$ and $K^0_S K^0_L$ estimates are noticeably lower in the DHMZ17 analysis. In addition, there is tension in the region between $1.8 \leq \sqrt{s} \leq 3.7$ GeV, where the choice to use data in this region has a higher integrated contribution to $a_\mu^{\text{had, LO VP}}$ than the DHMZ17 estimate from pQCD. This is particularly significant when reconsidering Figure 4.22, where it was observed that the sum of exclusive states from in the range $1.8 \leq \sqrt{s} \leq 2.0$ GeV has a cross section that is lower than the estimate from pQCD. The differences seen in Table 4.5 above 1.8 GeV are then caused by cross section data below the charm production threshold being higher than pQCD (see Figure 4.20) and lower than pQCD above it (see Figure 4.21). It should be noted that the estimate for the $\omega(\to \text{npp})3\pi$ final state from isospin relations, although only a small contribution to $a_\mu^{\text{had, LO VP}}$, exhibits a significant difference between the two analyses, suggesting a different relation has been used in the DHMZ17 analysis than in this work.

As well as the DHMZ analysis, an updated work by F. Jegerlehner (FJ17) [36] resulted in an estimate of $a_\mu^{\text{had, LO VP}}(\text{FJ17}) = (688.07 \pm 4.14) \times 10^{-10}$ based on the available e^+e^- data. Within errors, this result is in agreement with both this work and the DHMZ17 analysis. Interestingly, unlike the comparison with DHMZ17, the two-pion contribution in the energy range $0.316 \leq \sqrt{s} \leq 2.0$ GeV is found in the FJ17 analysis to be $a_\mu^{\pi^+\pi^-}(\text{FJ17}) = (502.16 \pm 2.44) \times 10^{-10}$ [239], which is in good agreement with the estimate from this work in the same energy range of $a_\mu^{\pi^+\pi^-}(\text{This work}) = (501.68 \pm 1.71) \times 10^{-10}$. However, a more detailed comparison with the estimates of other channels determined in [36,239] is not possible as the FJ17 analysis chooses to estimate certain resonance contributions using available parametrisations [16] instead of using the available data. A comparison of recent and previous evaluations of $a_\mu^{\text{had, LO VP}}$ determined from $e^+e^- \to$ hadrons cross section data is shown in Figure 4.28, which highlights the agreement between the different works and the improvement in the precision of the respective analyses.

4.6 The SM prediction of the anomalous magnetic moment of the muon, a_μ^{SM}

Following the review of the contributions to a_μ from the different sectors of the SM in Section 1.2.2, the new results for $a_\mu^{\text{had, LO VP}}$ and $a_\mu^{\text{had, NLO VP}}$ determined in this work allow for an updated determination of a_μ^{SM}. Summarising the different SM results

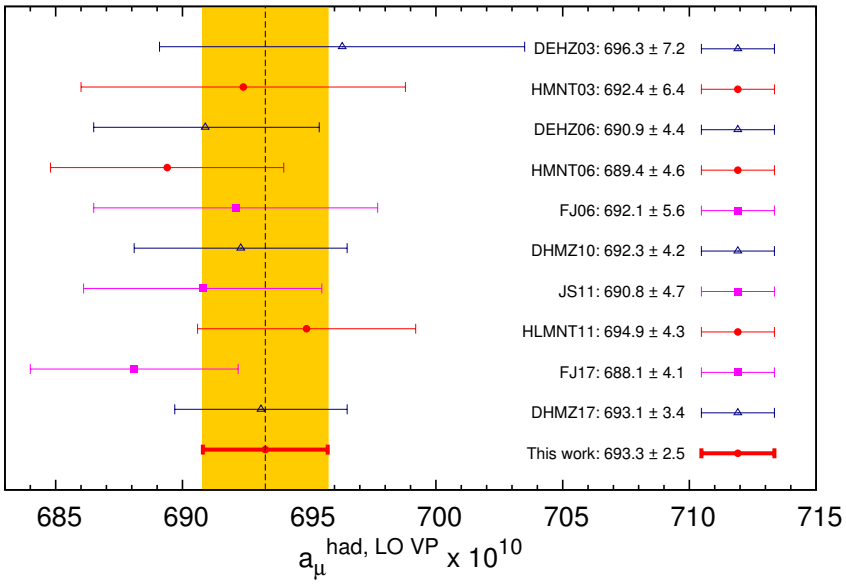

Fig. 4.28: Comparison of recent and previous evaluations of $a_\mu^{\text{had, LO VP}}$ determined from $e^+e^- \to$ hadrons cross section data. The analyses listed in chronological order are: DEHZ03 [48], HMNT03 [46], DEHZ06 [49], HMNT06 [47], FJ06 [50], DHMZ10 [51], JS11 [52], HLMNT11 [21], FJ17 [36] and DHMZ17 [45]. The prediction from this work defines the uncertainty band that the other analyses are compared to.

discussed previously, the QED contribution gives [9, 22]

$$a_\mu^{\text{QED}} = (11\ 658\ 471.8971 \pm 0.007) \times 10^{-10}\,. \tag{4.68}$$

From [34], the EW contribution is

$$a_\mu^{\text{EW}} = (15.36 \pm 0.10) \times 10^{-10}\,. \tag{4.69}$$

For the hadronic vacuum polarisation contributions, the leading order and next-to-leading order contributions have been calculated in this work. The LO contribution, from equation (4.65), was found to be $a_\mu^{\text{had, LO VP}} = (693.26 \pm 2.46) \times 10^{-10}$ and the NLO was given in equation (4.67) as $a_\mu^{\text{had, NLO VP}} = (-9.82 \pm 0.04) \times 10^{-10}$. From [35] the NNLO hadronic vacuum polarisation contribution was found to be $a_\mu^{\text{had, NNLO VP}} = (1.24 \pm 0.01) \times 10^{-10}$. Summing these, the total contribution to the anomalous magnetic moment from the hadronic vacuum polarisation is

$$a_\mu^{\text{had, VP}} = (684.68 \pm 2.42) \times 10^{-10}\,. \tag{4.70}$$

It should be noted that the negative NLO contribution results in an anti-correlation between its uncertainty and the uncertainty from the LO contribution, consequently resulting in a slight reduction in the overall uncertainty that has been incorporated into equation (4.70). The chosen estimate for the LO hadronic LbL contributions in

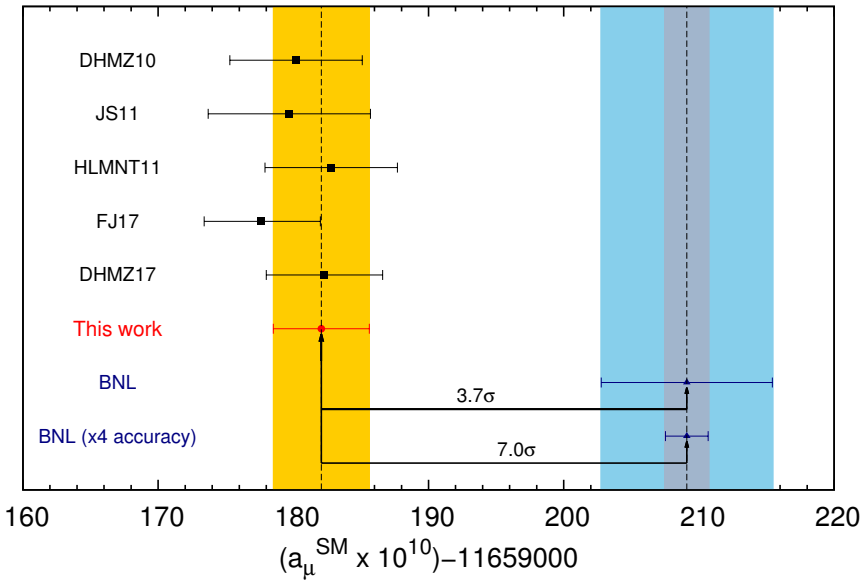

Fig. 4.29: A comparison of recent and previous evaluations of $a_\mu^{\rm SM}$. The analyses listed in chronological order are: DHMZ10 [51], JS11 [52], HLMNT11 [21], FJ17 [36] and DHMZ17 [45]. The prediction from this work defines the uncertainty band that other analyses are compared to. The current uncertainty on the experimental measurement [13–16] is given by the light blue band. The light grey band represents the hypothetical situation of the new experimental measurement at Fermilab yielding the same mean value for $a_\mu^{\rm exp}$ as the BNL measurement but achieving the projected four-fold improvement in its uncertainty [17].

this work is $a_\mu^{\rm had,\,LO\,LbL} = (9.8 \pm 2.6) \times 10^{-10}$ [43]. Summing this with the estimate for the NLO contributions of $a_\mu^{\rm had,\,NLO\,LbL} = (0.3 \pm 0.2) \times 10^{-10}$ [40], results in a total hadronic LBL estimate of

$$a_\mu^{\rm had,\,LbL} = (10.1 \pm 2.6) \times 10^{-10}\,. \tag{4.71}$$

Following equation (1.17) and equation (1.30), the sum of all the sectors of the SM results in a total value of the anomalous magnetic moment of the muon of

$$a_\mu^{\rm SM} = (11\ 659\ 182.04 \pm 3.56) \times 10^{-10}\,, \tag{4.72}$$

where the error is determined from the uncertainties of the individual SM contributions, added in quadrature. Comparing this with the current experimental measurement given in equation (1.19) results in a deviation of

$$\Delta a_\mu = (27.06 \pm 7.26) \times 10^{-10}\,, \tag{4.73}$$

corresponding to a 3.7σ discrepancy. This result is compared with other determinations of $a_\mu^{\rm SM}$ in Figure 4.29. Importantly, it can be seen here that should the new Muon $g-2$ experiment at Fermilab measure $a_\mu^{\rm exp}$ to have the same mean value as equation (1.30)

SM contribution	**HLMNT11** [21]	**This work**
QED	11658471.8 ± 0.0	11658471.9 ± 0.0
EW	15.4 ± 0.2	15.4 ± 0.1
had LO VP	694.9 ± 4.3	693.4 ± 2.5
had NLO VP	-9.8 ± 0.1	-9.8 ± 0.0
had NNLO VP		1.2 ± 0.0
had LO LbL	10.5 ± 2.6	9.8 ± 2.6
had NLO LbL		0.3 ± 0.2
Theory total	11659182.8 ± 4.9	11659182.0 ± 3.6
Experiment	11659209.1 ± 6.3	11659209.1 ± 6.3
Δa_μ	26.1 ± 8.0 (3.3σ)	27.1 ± 7.3 (3.7σ)

Table 4.6: Comparison of the contributions to a_μ^{SM} given in the HLMNT11 analysis [21] and in this work, where all results are given in units of $a_\mu \times 10^{10}$. The first column indicates the individual SM contribution, the second column states the HLMNT11 value and the last column gives the value from this work. The references for the evaluations for the individual SM contributions used to determine a_μ^{SM} in the HLMNT11 analysis are QED [240, 241], EW [32] and had LO LbL [37], with the hadronic VP contributions being calculated in [21].

but achieve the projected four-fold improvement in the experimental uncertainty [17], the $(g-2)_\mu$ discrepancy would increase to 7.0σ. It should be noted that although, as stated in Section 4.5.2, the DHMZ17 estimate for $a_\mu^{\mathrm{had,\,LO\,VP}}$ [45] is lower than the value obtained in this work, the estimate of a_μ^{SM} from DHMZ17 is higher than the estimate from this analysis as DHMZ17 choose to use the estimate for the hadronic light-by-light contribution of $a_\mu^{\mathrm{had,LbL}} = (10.5 \pm 2.6) \times 10^{-10}$ [37].

A comparison with the HLMNT11 estimate given in equation (1.27) shows an improvement in the total uncertainty of a_μ^{SM} of $\sim 27\%$. Table 4.6 compares the contributions from the individual sectors of the SM as given in the HLMNT11 analysis and in this work. Whereas in [21], the five-loop QED contributions were only estimated from [240], the full calculation of these contributions in [9, 22] has led to the small change in the QED estimate. For the EW sector, the now relatively well-known Higgs mass [16] has halved the uncertainty on this contribution since [21]. The comparison of the differences in $a_\mu^{\mathrm{had,\,LO\,VP}}$ and $a_\mu^{\mathrm{had,\,NLO\,VP}}$ between this work and the HLMNT11 analysis have been discussed in detail in Section 4.5.1. Importantly, although there has been a reduction of $\sim 1.5 \times 10^{10}$ in $a_\mu^{\mathrm{had,\,LO\,VP}}$ between the HLMNT11 analysis and this work, this difference is largely cancelled by the newly estimated NNLO VP contributions that were not included in [21]. The value for the LO LbL contributions has reduced due to the re-evaluation of the contribution to $a_\mu^{\mathrm{had,LbL}}$ from axial exchanges as discussed in Section 1.2.2, but this difference is also alleviated by the inclusion of the previously missing NLO LbL contributions. Notably, the uncertainty of $a_\mu^{\mathrm{had,\,LO\,VP}}$ is now smaller than the uncertainty of $a_\mu^{\mathrm{had,\,LO\,LbL}}$, making the hadronic light-by-light sector the largest error contribution to a_μ^{SM} for the first time. In total, the changes in

all the sectors of the SM have resulted in an increase in Δa_μ and, therefore, the $(g-2)_\mu$ discrepancy, largely due to the reduction in the uncertainty of $a_\mu^{\mathrm{had,\,VP}}$ as calculated in this work.

Chapter 5

Conclusions

5.1 Summary

The anomalous magnetic moment of the muon, $a_\mu = (g-2)_\mu/2$, provides a stringent test of the Standard Model (SM), where the $\sim 3.5\sigma$ (or higher) discrepancy between the experimental measurement $a_\mu^{\rm exp}$ and the SM prediction $a_\mu^{\rm SM}$ could be an indication of the existence of new physics beyond the SM. The uncertainty of $a_\mu^{\rm SM}$ is completely dominated by the hadronic contributions. This analysis has completed a full re-evaluation of the hadronic vacuum polarisation contributions to the anomalous magnetic moment of the muon, $a_\mu^{\rm had,\,VP}$. These quantities have been determined using the available $e^+e^- \to$ hadrons cross section data as input into corresponding dispersion relations, with an aim to achieve both accurate and reliable results from a predominantly data driven analysis.

Since the analysis preceding this work [21], all aspects concerning the radiative corrections of the data and the data combination have been reassessed in this work. The vacuum polarisation corrections have been updated and are found to have less effect on the data combination than in previous analyses due to the large quantity of data that have already been released as the bare cross section with FSR included, $\sigma^0_{{\rm had},\gamma}(s)$. This is also true of the FSR corrections, where for the $\pi^+\pi^-$ channel the overall impact of the FSR corrections and the corresponding additional radiative correction uncertainty on $a_\mu^{\pi^+\pi^-}$ is greatly reduced. In addition, studies into the previously applied FSR corrections for the K^+K^- channel have shown these to be an overestimate in this final state, as the possibility of FSR is limited by highly restricted phase space and, therefore, no FSR correction or additional uncertainty is now applied in this channel. For the data combination, a re-analysis of the previously used non-linear χ^2-minimisation highlighted the potential for systematic bias and that the method's reliance on fitting energy independent renormalisation factors prevented the use of correlated uncertainties to their full capacity. Instead, the data are now combined using an iterative, linear χ^2-minimisation developed in this work from a method that has been advocated to be free of bias and that has been studied in detail. Importantly, this data combination

method now allows for the full use of any available correlated statistical and systematic uncertainties, robustly incorporating them into the determination of both the resulting mean value and corresponding error.

The three precision measurements of the cross section $\sigma\big(e^+e^- \to \pi^+\pi^-\gamma(\gamma)\big)$ using initial state radiation by the KLOE collaboration provide an important input for the prediction of the hadronic contributions to the anomalous magnetic moment of the muon. These measurements are correlated for both statistical and systematic uncertainties and, therefore, the simultaneous use of these measurements requires covariance matrices that fully describe the correlations. The matrices constructed for this purpose prior to this work were found to be mathematically unstable and their construction had to be reassessed. To fully understand the correlations, it was necessary to re-open the experimental analyses of all three measurements. At each experimental correction stage, any corresponding statistical or systematic uncertainty was scrutinised and, in some cases, re-evaluated. This allowed for the improvement of the calculated cross sections and for correct covariance matrices to be constructed, which have been found to satisfy the necessary properties of positive semi-definite matrices. The use of these matrices has allowed for the determination of a combined KLOE measurement for $\sigma\big(e^+e^- \to \pi^+\pi^-\gamma(\gamma)\big)$ and yields a two-pion contribution to the muon magnetic anomaly in the energy range $0.3162 < \sqrt{s} < 0.9747$ GeV of $a_\mu^{\pi^+\pi^-} = (489.8 \pm 1.7_{\rm stat} \pm 4.8_{\rm sys}) \times 10^{-10}$.

For the full calculation of $a_\mu^{\rm had,\,LO\,VP}$ and $a_\mu^{\rm had,\,NLO\,VP}$, the large quantity of new hadronic cross section data (coupled with the changes in the data combination method) have resulted in improved estimates for nearly all hadronic channels. This is particularly true for the $\pi^+\pi^-$ channel, where the precision of this final state has improved by approximately one third compared to [21], with $a_\mu^{\pi^+\pi^-}$ from both analyses in very good agreement. Significant progress is also observed in the major sub-leading 3π, 4π and $K\bar{K}$ channels. Importantly, the inclusion of recent cross section measurements of neutral final states in the $KK\pi$ and $KK2\pi$ channels has removed the need to rely on isospin relations to estimate these final states. In addition, new inclusive hadronic R-ratio data from the KEDR collaboration have improved the inclusive data combination. In particular, they have provided the opportunity to reconsider the transition region between the sum of exclusive states and the inclusive data, which has resulted in the transition point being chosen to be at 1.937 GeV in this work, where the different choices for the data input in this point are in agreement within errors.

Importantly, the advancements of the data compilation in this work have yielded, for the first time, the full hadronic R-ratio and its covariance matrix in the energy range $m_\pi \leq \sqrt{s} \leq 11.2$ GeV. Using these combined data, this analysis found $a_\mu^{\rm had,\,LO\,VP} = (693.26 \pm 2.46) \times 10^{-10}$ and $a_\mu^{\rm had,\,NLO\,VP} = (-9.82 \pm 0.04) \times 10^{-10}$. This has resulted in a new estimate for the Standard Model prediction of $a_\mu^{\rm SM} = (11\,659\,182.04 \pm 3.56) \times 10^{-10}$,

which deviates from the current experimental measurement by 3.7σ.

5.2 Future prospects

For the hadronic vacuum polarisation contributions, there is scope to further improve the estimates. With regards to the prospect of new data, measurements of the $\pi^+\pi^-$ cross section are planned to be released in the near future from BaBar [242], CMD-3 [243], SND [244] and, possibly, BELLE-2 [245]. With the $\pi^+\pi^-$ channel still providing the largest error contribution to $a_\mu^{\text{had, LO VP}}$, new data here will be invaluable to the overall determination of the hadronic VP contributions. In addition, these new data may shed light on the issues regarding the tensions between the BaBar data and the other measurements, especially those between the BaBar data and the KLOE combination. Should the forthcoming high statistics cross section measurement by the BaBar collaboration agree more with the other measurements in this channel, discarding the current BaBar data may be a consideration. New data for both the $\pi^+\pi^-\pi^0$ and $\pi^+\pi^-\pi^0\pi^0$ channels would benefit both of these contributions, where new data for $\pi^+\pi^-\pi^0$ could reduce the effects of the local χ^2_{min}/d.o.f. error inflation and additional new data is needed for $\pi^+\pi^-\pi^0\pi^0$ to accompany the lone modern measurement from BaBar in this channel. For the K^+K^- channel, the reanalysis of the omitted CMD-2 data will be crucial in further understanding the increase of the cross section at the ϕ peak due to the new BaBar and CMD-3 data in this region. Data to reduce the reliance on isospin, as with the $KKn\pi$ channels in this work, are vital to drive this analysis towards the preferential data-based determination. Although the relative size of the remaining isospin estimated contributions are small, the differences in the $KK2\pi$ channel between the data and the isospin estimate have highlighted how these relations can produce inadequate representations of the cross section. Efforts are also currently being made to measure new inclusive R-ratio data by BESIII [246] and the experiments at Novosibirsk (SND, CMD-3, KEDR). In particular, a detailed analysis at Novosibirsk intends to determine the inclusive R-ratio at energies lower than 2 GeV [247], which would allow further study into the choices of the transition region between the sum of exclusive states and the inclusive data.

Further understanding and inclusion of correlations are paramount for future determinations of $a_\mu^{\text{had,VP}}$. This stems not only from the experimental data itself (although this is important for future data), but also to obtain a better understanding of how the correlated uncertainties should be included in these calculations. In this work, all available experimental correlations have been included and allowed to influence the data combination to their full capacity. This is seemingly not the case for the DHMZ17 approach [45], suggested by the higher value for $a_\mu^{\pi^+\pi^-}$ obtained in their work. With both these works quoting uncertainties for $a_\mu^{\text{had, LO VP}}$ that are smaller than $\sim 0.5\%$, it is important to understand the origins of these differences. These efforts are currently

under-way as part of the *Muon* $g-2$ *Theory Initiative* [248], where the dedicated groups involved within it show great progress in studying these differences between these and other similar analyses. The correlations between data in different channels, which are not included in this work as the available information is not available, are also a future step towards improving the hadronic vacuum polarisation contributions. However, to allow these correlations to influence the mean value in a full determination of the hadronic R-ratio would require a new (or extended) data combination method that allowed for a global fit of all channels simultaneously.

The concept of employing a new data combination method is further motivated by the limitations of the χ^2 minimisation approach used in this work. Specifically, the χ^2 minimisation method assumes the experimental uncertainties to be Gaussian which, in general, is not true for all experimental data. Although up until this point, most experimental uncertainties have been made available under the same assumption (i.e. symmetric with respect to the covariance matrix), the advancement of both the experimental analyses and the determinations of $a_\mu^{\text{had, VP}}$ to include non-Gaussian uncertainties would require a more developed data combination method than the more simplistic χ^2 minimisation.

Alternative approaches to determine $a_\mu^{\text{had, LO VP}}$ are developing at a promising rate. Lattice QCD determinations, in particular, are rapidly improving [249–251]. Recent work that combines data from lattice QCD with those from experimental R-ratio data have already provided extremely accurate results that are in good agreement with the current estimates from the dispersive method [251]. Furthermore, efforts to experimentally measure $a_\mu^{\text{had, LO VP}}$ are progressing [252, 253]. By measuring the running of the QED coupling in a high precision, space-like μ-e scattering experiment and subtracting the theoretical determinations of all contributions to $\Delta\alpha(q^2)$ other than the hadronic contributions would result in the experimentally measured quantity $\Delta\alpha_{\text{had}}(q^2)$, which can be used as input into an alternative dispersion relation to determine $a_\mu^{\text{had, LO VP}}$ [239]. This would provide the first direct experimental measurement of purely hadronic vacuum polarisation contributions to a_μ and would be an alternative check of the results from the dispersive approach.

In general, the predictions for a_μ^{SM} have been further scrutinised and are well established. In particular, the improvements in the uncertainty are on track in preparation for the new experimental results from Fermilab and J-PARC, with the *Muon* $g-2$ *Theory Initiative* showing great promise in improving the estimate of a_μ^{SM} further. This is further driven by the fact that the result for $a_\mu^{\text{had, VP}}$ determined in this analysis is the first estimate of the hadronic vacuum polarisation contribution that is more precise than the currently quoted uncertainties for $a_\mu^{\text{had, LbL}}$. Should any or all these advances reduce the uncertainty of $a_\mu^{\text{had, VP}}$ even further, the improvement of the hadronic light-by-light estimates will become particularly crucial. Importantly, however, it should be

noted that there is no indication thus far that the SM prediction does not deviate with the current experimental measurement by more than 3σ. Given these developments in improving the Standard Model prediction of a_μ and the formidable progress made by the new Muon $g-2$ experiments at Fermilab and J-PARC, the prospects of either establishing the existence of new physics contributing to a_μ, or to rule out many new physics scenarios, are highly compelling.

Appendix A

Measurement of the kicker pulse of the Muon $g-2$ experiment (E989)

A.1 The kicker system

At the Muon $g-2$ experiment at Fermilab [17], the muon beam is injected into the storage ring through the inflector onto an orbit that is displaced by 77mm radially outward from the ideal orbit of the storage ring. In order to direct the beam back onto the correct trajectory requires a 'kick' at the point where the muons on the displaced trajectory cross the path of the ideal orbit. This occurs at approximately 90° around the storage ring from the point where the muon beam exits the inflector, as can be seen in Figure A.2. The crossing angle at this point is 10.8 mrad, requiring an angular kick of 10.8 ± 0.4 mrad to maximise the muon capture efficiency [17]. To achieve this with an additional error of margin, the kicker for the Muon g-2 experiment was designed to reach a 14.0 mrad kick. Achieving a 10.8 - 14.0 mrad kick requires the kicker to reach a magnetic field strength of 200-280 Gauss (0.020-0.028 Tesla) over the 120ns that the muon beam pulse traverses the domain of the kicker and then return to zero before the muon beam again reaches the kicker 149ns later, as shown in Figure A.1.

The kicker itself is comprised of three 1.27m long magnets (which shall be denoted as K1, K2 and K3, with K1 being the magnet closest to the inflector that the muons reach first) that reside inside the storage ring at the location indicated in Figure 1.2. The requirements of field strength, pulse shape and time must be achieved by all three magnets in order to deliver the nominal kick. A voltage of ~ 55 kV delivers the 4.5kA current to the magnet plates of K1, K2 and K3 to produce the 200-280 Gauss field. To generate this, each kicker magnet system consists of:

- A high voltage (HV) power supply and charging circuit to produce the required ~ 55 kV.
- A thyratron switch to form the current as a pulse.

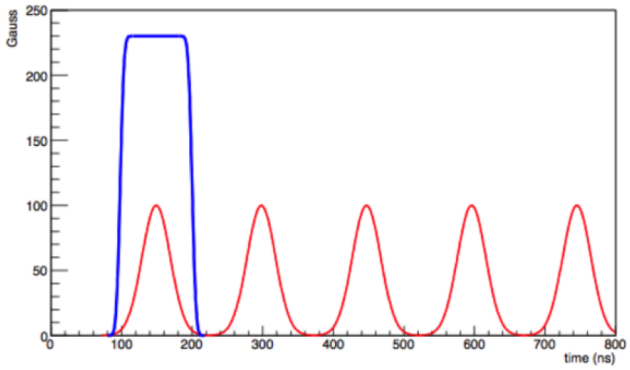

Fig. A.1: The ideal kicker pulse for the E989 experiment (blue) given in Gauss and the overlapped length of the corresponding muon beam cycle with 149 ns period (red) given in ns. This figure has been taken directly from [254].

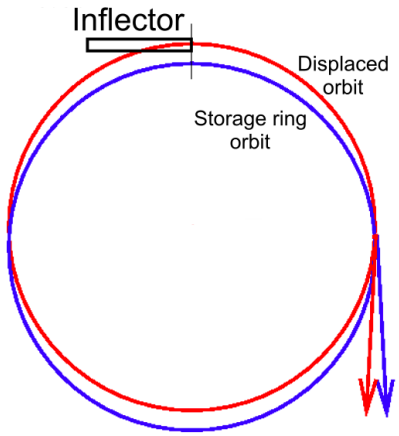

Fig. A.2: The displaced orbit of the muon beam that enters the storage ring from the inflector (red) and the required orbit (blue). This figure has been altered from [17].

- A transmission line (triaxial blumlein) to deliver the pulse to the kicker magnet.
- A load resistor ('bazooka' canister) to terminate the transmission and provide the required 4.5kA current to the kicker magnet.
- The kicker magnet plate which generates the 200-280 Gauss field.

The magnetic field map associated with the kicker magnet plates is shown in Figure A.3.

A.2 Measuring the kicker field using a Faraday magnetometer

A.2.1 The Faraday magnetometer: concept

It is essential that the effectiveness of the kicker field is tested in order to maximise the muon capture efficiency of the muon g-2 experiment. In order to do this, a Faraday

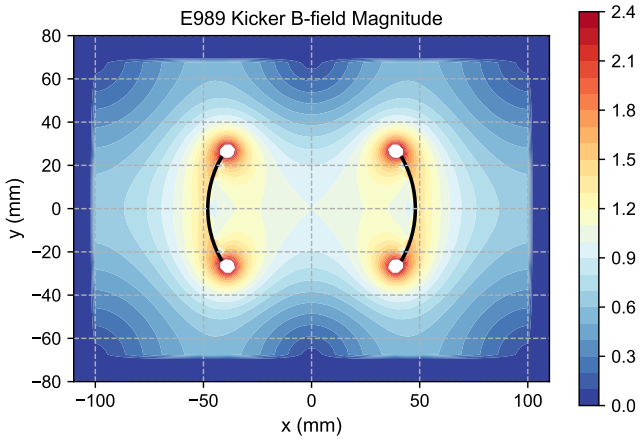

Fig. A.3: The relative magnitude of the magnetic field lines associated with the kicker magnet plates of the E989 experiment [256]. This diagram is taken as a slice of the radial direction of the beam, which is the direction of the magnetic field generated by the kicker magnet plates.

magnetometer can be used to measure the time-dependent field. This device makes use of the consequences of the Faraday effect, which states that when linearly polarized light passes through a Faraday rotator medium, the polarization angle rotates proportionally to the strength of the magnetic field B. The relationship between the plane of polarisation and the field B is given by

$$\Delta\theta = VBd\,, \tag{A.1}$$

where $\Delta\theta$ is the rotation angle of the plane of polarisation, V is the Verdet constant which describes the strength of the Faraday effect for that medium and d is the distance that the light travels through the medium. The chosen medium for the Faraday rotator is a terbium gallium garnet (TGG) crystal [255], which has a particularly high Verdet constant (≈ 134 rad $\mathrm{T}^{-1}\mathrm{m}^{-1}$ for 632 nm light) and is therefore more sensitive to the magnetic field.

The basic concept of the Faraday magnetometer is as follows. The TGG crystal is placed inside the B field to be measured and a laser light is passed through it. As the laser passes through the crystal, the B field acting on the crystal causes a rotation of the plane of polarisation of the laser light. The light is then directed through a polariser. By measuring the intensity after it has passed through the polariser, the change in the angle of polarisation can be determined from Malus' Law,

$$I = I_0 \cos^2\theta\,, \tag{A.2}$$

which states that the intensity of the light after passing through the polariser I is simply given by the cosine squared of the angle of polarisation θ multiplied by the

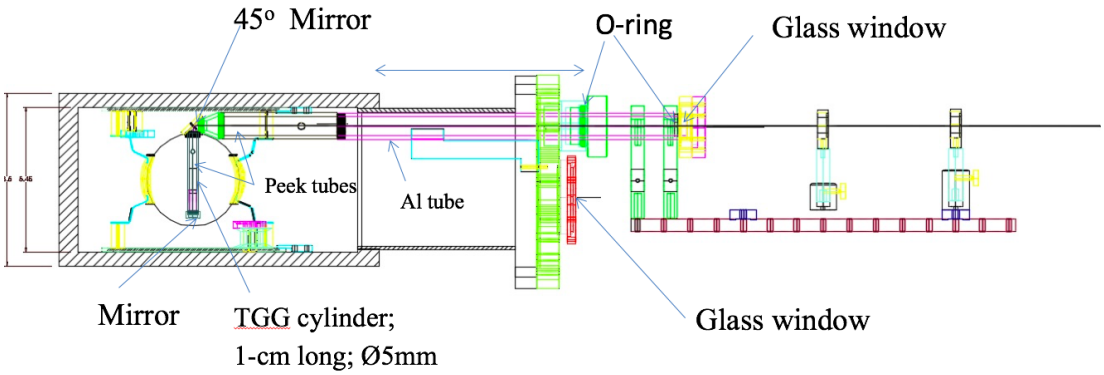

Fig. A.4: The design concept of the Faraday magnetometer used to measure the kicker field strength of the Muon $g-2$ experiment [255].

initial intensity I_0. By choosing the polariser to have an initial polarisation angle of $\theta = \frac{\pi}{4}$, the intensity of the light is given by $I = I_0 \cos^2(\frac{\pi}{4})$. Should the influence of the B field then introduce a rotation angle $\Delta\theta$ on the plane of polarisation, it follows that

$$\begin{aligned} I &= I_0 \cos^2(\frac{\pi}{4} + \Delta\theta) \\ &= I_0 \frac{1 + \cos(\frac{\pi}{2} + 2\Delta\theta)}{2} \\ &= I_0 \frac{1 - \sin(2\Delta\theta)}{2}, \end{aligned} \tag{A.3}$$

which, when rearranged to find $\Delta\theta$ and combined with equation (A.1), results in

$$B = \frac{1}{2Vd} \sin^{-1}\left(1 - \frac{2I}{I_0}\right). \tag{A.4}$$

Now, at the set angle of $\theta = \frac{\pi}{4}$, the measured intensity is given by $I = \frac{1}{2}I_0$. It follows that when measuring a signal that introduces a deviation $\Delta\theta$ from $\theta = \frac{\pi}{4}$, the deviation in the measured intensity is given by $I = \frac{1}{2}I_0 + \Delta I$. Therefore,

$$B = \frac{1}{2Vd} \sin^{-1}\left(1 - \frac{2(\frac{1}{2}I_0 + \Delta I)}{I_0}\right) \tag{A.5}$$

$$= \frac{-1}{2Vd} \sin^{-1}\left(\frac{2\Delta I}{I_0}\right), \tag{A.6}$$

meaning that to determine the field strength B requires knowing only know the Verdet constant of the Faraday rotator V for a given wavelength, the length of the Faraday rotator d, the measured signal ΔI and the initial intensity I_0.[1]

A.2.2 The Faraday magnetometer for the Muon $g-2$ experiment

To be able to measure the kicker field strength of the Muon $g-2$ experiment requires the TGG crystal to reside in the kicker field, specifically centred radially and vertically

[1] In addition, it is possible to calibrate the Faraday magnetometer by measuring the change in intensity induced by a magnetic field source with a field strength that is known to a high precision.

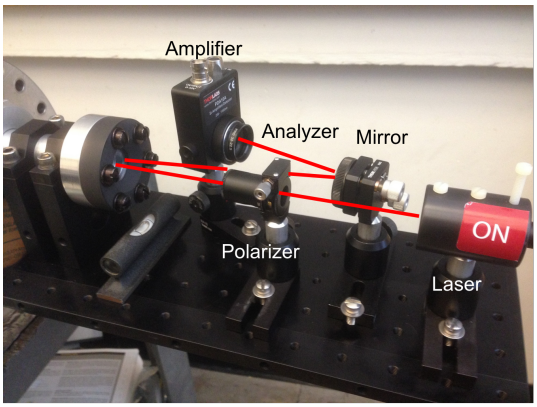

Fig. A.5: A photograph of the parts of the magnetometer that exist outside the vacuum chamber and the trajectory of the laser light. The laser light passes through the first polariser, along the magnetometer arm inside the SRV chamber, through the TGG crystal, back along the magnetometer arm out of the SRV chamber, reflected off the mirror into the second polariser and into the amplifier.

between the kicker magnet plates of either K1, K2 or K3 situated inside the vacuum chamber of the storage ring. The design concept of the magnetometer is shown in Figure A.4 [255]. The TGG crystal is attached at 90° to a tubing arm that passes through a flange and into the storage ring. The arm is rotatable and adjustable to ensure that the crystal is centred between the kicker plates without damaging the kicker plates or the crystal.[2] The laser is situated outside of the vacuum chamber and the light is directed first through a polariser (to counteract the polarisation of the laser light itself) and then projected through an A1 tube towards the crystal. This can be seen in the annotated picture in Figure A.5. Once the laser light has passed into the vacuum chamber through the A1 tube, a 45° mirror at the end of the tubing arm directs the laser light down through the crystal. It is then reflected by a second mirror back through the path it came from through the crystal, the 45° mirror and the A1 tube.[3] Should the crystal be subject to a magnetic field (such as the kicker field), then the polarisation angle of the laser light passing through it is shifted by $\Delta\theta$ which is proportional to the magnitude of the field, as given by equation (A.1). Following the trajectory of the laser light in Figure A.5, the light then passes out of the vacuum chamber, through a second polariser (which is set at the polarisation angle $\theta = \frac{\pi}{4}$) and is reflected by a mirror into an amplifier which records the signal as a change in voltage. This change in voltage ΔV is exactly the change in intensity ΔI that is used as input into equation (A.5).

[2]This freedom to rotate and retract the magnetometer arm also allows for the crystal to be moved out of the trajectory of the muon beam and the field trolley, which takes data regarding the magnetic field of the main storage ring magnet.

[3]As the laser passes through the crystal twice, this must be accounted for in the determination of the B field in equation (A.5). Hence, if the crystal has length l, then $d = 2l$.

Current (A)	Magnetometer measurement (T)	Metrolab measurement (T)
0.0	0.000	-
250.0	0.034	-
500.0	0.099	-
750.0	0.170	-
1000.0	0.247	-
1250.0	0.325	-
1500.0	0.403	-
1750.0	0.483	-
2000.0	0.555	-
2250.0	0.628	-
2500.0	0.708	-
2750.0	0.792	-
3000.0	0.871	0.88000
3250.0	0.950	-
3500.0	1.028	-
3750.0	1.103	-
4000.0	1.149	-
4250.0	1.214	-
4500.0	1.283	1.30000
4750.0	1.344	-
5000.0	1.401	-
5179.2	1.451	1.45103
5300.0		1.48000

Table A.1: The magnitude of the magnetic field of the $g-2$ storage ring magnet as measured by the Faraday magnetometer and a Metrolab device [258] at given values of the magnet current.

A.2.3 Testing the magnetometer: mapping the B field of the Muon $g-2$ storage ring magnet

The Muon $g-2$ storage ring magnet operates at a B field magnitude of 1.45 T, which corresponds to a generated current of 5179.2 A. When ramping up the magnet to the required current, the relationship between the current and the corresponding B field is non-linear and must be measured at specific points to determine the field corresponding to a given current. This has been done once previously using a Metrolab device [258], which measured the B field of the storage ring magnet at the values given in Table A.1 [259]. Below 3kA, the Metrolab is ineffective and could not measure the field magnitude.

In order to test the magnetometer, it was used to measure the relative B field of the storage ring magnet at different intervals of the current, which were then cross checked against the values taken by the Metrolab. The results of the raw data taken with the magnetometer over this exercise are shown in Figure A.6, where measurements of the change in signal intensity were taken at intervals of 250 A ramping down from

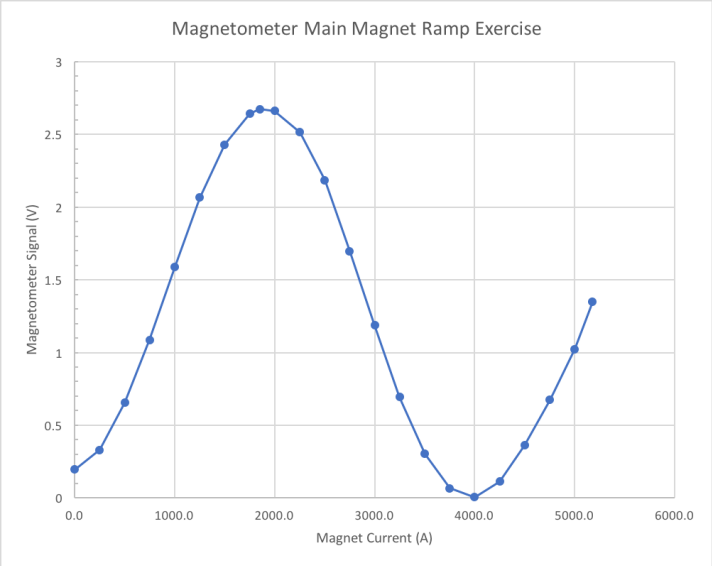

Fig. A.6: The data taken when using the magnetometer to measure the magnetic field of the storage ring magnet at intervals of 250 A.

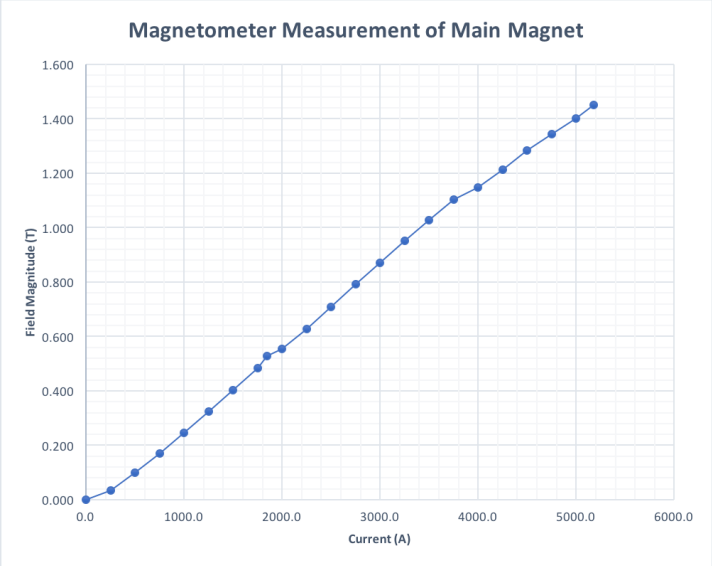

Fig. A.7: A map of the B field magnitude of the Muon $g-2$ storage ring magnet against the magnet current as measured by the Faraday magnetometer.

the nominal value of 5179.2 A to 0.0 amps.[4] It is clear from this that the change in the field magnitude is very well represented by change in the polarisation angle as given by Malus' Law in equation (A.2). Calculating the relative change of the B field magnitude with respect to the polarisation angle resulted in a map of the B field from 0.0 A to 5179.2 A as shown in Figure A.7. The values of the B field at each interval

[4]Note that although these measurements do not provide a resolution of the magnetic field at the level generated by the kicker plates, the magnetometer has been shown to have the sensitivity to measure the characteristics of the kicker pulse.

are given in Table A.1, which are compared with the available Metrolab measurements. The magnetometer is in fairly good agreement (without errors) with the Metrolab measurements and, therefore, provides a reliable map of the B field magnitude of the magnet at different current intervals. Following this, it can be assumed that the magnetometer can be used to make measurements of the kicker field strength, with the understanding that it will provide a reliable estimate of the field magnitude and pulse shape.

A.3 Results

A.3.1 Kicker 1

The measurements taken of the K1 pulse shape are shown in Figure A.8 and Figure A.9. Analysing these, it is important to note that the measurements taken by both the kicker pickup coil and the magnetometer are almost identical, confirming that the magnetometer measurements of the kicker pulse shape are reliable. For the principle pulse, this results in the following characteristics:

- Magnitude $= 169.4 \pm 14.1$ Gauss.[5]
- Duration ≈ 327.0 ns.
- Pulse average ≈ 82.5 Gauss.
- Full width, half maximum ≈ 149.5 ns.

Although the principle pulse magnitude is much smaller than the required 200-280 Gauss, it was discovered some time after the measurements of K1 were made that the TGG crystal was not radially centred between the kicker plates. This was seen in a photo taken by the field trolley during a pass around the storage ring, as can be seen in Figure A.10. Comparing this photo to the map of the B field magnitude associated

[5] Although the uncertainty on the magnitude here is much larger than required for a precision measurement of the kicker field, understanding the magnetometer in these initial stages of use required a conservative estimate of the corresponding error by correctly propagating the uncertainties on:

- The standard deviation of the DRSosc pulse averager.
- The uncertainty of the visual (by eye) determination DRS4 impedance correction: $C = (1.82 \pm 0.07)$.
- $2\times$ crystal length, $d = (0.022 \pm 0.00)$ m.
- Wavelength of the magnetometer laser $= (650 \pm 10)$ nm.
- Verdet constant of TGG crystal at 650 nm: $V = (-120.0 \pm 1.1)$ rad T^{-1} m^{-1}.
- Uncertainty of the visual (by eye) determination of the maximum signal voltage (intensity): $I_0 = (2.497 \pm 0.010)$ V.

The measurements of K2 and K3 have similar large errors. This was necessary it order for the measurements to be reliable but could very easily reduced by improving the magnetometer system and calculation procedure.

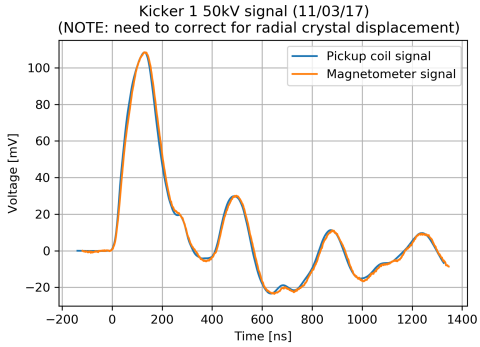

(a) Time (ns) vs. magnetometer signal (mV).

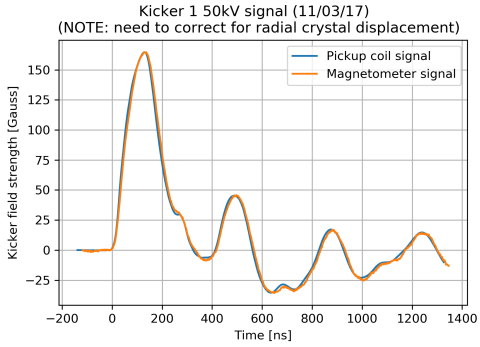

(b) Time (ns) vs. kicker field magnitude (Gauss).

Fig. A.8: Measurements of the field and pulse shape of kicker 1 taken from the magnetometer and kicker 1 pickup coil.

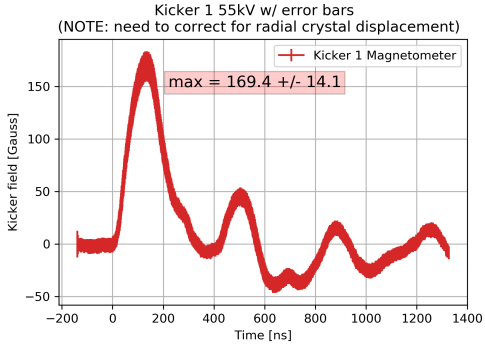

Fig. A.9: Measurements of the field and pulse shape of kicker 1 taken by the magnetometer in Gauss, where the width of the band represents the uncertainty on the field magnitude.

with the kicker plates shown in Figure A.3, it is evident that the positioning of the TGG crystal closer to the kicker plates could result in the magnetometer recording a larger field magnitude than the muon beam would be subject to when centred directly between the kicker plates. Therefore, it should be expected that the realistic B field magnitude that the muon beam would be subject to is even smaller than 169.4 Gauss. Having not met the required kick, it is clear this would result the muon beam not being

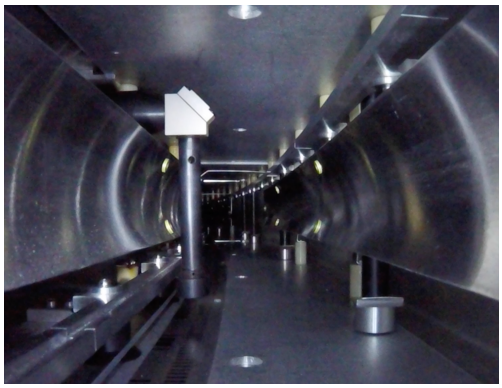

Fig. A.10: A picture of the position of the TGG crystal for the measurements made of K1 as seen by the field trolley in the radial direction of the beam.

fully displaced to the trajectory of the magic radius and would drastically impact the muon capture efficiency.

Another point of concern here is the behaviour of the tail of the pulse after ~ 350ns, where the shape is erratic and oscillates between a negative and positive value for the kicker field magnitude. Assuming a nominal B field magnitude for the kick, inputting this unwanted secondary feature of the pulse shape into muon injection simulations has been shown to have a large detrimental effect on the muon capture efficiency of the experiment, reducing the number of stored muons by $\sim 35\%$ [260]. It is therefore imperative that the source of this behaviour be understood and, if possible, eradicated in order to maximise the muon capture efficiency.

In order to determine whether certain environmental factors could have an influence on the pulse shape of the kicker and contribute to either the low pulse magnitude or the erratic tail behaviour, measurements of the pulse were taken under the following conditions to ascertain if they caused a variation of the pulse shape:

- Different levels of supplied kicker voltage.
- Interference from other kickers pulsing simultaneously.
- Interference from the electrostatic quadrupoles pulsing simultaneously.
- Interference from the B field of the Muon $g-2$ main storage ring magnet.

The results of all these tests are depicted in Figure A.11. In all cases it is evident that the pulse shape measured in Figure A.8 and, in particular, its secondary tail behaviour is not significantly influenced by any of these environmental factors. As such, it can be assumed that there is no reason to believe that the behaviour observed is not a feature of the kicker system itself. It should be noted, however, that plot (b) of Figure A.11 shows that the secondary pulse varies with the set voltage of the kicker, where the lower voltage causes the secondary pulse to occur later in the tail. This implies that the behaviour observed in the tail is dependent on the supplied voltage of the kick.

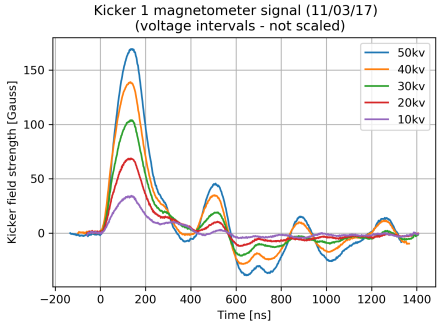

(a) Varying supplied kicker voltage.

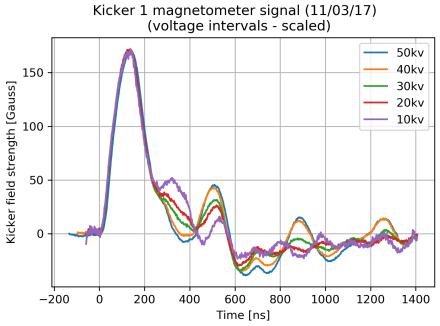

(b) Varying supplied kicker voltage (scaled to 50kV kicker magnitude).

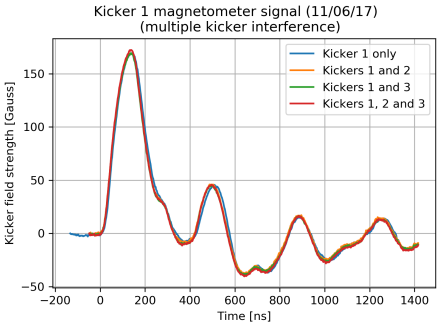

(c) Interference from other kickers.

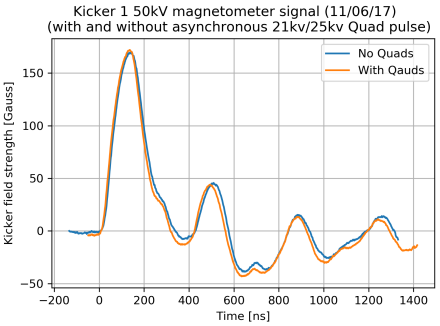

(d) Interference from quads.

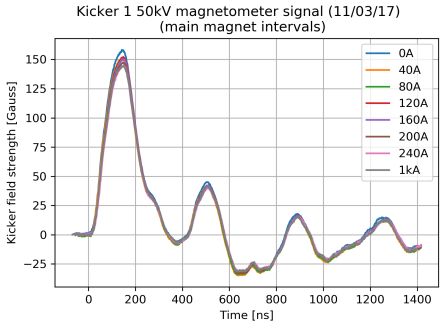

(e) Effect of the B field of the storage ring magnet.

Fig. A.11: Tests of environmental influence on the K1 pulse shape.

A.3.2 Kicker 2

For the K2 (and K3) measurements, the radial positioning of the TGG crystal that hindered the K1 measurements was corrected and the Faraday rotator was centred between the kicker plates as shown in Figure A.12. The measurements taken of the K2 pulse shape are shown in Figure A.13 and Figure A.14, where it is clear that the small magnitude and secondary tail behaviour of the pulse shape observed with K1 are features of the K2 measurements. Although the K2 pickup coil and magnetometer signals do not match as they do for the K1 signal, it should be noted that the pickup coil for K2 was damaged at the time of measurement and may consequently have influenced the signal. In addition to this, the K2 measurements suffered from the

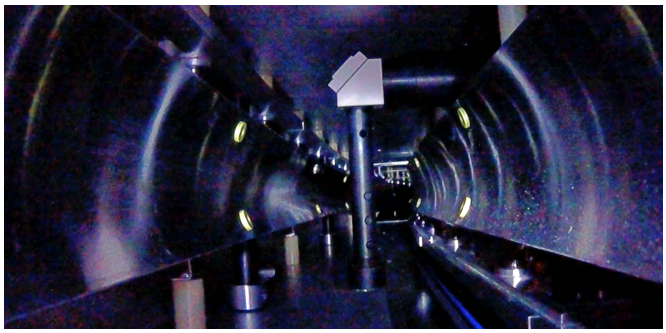

Fig. A.12: The radially centred position of the TGG crystal for the measurements made of K2 (and K3) as seen by the field trolley in the radial direction of the beam.

following setbacks:

1. When installing the magnetometer at the K2 position, it was discovered that a support stand for the kicker plate blocked the central entry of the magnetometer arm over the kicker plate. It was therefore necessary to rotate the magnetometer clockwise by one flange bolt-hole in order to bypass the support stand. This consequently altered the height of the TGG crystal relative to the kicker plate.

2. As the set-point voltages of the kicker GUI had not been calibrated at the time of measurement, the measurements made of K2 were taken when the kicker was pulsing at a voltage of ~ 62 kV.

Bearing these hindrances in mind, for the principle pulse, the results for K2 were:

- Magnitude $= 134.9 \pm 12.5$ Gauss.
- Duration ≈ 353.8 ns.
- Pulse average ≈ 60.4 Gauss.
- Full width, half maximum ≈ 145.2 ns.

A.3.3 Kicker 3

The measurements taken of the K3 pulse shape are shown in Figure A.15, where again the undesirable magnitude tail behaviour of the pulse seen in the measurements of K1 and K2 is also a feature of the K3 pulse shape. The measurements for K3 were taken at the correct position and at the nominal kicker voltage of 55 kV, making these the most reliable measurements of the true nature of the kicker field from the data of all three kickers in this work. The characteristic properties of the K3 principle pulse are:

- Magnitude $= 124.4 \pm 10.9$ Gauss.
- Duration ≈ 463.9 ns.

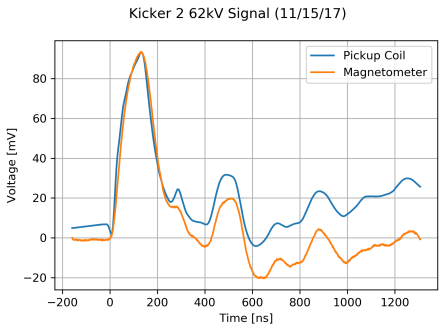

(a) Time (ns) vs. magnetometer signal (mV.)

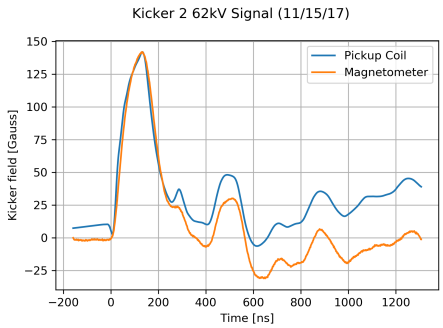

(b) Time (ns) vs. kicker field magnitude (Gauss).

Fig. A.13: Measurements of the field and pulse shape of K2 taken from the magnetometer and K2 pickup coil.

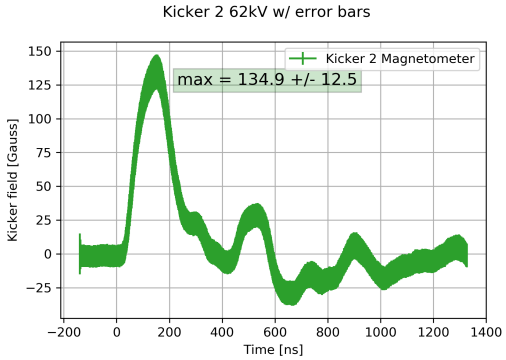

Fig. A.14: Measurements of the field and pulse shape of K2 taken by the magnetometer in Gauss, where the width of the band represents the uncertainty on the field magnitude.

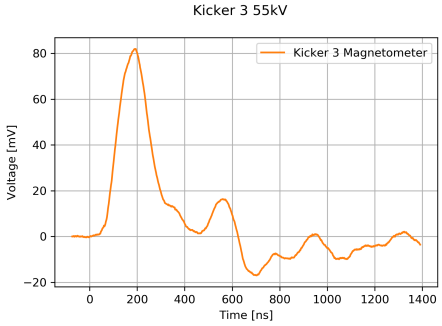

(a) Time (ns) vs. magnetometer signal (mV.)

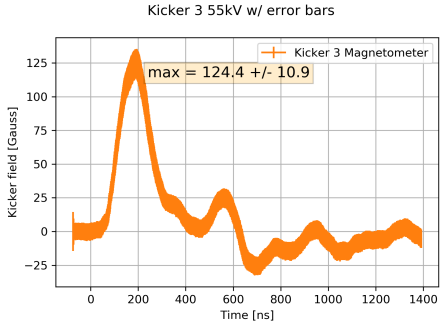

(b) Time (ns) vs. kicker field magnitude (Gauss). The width of the band represents the uncertainty on the field magnitude.

Fig. A.15: Measurements of the field and pulse shape of K3 made using the magnetometer.

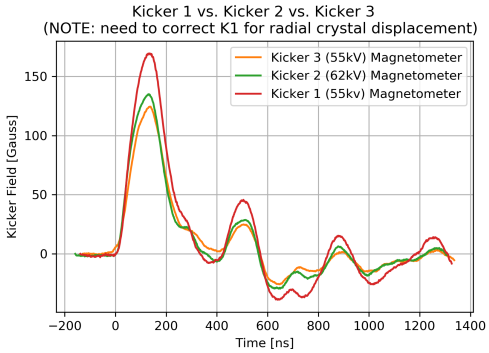

(a) Not scaled.

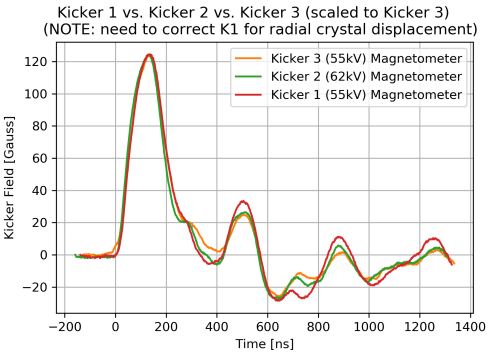

(b) Scaled to kicker 3 principle pulse magnitude.

Fig. A.16: A comparison of the pulse shapes of all three kickers.

- Pulse average ≈ 57.9 Gauss.
- Full width, half maximum ≈ 147.8 ns.

A.3.4 Comparing all three kickers

The comparison of the measured kicker pulse shapes of all three kickers is shown in Figure A.16, where plot (a) shows the unaltered comparison of the measurements and plot (b) compares the pulse shapes with all three measurements have been scaled to the principle pulse magnitude of K3. It should first be noted that, once scaled, the principle pulse shapes of all kickers are remarkably similar. However, this similarity continues into the tail, where the erratic negative behaviour is a prominent feature of all three kicks. Referring to the muon injection simulation using this pulse shape [260] implies that at the nominal voltage for all three kickers, the muon capture efficiency of the system as a whole is incurring a reduction of 35% due solely to this feature. As this secondary behaviour seems to oscillate between a positive and negative field value, the implication of the source of this behaviour point towards an impedance mismatch in the transmission of the pulse. It has been suggested that an impedance mismatch at the end of the blumlein could cause a reflection of the pulse back towards the thyratron [261]. Should a reflected voltage pass back to the thyratron, this could trigger a secondary

pulse and result in the pulse shape observed. This is (in part) supported by plot (b) of Figure A.11, where it is observed that the secondary pulse occurs sooner at a higher voltage, implying a dependence of the tail on the voltage.

A.4 Future improvements and conclusions

The Faraday magnetometer has been shown to be a useful tool in measuring the kicker field and pulse shape. It has been used to measure the properties of all three kicker plates. Moving forward, the measurements for all three kickers must be redone to improve their accuracy. Particularly, a digitiser other than the DRS4 should be used to record the signal, such that the dominant uncertainty due to this would therefore be removed. Indeed, an effort should be made to better understand the contributing uncertainties of all aspects of the magnetometer measurements in order to reliably minimise them. In addition, kicker 1 must be re-measured to account for the previous undesirable radial positioning of the TGG crystal between the kicker plates and kicker 2 must be re-measured at the nominal voltage.

Of particular importance are the magnitudes and secondary tail behaviour of the pulse shape of all three kickers, where the measurements taken here have been shown through simulation to have a detrimental effect of the muon capture efficiency. Being features of all three kickers and seemingly not due to an environmental factor influencing the shape, it is apparent that these effects are due to one or more elements of the kicker system itself. Above all, the magnitude of the kickers must be addressed in order to meet the requirements of the TDR and maximise the muon capture efficiency. These effects are currently being studied in great detail to ensure that resolutions to the issues are found and implemented in time for the high statistics data-taking period at Fermilab that is due to start in the very near future.

Appendix B

KLOE combination data

KLOE combination					
$s(\mathrm{GeV}^2)$	$\sigma^0_{\pi\pi(\gamma)}(\mathrm{nb})$	$\lvert F(\pi)\rvert^2$	$s(\mathrm{GeV}^2)$	$\sigma^0_{\pi\pi(\gamma)}(\mathrm{nb})$	$\lvert F(\pi)\rvert^2$
0.105	47.27 ± 8.41	1.74 ± 0.31	0.535	1154.56 ± 6.81	35.96 ± 0.21
0.115	70.65 ± 10.44	2.04 ± 0.30	0.545	1207.69 ± 6.83	38.20 ± 0.22
0.125	80.13 ± 10.97	2.00 ± 0.27	0.555	1243.32 ± 10.13	39.94 ± 0.33
0.135	80.42 ± 11.27	1.82 ± 0.26	0.565	1285.35 ± 7.14	41.92 ± 0.23
0.145	87.58 ± 11.70	1.86 ± 0.25	0.575	1277.36 ± 7.32	42.29 ± 0.24
0.155	102.88 ± 12.35	2.10 ± 0.25	0.585	1279.89 ± 7.31	42.98 ± 0.25
0.165	115.16 ± 13.85	2.29 ± 0.28	0.595	1274.03 ± 10.32	43.27 ± 0.35
0.175	122.58 ± 13.42	2.40 ± 0.26	0.605	1228.97 ± 12.29	42.18 ± 0.42
0.185	126.19 ± 12.61	2.45 ± 0.24	0.615	950.47 ± 20.95	34.85 ± 0.77
0.195	146.34 ± 14.10	2.84 ± 0.27	0.625	803.87 ± 4.65	29.94 ± 0.17
0.205	144.18 ± 13.35	2.80 ± 0.26	0.635	781.82 ± 4.39	29.24 ± 0.16
0.215	147.47 ± 12.68	2.88 ± 0.25	0.645	731.86 ± 5.74	27.61 ± 0.22
0.225	154.64 ± 11.98	3.04 ± 0.24	0.655	679.26 ± 3.93	25.90 ± 0.15
0.235	170.47 ± 12.40	3.39 ± 0.25	0.665	620.73 ± 3.46	23.93 ± 0.13
0.245	168.96 ± 11.53	3.40 ± 0.23	0.675	569.26 ± 4.63	22.20 ± 0.18
0.255	176.55 ± 10.84	3.60 ± 0.22	0.685	518.39 ± 5.62	20.45 ± 0.22
0.265	202.38 ± 11.63	4.18 ± 0.24	0.695	471.79 ± 2.69	18.82 ± 0.11
0.275	203.28 ± 10.70	4.26 ± 0.22	0.705	431.19 ± 2.44	17.39 ± 0.10
0.285	215.28 ± 10.60	4.58 ± 0.23	0.715	386.51 ± 3.21	15.76 ± 0.13
0.295	225.63 ± 10.46	4.87 ± 0.23	0.725	356.81 ± 2.03	14.70 ± 0.08
0.305	236.90 ± 10.49	5.19 ± 0.23	0.735	327.36 ± 1.91	13.63 ± 0.08
0.315	244.65 ± 10.11	5.45 ± 0.23	0.745	299.08 ± 1.96	12.59 ± 0.08
0.325	248.45 ± 9.83	5.62 ± 0.22	0.755	273.28 ± 1.80	11.62 ± 0.08
0.335	255.64 ± 9.62	5.88 ± 0.22	0.765	249.34 ± 1.45	10.71 ± 0.06
0.345	280.05 ± 9.46	6.54 ± 0.22	0.775	228.91 ± 1.94	9.93 ± 0.08
0.355	305.24 ± 4.55	7.24 ± 0.11	0.785	211.31 ± 1.27	9.26 ± 0.06
0.365	330.21 ± 7.67	7.96 ± 0.18	0.795	196.17 ± 1.36	8.68 ± 0.06
0.375	349.58 ± 4.60	8.56 ± 0.11	0.805	183.29 ± 1.08	8.19 ± 0.05
0.385	376.70 ± 4.63	9.37 ± 0.12	0.815	170.45 ± 1.00	7.69 ± 0.05
0.395	400.82 ± 4.57	10.12 ± 0.12	0.825	157.72 ± 1.09	7.19 ± 0.05
0.405	433.99 ± 6.28	11.13 ± 0.16	0.835	146.52 ± 0.95	6.74 ± 0.04
0.415	465.70 ± 4.79	12.13 ± 0.12	0.845	136.86 ± 0.79	6.36 ± 0.04
0.425	506.53 ± 4.87	13.39 ± 0.13	0.855	126.97 ± 0.78	5.95 ± 0.04
0.435	544.42 ± 4.84	14.61 ± 0.13	0.865	119.05 ± 0.89	5.63 ± 0.04
0.445	585.65 ± 5.04	15.95 ± 0.14	0.875	111.33 ± 0.83	5.31 ± 0.04
0.455	640.09 ± 7.95	17.69 ± 0.22	0.885	104.92 ± 1.81	5.05 ± 0.09
0.465	691.86 ± 7.66	19.41 ± 0.21	0.895	98.60 ± 0.59	4.79 ± 0.03
0.475	740.82 ± 8.20	21.09 ± 0.23	0.905	93.05 ± 0.56	4.56 ± 0.03
0.485	822.23 ± 5.82	23.75 ± 0.17	0.915	87.66 ± 0.74	4.33 ± 0.04
0.495	895.61 ± 17.85	26.26 ± 0.52	0.925	82.76 ± 0.49	4.13 ± 0.02
0.505	953.15 ± 13.08	28.36 ± 0.39	0.935	78.84 ± 0.65	3.96 ± 0.03
0.515	1032.72 ± 6.28	31.20 ± 0.19	0.945	74.74 ± 0.64	3.79 ± 0.03
0.525	1078.01 ± 8.23	33.06 ± 0.25	-	-	-

Table B.1: The combined KLOE measurement of the $\pi^+\pi^-\gamma(\gamma)$ bare cross section and pion form factor in 0.01 GeV^2 intervals from $0.10 < s < 0.95$ GeV^2. Here, s denotes the bin centre. For both $\sigma^0_{\pi\pi(\gamma)}$ and $|F(\pi)|^2$, the error shown is the total (statistical and systematic) uncertainty.

Appendix C

Determination of $\alpha(M_Z^2)$

The value of the effective QED coupling at the Z boson mass, $\alpha(M_Z^2)$, is the least precisely known of the three fundamental EW parameters of the SM (the Fermi constant G_F, M_Z and $\alpha(M_Z^2)$) and hinders the accuracy of EW precision fits. The uncertainty of $\alpha(M_Z^2)$ is dominated by the five-flavour hadronic contribution, $\Delta\alpha^{(5)}_{\text{had}}(M_Z^2)$, which (as with the hadronic contributions to a_μ) cannot be determined reliably using pQCD in the low energy regime and depends on experimentally measured hadronic cross section data. Following from the discussion of the VP corrections in Section 2.1.1, the five-flavour hadronic contribution to the QED coupling at the Z boson mass can be evaluated using the dispersion relation

$$\Delta\alpha^{(5)}_{\text{had}}(M_Z^2) = -\frac{\alpha M_Z^2}{3\pi}\text{P}\int_{s_{th}}^{\infty}\text{d}s\frac{R(s)}{s(s-M_Z^2)}\,. \tag{C.1}$$

The integral must be evaluated for the given energy range including the principal value $s = M_Z^2$, where the integrand in equation (C.1) is not well defined. The data input for $R(s)$ is identical to that used to determine $a_\mu^{\text{had, LO VP}}$ and $a_\mu^{\text{had, NLO VP}}$, except for the contribution from pQCD. The physical rapid variations that are part of the hadronic spectrum in the regions of flavour thresholds are not present in the pQCD determination of $R(s)$ as calculated by `rhad` [238]. For $\Delta\alpha^{(5)}_{\text{had}}(M_Z^2)$, to ensure that the contributions from the top quark threshold are not neglected, `rhad` is used to estimate $R^{(5)}(s)$ above 11.1985 GeV using only five active quark flavours. The top quark contributions are evaluated separately [62].

Due to the form of the integrand in equation (C.1), the integration procedure requires greater care than the trapezoidal rule integral utilised for $a_\mu^{\text{had, LO VP}}$. The behaviour of the kernel function $-1/\big(s(s-M_Z^2)\big)$ is shown in Figure C.1, where the nature of the principal value itself clearly indicates that the linear trapezoidal rule integral would provide a poor representation of the integrand and, consequently, an unreliable estimate of $\Delta\alpha^{(5)}_{\text{had}}(M_Z^2)$. Therefore, defining an interval ϵ to be some safe distance away from the principal value $s = M_Z^2$, the integral over $R(s)$ is determined individually over four energy regions:

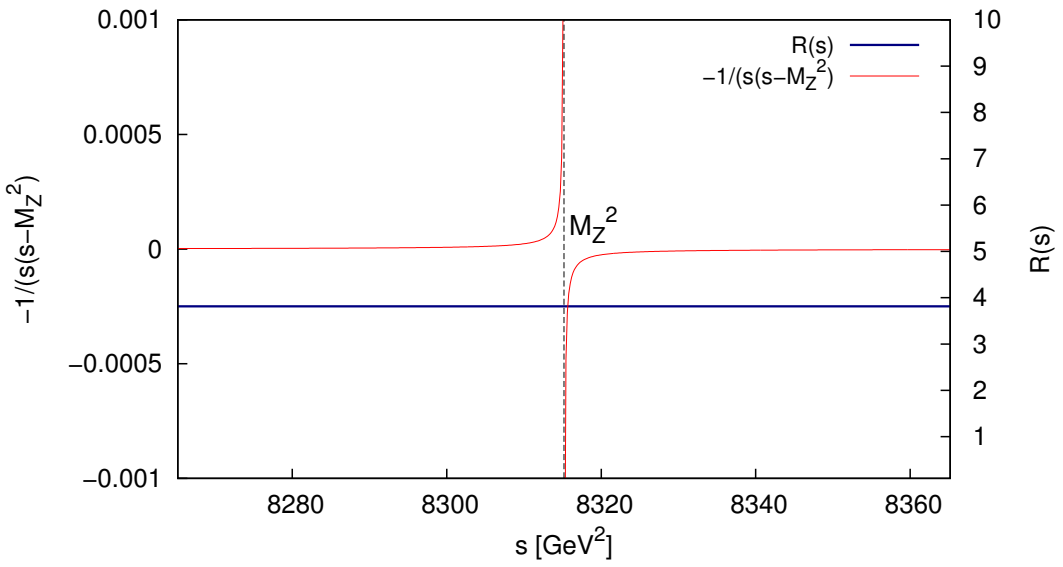

Fig. C.1: The behaviour of the function $-1/\big(s(s-M_Z^2)\big)$ at the principal value $s = M_Z^2$, which is present in the integrand of the dispersion relation for $\Delta\alpha^{(5)}_{\rm had}(M_Z^2)$. The behaviour of $R(s)$ in the same region is also plotted for reference. The value $s = M_Z^2$ is indicated by the dashed line.

- $m_\pi^2 \leq s \leq (M_Z^2 - \epsilon)$: this region is evaluated using the trapezoidal rule integration described in Section 2.5.

- $(M_Z^2 - \epsilon) \leq s \leq (M_Z^2 + \epsilon)$: to determine the principal value region, an iterative Gauss-Legendre integral is used. In this approach, the Lagrange polynomial interpolation provides a better and more accurate representation of the rapidly changing function than the linear approximation. The integration is performed iteratively where, at each stage, corresponding intervals either side of the principal value that are successively smaller and closer to the principal value are evaluated and summed. This is repeated until the integral converges to a well-defined solution.

- $(M_Z^2 + \epsilon) \leq s \leq (1000.1985\ \text{GeV})^2$: this region is evaluated using the trapezoidal rule integration described in Section 2.5.

- $(1000.1985\ \text{GeV})^2 \leq s \leq \infty$: the contribution to the dispersion integral above the pQCD cut-off and up to $s = \infty$ is not negligible as it is for $a_\mu^{\text{had, LO VP}}$. However, it can be estimated using the knowledge that, in this region, $R(s)$ is approximately constant. If from pQCD, $s_{\rm max} = (1000.1985\ \text{GeV})^2$, then in the range $s_{\rm max} \leq s \leq \infty$, the dispersion relation in equation (C.1) is then given by

$$\Delta\alpha^{(5)}_{\rm had}(M_Z^2)[s_{\rm max} \leq s \leq \infty] \simeq -\frac{\alpha M_Z^2}{3\pi} R(s_{\rm max}) \int_{s_{\rm max}}^{\infty} {\rm d}s \frac{1}{s(s-M_Z^2)}\,. \qquad \text{(C.2)}$$

Evaluating the integral by making the substitution $u = 1/s$ results in

$$\Delta\alpha^{(5)}_{\rm had}(M_Z^2)[s_{\rm max} \leq s \leq \infty] \simeq \frac{\alpha}{3\pi} R(s_{\rm max}) \ln\left(|(M_Z^2/s_{\rm max}) - 1|\right), \tag{C.3}$$

which can be safely evaluated.

As all contributions to $\Delta\alpha^{(5)}_{\rm had}(M_Z^2)$ above the principal value are negative due to the form of the kernel function displayed in Figure C.1, the correlation between data above and below $s = M_Z^2$ results in a reduction in the total uncertainty. In the case of $R(s)$ determined in this work, this is true for the correlated uncertainties from pQCD above 11.1985 GeV. This is fully accounted for in the determination of $\Delta\alpha^{(5)}_{\rm had}(M_Z^2)$.

Table C.1 lists all contributions from individual channels contributing to $\Delta\alpha^{(5)}_{\rm had}(M_Z^2)$, with the corresponding total. From the sum of these contributions, the estimate for $\Delta\alpha^{(5)}_{\rm had}(M_Z^2)$ is

$$\begin{aligned}\Delta\alpha^{(5)}_{\rm had}(M_Z^2) &= (276.11 \pm 0.26_{\rm stat} \pm 0.68_{\rm sys} \pm 0.14_{\rm vp} \pm 0.83_{\rm fsr}) \times 10^{-4} \\ &= (276.11 \pm 1.11_{\rm tot}) \times 10^{-4}\,. \end{aligned} \tag{C.4}$$

The errors from the individual channels and sources of uncertainty are added in quadrature to determine the total error. The fractional contributions to the total mean value and uncertainty of $\Delta\alpha^{(5)}_{\rm had}(M_Z^2)$ from various energy intervals is shown in Figure C.2. Notably, in comparison with Figure 4.24, the pie chart depicting the fractional contributions to the (error)^2 of $\Delta\alpha^{(5)}_{\rm had}(M_Z^2)$ reveals how the uncertainty on this quantity is dominated by the contributions from the radiative correction uncertainties. Mostly, this large error contribution comes from the uncertainty due to possible FSR applied to the inclusive data above 1.937 GeV. This, in particular, highlights the differences in the kernel functions of the respective dispersion integrals for $a_\mu^{\rm had,\,LO\,VP}$ and $\Delta\alpha^{(5)}_{\rm had}(M_Z^2)$, where contributions from higher energies have a larger influence on $\Delta\alpha^{(5)}_{\rm had}(M_Z^2)$ than on $a_\mu^{\rm had,\,LO\,VP}$. If, instead of a data driven analysis, the region above 1.937 GeV was estimated using pQCD, it would effectively eliminate the impacting radiative correction uncertainties in this region.

Combining equation (C.4) with the leptonic contribution $\Delta\alpha_{\rm lep}(M_Z^2) = (314.979 \pm 0.002) \times 10^{-4}$ [59,60] and the contribution due to the top quark $\Delta\alpha_{\rm top}(M_Z^2) = (-0.7180 \pm 0.0054) \times 10^{-4}$ [61, 62], the total value of the QED coupling at the Z boson mass is found in this work to be

$$\begin{aligned}\alpha^{-1}(M_Z^2) &= \Big(1 - \Delta\alpha_{\rm lep}(M_Z^2) - \Delta\alpha^{(5)}_{\rm had}(M_Z^2) - \Delta\alpha_{\rm top}(M_Z^2)\Big)\alpha^{-1} \\ &= 128.946 \pm 0.015\,. \end{aligned} \tag{C.5}$$

A comparison of these results with other determinations of $\Delta\alpha^{(5)}_{\rm had}(M_Z^2)$ and $\alpha^{-1}(M_Z^2)$ is given in Table C.2. The smaller error of the DHMZ17 analysis [45] is a further indication that the choice to use either the available inclusive data or pQCD above ~ 2 GeV can have a large impact. In [45], the choice to use pQCD in this region reduces the total uncertainty compared to the estimate found in this analysis.

Channel	**Energy range (GeV)**	$\Delta\alpha^{(5)}_{\text{had}}(M_Z^2) \times 10^4$
Chiral perturbation theory (ChPT) threshold contributions		
$\pi^0\gamma$	$m_\pi \leq \sqrt{s} \leq 0.600$	0.00 ± 0.00
$\pi^+\pi^-$	$2m_\pi \leq \sqrt{s} \leq 0.305$	0.01 ± 0.00
$\pi^+\pi^-\pi^0$	$3m_\pi \leq \sqrt{s} \leq 0.660$	0.00 ± 0.00
$\eta\gamma$	$m_\eta \leq \sqrt{s} \leq 0.660$	0.00 ± 0.00
Data based channels ($\sqrt{s} \leq 1.937$ GeV)		
$\pi^0\gamma$	$0.600 \leq \sqrt{s} \leq 1.350$	0.36 ± 0.01
$\pi^+\pi^-$	$0.305 \leq \sqrt{s} \leq 1.937$	34.26 ± 0.12
$\pi^+\pi^-\pi^0$	$0.660 \leq \sqrt{s} \leq 1.937$	4.77 ± 0.08
$\pi^+\pi^-\pi^+\pi^-$	$0.613 \leq \sqrt{s} \leq 1.937$	4.02 ± 0.05
$\pi^+\pi^-\pi^0\pi^0$	$0.850 \leq \sqrt{s} \leq 1.937$	5.00 ± 0.20
$(2\pi^+2\pi^-\pi^0)_{\text{no }\eta}$	$1.013 \leq \sqrt{s} \leq 1.937$	0.33 ± 0.03
$3\pi^+3\pi^-$	$1.313 \leq \sqrt{s} \leq 1.937$	0.09 ± 0.01
$(2\pi^+2\pi^-2\pi^0)_{\text{no }\eta\omega}$	$1.322 \leq \sqrt{s} \leq 1.937$	0.51 ± 0.06
K^+K^-	$0.988 \leq \sqrt{s} \leq 1.937$	3.37 ± 0.03
$K^0_S K^0_L$	$1.004 \leq \sqrt{s} \leq 1.937$	1.77 ± 0.03
$KK\pi$	$1.260 \leq \sqrt{s} \leq 1.937$	0.89 ± 0.04
$KK2\pi$	$1.350 \leq \sqrt{s} \leq 1.937$	0.75 ± 0.03
$\eta\gamma$	$0.660 \leq \sqrt{s} \leq 1.760$	0.09 ± 0.00
$\eta\pi^+\pi^-$	$1.091 \leq \sqrt{s} \leq 1.937$	0.39 ± 0.02
$(\eta\pi^+\pi^-\pi^0)_{\text{no }\omega}$	$1.333 \leq \sqrt{s} \leq 1.937$	0.21 ± 0.05
$\eta 2\pi^+2\pi^-$	$1.338 \leq \sqrt{s} \leq 1.937$	0.03 ± 0.00
$\eta\omega$	$1.333 \leq \sqrt{s} \leq 1.937$	0.10 ± 0.01
$\omega(\to \pi^0\gamma)\pi^0$	$0.920 \leq \sqrt{s} \leq 1.937$	0.19 ± 0.00
$\eta\phi$	$1.569 \leq \sqrt{s} \leq 1.937$	0.15 ± 0.01
$\phi \to$ unaccounted	$0.988 \leq \sqrt{s} \leq 1.029$	0.01 ± 0.01
$\eta\omega\pi^0$	$1.550 \leq \sqrt{s} \leq 1.937$	0.14 ± 0.04
$\eta(\to \text{npp})K\bar{K}_{\text{no }\phi\to K\bar{K}}$	$1.569 \leq \sqrt{s} \leq 1.937$	0.00 ± 0.01
$p\bar{p}$	$1.890 \leq \sqrt{s} \leq 1.937$	0.01 ± 0.00
$n\bar{n}$	$1.912 \leq \sqrt{s} \leq 1.937$	0.01 ± 0.00
Estimated contributions ($\sqrt{s} \leq 1.937$ GeV)		
$(\pi^+\pi^-3\pi^0)_{\text{no }\eta}$	$1.013 \leq \sqrt{s} \leq 1.937$	0.16 ± 0.01
$(\pi^+\pi^-4\pi^0)_{\text{no }\eta}$	$1.313 \leq \sqrt{s} \leq 1.937$	0.08 ± 0.08
$KK3\pi$	$1.569 \leq \sqrt{s} \leq 1.937$	0.02 ± 0.01
$\omega(\to \text{npp})2\pi$	$1.285 \leq \sqrt{s} \leq 1.937$	0.03 ± 0.01
$\omega(\to \text{npp})3\pi$	$1.322 \leq \sqrt{s} \leq 1.937$	0.06 ± 0.01
$\omega(\to \text{npp})KK$	$1.569 \leq \sqrt{s} \leq 1.937$	0.00 ± 0.00
$\eta\pi^+\pi^-2\pi^0$	$1.338 \leq \sqrt{s} \leq 1.937$	0.03 ± 0.02
Other contributions ($\sqrt{s} > 1.937$ GeV)		
Inclusive channel	$1.937 \leq \sqrt{s} \leq 11.199$	82.82 ± 1.05
J/ψ	-	7.07 ± 0.22
ψ'	-	2.51 ± 0.06
$\Upsilon(1S-4S)$	-	1.06 ± 0.02
pQCD	$11.199 \leq \sqrt{s} \leq \infty$	124.79 ± 0.10
Total	$m_\pi \leq \sqrt{s} \leq \infty$	276.11 ± 1.11

Table C.1: Summary of the contributions to $\Delta\alpha^{(5)}_{\text{had}}(M_Z^2)$ calculated in this analysis. The first column indicates the hadronic final state or individual contribution, the second column gives the respective energy range of the contribution and the third column states the determined value of $\Delta\alpha^{(5)}_{\text{had}}(M_Z^2)$. The last row describes the total contribution obtained from the sum of the individual final states, with the uncertainties added in quadrature.

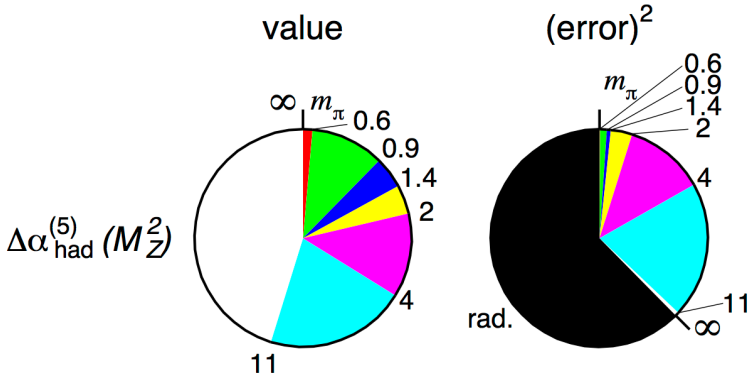

Fig. C.2: Pie charts showing the fractional contributions to the total mean value (left pie chart) and (error)^2 (right pie chart) of $\Delta\alpha^{(5)}_{\rm had}(M_Z^2)$ from various energy intervals. The energy intervals for $\Delta\alpha^{(5)}_{\rm had}(M_Z^2)$ are defined by the boundaries m_π, 0.6, 0.9, 1.43, 2.0, 4.0, 11.2 and ∞ GeV. The (error)^2 includes all experimental uncertainties (including all available correlations) and local $\chi^2_{\rm min}$/d.o.f. inflation. The fractional contribution to the (error)^2 from the radiative correction uncertainties are shown in black and indicated by 'rad.'.

Analysis	$\Delta\alpha^{(5)}_{\rm had}(M_Z^2)\times 10^4$	$\alpha^{-1}(M_Z^2)$
DHMZ10 [51]	275.59 ± 1.04	128.952 ± 0.014
HLMNT11 [21]	276.26 ± 1.38	128.944 ± 0.019
FJ17 [262]	277.38 ± 1.19	128.919 ± 0.022
DHMZ17 [45]	276.00 ± 0.94	128.947 ± 0.012
KNT18 [This work]	276.11 ± 1.11	128.946 ± 0.015

Table C.2: Comparison of recent and previous evaluations of $\Delta\alpha^{(5)}_{\rm had}(M_Z^2)$ determined from $e^+e^- \to$ hadrons cross section data and the corresponding results for $\alpha^{-1}(M_Z^2)$.

Bibliography

[1] P. A. M. Dirac, Proc. Roy. Soc. Lond. A **117** (1928) 610.

[2] P. A. M. Dirac, Proc. Roy. Soc. Lond. A **118** (1928) 351.

[3] J. S. Schwinger, Phys. Rev. **73** (1948) 416.

[4] S. Tomonaga, Prog. Theor. Phys. **1** (1946) 27.

[5] J. S. Schwinger, Phys. Rev. **74** (1948) 1439.

[6] R. P. Feynman, Phys. Rev. **76** (1949) 749.

[7] H. M. Foley and P. Kusch, Phys. Rev. **73** (1948) 412.

[8] P. Kusch and H. M. Foley, Phys. Rev. **74** (1948) 250.

[9] T. Aoyama, T. Kinoshita and M. Nio, Phys. Rev. D **97** (2018) 036001.

[10] D. Hanneke, S. Fogwell and G. Gabrielse, Phys. Rev. Lett. **100** (2008) 120801.

[11] D. Hanneke, S. F. Hoogerheide and G. Gabrielse, Phys. Rev. A **83** (2011) 052122.

[12] V. B. Berestetskii, O. N. Krokhin and A. K. Khelbnikov, Sov.Phys.JETP **3** (1956) 761.

[13] G. W. Bennett *et al.* [Muon g-2 Collaboration], Phys. Rev. Lett. **89** (2002) 101804 [Erratum: Phys. Rev. Lett. **89** (2002) 129903].

[14] G. W. Bennett *et al.* [Muon g-2 Collaboration], Phys. Rev. Lett. **92** (2004) 161802.

[15] G. W. Bennett *et al.* [Muon g-2 Collaboration], Phys. Rev. D **73** (2006) 072003.

[16] C. Patrignani *et al.* (Particle Data Group), Chin. Phys. C, 40, 100001 (2016) and 2017 update.

[17] J. Grange *et al.* [Muon g-2 Collaboration], arXiv:1501.06858.

[18] F. Jegerlehner and A. Nyffeler, Phys. Rept. **477** (2009) 1.

[19] P. J. Mohr, D. B. Newell and B. N. Taylor, Rev. Mod. Phys. **88** (2016) 035009.

[20] T. Mibe [J-PARC g-2 Collaboration], Chin. Phys. C **34** (2010) 745.

[21] K. Hagiwara, R. Liao, A. D. Martin, D. Nomura and T. Teubner, J. Phys. G **38** (2011) 085003.

[22] T. Aoyama, M. Hayakawa, T. Kinoshita and M. Nio, Phys. Rev. Lett. **109** (2012) 111808.

[23] P. A. Baikov, A. Maier and P. Marquard, Nucl. Phys. B **877** (2013) 647.

[24] A. Kurz, T. Liu, P. Marquard and M. Steinhauser, Nucl. Phys. B **879** (2014) 1.

[25] A. Kurz, T. Liu, P. Marquard, A. V. Smirnov, V. A. Smirnov and M. Steinhauser, Phys. Rev. D **92** (2015) 073019.

[26] A. Kurz, T. Liu, P. Marquard, A. Smirnov, V. Smirnov and M. Steinhauser, Phys. Rev. D **93** (2016) 053017.

[27] S. Laporta, Phys. Lett. B **772** (2017) 232.

[28] S. Volkov, Phys. Rev. D **96** (2017) 096018.

[29] A. Czarnecki, B. Krause and W. J. Marciano, Phys. Rev. D **52** (1995) R2619.

[30] A. Czarnecki, B. Krause and W. J. Marciano, Phys. Rev. Lett. **76** (1996) 3267.

[31] S. Peris, M. Perrottet and E. de Rafael, Phys. Lett. B **355** (1995) 523.

[32] A. Czarnecki, W. J. Marciano and A. Vainshtein, Phys. Rev. D **67** (2003) 073006 [Erratum: Phys. Rev. D **73** (2006) 119901].

[33] A. Czarnecki and W. J. Marciano, Phys. Rev. D **96** (2017) 113001 [Erratum: Phys. Rev. D **97** (2018) 019901].

[34] C. Gnendiger, D. Stöckinger and H. Stöckinger-Kim, Phys. Rev. D **88** (2013) 053005.

[35] A. Kurz, T. Liu, P. Marquard and M. Steinhauser, Phys. Lett. B **734** (2014) 144.

[36] F. Jegerlehner, EPJ Web Conf. **166** (2018) 00022.

[37] J. Prades, E. de Rafael and A. Vainshtein, Adv. Ser. Direct. High Energy Phys. **20** (2009) 303.

[38] K. Melnikov and A. Vainshtein, Phys. Rev. D **70** (2004) 113006.

[39] A. Nyffeler, Phys. Rev. D **79** (2009) 073012.

[40] G. Colangelo, M. Hoferichter, A. Nyffeler, M. Passera and P. Stoffer, Phys. Lett. B **735** (2014) 90.

[41] F. Jegerlehner, EPJ Web Conf. **118** (2016) 01016.

[42] V. Pauk and M. Vanderhaeghen, Eur. Phys. J. C **74** (2014) 3008.

[43] A. Nyffeler, Phys. Rev. D **94** (2016) 053006.

[44] A. Nyffeler, arXiv:1710.09742 [hep-ph].

[45] M. Davier, A. Hoecker, B. Malaescu and Z. Zhang, Eur. Phys. J. C **77** (2017), 827.

[46] K. Hagiwara, A. D. Martin, D. Nomura and T. Teubner, Phys. Rev. D **69** (2004) 093003.

[47] K. Hagiwara, A. D. Martin, D. Nomura and T. Teubner, Phys. Lett. B **649** (2007) 173.

[48] M. Davier, S. Eidelman, A. Hocker and Z. Zhang, Eur. Phys. J. C **31** (2003) 503.

[49] M. Davier, Nucl. Phys. Proc. Suppl. **169** (2007) 288.

[50] F. Jegerlehner, Nucl. Phys. Proc. Suppl. **162** (2006) 22.

[51] M. Davier, A. Hoecker, B. Malaescu and Z. Zhang, Eur. Phys. J. C **71** (2011) 1515 Erratum: [Eur. Phys. J. C **72** (2012) 1874].

[52] F. Jegerlehner and R. Szafron, Eur. Phys. J. C **71** (2011) 1632.

[53] B. A. Kniehl, Acta Phys. Polon. B **27** (1996) 3631.

[54] S. J. Brodsky and E. de Rafael, Phys. Rev. **168** (1968) 1620.

[55] B. E. Lautrup and E. de Rafael, Phys. Rev. **174** (1968) 1835.

[56] N. N. Achasov and A. V. Kiselev, Phys. Rev. D **65** (2002) 097302.

[57] B. Krause, Phys. Lett. B **390** (1997) 392.

[58] M. Gell-Mann and F. E. Low, Phys. Rev. **95** (1954) 1300.

[59] M. Steinhauser, Phys. Lett. B **429** (1998) 158.

[60] C. Sturm, Nucl. Phys. B **874** (2013) 698.

[61] K. G. Chetyrkin, J. H. Kuhn and M. Steinhauser, Phys. Lett. B **371** (1996) 93; Nucl. Phys. B 482 (1996) 213; Nucl. Phys. B 505 (1997) 40.

[62] J. H. Kuhn and M. Steinhauser, Phys. Lett. B **437** (1998) 425.

[63] A. Hoefer, J. Gluza and F. Jegerlehner, Eur. Phys. J. C **24** (2002) 51.

[64] J. Gluza, A. Hoefer, S. Jadach and F. Jegerlehner, Eur. Phys. J. C **28** (2003) 261.

[65] J. P. Lees *et al.* [BaBar Collaboration], Phys. Rev. D **92** (2015) 072015.

[66] T. Kinoshita, J. Math. Phys. **3** (1962) 650.

[67] T. D. Lee and M. Nauenberg, Phys. Rev. **133** (1964) B1549.

[68] A. Carroll, *Investigation into reduction of the uncertainties associated with the leading order hadronic contributions to the anomalous magnetic moment of the muon*, MSc Thesis (2013), University of Liverpool, UK.

[69] R. R. Akhmetshin *et al.*, Phys. Lett. B **364** (1995) 199.

[70] M. N. Achasov *et al.*, Phys. Rev. D **63** (2001) 072002.

[71] R. D. Ball *et al.* [NNPDF Collaboration], JHEP **1005** (2010) 075.

[72] M. Benayoun, P. David, L. DelBuono and F. Jegerlehner, Eur. Phys. J. C **75** (2015) 613.

[73] G. D'Agostini, Nucl. Instrum. Meth. A **346** (1994) 306.

[74] V. Blobel, eConf C **030908** (2003) MOET002.

[75] N. N. Achasov and A. V. Kiselev, Phys. Rev. D **65** (2002) 097302.

[76] G. Colangelo, M. Finkemeier and R. Urech, Phys. Rev. D **54** (1996) 4403.

[77] S. R. Amendolia *et al.* [NA7 Collaboration], Nucl. Phys. B **277** (1986) 168.

[78] E. A. Kuraev and Z. K. Silagadze, Phys. Atom. Nucl. **58** (1995) 1589.

[79] A. I. Ahmedov, G. V. Fedotovich, E. A. Kuraev and Z. K. Silagadze, JHEP **0209** (2002) 008.

[80] A. Pais, Annals Phys. **9** (1960) 548.

[81] D. J. Griffiths, NEW YORK, USA: WILEY (1987) 392.

[82] R. Liao [HLMNT11], *The anomalous magnetic moment of the muon and the QED coupling at the Z boson mass*, Doctoral Thesis (2011), University of Liverpool, UK.

[83] R. R. Akhmetshin *et al.*, JETP Lett. **84** (2006) 413.

[84] R. R. Akhmetshin *et al.* [CMD-2 Collaboration], Phys. Lett. B **648** (2007) 28.

[85] M. N. Achasov *et al.*, J. Exp. Theor. Phys. **103** (2006) 380.

[86] R. R. Akhmetshin *et al.* [CMD-2 Collaboration], Phys. Lett. B **669** (2008) 217.

[87] A. Keshavarzi, D. Nomura and T. Teubner, arXiv:1802.02995 [hep-ph].

[88] F. Ambrosino *et al.* [KLOE Collaboration], Phys. Lett. B **670** (2009) 285.

[89] F. Ambrosino *et al.* [KLOE Collaboration], Phys. Lett. B **700** (2011) 102.

[90] D. Babusci *et al.* [KLOE Collaboration], Phys. Lett. B **720** (2013) 336.

[91] S. Müller *et al.*, KLOE Note n. 221 (2008), `http://www.lnf.infn.it/kloe/pub/knote/kn221.pdf`.

[92] P. Beltrame *et al.*, KLOE Note n. 225 (2011), `http://www.lnf.infn.it/kloe/ppg/ppg_2010/kn225.pdf`.

[93] P. Lukin *et al.*, KLOE-2 Note K2PD-6 (2012), `http://www.lnf.infn.it/kloe2/tools/getfile.php?doc_fname=K2PD-6.pdf&doc_ftype=docs`.

[94] F. Jegerlehner (2003), `https://www-com.physik.hu-berlin.de/~fjeger/alphaQEDn.uu`.

[95] F. Jegerlehner (2016), `www-com.physik.hu-berlin.de/~fjeger/alphaQED16.tar.gz`, also see talk by F. Jegerlehner at Linear Collider Workshop 2010 (`http://www-com.physik.hu-berlin.de/~fjeger/SMalphas1.pdf`).

[96] S. Müller, Talk given at Radio MonteCarLOW Meeting, ECT, Trento (2013), '*The Whys and Hows of covariance matrices in the KLOE ISR analyses*', (`https://agenda.infn.it/getFile.py/access?contribId=35&sessionId=15&resId=0&materialId=slides&confId=6104`).

[97] S. Müller, Talk given at Radio MonteCarLOW Meeting, LNF, Frascati (2013), '*A combined estimate of the KLOE08, KLOE10 and KLOE12 ISR measurements*', (`https://agenda.infn.it/getFile.py/access?contribId=3&sessionId=2&resId=0&materialId=slides&confId=6618`).

[98] V. De Leo [KLOE and KLOE-2 Collaborations], EPJ Web Conf. **96** (2015) 01009.

[99] S. Müller, contribution to 'Constraining the Hadronic Contributions to the Muon Anomalous Magnetic Moment', edited by P. Masjuan *et al.*, arXiv:1306.2045 [hep-ph].

[100] G. D'Agostini, Nucl. Instrum. Meth. A **362** (1995) 487.

[101] G. D'Agostini, arXiv:1010.0632 (2010).

[102] S. Actis *et al.* [Working Group on Radiative Corrections and Monte Carlo Generators for Low Energies], Eur. Phys. J. C **66** (2010) 585.

[103] KLOE combination (2017) $\pi^+\pi^-\gamma$ (ppg) data web link, `http://www.lnf.infn.it/kloe/ppg/ppg_2017/ppg_2017.html`.

[104] M. N. Achasov *et al.*, Eur. Phys. J. C **12** (2000) 25.

[105] M. N. Achasov *et al.*, Phys. Lett. B **559** (2003) 171.

[106] R. R. Akhmetshin *et al.* [CMD-2 Collaboration], Phys. Lett. B **605** (2005) 26.

[107] M. N. Achasov *et al.* [SND Collaboration], Phys. Rev. D **93** (2016) 092001.

[108] M. Bernardini *et al.*, Phys. Lett. **46B** (1973) 261.

[109] D. Bollini, P. Giusti, T. Massam, L. Monari, F. Palmonari, G. Valenti and A. Zichichi, Lett. Nuovo Cim. **14** (1975) 418.

[110] B. Esposito *et al.*, Phys. Lett. **67B** (1977) 239.

[111] A. D. Bukin *et al.*, Phys. Lett. **73B** (1978) 226.

[112] A. Quenzer *et al.*, Phys. Lett. **76B** (1978) 512.

[113] I. A. Koop [OLYA Collaboration], Preprint, INP-79-67 (1979).

[114] I. B. Vasserman, L. M. Kurdadze, V. A. Sidorov, A. N. Skrinsky, A. G. Khabakhpashev, Y. M. Shatunov and B. A. Shvarts, Sov. J. Nucl. Phys. **30** (1979) 519.

[115] B. Esposito *et al.*, Lett. Nuovo Cim. **28** (1980) 337.

[116] I. B. Vasserman *et al.*, Sov. J. Nucl. Phys. **33** (1981) 368.

[117] S. R. Amendolia *et al.*, Phys. Lett. **138B** (1984) 454.

[118] L. M. Barkov *et al.*, Nucl. Phys. B **256** (1985) 365.

[119] D. Bisello *et al.* [DM2 Collaboration], Phys. Lett. B **220** (1989) 321.

[120] S. I. Dolinsky *et al.*, Phys. Rept. **202** (1991) 99.

[121] R. R. Akhmetshin *et al.* [CMD-2 Collaboration], Phys. Lett. B **578** (2004) 285.

[122] V. M. Aulchenko *et al.* [CMD-2 Collaboration], JETP Lett. **82** (2005) 743.

[123] M. N. Achasov *et al.*, J. Exp. Theor. Phys. **103** (2006) 380.

[124] R. R. Akhmetshin *et al.*, JETP Lett. **84** (2006) 413.

[125] R. R. Akhmetshin *et al.* [CMD-2 Collaboration], Phys. Lett. B **648** (2007) 28.

[126] B. Aubert *et al.* [BaBar Collaboration], Phys. Rev. Lett. **103** (2009) 231801.

[127] M. Ablikim *et al.* [BESIII Collaboration], Phys. Lett. B **753** (2016) 629.

[128] A. Anastasi *et al.* [KLOE-2 Collaboration], JHEP **1803** (2018) 173.

[129] A. Cordier *et al.*, Nucl. Phys. B **172** (1980) 13.

[130] L. M. Barkov [CMD Collaboration], Preprint, INP-89-15 (1989).

[131] A. Antonelli *et al.* [DM2 Collaboration], Z. Phys. C **56** (1992) 15.

[132] R. R. Akhmetshin *et al.*, Phys. Lett. B **434** (1998) 426.

[133] M. N. Achasov *et al.*, Phys. Rev. D **66** (2002) 032001.

[134] M. N. Achasov *et al.*, Phys. Rev. D **68** (2003) 052006.

[135] B. Aubert *et al.* [BaBar Collaboration], Phys. Rev. D **70** (2004) 072004.

[136] R. R. Akhmetshin *et al.*, Phys. Lett. B **642** (2006) 203.

[137] V. M. Aul'chenko *et al.*, J. Exp. Theor. Phys. **121** (2015) 27.

[138] S. Eidelman and F. Ignatov, private communication (2017).

[139] G. Cosme *et al.*, Phys. Lett. **63B** (1976) 349.

[140] A. Cordier *et al.*, Phys. Lett. **81B** (1979) 389.

[141] C. Bacci *et al.*, Phys. Lett. **95B** (1980) 139.

[142] A. Cordier, D. Bisello, J. C. Bizot, J. Buon, B. Delcourt, L. Fayard and F. Mane, Phys. Lett. **109B** (1982) 129.

[143] L. M. Kurdadze *et al.*, JETP Lett. **47** (1988) 512.

[144] L. M. Barkov *et al.*, Sov. J. Nucl. Phys. **47** (1988) 248.

[145] D. Bisello *et al.* [DM2 Collaboration], LAL-90-35.

[146] R. R. Akhmetshin *et al.* [CMD-2 Collaboration], Phys. Lett. B **475** (2000) 190.

[147] R. R. Akhmetshin *et al.* [CMD-2 Collaboration], Phys. Lett. B **491** (2000) 81.

[148] M. N. Achasov *et al.*, J. Exp. Theor. Phys. **96** (2003) 789.

[149] R. R. Akhmetshin *et al.* [CMD-2 Collaboration], Phys. Lett. B **595** (2004) 101.

[150] J. P. Lees *et al.* [BaBar Collaboration], Phys. Rev. D **85** (2012) 112009.

[151] R. R. Akhmetshin *et al.*, Phys. Lett. B **768** (2017) 345.

[152] B. Aubert *et al.* [BaBar Collaboration], Phys. Rev. D **71** (2005) 052001.

[153] C. Paulot, Doctoral Thesis (1979) Preprint, LAL-79/14.

[154] J. P. Lees *et al.* [BaBar Collaboration], Phys. Rev. D **96** (2017) 092009.

[155] C. Bacci *et al.*, Nucl. Phys. B **184** (1981) 31.

[156] B. Esposito *et al.*, Lett. Nuovo Cim. **31** (1981) 445.

[157] L. M. Kurdadze *et al.*, JETP Lett. **43** (1986) 643.

[158] R. R. Akhmetshin *et al.* [CMD-2 Collaboration], Phys. Lett. B **466** (1999) 392.

[159] A. Cordier, D. Bisello, J. C. Bizot, J. Buon, B. Delcourt and F. Mane, Phys. Lett. **106B** (1981) 155.

[160] B. Aubert *et al.* [BaBar Collaboration], Phys. Rev. D **76** (2007) 092005 [Erratum: Phys. Rev. D **77** (2008) 119902].

[161] D. Bisello, J. C. Bizot, J. Buon, A. Cordier, B. Delcourt and F. Mane, Phys. Lett. **107B** (1981) 145.

[162] M. Schioppa [DM2 Collaboration], *Thesis, Universita di Roma 'La Sapienza'* (1986).

[163] B. Aubert *et al.* [BaBar Collaboration], Phys. Rev. D **73** (2006) 052003.

[164] R. R. Akhmetshin *et al.* [CMD-3 Collaboration], Phys. Lett. B **723** (2013) 82.

[165] B. Delcourt, D. Bisello, J. C. Bizot, J. Buon, A. Cordier and F. Mane, Phys. Lett. **99B** (1981) 257.

[166] P. M. Ivanov *et al.*, Phys. Lett. **107B** (1981) 297.

[167] J. E. Augustin *et al.*, LAL-83-21.

[168] D. Bisello *et al.* [DM2 Collaboration], Z. Phys. C **39** (1988) 13.

[169] M. N. Achasov *et al.*, Phys. Rev. D **63** (2001) 072002.

[170] M. N. Achasov *et al.*, Phys. Rev. D **76** (2007) 072012.

[171] J. P. Lees *et al.* [BaBar Collaboration], Phys. Rev. D **88** (2013) 032013.

[172] M. N. Achasov *et al.*, Phys. Rev. D **94** (2016) 112006.

[173] E. A. Kozyrev *et al.*, Phys. Lett. B **779** (2018) 64.

[174] S. Eidelman, F. Ignatov and E. Kozyrev, private communication (2017).

[175] F. Mane, D. Bisello, J. C. Bizot, J. Buon, A. Cordier and B. Delcourt, Phys. Lett. **99B** (1981) 261.

[176] R. R. Akhmetshin *et al.* [CMD-2 Collaboration], Phys. Lett. B **466** (1999) 385 [Erratum: Phys. Lett. B **508** (2001) 217].

[177] R. R. Akhmetshin *et al.*, Phys. Lett. B **551** (2003) 27.

[178] M. N. Achasov *et al.*, J. Exp. Theor. Phys. **103** (2006) 720.

[179] J. P. Lees *et al.* [BaBar Collaboration], Phys. Rev. D **89** (2014) 092002.

[180] E. A. Kozyrev *et al.* [CMD-3 Collaboration], Phys. Lett. B **760** (2016) 314.

[181] F. Mane, D. Bisello, J. C. Bizot, J. Buon, A. Cordier and B. Delcourt, Phys. Lett. **112B** (1982) 178.

[182] D. Bisello *et al.* [DM2 Collaboration], Nucl. Phys. Proc. Suppl. **21** (1991) 111.

[183] D. Bisello *et al.*, Z. Phys. C **52** (1991) 227.

[184] B. Aubert *et al.* [BaBar Collaboration], Phys. Rev. D **77** (2008) 092002.

[185] J. P. Lees *et al.* [BaBar Collaboration], Phys. Rev. D **95** (2017) 052001.

[186] M. N. Achasov *et al.*, Phys. Rev. D **97** (2018) 032011.

[187] J. P. Lees *et al.* [BaBar Collaboration], Phys. Rev. D **95** (2017) 092005.

[188] B. Aubert *et al.* [BaBar Collaboration], Phys. Rev. D **76** (2007) 012008.

[189] J. P. Lees *et al.* [BaBar Collaboration], Phys. Rev. D **86** (2012) 012008.

[190] A. Cordier, D. Bisello, J. C. Bizot, J. Buon, B. Delcourt, L. Fayard and F. Mane, Phys. Lett. **110B** (1982) 335.

[191] D. N. Shemyakin *et al.*, Phys. Lett. B **756** (2016) 153.

[192] M. N. Achasov *et al.* [SND Collaboration], Preprint, INP-97-78 (1997).

[193] R. R. Akhmetshin *et al.* [CMD-2 Collaboration], Phys. Lett. B **460** (1999) 242.

[194] R. R. Akhmetshin *et al.* [CMD-2 Collaboration], Phys. Lett. B **509** (2001) 217.

[195] M. N. Achasov *et al.*, Phys. Rev. D **76** (2007) 077101.

[196] M. N. Achasov *et al.*, Phys. Rev. D **90** (2014) 032002.

[197] A. Antonelli *et al.* [DM2 Collaboration], Phys. Lett. B **212** (1988) 133.

[198] R. R. Akhmetshin *et al.* [CMD-2 Collaboration], Phys. Lett. B **489** (2000) 125.

[199] M. N. Achasov *et al.*, Phys. Rev. D **97** (2018) 012008.

[200] J. P. Lees *et al.* [BaBar Collaboration], Phys. Rev. D **97** (2018) 052007.

[201] R. R. Akhmetshin *et al.* [CMD-3 Collaboration], Phys. Lett. B **773** (2017) 150.

[202] M. N. Achasov *et al.*, Phys. Rev. D **94** (2016) 092002.

[203] M. N. Achasov *et al.*, Phys. Rev. D **94** (2016) 032010.

[204] S. I. Dolinsky *et al.*, Phys. Lett. B **174** (1986) 453.

[205] M. N. Achasov *et al.*, Nucl. Phys. B **569** (2000) 158.

[206] M. N. Achasov *et al.*, Phys. Lett. B **486** (2000) 29.

[207] R. R. Akhmetshin *et al.* [CMD-2 Collaboration], Phys. Lett. B **562** (2003) 173.

[208] F. Ambrosino *et al.* [KLOE Collaboration], Phys. Lett. B **669** (2008) 223.

[209] M. N. Achasov *et al.*, JETP Lett. **94** (2012) 734.

[210] M. N. Achasov *et al.*, Phys. Rev. D **94** (2016) 112001.

[211] B. Delcourt *et al.*, Phys. Lett. **86B** (1979) 395.

[212] D. Bisello *et al.*, Nucl. Phys. B **224** (1983) 379.

[213] D. Bisello *et al.* [DM2 Collaboration], Z. Phys. C **48** (1990) 23.

[214] A. Antonelli *et al.*, Phys. Lett. B **334** (1994) 431.

[215] B. Aubert *et al.* [BaBar Collaboration], Phys. Rev. D **73** (2006) 012005.

[216] R. R. Akhmetshin *et al.* [CMD-3 Collaboration], Phys. Lett. B **759** (2016) 634.

[217] A. Antonelli *et al.*, Nucl. Phys. B **517** (1998) 3.

[218] A. Antonelli *et al.*, Phys. Lett. B **313** (1993) 283.

[219] M. N. Achasov *et al.*, Phys. Rev. D **90** (2014) 112007.

[220] P. Bock *et al.* [DESY-Hamburg-Heidelberg-Munich Collaboration], Z. Phys. C **6** (1980) 125.

[221] H. Albrecht *et al.*, Phys. Lett. **116B** (1982) 383.

[222] E. Rice *et al.*, Phys. Rev. Lett. **48** (1982) 906.

[223] B. Niczyporuk *et al.* [LENA Collaboration], Z. Phys. C **15** (1982) 299.

[224] A. Osterheld *et al.*, SLAC-PUB-4160 (1986).

[225] Z. Jakubowski *et al.* [Crystal Ball Collaboration], Z. Phys. C **40** (1988) 49.

[226] C. Edwards *et al.*, SLAC-PUB-5160 (1990).

[227] A. E. Blinov *et al.*, Z. Phys. C **70** (1996) 31.

[228] R. Ammar *et al.* [CLEO Collaboration], Phys. Rev. D **57** (1998) 1350.

[229] J. Z. Bai *et al.* [BES Collaboration], Phys. Rev. Lett. **84** (2000) 594.

[230] J. Z. Bai *et al.* [BES Collaboration], Phys. Rev. Lett. **88** (2002) 101802.

[231] M. Ablikim *et al.* [BES Collaboration], Phys. Lett. B **641** (2006) 145.

[232] M. Ablikim *et al.*, Phys. Rev. Lett. **97** (2006) 262001.

[233] D. Besson *et al.* [CLEO Collaboration], Phys. Rev. D **76** (2007) 072008.

[234] B. Aubert *et al.* [BaBar Collaboration], Phys. Rev. Lett. **102** (2009) 012001.

[235] M. Ablikim *et al.* [BES Collaboration], Phys. Lett. B **677** (2009) 239.

[236] V. V. Anashin *et al.*, Phys. Lett. B **753** (2016) 533.

[237] V. V. Anashin *et al.*, Phys. Lett. B **770** (2017) 174.

[238] R. V. Harlander and M. Steinhauser, Comput. Phys. Commun. **153** (2003) 244.

[239] F. Jegerlehner, Springer Tracts Mod. Phys. **274** (2017) 1.

[240] T. Aoyama, M. Hayakawa, T. Kinoshita and M. Nio, Phys. Rev. D **77** (2008) 053012.

[241] T. Kinoshita and M. Nio, Phys. Rev. D **73** (2006) 053007.

[242] M. Davier [BaBar Collaboration], Talk given at Workshop on hadronic vacuum polarization contributions to muon $g-2$, KEK, Tsukuba (2018), '*Hadronic Vacuum Polarization Contributions to muon $g-2$: Recent Results and Status of Ongoing Analyses in BaBar*', (`https://kds.kek.jp/indico/event/26780/session/5/contribution/10/material/slides/0.pdf`).

[243] I. B. Logashenko [CMD-3 Collaboration], Talk given at Workshop on hadronic vacuum polarization contributions to muon $g-2$, KEK, Tsukuba (2018), '*Recent results from CMD-3*', (`https://kds.kek.jp/indico/event/26780/session/16/contribution/12/material/slides/0.pdf`).

[244] S. Serednyakov [SND Collaboration], Talk given at Workshop on hadronic vacuum polarization contributions to muon $g-2$, KEK, Tsukuba (2018), '*Recent results from SND*', (`https://kds.kek.jp/indico/event/26780/session/16/contribution/13/material/slides/0.pdf`).

[245] Y. Maeda [BELLE-2 Collaboration], Talk given at Workshop on hadronic vacuum polarization contributions to muon $g-2$, KEK, Tsukuba (2018), '$e^+e^- \to \pi^+\pi^-$ *cross section measurement in Belle II*', (`https://kds.kek.jp/indico/event/26780/session/5/contribution/9/material/slides/0.pdf`).

[246] C. Redmer [BESIII Collaboration], Talk given at Workshop on hadronic vacuum polarization contributions to muon $g-2$, KEK, Tsukuba (2018), '*Hadronic Cross Sections at BESIII*', (`https://kds.kek.jp/indico/event/26780/session/5/contribution/11/material/slides/0.pdf`).

[247] S. Eidelman, Talk given at Radio MonteCarLOW Meeting, JGU, Mainz (2017), '*Generator for* $e^+e^- \to$ hadrons', (`https://agenda.infn.it/getFile.py/access?contribId=11&resId=0&materialId=slides&confId=13068`).

[248] *The Muon* $g-2$ *Theory Initiative*, `https://indico.fnal.gov/event/13795/`.

[249] B. Chakraborty *et al.* [Fermilab Lattice and LATTICE-HPQCD and MILC Collaborations], Phys. Rev. Lett. **120** (2018) 152001.

[250] M. Della Morte *et al.*, JHEP **1710** (2017) 020.

[251] T. Blum *et al.*, arXiv:1801.07224 [hep-lat].

[252] C. M. Carloni Calame, M. Passera, L. Trentadue and G. Venanzoni, Phys. Lett. B **746** (2015) 325.

[253] G. Abbiendi *et al.*, Eur. Phys. J. C **77** (2017) 139.

[254] S. Kim, Nucl. Part. Phys. Proc. **273-275** (2016) 198.

[255] A. Mikhailichenko,
Notes/talks on the design and construction of the Faraday magnetometer, https://www.classe.cornell.edu/∼dlr/g-2/kicker/kicker/magnetometer/magnetometer.html.

[256] N. Froemming, *private communication*.

[257] Northrop Grumman International Trading Inc., SYNOPTICS,
$g-2$ experiment DocDB 9302-v1 [submitted by A.Keshavarzi],
https://gm2-docdb.fnal.gov/cgi-bin/private/ShowDocument?docid=9302.

[258] Metrolab Technology, https://www.metrolab.com/.

[259] B. Kiburg, *private communication*.

[260] D. Rubin, $g-2$ experiment DocDB 9425-v3,
https://gm2-docdb.fnal.gov/cgi-bin/private/RetrieveFile?docid=9524&filename=InjDepCollab20171201.pdf&version=3.

[261] B. Morse, *private communication*.

[262] F. Jegerlehner, arXiv:1711.06089 [hep-ph].